

Seismic basin effects over soft-sediment filled basins in Ottawa, Canada

by

Sylvia J. Hayek

A thesis submitted to the Faculty of Graduate and Postdoctoral

Affairs in partial fulfillment of the requirements

for the degree of

Master of Science

in

Department of Earth Sciences

Carleton University

Ottawa, Ontario

©2016

Sylvia J. Hayek

Abstract

Investigations were carried out for three soft-sediment filled basins in the Ottawa, Canada region to examine the contributions of 2 and 3D site effects on ground motions due to weak motion earthquakes. In order for a 1D ground motion modelling software program to produce transfer functions approaching the frequency peaks obtained from soil-to-rock ratios of local earthquake recordings, a detailed soil profile, local modulus reduction and damping ratio curves, and local earthquake recordings are required as input. However, soil-to-rock amplifications and spectral curves varied from the predicted 1D output, suggesting the influence of 2 and 3D effects. Horizontal particle motions on the soil sites do not match the orientations recorded on the rock site, with the direction of the motions depending on the frequencies examined.

Acknowledgements

I would like to express my profound gratitude to my thesis advisors Dr. Dariush Motazedian and Dr. James Hunter, who kept me on track with their advice, comments and their never ending enthusiasm. They're support has made this a truly enjoyable experience.

Furthermore, I would like to thank the homeowners who were willing to host a seismic station at their homes. In particular, many thanks to Patrick Cote, Keith Davidson and Bill and Iva Duncan, who went above and beyond to welcome the whole team on their properties. Also many thanks to the technicians, particularly Kevin Brewer who worked tirelessly on making sure the seismic stations were up and running even in the most inhospitable weather. Without these people, there would not have been any data to study.

Many thanks also to Heather Crow, Dr. Andre Pugin, Dr. Allison Bent, and Stephen Crane for their constant willingness to share their time to discuss their research, including data and results, and to the members of the thesis committee who provided valuable input and feedback.

And finally, I need to thank my loved ones who supported me, including my parents who have been behind me since I was little, my kids who put up with mommy always being busy, and especially my husband, who not only provided moral support but also editing and debugging advice!

Table of Contents

Abstract	i
Acknowledgements	ii
Table of Contents	iii
List of Tables	vi
List of Illustrations	viii
1. Introduction	1
2. Background	5
2.1 Source effects	6
2.2 Path effects	7
2.3 Instrument effects	8
2.4 Site effects	9
2.4.1 Seismic impedance	10
2.4.2 Resonance	11
2.4.3 Focusing/defocusing	13
2.4.4 Basin-edge effect	15
2.4.4 Other possible factors influencing local ground motion	16
2.4.6 Summary	21
2.5 Literature review of basin-edge effects	22
2.5.1 Basin-edge field experiments	23
2.5.2 Experimental results with regard to basin parametres	32
2.5.3 Summary of observations and modeling results of basin-edge effects	38
3. Setting and Data	47
3.1 Regional geology	47
3.2 Seismological setting.....	52
3.2.1 Tectonics	52
3.2.2 Seismicity	54
3.3 Study sites and experimental design	56
3.3.1 Lefaivre, Ontario	58
3.3.2 Heritage Park, Orleans, Ontario	60
3.3.3 Kinburn, Ontario	61
3.4 Horizontal to vertical spectral ratios (HVSR)	63
4. Data Observations	67

4.1 Time domain observations	68
4.1.1 Large amplifications	68
4.1.2 Duration	71
4.1.3 Character of signal	72
4.1.4 Particle motion	73
4.1.5 Delayed body wave arrivals on horizontals	80
4.2 Frequency domain observations	82
4.2.1 Data processing and sensitivities	86
4.2.2 General shape of soil-to-rock spectral amplification curves	92
4.2.3 Amplification	97
4.2.4 Fundamental frequency, f_0	99
4.2.5 Higher harmonics	100
4.2.6 Effects of source variables	105
4.2.7 Later “beats”	121
4.3 Discussion	123
5. 1D Ground Motion Modelling	135
5.1 1D modeling software	137
5.2 1D profiles for each of the basins	140
5.2.1 Lefaivre, ON	141
5.2.2 Heritage Park, Orleans, Ontario	143
5.2.3 Kinburn, Ontario	144
5.3 Input motions	147
5.4 Damping ratio and modulus reduction curves	148
5.4.1 Rock damping ratio and modulus reduction curves	150
5.4.2 Gravel damping ratio and modulus reduction curves	150
5.4.3 Sand damping ratio and modulus reduction curves	150
5.4.4 Clay damping ratio and modulus reduction curves	151
5.5 Testing variable dependency and sensitivity	154
5.5.1 Test profiles	155
5.6 Input waveforms	162
5.7 Results	163
5.7.1 Test profiles	163
5.7.2 Input waveforms	184
5.7.3 1D modeling results as compared to the recorded spectral ratios	188
5.7.4 Note about Proshake assumptions and limitations	193
5.8 Discussion of 1D modeling results	195
5.8.1 Test profile results – sensitivities to variables	195
5.8.2 1D modeling results versus the recorded spectral ratios	204
5.9 Conclusions	207

6. Particle Motion Analysis	210
6.1 Background	210
6.2 Particle motion plots.....	213
6.3 Azigram	218
6.4 Tests to determine program settings.....	220
6.4.1 Filtering and weighting	221
6.4.2 Displacement versus velocity plots	221
6.4.3 Response of rock site	221
6.4.4 Noise	222
6.4.5 Deconvolving rock from soil	223
6.5 Seismic particle motions on ORHO	224
6.6 Interpretation	227
6.7 Discussion	230
7. Discussion	232
7.1 Discussion of results of this study.....	232
7.2 Future work	241
7.3 Requirements for further study	243
8. Conclusions	247
References	250
Appendix A: Instrumentation	269
I. Station information.....	270
II. SAC displacement instrument response files	272
Appendix B: Seismic Data	274
I. List of strong motion recordings	275
II. List of weak motion recordings.....	275
III. SAC macros.....	282
Appendix C: Basin Profiles	284
I. Proshake	285
II. Data for basin profiles	286
Appendix D: Azigram	291

List of Tables

Table 3-1: Shear wave velocity readings for the most prominent bedrock types measured within the Ottawa region. Data from Hunter et al. (2010).....	50
Table 4-1: Orleans earthquake data used for spectral ratios	93
Table 4-2: Kinburn earthquake data used for spectral ratios	95
Table 4-3: Lefaiivre earthquake data used for spectral ratios	95
Table 4-4: Observed frequencies for peaks in amplifications for the three basins	100
Table 4-5: Calculated $V_{s_{equiv}}$, using HVSR-determined f_0 and the thickness of the clay down to the first major reflector (till layer)	102
Table 4-6: Calculated frequency of higher harmonics (in Hz), using $V_{s_{equiv}}$ calculated in Table 4-5	103
Table 4-7: V_s and f_0 determined from using the H_{equiv} method of Dobry et al. (1976)	104
Table 5-1: Strong motion records available in Proshake that were used for testing various profiles.....	147
Table 5-2: Local earthquakes used in the 1D ground motion analysis	148
Table 5-3: Fundamental frequencies and amplifications determined through 1D modelling using a simple two-layer profile (clay over rock) versus the values calculated using the Eqn 2.5 for determining the harmonic frequencies and Eqn 2.6 for resonance amplification, A_{res}	164
Table 5-4: Results for the till layer tests using a simple 3-layer model as seen in Fig. 5-6B, varying the till thickness, V_s , γ_b , modulus reduction and damping ratio curves, and ratio of till:clay.....	170
Table 5-5: Results for the clay layer tests using a simple 2-layer model as seen in Fig. 5-6A, varying the clay γ_b , V_s and thickness.....	173
Table 5-6: Results comparing the simple 2-layer model with the detailed profile built from the Kinburn borehole data, and the varying V_s of clay using the power equation, with and without a 6m crust of higher V_s	175
Table 5-7: Results comparing the various modulus reduction (MR) and damping ratio (DR) curves for clay for simple 2-layer model	176
Table 5-8: Results comparing the various modulus reduction and damping ratio curves for clay for simple 2-layer model	178
Table 5-9: Results comparing the Sun et al. (1988) MR curves with varying PIs and damping ratio curves.....	182

Table 5-10: List of recordings used for modelling the Kinburn basin.....	186
Table 5-11: List of recordings used for modelling the Lefaivre basin.....	187
Table 5-12: List of recordings used for modelling the Orleans basin.....	187

List of Illustrations

Fig. 2-1: Potential site-effects occurring over a sediment-filled basin: A) seismic impedance; B) resonance; C) focusing/defocusing; and D) basin-edge effects	9
Fig. 2-2: Configuration of array used in Cornou and Bard’s experiment in Grenoble, France	29
Fig. 2-3: Results of frequency analysis from the Alpine Valley experiment showing the expected amplification due to one-dimensional effects, and the actual recorded amplification	29
Fig. 2-4: A) Map of the Parkway basin showing the set-up of the array for the experiment, with the inset showing the location of the basin within New Zealand. B) The results showing the preferred direction of travel of the waves as determined from the Parkway experiment	31
Fig. 2-5: Results of Rayleigh wave motion modeling showing the change in expected motion as a function of period due to different velocity contrasts between the rock and overlying soil in a simple two layer model	35
Fig. 2-6: Recordings of a local earthquake (Rockland, ON; M3.1; 2012/09/22 at 17:36UT) from the Orleans basin comparing the three components of the rock site ORIO with the soil site ORHO recordings underneath at various bandpasses	40
Fig. 3-1: Map showing the approximate maximum extent of the Champlain Sea	48
Fig. 3-2: Average shear wave velocity data collected from various geophysical methods (surface reflection sites, landstreamer profiles and downhole surveys)	49
Fig. 3-3: Bedrock geology map of the Ottawa, ON – Hull, QC region	51
Fig. 3-4: Map of the west Quebec seismic zone, with ~5 years of regional seismicity ..	55
Fig. 3-5: Vs30 map of the Ottawa region from microzonation website	57
Fig. 3-6: 3D model of the Lefaivre basin showing the estimated topography (for 10m intervals), and the approximate location of borehole JA02-4	59
Fig. 3-7: Topographic map of Orleans basin, with location of cross-sections marked in yellow dashed lines	61
Fig. 3-8: Topographic map of the Kinburn basin	62
Fig. 3-9: Combined John Shaw Road - Grant Side Road sections	62

Fig. 3-10: Horizontal to vertical spectral ratios as determined at the seismograph site situated on the soft sediments at each basin	65
Fig. 3-11: Relation between fundamental site frequency and thickness of the soft soil sediment as determined empirically for the Ottawa region	66
Fig. 4-1: Three-component recordings of the $m_N3.6$ earthquake near Barry's Bay, ON on 2013/10/20 at 10:40 UT from all three basins	70
Fig. 4-2: Recordings of a local earthquake (Rockland, ON; $M3.1$; 2012/09/22 at 17:36 UT) from the Orleans basin comparing the three components of the rock site ORIO and then the soil site ORHO recordings underneath at various pass bands	74
Fig. 4-3: Plot of seismograph data from the three components of the Orleans basin pair (ORHO: black; ORIO: grey) plotted on the bottom with time in seconds, with particle motion plots of E-W vs Vertical (V), N-S vs V, and E-W vs N-S.....	76
Fig. 4-4: Particle motion plots (top 12 plots) of horizontal components of ORHO (E-W vs N-S) for the 2012/10/10 Vercheres, QC 4.5 m_N earthquake	78
Fig. 4-5: Bottom shows the P-arrival on the 3-component data from ORHO (black) and ORIO (grey) for the 2013/05/17 $m_N4.1$ earthquake near Shawville, QC. Top three plots are the particle motion plots (E vs Z; N vs Z; and E vs N) for the same time frame	79
Fig. 4-6: Three seconds of data around the P-arrivals for ORHO (black) and ORIO (grey) for the E-W, N-S and Vertical components of data respectively	82
Fig. 4-7: Plots A-C show the frequency content (JSSS in green and JSBS in black) for the three components: E-W, N-S and Z (vertical) respectively. Plot D is the root mean-squared average of the horizontals. Plot E shows the ratio of the horizontal to vertical components. Plot F is the soil to rock spectral ratio	84
Fig. 4-8: Data for the Buckingham $m_N4.1$ earthquake of 2011/09/18 using various degrees of smoothing of the FFT results, and then taking the soil to rock ratio	85
Fig. 4-9: Soil:Rock ratio of 30 s of shear wave data from the $M4.1$ Shawville, QC earthquake. Top figure shows when the start time of both rock and soil data is moved -2, -5 and +5 s from the original 30 s shear data. Bottom plot shows when only the start time of the soil data is moved -2, -5 and +5s	88
Fig. 4-10: Spectral ratios calculated for the $M4.5$ Vercheres, QC earthquake on the Orleans station pair for various durations of shear wave	91
Fig. 4-11: Orleans basin plotting the root mean squared average horizontals of the soil:rock for 11 individual, well recorded earthquakes in grey, and their average in black	96

Fig. 4-12: Kinburn basin data plotting average horizontal soil:rock ratios for 9 individual earthquakes (grey) and their average (black)	96
Fig. 4-13: Lefaivre basin data plotting average horizontal soil:rock ratios for 9 individual earthquakes (grey) and their average (black)	97
Fig. 4-14: Compilation of V_{int} data from various boreholes in the Ottawa region. A least-squares power law curve fit following the form of Dobry et al. (1976)	104
Fig. 4-15: Recorded spectral ratios with each earthquake colour-coded by time (red=oldest to purple=newest) for the Lefaivre basin data at top, followed by Orleans and Kinburn data	106
Fig. 4-16: Spectral ratios for earthquakes sorted by magnitude for Kinburn basin	109
Fig. 4-17: Spectral ratios for earthquakes sorted by distance for the Lefaivre basin ...	109
Fig. 4-18: Spectral ratios for earthquakes sorted by azimuth (from earthquake to seismic station) for the Lefaivre basin	110
Fig. 4-19: Transfer functions for earthquakes sorted by azimuth (from earthquake to seismic station) for the Orleans basin	111
Fig. 4-20: Spectral ratios for earthquakes sorted by azimuth (from earthquake to seismic station) for the Kinburn basin	112
Fig. 4-21: Soil to rock ratios for 3 earthquakes occurring in May 2013 located near Shawville, QC as recorded on the Orleans station pair	114
Fig. 4-22: Soil to rock ratios for 4 earthquakes occurring near Val-des-Bois, QC as recorded on the Orleans station pair	115
Fig. 4-23: Soil to rock ratios for 4 earthquakes occurring near Shawville, QC as recorded on the Lefaivre station pair	116
Fig. 4-24: Soil to rock ratios for 4 earthquakes occurring near Shawville, QC as recorded on the Kinburn station pair	116
Fig. 4-25: Soil to rock ratios for the 2011/08/23 Richmond, VA M5.8 earthquake as recorded on the Orleans station pair compared with the average ratios recorded from local earthquake data	118
Fig. 4-26: Soil to rock ratios for the 2012/10/28 Haida Gwaii, B.C. Mw 7.7 earthquake as recorded on the Orleans station pair compared with the average ratios recorded from local earthquake data	119
Fig. 4-27: Soil to rock ratios for the 2011/08/23 Richmond, VA M5.8 earthquake and the 2012/10/28 Haida Gwaii, B.C. Mw 7.7 earthquake as recorded on the Orleans station pair as compared with the average ratios recorded from local earthquake	120

Fig. 4-28: Soil to rock ratios (mean-squared horizontals) for the 2012/10/10 $m_N4.5$ Vercheres, QC earthquake as recorded on the Orleans basin pair. Time intervals are A) 0-30 s of shear; B) 30-60s of shear; C) 60-90s of shear; D) 90-120s of shear; and 0-120s of shear	122
Fig. 5-1: Stress-strain curve illustrating the behavior of a typical soil undergoing cyclical loading	138
Fig. 5-2: Detailed profile as entered into Proshake of the Kinburn basin near the soft-soil site JSSS	146
Fig. 5-3: Various relations of % damping ratio versus % strain for clays	153
Fig. 5-4: Schematic showing the standard layout and values used for: A) the simple two layer model of clay over bedrock; and B) the simple three-layer model with clay overlying till and bedrock	156
Fig. 5-5: Transfer functions as calculated with Proshake using the simple 2-layer profile (Fig. 5-6 A) with standard values, changing only the bulk unit weight of the rock layer from the standard value of 26 kN/m^3 to 24 kN/m^3 and 28 kN/m^3	164
Fig. 5-6: Transfer functions as calculated with Proshake using the simple 2-layer profile (Fig. 5-6 A) with standard values, changing only the V_s of the rock layer	165
Fig. 5-7: Transfer functions as calculated with Proshake using the simple 2-layer profile (Fig. 5-4 A) with standard values, changing only the modulus reduction and damping curves that define the rock layer	165
Fig. 5-8: Transfer functions as calculated with Proshake using the simple 3-layer profile (Fig. 5-6 B) with standard values, changing only the bulk unit weight of the till layer from the standard value of 21.7 kN/m^3 to 18 kN/m^3 and 24 kN/m^3	166
Fig. 5-9: Transfer functions as calculated with Proshake using the simple 3-layer profile (Fig. 5-4 B) with standard values, changing only the V_s of the till layer	167
Fig. 5-10: Transfer functions as calculated with Proshake using the simple 3-layer profile (Fig. 5-4 B) with standard values, changing only the choice of modulus reduction and damping curves of the till layer	168
Fig. 5-11: Transfer functions as calculated with Proshake using the simple 3-layer profile (Fig. 5-4 B) with standard values, changing only the thickness of the till	169
Fig. 5-12: Transfer functions as calculated with Proshake using the simple 3-layer profile (Fig. 5-4 B) with standard values, changing only the ratio of the clay and till layer thicknesses	170

Fig. 5-13: Transfer functions as calculated with Proshake using the simple 2-layer profile (Fig. 5-4 A) with standard values, changing only the bulk unit weight of the clay	172
Fig. 5-14: Transfer functions as calculated with Proshake using simple 2-layer profile (see Fig. 5-4 A) with standard values, changing the thickness of the clay layer	172
Fig. 5-15: Transfer functions as calculated with Proshake – comparing the results from the simple 2-layer profile (Fig. 5-4 A) with varying V_s	173
Fig. 5-16: Transfer functions as calculated with Proshake – comparing the results from the simple 2-layer profile (Fig. 5-4 A) with the results for increasing V_s with depth for the clay layer according to Eqn 5.9 power law	174
Fig. 5-17: Transfer functions as calculated with Proshake – comparing the results from the various modulus reduction and damping ratio curves as provided in Proshake. Using $PI = 40$ for Vucetic-Dobry and Ishibashi-Zhang curves	176
Fig. 5-18: Transfer functions as calculated with Proshake for 5 Californian strong motion recordings, as well as their average. Using Sun et al.'s modulus reduction curve for PI range of 40-80, with the upper bound damping ratio curve	178
Fig. 5-19: Transfer functions as calculated with Proshake for 5 Californian strong motion recordings, as well as their average. Using Vucetic-Dobry's modulus reduction and damping ratio curves for PI of 40	179
Fig. 5-20: Transfer functions as calculated with Proshake for 5 Californian strong motion recordings, as well as their average. Using Vucetic-Dobry's modulus reduction and damping ratio curves for PI of 40	179
Fig. 5-21: Transfer functions as calculated with Proshake for 5 Californian strong motion recordings, as well as their average. Using Vucetic-Dobry's modulus reduction and damping ratio curves for PI s of 20, 40 and 80	181
Fig. 5-22: Transfer functions as calculated with Proshake for 5 Californian strong motion recordings, as well as their average.; using Sun et al.'s modulus reduction for PI of 40-80 and upper bound damping ratio curve	182
Fig. 5-23: Comparison of the modelled transfer functions as calculated with Proshake, using the average from 5 Californian strong motion recordings as input, for the modulus reduction and damping ratio curves of Vucetic-Dobry ($PI=40$), Sun et al. ($PI=40-80$, upper bound), and Law et al.'s Leda Clay	183
Fig. 5-24: Comparison of the modelled transfer functions as calculated with Proshake, using the Leda Clay curves (Law et al., 1985) for the average from 5 Californian	

strong motion recordings as input versus the average from 12 local recordings from the weak motion seismograph site at the Kinburn basin rock site	185
Fig. 5-25: Comparison of the modelled transfer functions as calculated with Proshake, using the average from 12 local recordings from the weak motion seismograph site at the Kinburn basin rock site for the modulus reduction and damping ratio curves of Vucetic-Dobry (PI=40), Sun et al. (PI=40-80, upper bound), and Law et al.'s Leda Clay	185
Fig. 5-26: Comparison of the modelled transfer functions for various earthquakes using the detailed profile for Kinburn and Law et al.'s (1985) Leda clay curves as calculated with Proshake	188
Fig. 5-27: Comparison of the soil:rock ratios from actual recordings of 9 M3.5+ earthquakes at the Kinburn basin, versus the modelled transfer function for the detailed profile as calculated with Proshake	190
Fig. 5-28: Comparison of the soil:rock spectral ratios from averages of recordings of 9 M3.0+ earthquakes at the Lefavre basin, versus the modelled transfer function for the detailed profile as calculated with Proshake	191
Fig. 5-29: Comparison of the soil:rock ratios from actual recordings of 11 M3.5+ earthquakes at the Orleans basin, versus the modelled transfer function for the detailed profile as calculated with Proshake	192
Fig. 6-1: Graphical representation of the two body waves, P and S, showing the direction of travel and the direction of particle motion	211
Fig. 6-2: Graphical representation of the two types of surface waves, Love and Rayleigh waves, showing the direction of travel and the direction of particle motion	212
Fig. 6-3: Bottom shows the P-arrival on the 3 component data for the rock site (ORIO in light grey) for the 2013/05/17 $m_N4.1$ earthquake near Shawville, QC. Top three plots are the particle motion plots (E vs Z; N vs Z; and E vs N)	213
Fig. 6-4: ORHO data for the $m_N4.1$ 2013/05/17 Shawville, QC earthquake. The lower plot shows the 3-component waveform as recorded on the soil site. The rose plots at the top show the particle motion direction on ORHO for the following time segments: 40-95s (P, S and surface waves included), 41-51s (P wave only), 51-65s (mostly S wave), and 65-95s (mostly surface wave energy)	216
Fig. 6-5: ORHO (Orleans soil site) data for the $m_N4.1$ 2013/05/17 Shawville, QC earthquake. The lower plot shows the vertical component as recorded on the soil site. The rose plots at the top show the corresponding particle motion directions from	

ORHO for the entire P wave coda, and followed by 1s time windows throughout the P phase arrival (from 41-50s)	217
Fig. 6-6: The angle of particle motion for each sample of the two horizontal components (shown in the bottom plot: east in blue and north in black), is calculated and plotted in the top plot	219
Fig. 6-7: Particle motion analysis versus time for the bedrock site ORIO, showing the azimuth (black horizontal dashed line) and the backazimuth (white dashed line) for the 2013/05/17 m_N 5.2 Ladysmith, QC earthquake: a) broadband filtered from 0.3 – 5.0 Hz; and b) same filter but number of counts in bin multiplied by the amplitude	223
Fig. 6-8: Particle motion with respect to time for the soil site ORHO (dashed black line representing the event azimuth; backazimuth in white) for the 2013/05/30 m_N 3.7 Ladysmith, QC earthquake.	226
Fig. 6-9: Particle motion analysis with respect to time for the soil site ORHO (event azimuth in black, backazimuth in white) for the 2013/05/30 m_N 3.7 Shawville, QC earthquake, with data filtered around the fundamental frequency (0.8 ± 0.3 Hz) of the basin	226
Fig. 6-10: Particle motion analysis on soil site ORHO for three earthquakes from similar azimuths, narrowband filtered around the fundamental frequency	228

1. Introduction

Determining site effects on ground motion due to an earthquake is an important aspect of seismic hazard assessment. One-dimensional effects, like seismic impedance contrasts, can be estimated relatively easily if seismic properties of soil and rock are well known in regions where layers of soil overly flat bedrock. Numerous software programs exist to allow these effects to be modelled even for soils whose profiles change significantly with depth. However, in regions where the bedrock is not flat, the bedrock topography can contribute two- and three-dimensional effects, which can play a significant role in the resulting ground motion.

There are several different two- and three-dimensional effects to consider, including focusing/defocusing, resonance, and basin-edge effects (Hunter et al., 2010). Basin-edge effects arise as body waves convert to surface waves at a basin edge (Kawase, 1996). Surface waves traveling through a relatively low shear wave velocity soil can significantly amplify, at least for the weak seismic motions, and increase the duration of the resulting ground motions over the basin.

Several sediment-filled basins have been discovered underlying the mostly flat surface terrain in the Ottawa, Ontario valley (e.g. Aylsworth et al., 2000; Benjumea et al., 2003; Hunter et al., 2010). The Ottawa region is located along the edge of a moderately active seismic zone where there are several basins of various shapes and sizes being investigated for this study; hence, the role of the basin geometry as well as the role of

various earthquake source parameters can be compared. In this region, the shear wave seismic impedance contrast between the bedrock and overlaying sediments is large (Hunter et al., 2010), making site condition considerations even more important and complicated.

As a part of microzonation studies for city of Ottawa (<http://http-server.carleton.ca/~dariush/Microzonation/main.html>), three such soft-sediment filled basins have been instrumented with pairs of identical seismographs, one on bedrock and one on soil. The three basins are located in and around the Ottawa, Ontario region: one to the east near Lefaivre, ON; a second to the west, in Kinburn, ON; and a third is located in the east end of the city in Orleans, ON. All three basins have been extensively investigated in the past using various geophysical techniques in order to define their geometry and the material properties of the in-filling sediments and surrounding rock.

The primary goal of this thesis is to examine the earthquake recordings on the three soft-sediment filled basins in the Ottawa area in terms of their amplification, frequency content, and particle motion to determine the possible three-dimensional effects from the buried bedrock topography on the surface recordings, and specifically how much of this can be attributed to basin-edge effects.

Chapter 2 provides a background of multi-dimensional effects that may occur over a soft-sediment basin. A brief literature review is presented of previous experimental and observational results with regard to soil response over sediment filled basins, as well as a summary of results found through modeling work.

The general geological and seismological setting of the study area and a description of the basic experimental design are introduced in Chapter 3. Also included in this chapter are a detailed description of each of the three basins and the geophysical data that have been collected to help outline the basic geometry of the basins and the material properties of the infilling soils and surrounding bedrock.

Chapter 4 describes some general observations noted from the recorded data sets in both the time and frequency domains. Where possible these observations are compared with observations from other studies around the world, in order to determine and compare the resulting ground motions of the Ottawa region basins in terms of sediment-filled basins.

In order to quantify the two- and three-dimensional ground motion effects, the one-dimensional (1D) effects must first be determined. A thorough one-dimensional analysis is provided in Chapter 5. This includes the data used to build a 1D profile for each of the basins, a discussion on the sensitivity of the modelled output to each of the input variables, and some of the software limitations encountered. The model results are then compared to the recorded data in terms of frequency content and amplitude.

In Chapter 6, the recorded particle motion is investigated. The method used for processing and plotting the data is introduced, and the results of the analysis presented. The particle motions recorded on each basin with respect to earthquakes of varying parameters (e.g. magnitude, azimuth, distance, etc.) are discussed. Then each basin is

compared with the other two to determine whether the basin geometry and size control the results.

Finally, a summary of the results and the conclusions from this study are presented in Chapter 7. This chapter also includes a discussion of any limitations found, and further work that may be required for a better understanding of ground motions that can occur over these soft-sediment-filled basins due to local and regional earthquakes.

2. Background

Although it had been known for a long time that local geological conditions can greatly affect seismic site response, the subject of basin effects was brought to the forefront as a result of the 1985 Mexico M8.0 earthquake, which caused great damage within Mexico City, despite the epicentre being ~400 km away (Singh et al., 1988).

The recorded signals from sites located over the Mexico City basin showed amplifications that were significantly more than predicted by simple site amplification models (e.g.; Singh et al., 1988; Chávez-García et al., 1991; Cornou and Bard, 2003; Ramos-Martínez et al., 1997). Furthermore, the long duration of the signal could not be accounted for (e.g. Chávez-García and Bard, 1994), and the damage concentrations were not uniform over the basin (e.g. Flores et al., 1987). Some of these characteristics are also observed on the recordings made in the Ottawa region study area from local events over the last several years.

In order to understand and interpret the seismograph records, the factors that contribute to the earthquake recording must first be understood. The output of the seismograph is a convolution of the earthquake source, the path along which the waves travel, the local site conditions on which the site is located, and the instrument which records the motion.

$$Output = (Source) * (Path) * (Site) * (Instrument) \quad \dots [Eqn 2.1]$$

where * represents a convolution.

In the frequency domain this equation becomes a multiplication:

$$F(\text{Output}) = F(\text{Source}) \cdot F(\text{Path}) \cdot F(\text{Site}) \cdot F(\text{Instrument}) \quad \dots \text{ [Eqn 2.2]}$$

where $F(\text{output})$, $F(\text{Source})$, $F(\text{Path})$, $F(\text{Site})$ and $F(\text{Instrument})$ represent the Fourier transforms of each of the terms. In order to isolate the site effects from the rest of the recording, the other three terms must be understood and accounted for or removed by deconvolution.

2.1 Source effects

Earthquake characteristics, such as its magnitude and focal mechanism, give rise to a distinct source pattern. The signature of that earthquake is the energy created by a particular fault rupturing. Although this signature will be added to, damped, or modified in some way along its path to the recording site, this input signature can be detected in the final recordings.

When comparing the same earthquake recorded at two adjacent sites (e.g. rock and soil sites), the source signature measured at the rock surface will be similar. Hence, the recording from the rock site can be used as a reference site to remove the source signal from the soil site recording (e.g. Cornou and Bard, 2003; Stephenson et al., 2006).

When comparing different earthquakes recorded at the same site, however, source parameters such as magnitude, seismic moment, source spectra, stress drop, fault dimensions, slip, duration, and focal mechanism, etc. will have to be considered. Field et al. (2000) noted the importance of the focal mechanism (as well as other non-source parameters, such as azimuth) to the strength of the arriving signal in his investigations. In

general, the focal mechanisms for most of the events in the West Quebec Seismic Zone have not been determined due to a lack of data. Hence, only a comparison of different magnitudes can be used for comparing the effects of source parameters on the ground motions recorded at the study sites.

2.2 Path effects

Path effects arise from the signal being modified by the medium through which it passes. The path of a seismic wave will depend on the seismic properties of the medium (such as Q-value, seismic wave velocity, density), geometry of earth crust layering (such as Moho and other reflectors), azimuth (such as directivity effects) and distance of the earthquake focus vis-à-vis the recording site. Path effects have been found to have a significant result on the resulting ground motions recorded over basins (e.g. Kato et al., 1993), but cannot adequately account for the long duration and later arriving waves.

For the three Ottawa-area study basins, the rock sites were chosen to be placed immediately adjacent to the soil site on the basin – within a few kilometres. For earthquakes from the West Quebec seismic zone, the epicentral distances are generally of the order of at least a few tens of kilometres. Hence, the paths from the earthquake source to the rock and soil site are almost equivalent, except for the final few kilometres. In other words, the difference in the recordings on the station pairs should only reflect the last kilometres or the local geological (aka site) conditions.

The importance of path on soil response on the basins in the Ottawa region was unclear in earlier work done in the region. Due to lack of available data, no azimuthal

dependencies could be determined (Kolaj, 2010). Since 2010, there have been a significant number of additional events with a reasonable azimuthal and distance range variations. These new data are investigated to determine if any such path dependencies can be detected for the study basins.

2.3 Instrument effects

Each instrument has its own response to ground shaking, which it imparts to the recorded signal. In general, the instruments are designed to have a relatively flat response over the frequency band of interest. Short-period seismographs, for example, are used mainly for local, high frequency events, and hence have a flat response over the higher frequency range, whereas long-period seismographs have flat response over the lower frequencies to record larger, more distant teleseisms.

The instruments used in this experiment are identical broad-band seismographs, with a reasonably wide flat response over the range 0.1 Hz up to 10 Hz. Therefore, it is expected that the instruments affect all recorded frequencies of interest equally, and the results of any soil amplification effects can be compared directly.

However, in order to compare the results from different stations, the instrument response must first be removed. This can be done as long as the instrument response is known. For this study, identical instrument pairs were installed at the soil and rock site at each basin so that the two recordings at each basin can be compared directly. Details of the equipment used at each site are covered in Section 3.3 and in Appendix A.

2.4 Site effects

The known site effects are seismic impedance, resonance, focusing/defocusing and basin edge effects (see Fig. 2-1). The main purpose of this study is to examine basin-edge effects; however, in order to isolate these edge effects, other effects must first be understood and isolated. Below is a summary of each of these effects, their importance, and how their influence can be accounted for or quantified.

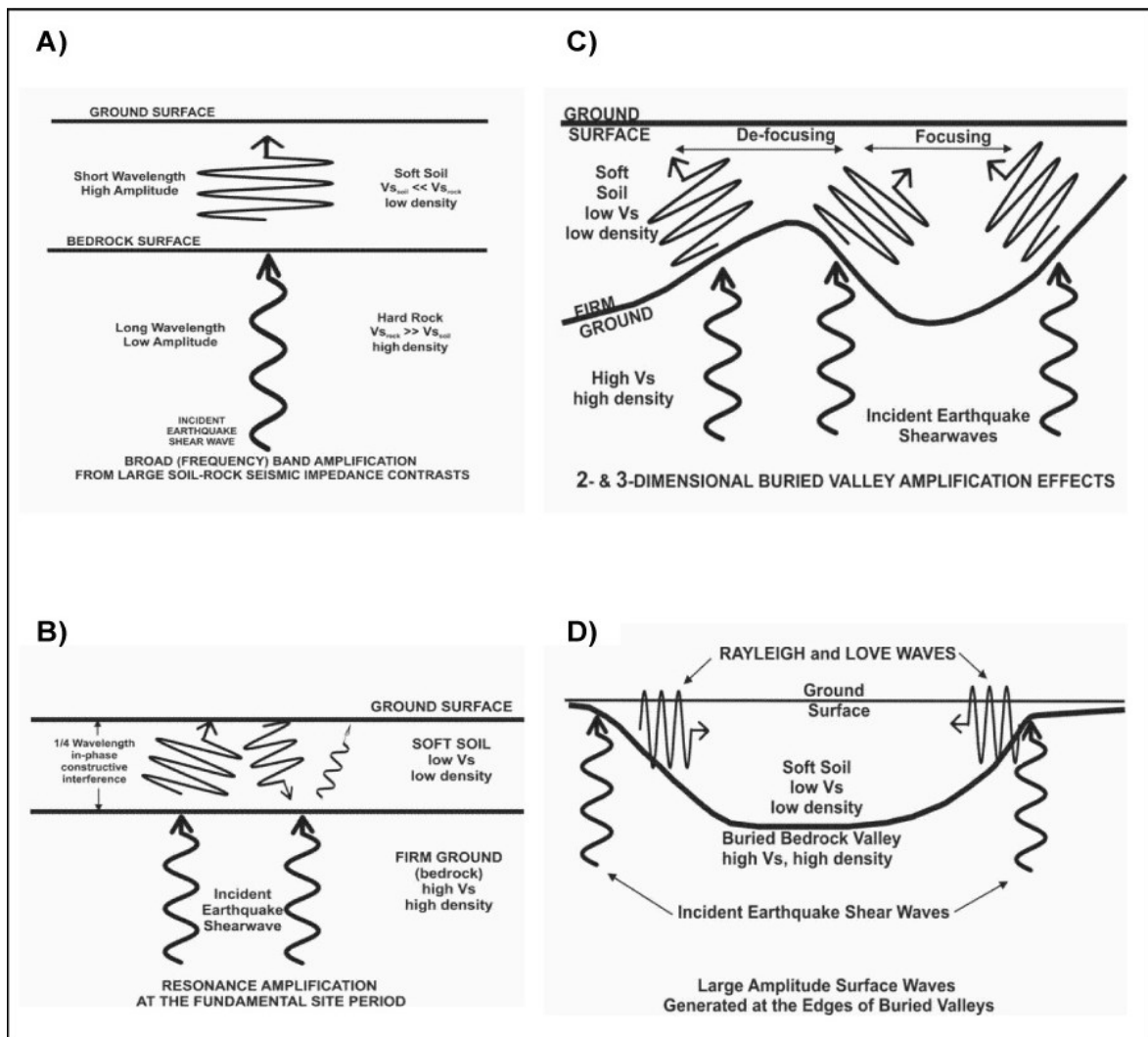


Fig. 2-1: Potential site-effects occurring over a sediment-filled basin: A) seismic impedance; B) resonance; C) focusing/defocusing; and D) basin-edge effects (after Hunter et al., 2010).

2.4.1 Seismic Impedance

Seismic shear wave impedance, which is the product of density (ρ) and shear wave velocity (V_s), is a seismic property of a material in regards to how much seismic energy is allowed to pass through. As the medium changes, for example from bedrock to soil, the amount of seismic impedance will also change. The seismic impedance contrast between two layers is the controlling factor on the amount of energy reflected or transmitted. For conservation of energy across an impedance boundary, as the wave passes through from the denser medium to the less dense medium, and the velocity of the wave decreases, the amplification must increase (see Fig. 2-1A). There is an unusual soil to rock seismic shear wave impedance contrast in the study area, commonly in the range of 12 to 45 (Hunter et al., 2010). Hence, seismic shear wave impedance plays an important role in the site response in the Ottawa region.

Not taking attenuation into account, the amplification due to seismic impedance contrast between soil and rock according to Shearer and Orcutt (1987) is:

$$A_{imp} = \sqrt{\frac{\text{Rock seismic impedance}}{\text{Soil seismic impedance}}} = \sqrt{\frac{\rho_{rock}V_{srock}}{\rho_{soil}V_{ssoil}}} \quad \dots \text{ [Eqn 2.3]}$$

where ρ is density and V_s is the shear wave velocity of the rock and soil respectively.

This amplitude approximation works well for regions where the density and shear wave velocity of the soil layer have well-defined average values, without gradual changes in the properties of the soil and rock.

Alternatively, Boore and Joyner (1997) used a quarter wavelength approximation with the amplification being:

$$A_{imp} = \sqrt{\frac{\text{Seismic impedance at rock reference depth}}{\text{Average Seismic impedance of soil over } 1/4 \text{ wavelength depth}}} = \sqrt{\frac{\rho_{ref}V_{sref}}{\rho_{avg}V_{savg}}} \dots \text{ [Eqn 2.4]}$$

where the set of values in the numerator are for a reference depth (e.g. bedrock surface boundary), and in the denominator the values are averaged soil seismic impedance from surface to a depth corresponding to a quarter of the wavelength of the incoming energy, thus making the calculated amplification frequency dependent.

As seismic impedance is relatively easy to calculate, this effect is now included in many models. However, over soft sediment-filled basins, these models commonly underestimated the amount of amplification, and are not able to predict the duration of the recordings (e.g., Kawase and Aki, 1989; Sanchez-Sesma et al., 1988, Chávez-García and Bard, 1994). Nor do they account for all the energy recorded at certain frequencies (Cornou and Bard, 2003). Thus, seismic shear impedance cannot be the only factor that needs to be considered for surface ground motions over basins.

2.4.2 Resonance

Resonance occurs when the incoming seismic waves become trapped within a sediment layer. For a horizontal surface layer of low velocity soil over high velocity bedrock, the waves become trapped and reflect back and forth between large impedance-contrast boundaries to produce resonance effects (see Fig. 2-1 B). The one-dimensional

resonance frequency depends on the soil thickness (H) and the average shear wave velocity of the soil ($V_{S_{avg}}$) (Rial et al., 1992).

The frequencies at which the resonance will occur are:

$$f_n = \frac{V_{S_{avg}}}{4H} (1 + 2n), \quad n = 0, 1, 2, 3 \dots \quad \dots \text{ [Eqn 2.5]}$$

where $V_{S_{avg}}$ is the average shear wave velocity of the soil and H is the height of the soil column. The fundamental frequency, f_0 , is the lowest frequency, and rest of the values of n represent the higher harmonics (Kramer, 1996).

The amplification produced by this is approximately:

$$A_{res} = \frac{\text{Rock seismic impedance}}{\text{Soil seismic impedance}} = \frac{\rho_{rock} V_{S_{rock}}}{\rho_{soil} V_{S_{soil}}} \quad \dots \text{ [Eqn 2.6]}$$

However, in a 2D or 3D basin, the sides of the basin also act to further confine the seismic waves. Bard and Bouchon's (1985) modeling of resonance showed that the energy of the incident wave is trapped within the valley, possibly explaining both the amplitude and the duration of the wave. The peak frequency was consistent across the basin, regardless of depth, and the motion was found to be in phase across the whole valley, with the greatest amplitude effect being at the centre of the basin, and diminishing towards the edges. This effect was much larger than that modeled by seismic impedance contrast only.

One of the prominent features found in 2D and 3D basins was the development of Love waves (see upcoming section S2.4.4 on Basin-Edge Effects) within the sediment

layer that propagated back and forth across the valley. Their models showed that the amplitude and dominant frequency was dependent on the ratio of the depth to width of the basin, both becoming larger for deeper basins (Bard and Bouchon, 1985).

Similar correlation with depth was described in Field et al. (2000) for the Los Angeles basin. Bard and Bouchon (1985) found the shallowest basin model showed a dominant frequency near to the one-dimensional resonance frequency, $V_{s,avg}/(4H)$. The results from this and previous studies (e.g.; King and Tucker, 1984) suggests that two-dimensional resonance occurred only for deeper, sediment-filled basins, as the resonance patterns involve both vertical and lateral interferences.

Kolaj (2010) found a significant resonance effect in the Orleans basin. Using mostly small to moderate-sized, local earthquakes at epicentral distances that were in general much greater than the distance between the soil and reference site (~2 km), the frequency content of the sites were compared. The frequency content of the site situated on the basin had significant amplification for the frequency matching the fundamental frequency and higher modes of the soil, mostly attributed to the thick layer of Leda clay.

2.4.3 Focusing/defocusing

Focusing occurs when the geometry/topography of the basin causes the incoming waves to be refracted to concentrate towards one point (see Fig. 2-1 C). For example, in a bowl-shaped basin, the incoming waves would all be concentrated around the centre of the basin. However, for the case of a topographic high within the centre of the floor of a

bedrock basin, the opposite will happen. The incoming waves will be diffracted outward from the bump causing a defocusing in the centre of the basin.

Focusing is one explanation as to why some areas in a basin are affected more strongly than other places immediately adjacent. Constructive interference of waves from the underground structures in the Santa Monica region was found to provide an explanation for the damage pattern within Santa Monica by Graves et al. (1998). This implies that the damage pattern will depend on the azimuth of the source, which is supported by aftershock observations (Field et al., 2000).

Semblat et al. (2002) investigated two basins with very different geometry. They found that the wide (2 km) and shallow (60 m) basin in Nice did not show any focusing effects, while the deeper and wider (300 m by 3.6 km), irregularly-shaped basin in Caracas, Venezuela, which is surrounded by mountains, showed potential amplification due to focusing effects. Hence, not all basins will necessarily be subjected to strong focusing effects.

Some caution must be taken when discussing focusing, as some authors refer to basin-edge effects when they are actually referring to focusing. It might be difficult to distinguish the effects on the waveform of one from the other. However, Kawase (1996) suggests that when focusing is the cause, then the damage location would not be frequency dependent.

2.4.4 Basin-Edge Effect

When an earthquake occurs it produces both body waves and surface waves. The body waves travel outward from the hypocentre through the earth, whereas the surface waves travel outward along the surface of the earth. There are two main types of body waves: the primary (P) wave which is a compressional wave, and the secondary (S) wave, also known as the shear wave. There are also two types of surface waves: the Rayleigh wave (Rg) which generally travels along a prograde elliptical path, and the Love wave, which has purely horizontal motion.

Basin-edge effects result from the conversion of the incoming energy to surface waves as impinging wave encounters the edge of the basin. The surface waves subsequently propagate from one edge of the basin to the other (see Fig. 2-1 D). This may lead to larger amplifications and longer durations of the recorded ground motions. Bard and Bouchon (1980a, 1980b, 1985) noted that surface waves develop in valleys and that the waves, generated at the basin edge, travel back and forth and are trapped within the sediment layer. Kawase and Aki (1989) postulated that these basin-edge generated surface waves may be responsible for the long duration seen on the Mexico City basin records for the 1985 earthquakes. Using a model based on the limited data available for the Mexico City basin at that time, they showed that basin-edge generated waves would increase the amplitudes recorded on both horizontal and vertical components due to Love and Rayleigh waves.

In his 1996 paper on the Kobe earthquake, Kawase showed that the “basin-induced diffracted waves become Rayleigh (Rg) waves of the fundamental and first higher modes soon after the departure into the basin from the edge”, which he noted occurred near the sharp edge of a basin, and was separate from other two- and three-dimensional effects such as focusing. To distinguish between focusing and basin-edge effects, Kawase postulated that the location of the focusing should be constant, while the basin-edge effects would be affected by frequency content of the incoming waveform).

2.4.5 Others possible factors influencing local ground motion

Influence of structures

As discussed, during an earthquake, the local geological conditions can change the amplitude, duration and frequency content of seismic wave striking structures built on the soft layers. It is also known that buildings can affect the seismic behaviour of the soil layers beneath, through a complex process called soil-structure interaction (e.g. Borchardt, 1970). Semblat et al. (2008) took this concept further to show that cities as a whole must be considered, as their influence can have a significant effect on the overall wave-field in a basin. This effect was found to be dependent on the properties of the structures, and could alter the duration and amplitude of the propagating seismic waves (Semblat et al., 2008). In general this effect was mainly seen when the resonant frequency of the soil was similar to the natural frequency of the buildings, resulting in a reduction of amplitude but an increase in duration of the signal. It should be noted that the natural period of a building is considered to be:

$$T = N * 0.1s \quad \dots [Eqn 2.7]$$

where N is the number of storeys. Hence, for a one storey building, the expected period of the building is expected to be 0.1 s and the frequency of 10 Hz, while for a two storey building it would be $T_0 = 0.2$ s or $f_0 = 5$ Hz.

The only basin within city limits that is currently being investigated in the high population density of the Ottawa region is the Orleans basin, which is situated in a residential area. The soil site (assigned the station name ORHO), was located in the basement of a two storey home, while the rock site (given station name ORIO) was sited within 20 m of a water tower, with a probable height of 39.3 m (Dr. J.A. Hunter, pers. comm., 2016). The water tower would be estimated to have a lower resonant frequency, likely in the range of 1.28 s, or 0.78 Hz. However, no resonance has been noted in this range for observations of ambient noise for ORIO made in varying wind and other weather conditions (Dr. J.A. Hunter, pers. comm., 2016).

At the Kinburn basin, the rock site (station name JSBS) was located in the basement of a bungalow, while the soil site (station names JSSS) was placed on the cement pad of a garage. The surrounding area is mostly farm land, with only a few structures widely spaced. No major structures are located near either of the Lefaivre basin sites.

Channelling along basins

In places where several basins are similarly oriented and connected or near to each other, they act as a channel for seismic energy. The incoming seismic energy going

into the first basin becomes polarized and channelled into the following basin, and could increase the amplitude of the waves in the following basins (Day et al, 2012).

Neither the Orleans nor the Lefaiivre basins are shaped favourably for this effect. Both are more bowl-shaped, with no real prominent direction. Nor are there any adjacent basins with a strong preferred orientation.

The Kinburn basin, on the other hand, is not only definitely elongated in one direction, but it is also part of a longer series of interconnected basins, all with the same alignment. Hence, the Kinburn basin is likely to be affected by channelling. However, further instrumentation is required on the current sub-basin being studied, as well as the adjoining basins to verify the existence of this effect.

Multi-pathing

Multi-pathing occurs when the signal from one earthquake arrives at the site along more than one path, such as reflected/refracted waves from any other local or regional structures in the earth crust. Hence the signal will arrive more than once at varying time shifts, amplitudes and from various angles.

In their 1993 paper concerning the 1985 Mexico City basin response, Singh and Ordaz argue that it is possible that the long duration may already be present in the hill side coda. Unfortunately the strong motion sites on the hill side did not trigger long enough time series for the September 1985 events. The amplitude of one of the hill-side recordings was noted to be higher by about 10% than was calculated given the distance to the epicentre and the expected attenuation (Singh and Ordaz, 1993). Using recordings

from subsequent earthquakes, Singh and Ordaz show that the long duration and the harmonic beating are also present in both lakebed and hill side recordings. They proposed that multi-pathing as the cause for both the amplitude and duration increase.

Modeling work by Furumura and Kennett (1998) shows that the Lg phase (a wave group of multiple S-wave reverberations and conversions, developed and observed at larger distances, as defined by IASPEI, 2016) that is present but not evident on the rock site, might cause the soft sediments in a basin to resonate. This would support Singh and Ordaz theory, which does not require a more complicated two- or three-dimensional explanation. Chávez-García and Bard (1994) concur that this was one of the more plausible explanations, but they did have some concerns with respect to a second rock site which showed remarkably lower amplitudes. And although it recorded for much longer, the second site showed no long duration signal. Furthermore, they were unsure if this could account for the late, high amplitude arrivals.

Chávez-García and Bard (1994) attempted to numerically model the two-dimensional effects, but their results did not indicate that two-dimensional structures along the path near the Mexico basin could account for the amplitude and duration of the signals recorded for the 1985 earthquakes.

Gravity waves

A Rayleigh (Rg) wave is a surface wave, with elliptical motion (generally retrograde), with vertical motion and horizontal motion in the direction of travel, but no transverse or perpendicular motion (U.S. Geological Survey, 2012). When Rg waves

travelling through a solid encounter a fluid it has been theorized that they convert to a form known as gravity waves (Gilbert, 1967). Gravity waves are generated in a fluid medium when the equilibrium is disturbed, and gravity acts to restore the equilibrium resulting in an oscillation of the fluid (Pedley, 1997). Note that gravity waves only exist in a fluid medium, while Rayleigh waves can only exist in a solid medium. This theory, originally put forward by Gilbert (1967), was proposed by Lomnitz (1990) to explain the damage pattern created by the 1985 Mexico City event and the long duration of the signal. He suggested that due to the high-water content of the clay in the Mexico basin, and possible nonlinear effects at ultra-short wavelengths, this may have caused the soil to behave like a fluid, allowing the propagation of gravity waves (Lomnitz 1990, 1996).

Chávez-García and Bard reviewed the proposed gravity wave theory in two papers (1993a, b) and their calculations did not support the transition between Rg waves in solids and gravity waves in fluids, and the frequencies they calculated for Mexico City were well below the frequency of damaging motion for the 1985 event. Nor would this theory explain the long duration of the signal recorded during the event (Chávez-García and Bard, 1993a). They did not discount the possibility gravity waves occurring in other settings.

Faraday Resonance

Faraday resonance is a subharmonic resonance, a secondary resonance mechanism created in a surface sediment layer that could lead to the generation of surface waves. It was an effect initially shown by Faraday in 1831, and has been proposed by Foda and Chang (1996) as a mechanism to produce the long duration

waves seen on some soil sites. They note that no 3D structure is required, only flat lying horizontal layers. As with the gravity wave theory, this requires the ground behave like a fluid; therefore the ground is considered to be fully saturated.

2.4.6 Discussion

To study edge-effects on ground motions over soft-sediment filled basins, the three basins were instrumented with identical pairs of instruments on rock and soil (see Chapter 3 for more details on the stations and data used). Using the rock site as the reference, the source, path and instrument effects can then be eliminated, at least to a first approximation, leaving only the site effects as the major factor in anomalous amplification.

To a first approximation, seismic shear wave impedance and resonance can be estimated if the material properties of the basin are known. For the current basins being studied, numerous geophysical data have been collected to allow a detailed profile of material properties, as well as a good geometric approximation of each of the basin shapes (e.g. Benjumea et al, 2003; Medioli et al., 2010; Motazedian and Hunter, 2008, etc.). See Chapter 3 and Appendix C for more details on the data for each basin. These data will be used to model the seismic shear wave impedance and resonance effect using 1D ground motion analysis software in Chapter 5.

However, distinguishing between focusing and basin-edge effects can be more difficult. Kawase (1996) suggests that the location of the basin-edge amplification will change with the frequency content of the incoming wave, whereas the location of the

amplification due to focusing will stay fixed. However, for this study we are limited to the data from one station located on the basin, which does not allow us to compare the differences of amplifications throughout the basin from one event as compared to another.

Particle motion and frequency content is examined in detail (see Chapters 4 and 6) to see if patterns can be detected that would suggest any preferred orientations. If the particle motion and strength of signal is aligned with the basin-edge as opposed to the azimuth of the earthquake, this would strongly suggest basin-edge generation as a mechanism.

2.5 Literature review of basin-edge effects

Since the Mexico City earthquake, there have been numerous studies on the effects controlling ground motion over soft-sediment filled basins (e.g. Bard and Bouchon, 1980a, 1980b, and 1985; Kawase, 1996; Olsen et al. 1995; Olsen 2000; Semblat et al., 2002; Semblat et al., 2005). However, only a few of these studies have focussed specifically on the basin-edge effect. Bard and Bouchon (1980a, 1980b, 1985) noted that surface waves develop in valleys and that the waves, generated at the basin edge, travel back and forth within the sediment layer. Kawase and Aki (1989) postulated that these were due to an effect, separate from resonance, and that these basin-edge generated surface waves may be responsible for the long duration seen on the Mexico City basin records for the 1985 earthquakes. Their initial modeling showed these

Rayleigh and Love waves could have the potential to increase the amplitudes recorded on both horizontal and vertical components.

In recent literature there have been a few studies using modeling, field observations or a combination of both to further the understanding of and to quantify the role of these basin-edge effects. Below is a summary of experiments based on recorded field data, as well as some of the modeling results for basin-edge effects. Also included is a short overview of modeling results for soft-sediment filled basins showing the importance of basin material properties and geometric parameters.

2.5.1 Basin-edge field experiments

Kobe, Japan

In 1995, a large earthquake struck Kobe, leaving a damage belt that was parallel to, but 500 to 1000 metres away from, the fault (Kawase, 1996). Results of work by Kawase showed that basin-edge diffracted body waves were converted at the sharp basin edge into Rg waves of the fundamental and first higher modes as they propagated along the free-surface; these constructively interfered with direct S-waves, causing what he termed “the basin-edge effect”, which was responsible for this band of damage. The converted Rg waves did not attenuate as quickly as the diffracted body waves would have, but modeling results showed that this effect extended only out to approximately 1200 m from the fault. Also, even when no vertical motion was applied into the model, there were vertical components to the motion near the fault, suggesting that all the vertical response shown by the model was associated with basin effects.

Kawase (1996) suggested that two controls on the distance between the basin edge and the damage were the depth of the basin and the predominant frequency of the incoming wave. The deeper the basin, the further the damage in the basin is from the edge. Conversely, the higher the frequency input, the closer the damage is to the edge. This is because the higher frequency would mean that the diffracted basin-edge induced wave would travel more slowly, and hence not as far before meeting the S-wave.

Los Angeles and San Fernando basins, U.S.A.

A similar result, to that of Kawase for Kobe, was found by Vidale and Helmberger (1988) who investigated the effects of the 1971 San Fernando earthquake on the San Fernando and Los Angeles basins. Although the nearby mountains should have protected the basin against incoming shallow surface waves, the sharp basin edges nearest the earthquake tended to convert the body waves back to shallow surface waves.

Liu and Heaton (1984) were able to demonstrate from the array analysis of the 1971 San Fernando earthquake that the surface waves recorded over the basins were body waves that were converted at the basin edge. A similar observation was made by Field (1996) for the 1992 Landers earthquake in the Coachella Valley. Field et al. (2000) note that the largest amplitudes come not from the initial S waves but from the wave that propagates across the valley from the northeastern edge. Furthermore, this region also experienced very strong shaking during the 2000 Hector Mine earthquake, which Field et al. (2000) attribute to basin-edge-induced waves.

Santa Monica Area, U.S.A.

Graves et al. (1998) studied the effects of the 1994 Northridge earthquake and its aftershocks on the ground motions in the Santa Monica region. Results were somewhat limited as all the earthquakes used were from one source region. However, they built a fairly detailed model of the basin-edge region, with well-defined velocity profiles. And records of the 1994 Northridge earthquake from stations within the study region and damage reports were used to verify the validity of the results.

Graves et al. (1998) found a zone of heavier damage that resembled the damage zone found by Kawase in the Kobe region after the 1995 earthquake. Their models, which showed a zone of stronger ground motion, approximately 1 to 2 km wide, with ground motions dominated by SH waves, were in good agreement with the zones of heaviest damage after the earthquake. Their models also suggested that it was the first, and shallower, fault scarp that controlled the ground motions; the deeper structure had only a limited effect. The amplification was not uniform along the basin edge in their simulations because of the variability of the geometry along the fault scarps. This was echoed by the actual variability in the damage areas from the 1994 earthquake. They also postulate that lateral focusing effects due to 3D structure along the basin edge may strongly influence local response.

Further observations by Graves et al. (1998) showed that the structures affected in the Santa Monica region suggest that the most damaging ground motions had a frequency range of 1 Hz to several Hz, hence the frequency range of the amplification must also be across a broader frequency band, likely due to the constructive interference

of the shorter-period direct body waves with the longer-period basin-generated surface waves (e.g.; Graves et al., 1998; Kawase, 1996). The peak ground acceleration was observed to occur several seconds prior to the peak velocity, which Graves, et al. (1998) suggest must require different wave propagation mechanisms at different periods (shorter periods for acceleration, longer periods for velocity). Furthermore, the large long period velocity pulse, which was slightly delayed from the direct arrival, was shear wave energy that had been generated at the basin edge, coincident with the shallower fault scarp.

Mexico City, Mexico experiments

Mexico City has a high velocity contrast between bedrock and basin sediments. The overlying low-velocity clay layer is extremely soft, has high water content and may have shear wave velocities as low as 40 m/s. The clay layer is approximately 40 metres in depth and extends tens of kilometres in width, overlaying stiffer sediments and volcanic rock (Ramos-Martínez et al., 1997).

Although numerous studies were done in the Mexico City basin to determine the exact cause of the damage that was observed during the 1985 earthquakes, the earlier studies were hampered by the limited knowledge of the basic basin geometry and the physical parameters of the sediments within (Chávez-García and Bard, 1994). Since then, however, many investigations in the Mexico City basin have helped gather the necessary geophysical and geometric data of the basin (Ramos-Martínez et al, 1997; Chávez-García et al, 1995; Chávez-García et al, 2002; Stephenson et al., 2006), removing some uncertainty from the more recent study results.

For their report published in 2006, Stephenson et al. set up an array of seismometers and accelerometers to monitor the propagation of the coherent surface waves and to understand the wavefield generated by large earthquakes. The array was set up at the Texcoco site, located on the extended valley north-east of Mexico City, with the soil having similar composition as those within the city. For bigger basins, locally generated basin waves can be greatly delayed as the distances travelled are greater, and the generated waves travel at low speeds, making them easier to isolate from the signal of the main event.

The data consisted of two large, distant earthquakes, with epicentres both from the west, but at different azimuths. The smaller, but closer earthquake showed obvious late energetic arrivals that had a different frequency content than the earlier arrivals (0.48 vs 0.4 Hz). And the direction of travel in the wave number spectrum of the later arrival was not directly from the source.

Using array processing techniques, it was possible to determine a group velocity for this late energetic wave packet from the first event, as it travelled across the array. Particle motion for this wave packet showed it to be prograde elliptical, which is not normally expected for Rg wave, but has been shown to occur under certain conditions (e.g. Malischwesky Auning et al., 2006). The group velocity indicated that the energy originated from a P phase. Note that the calculated conversion does not occur right at the basin boundary, but it is postulated that there may be some unknown subsurface structure that might be responsible, a result consistent with other researchers (Stephenson et al., 2006). The second larger, but more distant, event did not appear to

have obvious late energetic arrivals. However, once the data was processed in the same manner as the first event, similar results were found. In particular it was found that the direction of travel was the same, despite the earthquake being from a different azimuth.

It is noted by Stephenson et al. (2006) that this conclusion is based on only two events. Data from additional events at varying distance and azimuths would greatly increase confidence in the assumption that the frequency and direction of the late arriving wave packet are consistent for all events.

Grenoble, France (Alpine valley) experiment

The experiment by Cornou and Bard (2003) was set up over an alluvial basin in a mountain valley, 900 metres deep by 5 km wide, to look at the expected versus the recorded amplitudes as well as the direction of energy. The dense array of 29 three-component seismometers was located on the basin, and the reference rock site used was over 100 km away (see Fig. 2-2). Due to this large distance between the basin and the reference rock site, only lower frequencies could be considered, hence teleseisms were used instead of local events or blasts in this study. The dense array configuration allowed for array processing of the data.

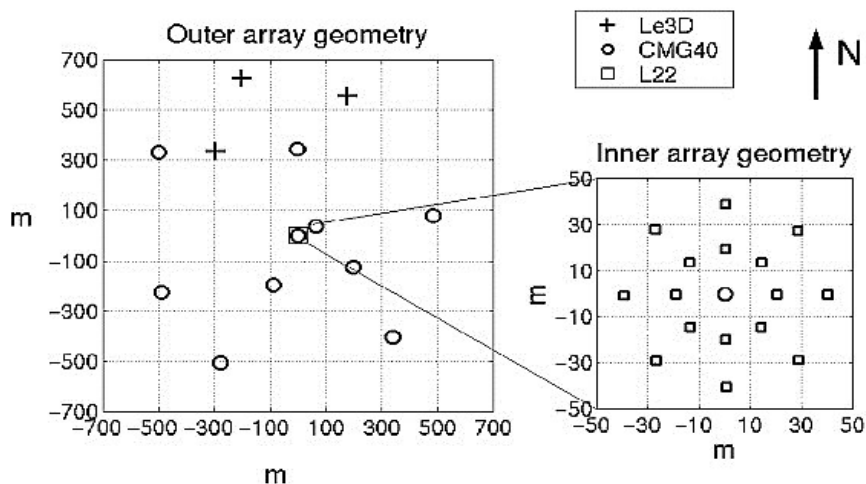


Fig. 2-2: Configuration of array used in Cornou and Bard's experiment in Grenoble, France (after Cornou and Bard, 2003).

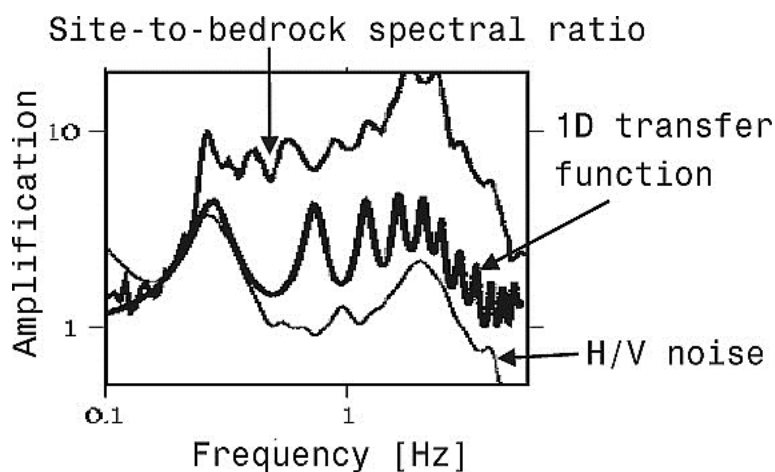


Fig. 2-3: Results of frequency analysis from the Alpine Valley experiment showing the expected amplification due to one-dimensional effects, and the actual recorded amplification (after Cornou and Bard, 2003).

The results of the Cornou and Bard (2003) study showed that only a small portion of the energy within the wavetrains could be explained by one-dimensional effects (see Fig. 2-3). The remaining motion is therefore attributed to two- and three-dimensional effects. Although the sources were from different azimuths, diffracted wave-trains

exhibited two main stable directions of propagation coming clearly from the two closest basin edges (Cornou and Bard, 2003). In fact, between 0.2 Hz and 0.3 Hz, all the energy seems to be basin-edge generated. Above 0.3 Hz, not all the energy is coherent across the array, so it was not possible to use array processing techniques. However, if it is assumed that all the energy is from impinging diffracted rays, then those amplitudes also match well with predicted basin-edge generated effects according to Cornou and Bard (2002b).

Below the fundamental frequency of the basin (in this case 0.2 Hz), basin-edge effects do not seem to play a major role; instead, direct energy was found to be the main contributor at this frequency range (Cornou and Bard 2002b). Furthermore, the apparent velocities lay between the theoretical dispersion curves of the first modes of the Love and Rg waves (Cornou and Bard, 2003).

Parkway, New-Zealand experiment

The alluvial basin in Parkway, New Zealand is roughly 1.3 km and 0.4 km wide, fairly shallow at about 70 m, and open to the south. It was covered by a network of approximately 20 three-component seismometers, with several additional instruments on the rock immediately surrounding the basin, and another reference rock site 2 km away (see Fig. 2-4 A). This allowed for the investigation of the variability of the rock sites (Stephenson, 2007).

In order to bridge the gap between observation and theory, Chávez-García et al. (2002) did a detailed analysis of the Parkway data. They computed f-k spectra for

seismic data as a function of frequency and time window along seismograms. They found that the majority of energy was from surface waves (Love and Rayleigh waves), which would appear shortly (due to small basin size) after the direct P and S wave arrival times.

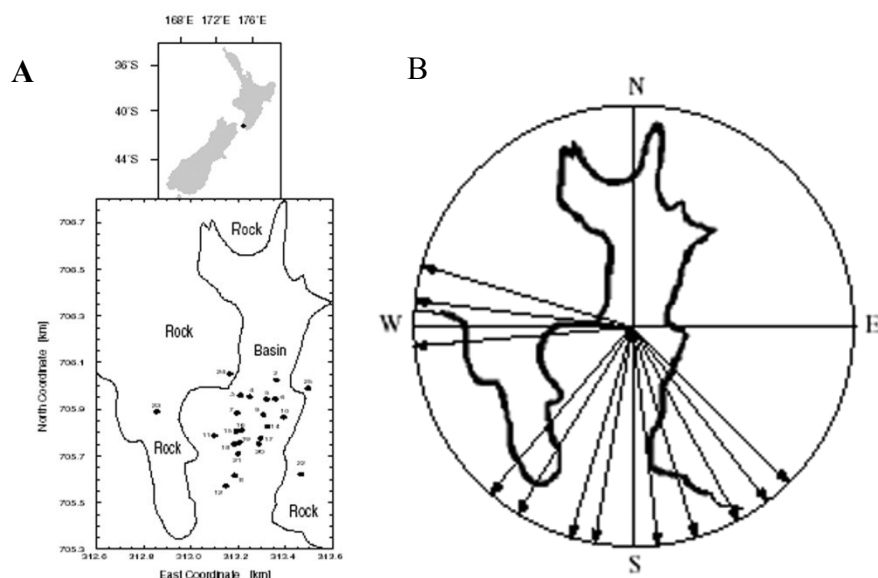


Fig. 2-4: A) Map of the Parkway basin showing the set-up of the array for the experiment, with the inset showing the location of the basin within New Zealand. B) The results showing the preferred direction of travel of the waves as determined from the Parkway experiment. Note the preferred southerly direction, regardless of the azimuth of the source (after Chávez-García et al., 2002).

They were not successful in isolating specific wave trains, but direction of propagation appeared to be mainly southerly, particularly at lower frequencies, and early on in seismogram (see Fig. 2-4 B). Stephenson (2007) did further analysis on the data and determined that the waves were locally generated by looking at the wavenumber spectra of the vertical component. Waves which were stable in direction (down the valley) and speed were found with resonances of 1.58 and 1.68 Hz. These

modes had been found to be Rg waves, as well as transverse waves akin to Love waves, but with a vertical component.

Stephenson (2007) noted that the experiment showed larger motions in the centre of the Parkway basin rather than at the edge, as suggested by Kawase (1996) for the 1995 Kobe event. However, he postulated that given the relatively small dimensions of the basin in question, it was more likely that the edge-effects of the incoming waveforms from the basin edges were likely constructively interfering closer to the centre of the basin.

2.5.2 Experimental results with regard to basin parameters

Modeling has been shown to be essential in our understanding of the observations made in the field (Kawase, 2008), and has been used extensively to show the effects of geometry and basin properties on the resulting ground motions. Below is a summary of some of the results and how they relate to the Ottawa region basins.

Geometry of basin

Semblat et al., (2005) showed geometry can strongly influence both amplitude and duration of the signal, but that this is more important for investigating higher frequencies (> 2 Hz) than it is for lower frequencies. Flores et al. (1997) showed how the geometry affected the resonance pattern. Graves et al. (1998) showed how a buried fault could cause basin-edge effects, and Stephenson et al. (2006) showed how the subsurface feature could convert an incoming phase, causing delayed surface waves over a site at the basin.

Depth of basin

The amount of amplification and the affected frequencies depended on the soil thickness (Borcherdt, 1970; Riepl et al, 1998; Kham et al., 2013). The maximum amplitude was found over the thickest parts of the basin, at the lowest frequencies (< 1 Hz), while the thinner outer regions of the basin had a lower amplification with the maximum found to be at higher frequencies (> 1 Hz to ~5+ Hz).

Field et al. (2000) also found that the depth of the basin seems to correlate with the amplitude and duration of the signal; however, the physical mechanism for this effect was not determined. In general, most models implied that the greatest ground-motion levels will be found over the deepest basin sites (Field et al., 2000). Field et al. (2000) speculate that one might expect peak ground acceleration (PGA) to be reduced due to anelastic attenuation over the deep sites, but that perhaps focusing from basin concavity outweighs the attenuation effect. Perhaps general focusing from basin concavity dominates the influence of anelasticity.

Field et al. (2000) noted that although models predict higher ground amplification due to depth at the deepest part of the basin, other effects like focusing may cause greater motion near basin edges. However, these focusing effects are far more variable, and don't represent the average amplification pattern due to an earthquake. Thus, they concluded that in many instances for basins in California the knowledge of basin depth was more important than V_{S30} (the average shear wave velocity to a depth of 30 m at a

site) for estimating PGA. V_{S30} is the parameter used in some building codes to determine the geology, and hence the seismic hazard at a site.

For relatively broad, flat basins, on the other hand, Semblat et al. (2000) found that a 1D approximation worked fairly well for determining the resonant frequencies, but underestimated the surface amplification by as much as three times.

Velocity contrast

In 1998, Konno and Ohmachi published their modeling results of Rg wave motion depending on the velocity contrast of the rock and overlying soil. Their models showed that for a low velocity contrast ($V_{S_{\text{rock}}}:V_{S_{\text{soil}}} \leq 2.5$), the Rg wave had the usual retrograde motion. For a higher velocity contrast ($V_{S_{\text{rock}}}:V_{S_{\text{soil}}} \approx 2.5$), however, there was a transition between normal retrograde motion at short periods, transitioning to prograde motion at medium periods, and back to retrograde at longer periods. At the transition points from retrograde to prograde and back, the motion was modelled to be purely vertical. (See Fig. 2-5).

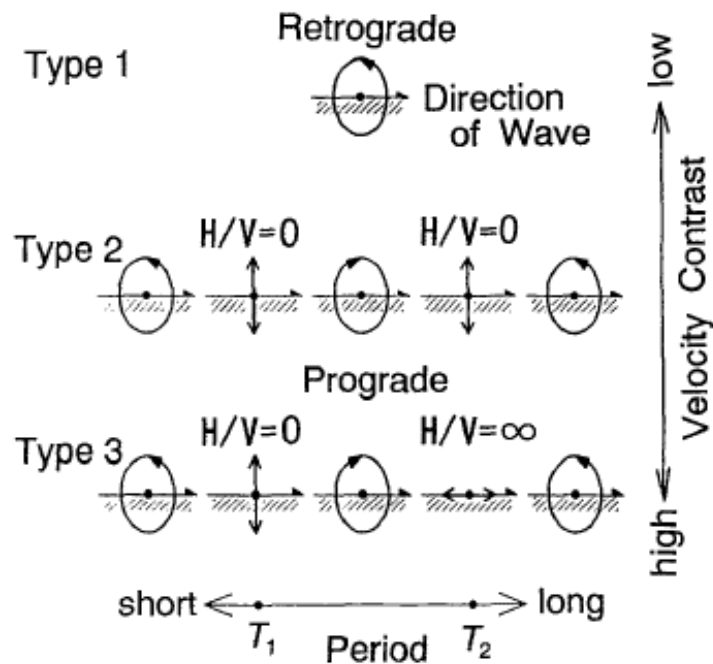


Fig. 2-5: Results of Rayleigh wave motion modeling showing the change in expected motion as a function of period due to different velocity contrasts between the rock and overlying soil in a simple two layer model (after Konno and Ohmachi, 1998).

At even higher velocity contrasts ($V_{\text{rock}}:V_{\text{soil}} \geq 2.5$), the pattern was the same as seen for the medium contrast, except that the second transition from prograde back to retrograde was modelled to have purely horizontal motion.

Although a simplified soil profile could be sufficient in some cases, Semblat et al. (2005) found that depending on the basin, some important details in the amplification and frequency of the resulting ground motions would be lost. Deplépin and Semblat (2012) showed how a strong velocity gradient can strongly amplify the resulting ground motions. The soil layers, particularly the superficial layers, seem to play a large role in the prediction of higher frequency content, and surface wave propagation (Semblat et al,

2005). Vrettos (2013) showed how the soil's stiffness profile can shift both the maximum amplitude and the location of the frequency peaks.

Seismic Damping

The quality, Q , of the bedrock and soil which make up the basins, determines the amount of damping on the recorded ground motion. As was noted by Ramos-Martínez et al., (1997), Q has an important influence on the amplitude and duration of the soil response. The surface waves, guided by shallow layers, can attenuate quickly. Therefore, knowing Q can help determine the placement of the soil sites on the basin.

The results of various numerical models dealing with basin-edge effects depend on the value of Q (e.g. Aki and Kawase, 1989; Chávez-García and Bard, 1994). Q can have a significant effect on the frequency of the maximum peak, particularly at higher frequencies, and on the amount of amplification (Semblat et al., 2000).

Frequency of incoming signal

Joyner (2000) proposed that for longer periods that the effect seen is not a result of basin depth, but rather from the distance of the earthquake to the edge of the basin, where the entering waves are dramatically slowed, and depending on the exact geometry of the basin, the geometric spreading is dramatically reduced. Joyner's model shows amplification of the waves continuing as they travel through the basin, with the largest amplitudes actually occurring on the opposite edge of the basin. This is supported by modeling work done by Olsen (2000) which shows a similar pattern for a San Andreas earthquake on the Los Angeles basin. That would imply that the effect

may differ between longer and shorter period ground motion, which a correction based only on basin depth will not account for. Also, there would be an underestimation, generally for the far sides of the basin, of the amplification of the ground motion (Field et al., 2000).

The amplification of the signal seems to be the greatest at the fundamental frequency of the basin and the first few harmonics (e.g. Kham et al., 2013; Semblat et al., 2000; Riepl et al., 1998). However, in comparing multiple recordings at the same point, the maximum amplitude has been shown to shift slightly (Semblat et al., 2000). There seems to be little to no amplification of the signal below the fundamental frequency (Cornou and Bard, 2003; Semblat et al., 2000).

Current 3D modeling seems to be able to predict the lower frequency responses of basins (Semblat et al., 2000). However the higher frequencies (>2 Hz) are more erratic and harder to predict (Kham et al, 2013; Riepl et al, 1998). This may be due to the small scale complexities (Semblat et al., 2000) and the complexity of the surface layers (Riepl et al, 1998).

Incident angle

The incident angle of an incoming wave has been found to have an influence the amount of amplification over a basin, but how it affects a basin seems to differ depending on the geometry of the basin in question. For example, Kham et al. (2013) found that for their basin in Tunis, Tunisia that the amplification factors were highest for low or mid-range incident angles (50° to 80°), whereas Semblat et al. (2000) found

the exact opposite occurred for their study basin in Nice, France. Kham et al. (2013) attributed this to the fact that the Tunis basin was more irregular in its geometry and not as shallow as the Nice, France basin, making it more susceptible to focussing and basin-edge effects.

Wave type

Different wave types are amplified at different frequencies and to different maximum amplitudes. Semblat et al. (2000) found that in general shear (S) waves showed larger amplification than the incoming compressional (P) waves, and furthermore that the horizontal shear (SH) again had a larger maximum amplification when compared to the vertical shear (SV) wave. However, the location of the maximum amplification did not coincide either in frequency or physically on the basin. This result was confirmed in later study on a different basin by Kham et al. (2013). However, SV seems to be more affected by basin geometry, and hence Semblat et al. (2005) did not think it should be left out from analysis.

2.5.3 Summary of Observations and Modeling results of Basin-edge effects

The experiments and field observations mentioned above come from basins with various different geological settings and of various shapes and sizes. Some of the experiments were more detailed than others, but there are several characteristics that were consistently noted over the majority of the basins, including the ones in the Ottawa region. Fig. 2-6 shows a typical local earthquake ($m_N 3.1$ near Rockland, ON 2012/09/22) as recorded by the Orleans seismograph station pair, with the three components (east-

west, north-south and vertical respectively) of the rock site ORIO above and the three components from soil site ORHO underneath. The data have been filtered with various band pass filters (A: 0.5 to 1.0 Hz; B: 1.0 – 1.5 Hz; C: 2.0 – 3.0 Hz; and D 5.0 - 10 Hz, all using the Butterworth filter) to highlight the differences between the soil and rock site for various frequency ranges. Recordings from earthquakes on all three basins showed similar characteristics to the ones seen in Fig. 2-6.

Larger than expected amplitudes

Amplitudes recorded in sediment filled basins have been noted to be much higher than would be expected from simple changes in geology. In Mexico City, some soil sites situated on the basin showed amplification of up to 50 times that recorded on nearby rock sites in the frequency range of 0.25 to 0.7 Hz (Singh and Ordaz, 1993).

These values are larger than those predicted from simple seismic impedance models (e.g.; Singh et al., 1988; Chávez-García et al., 1991; Cornou and Bard, 2003; Ramos-Martínez et al., 1997). In fact, Singh and Ordaz (1993) note that the hill zone was also amplified by about 10 times expected at some sites in the frequency range of 0.2 to 0.7 Hz, making the net amplification of 500 at some lake bed sites. Cornou and Bard (2003) suggest that this difference in the expected one-dimensional amplification and the observed amplification can be used to define the amount of two- and three-dimensional amplification at a site.

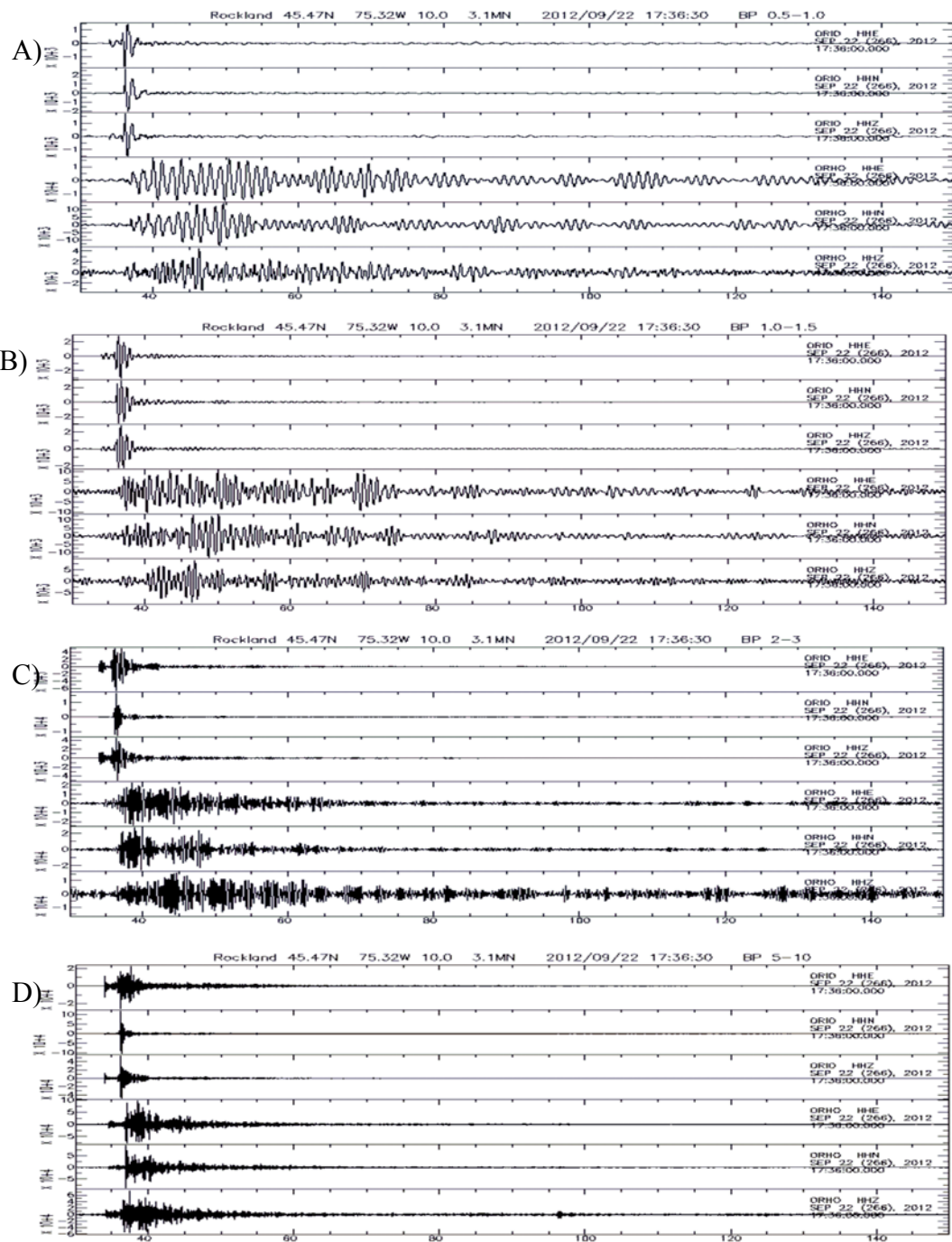


Fig. 2-6: Recordings of a local earthquake (Rockland, ON; M3.1; 2012/09/22 at 17:36UT) from the Orleans basin comparing the three components (east, north and vertical) of the rock site ORIO on top, with the soil site ORHO recordings underneath at various bandpasses: A) 0.5 to 1.0 Hz; B) 1.0 to 1.5 Hz; C) 2.0 to 3.0 Hz; and D) 5.0 to 10.0 Hz.

Duration and character of signal

A long duration, mono-frequency coda is mentioned by numerous researchers (e.g.; Flores et al., 1987; Singh and Ordaz, 1993; Chávez-García and Bard, 1994; Ramos-Martínez et al., 1997) as a characteristic signal from basins from all over the world, including the one in Kobe (Kawase, 1996) and in Texcoco, Mexico (Stephenson et al., 2006). The coda also exhibited roughly harmonic beats with late energetic arrivals (e.g.; Singh and Ordaz, 1993; Chávez-García and Bard, 1994). Kato et al. (1993) postulated that these late arrivals were due to the reverberated SH waves and to Love waves.

The mono-frequency recordings were noted to be of a different frequency than on recordings from sites on firmer ground (e.g. Flores et al., 1987). For the Mexico City recording, the frequency recorded on the soft soil site matched the period (~2.0 s) of the buildings most affected by the earthquakes, between five and fifteen storeys high (Flores et al., 1987). Michal Kolaj (2010) noted that the arrival of the body waves from the Haiti teleseism caused the station located on the Orleans basin to resonate at its fundamental frequency of approximately 0.8 Hz. The body waves of the earthquake were greatly amplified at the fundamental frequency on the soil site, compared to the neighbouring rock site, which did not exhibit this mono-frequency ringing. The surface waves were unaffected, which is not surprising as their wavelengths exceed the length of the basin (Kolaj, 2010). This effect can also be seen on the recording of the local event in Fig. 2-6, where the duration of the recording for frequencies 0.5 to 1.5 Hz (A

and B) are much longer than the higher frequency recordings (C and D) which do not have a long coda or late arriving energetic beats.

The long duration of the signal seems to be one of the most difficult effects to account for (Chávez-García and Bard, 1994), but it has also been identified as an important factor in the damage potential of the ground motion (Beck and Hall, 1986).

Polarization

Several studies note that the generated surface waves are not aligned with the source, but rather to the basin-edges (e.g.; Field et al., 2000; Stephenson et al., 2006; Somerville et al., 2002). In particular, Somerville et al. (2002) note that Love waves are predominately polarized parallel to the basin-edge, while the Rg waves were normal to the basin-edge. The attenuation of Rg waves was lower than that of the Love waves. Joyner (2000) accounted for this in his model for predicting ground motions over a basin, by having different ground motion prediction equations for vertical, parallel and perpendicular directions.

Damage concentrations not uniform over basin

Borchert (1970) noted that certain areas in the San Francisco basin that had recorded the most damage for the 1906 earthquake corresponded to the sites that recorded the largest motion for subsequent events. Flores et al. (1987) thought that the damage pattern in Mexico City after the 1985 earthquakes was oddly uneven, and could change drastically within just a few city blocks. They suggested a possible standing wave, with damage areas corresponding to nodes and antinodes. Similar patterns of

damage, but with significant variations in some neighbourhoods had been noted for previous earthquakes in Mexico City as well (Flores et al., 1987).

Pal and Atkinson (2012) showed pockets of larger intensity reports in the Ottawa region for the 2010 M5 Val-des-Bois earthquake. There seems to be some correlation with the V_{S30} map in the region (V_{S30} is the average shear wave velocity of a site measured from surface to a depth of 30 m). However, due to the limitations of the data, the bin areas used are too coarse to define the correspondence with the basins being studied, and certainly do not contain enough detail to show the variation within any particular basin. Note that only the Orleans basin is in a reasonably well populated area, but it also happens to be the smallest basin of the ones being studied.

Type of motion

It has been noted from various records that surface waves were predominant over basins (e.g. Bard and Bouchon, 1985; Field et al., 2000). The energy that has been associated with the extended duration and late energetic arrivals are Love and Rayleigh waves (e.g. Cornou and Bard, 2003; Joyner, 2000; Somerville et al., 2002).

Waves travelling similar to Rg waves, but with prograde rather than retrograde motion have been recorded in certain basins, most clearly in the Mexico City basin (Stephenson, et al., 2006; Malischewsky Auning et al., 2006). Malischewsky Auning et al. (2006) in their modeling work found that a higher velocity layer overlaying a lower velocity layer seemed to be the root cause of this change in motion. Note, however, that other factors also played a role as to whether this change of motion to prograde

occurred. According to the modeling work of Konno and Ohmachi (1998), given the high velocity contrast between the bedrock and overlying soil in the Ottawa region, the Rg waves could be retrograde, prograde, purely vertical, or purely horizontal, depending on the frequency.

Lomnitz (2006) gives arguments supporting the importance of considering prograde motion when assessing risk, as prograde motion seemed to have much greater damage potential on structures. He noted, however, that this phenomenon is rarely modeled or considered in the design of the structure.

Basin size

It is easier to identify individual wave packets in larger basins, as there is significant separation between the arrivals of shear-wave and the much slower, edge-converted surface waves (Stephenson et al., 2006). In smaller basins, not only are the initial phases occurring very close to each other in time, but the reflections from the opposite basin-edge create further interference, making it difficult to identify individual wave packets (e.g. Stephenson, 2007; Cornou and Bard, 2003).

The size and depth of the basin, as well as the frequencies of the incoming waves, also determine where the basin-edge effect is strongest. Although, for the relatively large Kobe basin, Kawase (1996) stated the effect was larger closer to the edge, for the smaller Parkway basin, Stephenson (2007) noted the basin-edge effect was strongest near the centre.

The fundamental frequency and size and geometry of each basin should be taken into consideration when choosing which source or sections of the waveforms to be used when analysing the data. As was shown by Kolaj (2010), the wavelengths of the impinging surface waves of teleseisms exceed the lengths affected by the Orleans basin. The basin-edge effects were restricted to a narrow frequency band above the fundamental frequencies (Cornou and Bard, 2003).

The best seismic sources to use for the experiment depend on the frequencies under investigation, which will, in part, be a function of the basin and its geometry. Impulsive blasts can be used for areas which do not have natural earthquake sources; however, the frequency range of blasts can be limited compared to that of earthquakes, and in turn may affect the results obtained from this source.

Experimental configuration

For smaller basins, the current consensus amongst researchers suggests that an array of seismographs is the best tool in order to positively identify basin-edge effects (Stephenson et al., 2006; Cornou and Bard, 2003; Chávez-García et al., 2002). Some basins seemed to yield better results than others; this is commonly related to the basin geometry and the material properties of the soils and rocks. Lack of knowledge of these parameters has also hindered results in past research. For the current study, there are three basins across which data can be compared, all with reasonably well defined geometries and physical properties. Hence, it may be possible to identify the relevant packets of energy associated with basin-edge effects without the use of an array.

Particle motion plots can help identify Rg and Love waves, versus shear waves, and

potentially may help determine the alignment of these waves to either the azimuth of the earthquake or to the orientation of the basin.

3. Setting and Data

The three basins selected for this study vary in size and shape. They were instrumented with seismograph station pairs, which will allow some comparison of the basin parameters on site effects. The geophysical properties (e.g. velocity profiles, density, porosity, etc.) of the infilling soil material and surrounding bedrock, as well as the basin geometries, have been well defined to allow modelling to be done with fewer assumptions required (e.g., Graves et al., 1998; Bard and Bouchon, 1985). Hence the uncertainties in results were reduced.

The general geological and seismological setting of the study area and a detailed description of each of the three basins are described below, including references to the geophysical data, as well as a description of the equipment used and the data collected.

3.1 Regional Geology

The crust of the earth in the Ottawa valley region was depressed during the last glaciation. A thin layer of glacial till generally only a few metres thick was deposited beneath the glacier (Hunter et al., 2010). After deglaciation the topographically lower land surface, became flooded and an inland sea called the Champlain Sea (Gadd, 1986) was formed between 13000 and 9000 BP as shown in Fig. 3-1. A thick deposit of marine sediments known as Leda Clay was deposited in the Champlain Sea (Gadd, 1986) during that time period before isostatic rebound resulted in drainage of the water body.

Leda Clay, a rock flour composed of glacially-eroded clay- and silt-sized particles, commonly has a very high water-content and, in some areas where long term leaching by surface water has replaced saline porewater, may be geotechnically sensitive (Aylsworth et al., 1997). The average shear wave velocity (V_s) of this layer has been found to be approximately $150 \text{ m/s} \pm 29 \text{ m/s}$, except for the top crust which tends to have elevated velocities (Hunter et al., 2010). This crust, due to over-consolidation of the clay from freeze-thaw cycles (Eden, 1957), extends from surface down to approximately 5 to 10 m and has a wide range of observed velocities from $\sim 80 \text{ m/s}$ to up to 500 m/s , but the majority of the V_s readings are between $100 - 200+ \text{ m/s}$ (see Fig. 3-2).



Fig. 3-1: Map showing the approximate maximum extent of the Champlain Sea (in pale blue). After Crow et al., 2007.

Below the thin, over-consolidated surface clay crust, Hunter et al. (2010) showed that the interval shear wave velocity ($V_{s_{int}}$) increased with depth, and the average shear wave velocity ($V_{s_{av}}$) over the entire thickness of the Leda clay is best fit by the equation:

$$V_{s_{av}} = 123.86 + 0.88z \pm 20.3 \text{ m/s} \quad \text{for } 10 \text{ m} \leq z \leq 100 \text{ m} \quad \dots \text{ [Eqn 3.1]}$$

where z is depth in metres.

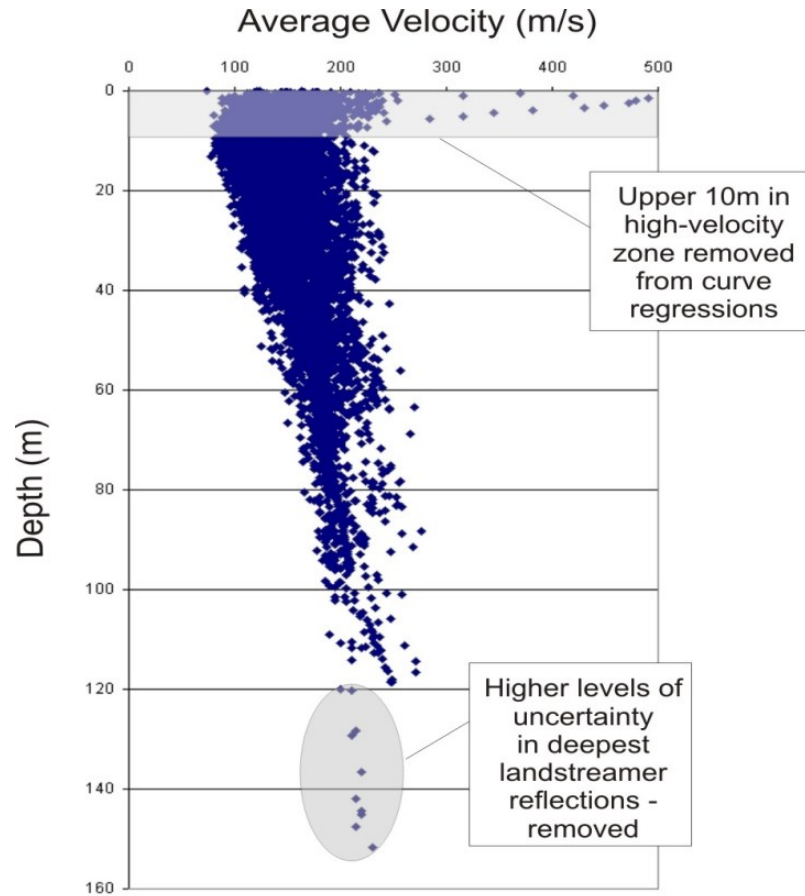


Fig. 3-2: Average shear wave velocity data collected from various geophysical methods (surface reflection sites, landstreamer profiles and downhole surveys) – graphic after Hunter et al. (2010).

The glacial till layer, which may include till-derived sand and/or gravel, is generally only a few metres thick, with a mean thickness of 3.5 m in the Ottawa area. However, it has been observed to be as thick as 35 m in some places in the region where bedrock topographic lows occur (Hunter et al., 2010). The average V_s readings for this layer ranged from 205 m/s to 931 m/s, with the mean shear wave interval velocity of these glacial sediments estimated to be $580 \text{ m/s} \pm 174 \text{ m/s}$ (Motazedian et al., 2011).

The underlying bedrock in the southern part of the region is mostly Paleozoic-age and with Precambrian-age bedrock in the northern part. The bedrock in this region has a high Q, or quality factor; in other words, the bedrock has a very low attenuation. Because of glacial overriding and erosion, the bedrock surface commonly shows little mechanical weathering and is firm and rigid compared to the soft sediments above it.

The Paleozoic bedrock is composed of Cambrian sandstone or Ordovician limestone, shale, dolomite and sandstone (Williams, 1991). The mean Vs for all rock types in the Ottawa region as determined by Hunter et al. (2010) can be found in Table 3-1 below:

Table 3-1: Shear wave velocity readings for the most prominent bedrock types measured within the Ottawa region. Data from Hunter et al. (2010).

Name of formation	Mean Vs (m/s)	Standard Dev. (m/s)	Range of readings (m/s)	Number of observations
Precambrian	2783	504	1387 - 3507	31
Dolomite and Limestone	2890	675	1172 – 4786	182
Shale	2166	401	998 - 3200	111
Limestone and Shale Interbed	2815	580	1403 – 4008	70
Sandstone and Dolomite Interbed	2808	682	1124 – 3975	20
Nepean Sandstone	2328	282	1904 - 2657	8
All bedrock types combined	2700	680	940 - 4895	505

Details on the collection and analysis of the shear wave data for all the materials can be found in Hunter et al. (2007), Crow et al. (2007), Hunter et al. (2010), Kolaj (2010), and Motazedian et al. (2011).

Figure 3-3 shows the Kinburn and Orleans basins on a bedrock geology map of the Ottawa-Hull region. The Paleozoic bedrock is coloured in pale blues, greys and yellow, while the Precambrian is shown in the bright blues, yellows, pinks and oranges. The approximate location of the basins is outlined in red. It is apparent from the map that the location and orientation of the Kinburn basin is controlled by the adjacent Hazeldean fault, which is striking in the south-east, north-west direction similar to other faults in the region (Williams, 1991).

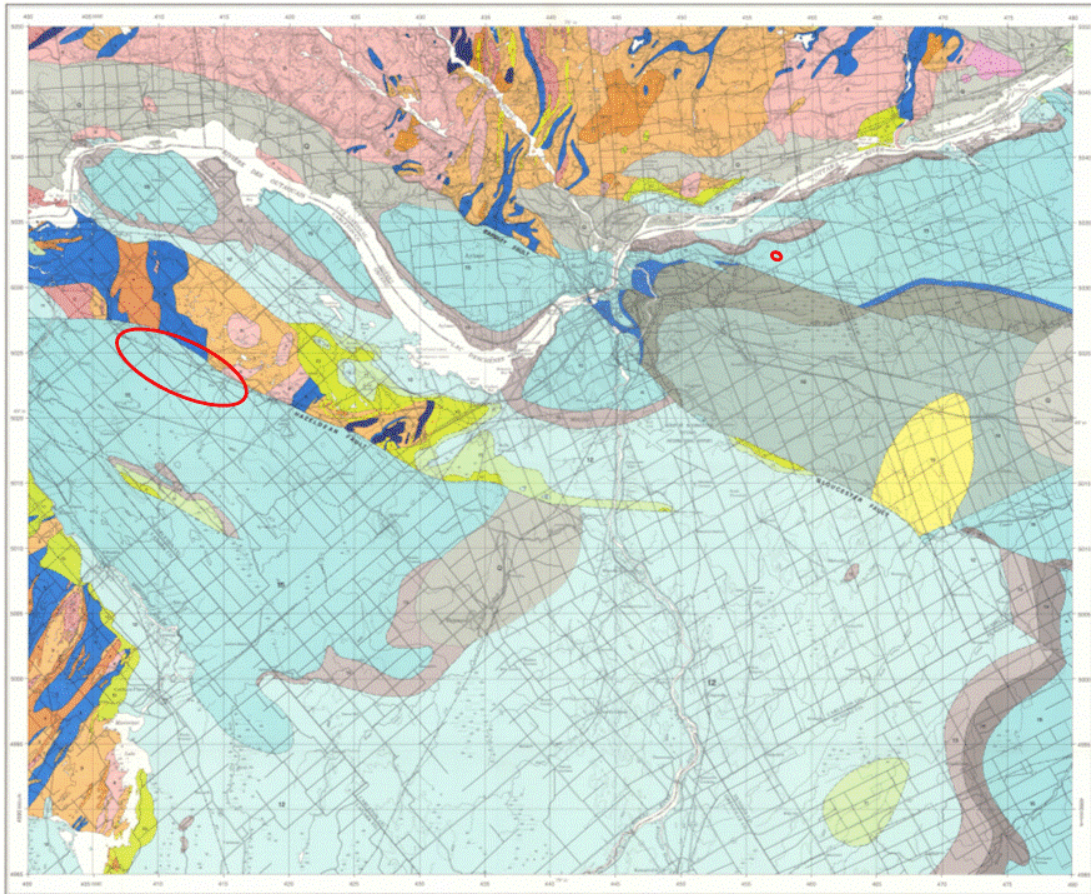


Fig. 3-3: Bedrock geology map of the Ottawa, ON – Hull, QC region. Paleozoic rock is represented by the pale blues, greys and yellows; Precambrian is represented by the bright blues, oranges, pinks and yellows. The approximate locations of the Kinburn (west) and Orleans (east) basins are outlined in red - modified from Harrison and MacDonald (1979).

However, there is no obvious reason for the bedrock erosion at the Orleans site, which is surrounded by Paleozoic rock on all sides. The joint sets within the Paleozoic for this region occur at 015°, 055°, 100° and 145° (Williams, 1991), while some carbonate dikes have been found in the eastern part of the city, striking easterly. However, the Orleans basin is elongated along an axis closer to 30°. Hence, there is no evidence based on the current geological knowledge to explain the location and orientation of the Orleans basin.

The Lefaivre basin does not seem to have a strong orientation in a particular azimuth, and so no strong case for any relation to a particular geologic feature can be made for this basin either.

3.2 Seismological Setting

3.2.1 Tectonics

Eastern Canada is located in a stable craton region within the North American Plate. Like most stable craton regions, it generally has a low rate of seismicity; however several pockets of elevated seismicity exist within this region as compared to the surrounding areas. The causes of earthquakes in eastern Canada are thought to be related to the regional stress field (oriented northeast to east) reactivating areas where the crust has been weakened by past geologic stresses, such as failed rift systems (Cassidy et al., 2010).

Two of the areas with an increased rate of seismicity relevant to our study are: the West Quebec Seismic Zone (WQSZ), which lies just north of our study region and

extends from the Temiscamingue region, along the Ottawa River, past Montreal (Basham et al., 1979); and the Charlevoix Seismic Zone (CSZ) located in the Charlevoix-Kamouraska, QC region approximately 480 km to the east of our study region (www.earthquakescanada.ca).

The WQSZ is made up of two parallel bands of seismicity, one trending from the Baskatong Reservoir south-east, through the Montreal, QC region; the second less active band trends parallel to the first but further south, along the Ottawa River, and as far as Temiskaming, QC. Earthquakes in this region typically result from thrust faulting in a NW-SE striking plane in response to NE-E compression, consistent with the general North American trend (Adams and Basham, 1991; Bent et al., 2003; Kao et al., 2012). The earthquakes depths have been found to typically be 15 to 20 km, but with a high degree of scatter (Bent and Perry, 2002). This finding was echoed by Ma and Atkinson's findings (2006) which found depths between 2 and 25 km using the regional depth phases to determine depths of earthquakes $m_N \geq 2.8$.

This lower band of seismicity is thought to be from the reactivation of Paleozoic rift faults within the Bonnechère graben, part of the larger St. Lawrence rift system (Adams and Basham, 1989, 1991; Forsyth, 1981), although as Lamontagne and Ranalli (2014) suggest, this cannot explain all the pockets of seismicity found within this stable craton region. The upper, more active, band of seismicity does not lie within the Bonnechère graben, and hence is unlikely to be associated to the ancient rift zone. This band does, however, lie over the track of the Mesozoic Great Meteor hotspot and may possibly be due to the thermal rejuvenation of pre-existing fault (Ma and Eaton, 2007).

Alternatively, as Dineva et al. (2007) theorized for the region near Go-Home-Lake, ON, the activity could be caused by stress concentrations due to the strength contrast of the mafic rocks (from passing hot spot) to felsic rocks.

The CSZ is one of the highest earthquake hazard regions in eastern Canada. Like the WQSZ, this region is also part of an ancient rift fault that extends along the St. Lawrence River (Adams and Basham, 1989, 1991) as mentioned above. However, the setting is complicated by a meteor impact structure of Devonian age (Lamontagne, 1987). The area of active seismicity appears to only occur in the St. Lawrence River in conjunction with meteorite impact. The areas upstream and downstream of the crater have a distinctly lower rate of seismicity. Baird et al. (2010) showed that it was likely the superposition of the weaknesses created by the failed rift along with those caused by the meteorite impact that make this specific region more prone to seismic activity than the surrounding regions that experienced just one or the other (or neither) of these geologic stresses.

3.2.2 Seismicity

The study region is situated along the southern edge of the WQSZ, which historically has experienced several larger earthquakes, including a M6.1 in 1935 in the Temiscamingue region, and a M5.8 in 1944 in the Cornwall-Massena region (Cassidy et al., 2010). More recently, the M5.0 near Val-des-Bois, QC provided some of the strongest recent shaking in the region, at a distance of only 60 km from the city of Ottawa (Lin and Adams, 2010). Using the data from the Canadian National Earthquake Database found at www.earthquakescanada.nrcan.gc.ca, an event this size happens on average

every 20 years within the west Quebec seismic zone. Lower level seismicity, however, is recorded on a regular basis as seen on Fig. 3-4. Annually, an average of 150 local earthquakes are located within the west Quebec seismic zone, approximately 50 of which are above M2, and between 10 to 15 of which are large enough to be felt. Larger regional earthquakes may also be recorded by stations in the Ottawa area; in particular, the Charlevoix region has a magnitude 4 and above every two to three years.

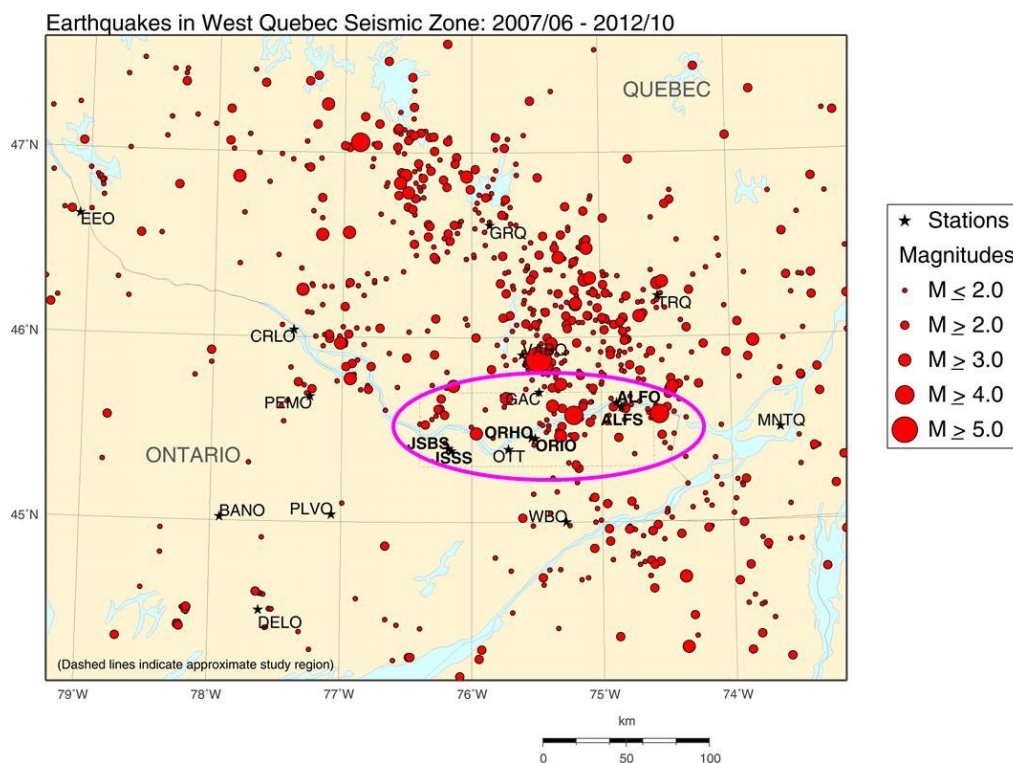


Fig. 3-4: Map of the west Quebec seismic zone, with ~5 years of regional seismicity marked with red dots, seismograph stations marked with stars and the name of the station. The approximate study region circled in purple. Earthquake data were obtained from Natural Resources Canada website (www.earthquakescanada.nrcan.gc.ca).

In addition, Brooks (2013, 2014) found several large earthquake-triggered landslides in the Ottawa/Gatineau area, evidence of a paleoearthquake of $M \geq 6.1$ dated between 980 to 1060 years before present (BP). Aylsworth et al. (2000) dated

earthquake-triggered landslides in the east of Ottawa, which all occurred within a specific date range suggesting a large local earthquake 4550 years BP. Another dating of a disturbed region of land near Alfred, ON suggests an earthquake produced a large ground disturbance in the area roughly 7060 years BP.

All three basins that have been instrumented with soil-rock seismograph pairs are located in the middle of the southern edge of the west Quebec seismic zone, and hence all three record a reasonable number of weak motion events per year at varying distances and azimuths allowing for investigations of earthquake parameters on the site effects. Teleseisms and regional events are also recorded, along with the occasional strong motion event. There are several other CNSN stations sited on bedrock in the general region (e.g. OTT, GAC) that can be used as reference rock sites for any of the basins for earthquakes, if the epicentral distance is significantly larger than the distance between the reference station and the soil site over the basin; that is to say, most of the travel path to the reference site and the soil site should be the same.

For a list of earthquake data recorded by the three station pairs and used for this study, see Appendix B. The data for all these recordings are available on an accompanying DVD.

3.3 Study sites and experimental design

The three basins which were examined for this study are located in the Ottawa region (see Fig. 3-5). The basins range in size from small (3 by 5 km) to moderate (10 by 18 km), and vary in shape from the more elongated Kinburn basin, to the more small and

large bowl-shapes of the other two basins. For all three basins, the soil and bedrock seismograph pairs were located within one to three kilometres of each other.

The largest basin is located on conservation and farm land just east of the town of Lefaivre, ON, approximately 65 km east of Ottawa. The Orleans basin is located in the residential area around Heritage Park within the eastern part of the city. And lastly, the third basin extends southeast of Kinburn, ON approximately 40 km to the west of Ottawa.

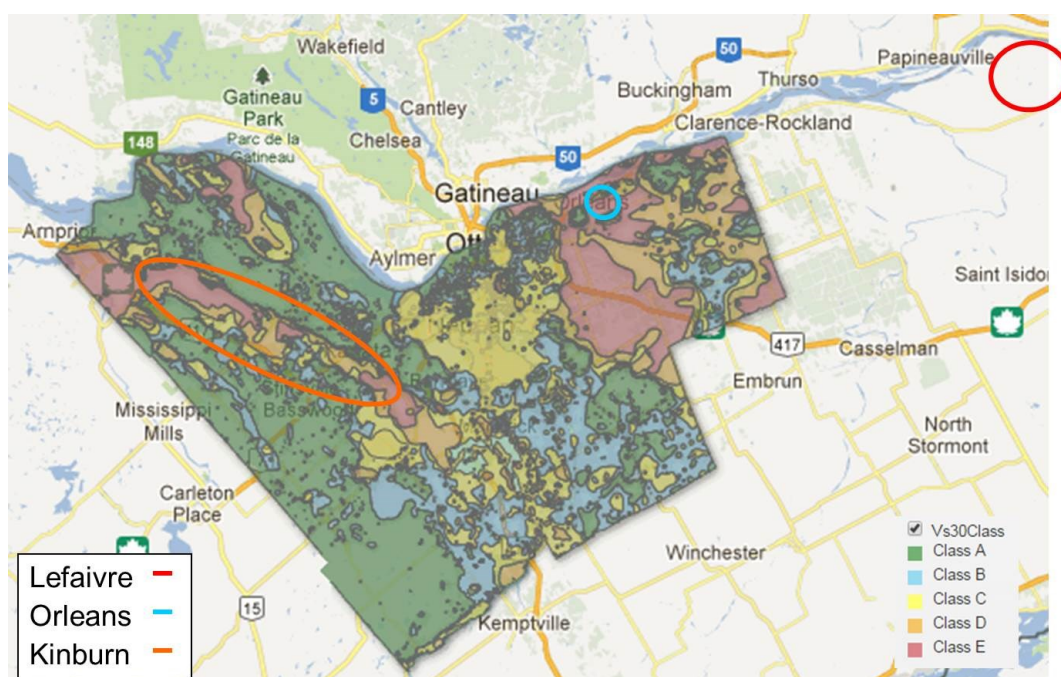


Fig. 3-5: Vs30 map of the Ottawa region from microzonation website – see Motazedian et al. (2011b). The location of the three basins are indicated by the coloured circles.

The model parameters of each of the three basins are based on data from various geophysical methods: seismic reflection and refraction profiles, boreholes, horizontal-to-vertical spectral ratios (HVSr), shear wave velocity measurements, etc. These methods and the data collected for the city of Ottawa are described in Hunter et al. (2010).

Accompanying references which further describe the process used to obtain the data for each basin are included below for each basin.

3.3.1 Lefaivre, Ontario

The Lefaivre basin is the largest of the basins being studied, with approximate dimensions of 18 by 10 km. Seismic surveys have been used to build a 3-D model of the basin (see Fig. 3-6), showing steep walls and a maximum depth of approximately 180 m (Benjumea et al, 2003). A high resolution profile shows the basin is filled with glacio-fluvial sediments and glacial till (Benjumea et al., 2003) overlain by post-glacial Champlain Sea silts and sand that have been determined to be geotechnically non-sensitive. On surface, over the bedrock basin, the soil is “disturbed” down to 50+ m (Benjumea et al., 2003), with an imposed surface relief between three and eight metres (Aylsworth et al, 2000). The upper 50 m also contains sand layers within the Leda Clay (Aylsworth et al, 2000). Evidence suggests that these regions of disturbed ground were likely created by an earthquake of significant size at around 7060 B.P. (Aylsworth et al., 2000). Details on the surveys done on this basin can be found in Benjumea et al. (2003) and Aylsworth and Hunter (2004).

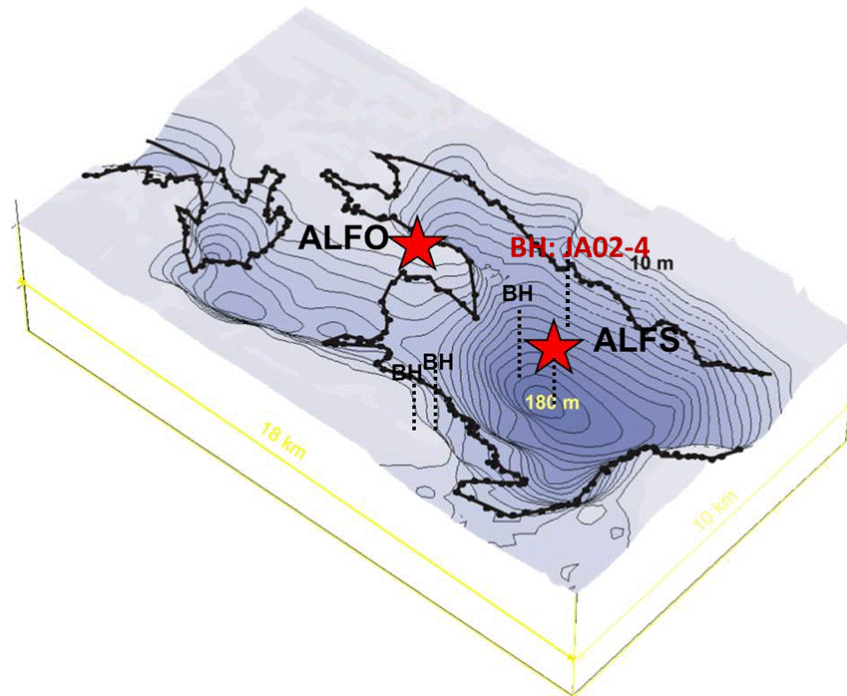


Fig. 3-6: 3D model of the Lefaiivre basin showing the estimated topography (for 10m intervals), and the approximate location of borehole JA02-4, after Benjumea et al. (2003). The approximate locations of the seismic stations (ALFS = soil site; ALFO = bedrock site) have been marked with red stars, while borehole JA02-4 is marked with a black dashed vertical line and labelled in dark red.

Although a bedrock seismograph has been associated with this basin site since 2003, the current soil site was only installed in the summer of 2012. The rock site is part of the Canadian Seismograph Network (CNSN) and, as such, the seismic data from it is available continuously from the NRCan website. However, the data from the soil site is retrieved only on request. The two sites were set up to have similar response, with broad band CMG-3 seismometers recording at 100 samples per second. This simplifies the comparison of the data. See Fig. 3-6 for approximate locations of seismograph sites, and Appendix A for more detailed station information, including response files.

3.3.2 *Heritage Park, Orleans, Ontario*

The Orleans basin is located in a residential area in the eastern part of the city of Ottawa. It is much smaller in size, approximately 3 by 5 km, with steep sides, (Motazedian and Hunter, 2008) oriented in a north-east to south-west direction. The maximum depth to bedrock is around 100 m (see Fig. 3-7). There is a broad opening to the NW, and a narrow one to the SW (Kolaj, 2010). The seismic profiles indicate there is no layer of disturbed ground (Dr. J.A. Hunter, personal comm., 2012). The fine-grained sediments filling the basin are geotechnically sensitive, and have a low shear wave velocity (V_s less than 180 m/s) (e.g. Motazedian and Hunter 2008; Hunter et al., 2010). Details of the surveys done in this area can be found in Kolaj (2010), Motazedian and Hunter (2008), Motazedian et al. (2011), and Crow et al. (2007).

This basin was the first one to be instrumented with a soil site seismograph, ORHO, in the summer of 2007. The instrument, a broadband CMG-3 seismograph, was placed approximately over the deepest part of the basin (see Fig. 3-7). The rock site, ORIO, was installed a year later with the same type of seismometer (see Appendix A for station details). Both stations are part of the CNSN, and hence the station responses and the continuous waveform data are also available from the site:

www.earthquakescanada.nrcan.gc.ca.

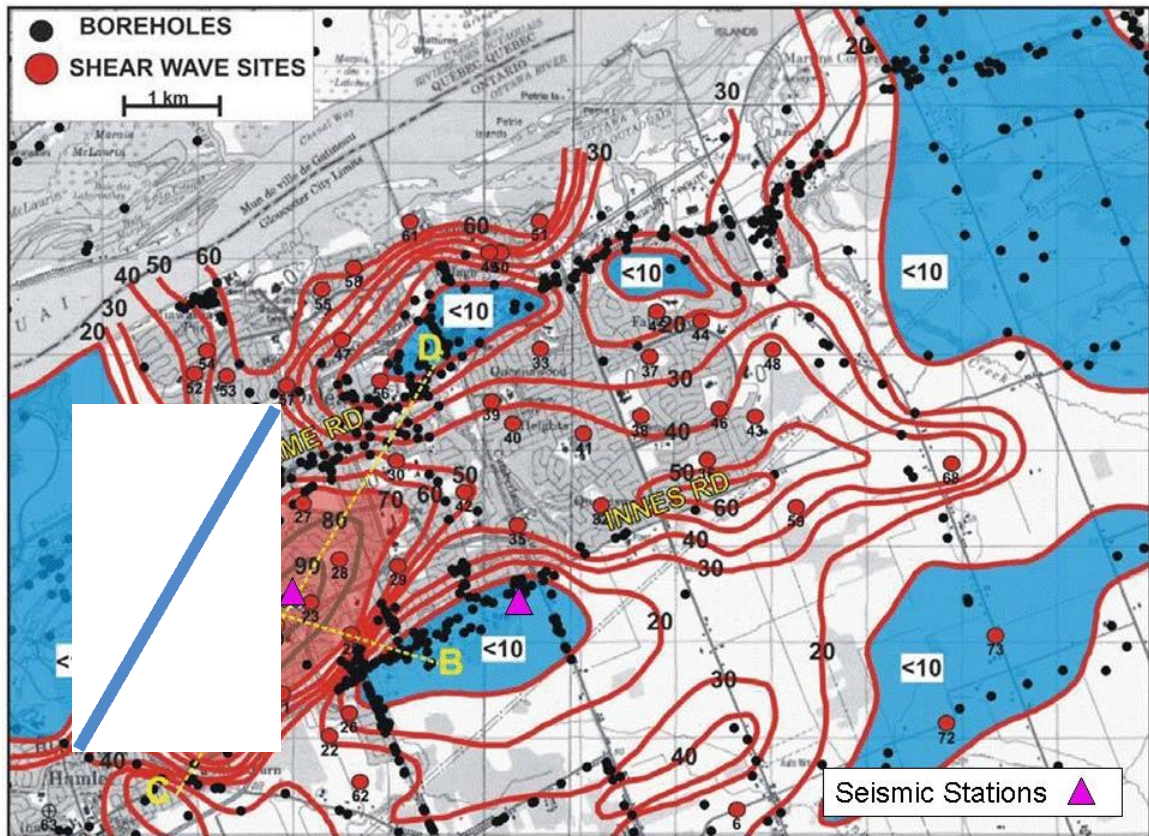


Fig. 3-7: Topographic map of Orleans basin, with location of cross-sections marked in yellow dashed lines (after Hunter and Motazedian, 2008). Approximate locations of seismic stations have been added as purple triangles.

3.3.3 Kinburn, Ontario

The Kinburn basin is made up of a series of smaller interconnected basins, approximately 5 km wide by 20 km long, oriented in a NW-SE direction, approximately parallel to the seismic zone (see Fig. 3-8). The maximum depth to bedrock of the basin is approximately 140 m, but the current soil site is located over the centre of a shallower section of the basin, but which still reaches a depth to bedrock of approximately 130 m.

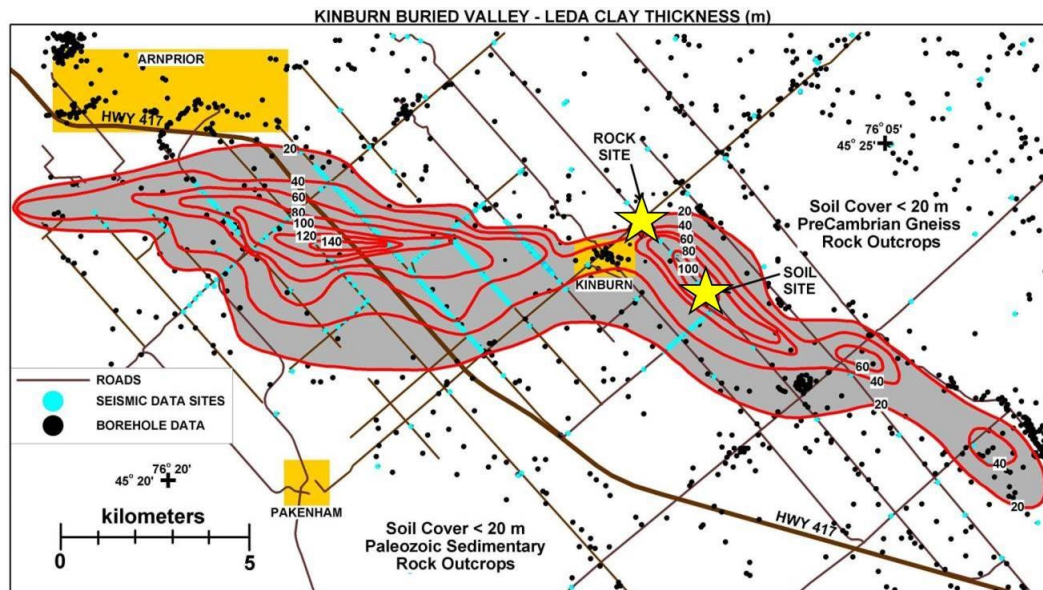


Fig. 3-8: Topographic map of the Kinburn basin, as prepared by Dr. J.A. Hunter (2012). Approximate locations of seismic stations are marked with yellow stars.

The basin is bounded on the NE side by steep faults, whereas the southwestern edge is more gently sloped (see Fig. 3-8 and 3-9). The basin is filled with low Vs, non-sensitive, Leda clay, with a till layer directly above the bedrock surface in many locations. There is no evidence of disturbed ground (Dr. J.A. Hunter, pers. comm. 2012).

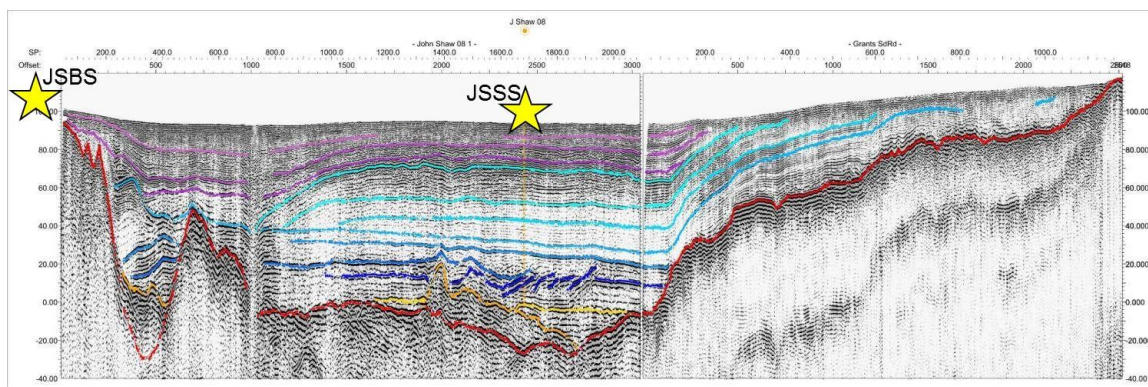


Fig. 3-9: Combined John Shaw Road - Grant Side Road sections, as prepared and interpreted by Dr. A. Pugin (see Pugin et al., 2013). The red line marks the top of bedrock, while the yellow line is interpreted as the top of the gravel/till deposits. The location of the borehole is marked with a yellow star over the section, and the approximate locations of the seismograph sites are marked with yellow stars.

A borehole, located approximately 330 m to the SSE of the soft soil seismograph site JSSS, was drilled and logged through the soft sediments to the interpreted top of the till-derived coarse-grained layer (a significant shear wave impedance boundary determined from reflection seismic), as represented in Fig 3-8 with a yellow line. The red line is the location of the interpreted top of the bedrock. The detailed report on this borehole can be found in Medioli et al. (2010), while the seismic sections from Fig. 3-9 are described in Pugin et al., 2013. Further details on the data collected in and around the Kinburn basin is included in the report by Hunter et al. (2010).

The station pair JSSS (soil site) and JSBS (rock site) was installed in 2010, with identical equipment: Trillium 120p seismometers and Taurus digitizers. This allows for easy comparison between the two sites. These stations are not part of the national network, so event data is requested and saved as needed. Two Etna accelerographs were also installed at each site to measure strong motion events that might be clipped on the weak motion instruments, particularly the soil site. For more details on station information and response files see Appendix A.

3.4 Horizontal to Vertical Spectral Ratios (HVSR)

Due to the possibility of resonance in a basin setting, with high shear wave seismic impedance contrast between the soil and bedrock, it is important to determine the fundamental period (T_0) or frequency ($f_0 = 1/T_0$) of a site (e.g. Kramer, 1996; Rial et al., 1992). The fundamental frequency was determined at the soft soil site at each basin (see Fig. 3-10), using 30 minute recordings of ambient noise on a Tromino instrument at one

site and comparing the horizontal versus the vertical components (see Appendix A for instrument information). These recordings are then divided into 30 s segments, the Fourier transform calculated for each, which are then analyzed and interpreted individually, with noisy or anomalous segments removed. The remaining segments are arithmetically averaged and combined to obtain a final spectrum. This method was first proposed by Nakamura (1989), and the data from the basin sites were collected following the guidelines described in S4.7 of Open File 6273 (Hunter et al., 2010). The fundamental frequency calculated for each of the basins is as follows: ~0.5 Hz for the Lefaivre basin, ~0.7 Hz at the Kinburn site, and ~0.8 Hz for the Orleans basin. Note that the amplification of the horizontal versus the vertical can be highly variable depending on the time of observations (e.g. time of day, time of year, local noise, weather, etc). However, the frequency of the peak tends to be fairly constant for each site.

In the 2005 National Building Code (NBCC), the following relation is given between T_0 and the thickness of the soft soil:

$$T_0 = (4H/V_{s_{avg}}) \quad \dots [Eqn 3.2]$$

where H is the thickness of the soil in m, and $V_{s_{avg}}$ is the average shear wave velocity from surface down to the soil-rock boundary. Hence, if $V_{s_{avg}}$ is known, one should be able to determine the thickness of the soil from T_0 or f_0 . However, using borehole data as ground truth, it has been found that there is a slight shift in this relation for the local data. Instead, the following equation was found to fit the data for the Ottawa region:

$$H = 64.44 * f_0^{(-1.365)} \pm 2\sigma = 7.94 \text{ m} \quad \dots [Eqn 3.3]$$

where H is the depth in m, f_0 is the fundamental frequency in Hz (see Fig. 3-11).

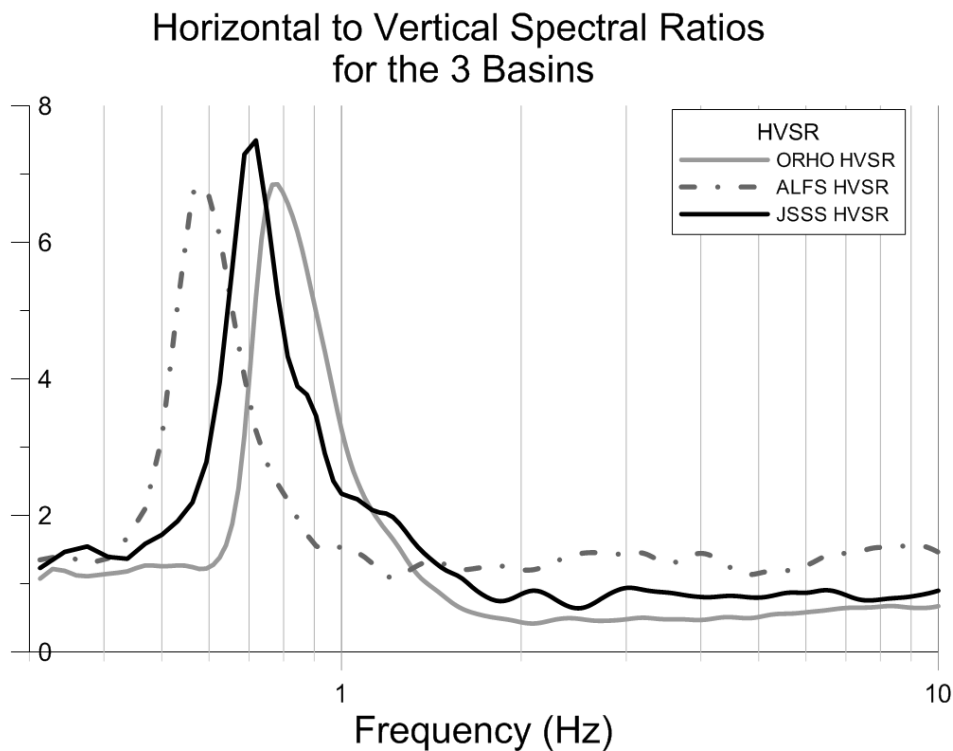


Fig. 3-10: Horizontal to vertical spectral ratios as determined at the seismograph site situated on the soft sediments at each basin. Data collected and prepared by Dr. J.A. Hunter.

The above relationship has been used to determine depths to the first major shear wave seismic impedance contrast, taken to be either bedrock or the till layer. In this way, many additional measurements of depth of the soft sediment have been used to help define the geometry of the Kinburn basin. See Crane's thesis entitled "Numerical Modelling of Seismic wave propagation through a soft soil basin: Kinburn, Ontario" (S. Crane, PhD Candidate, Earth Sciences, Carleton University) for the details on the data collected and methods used for modelling of the basin.

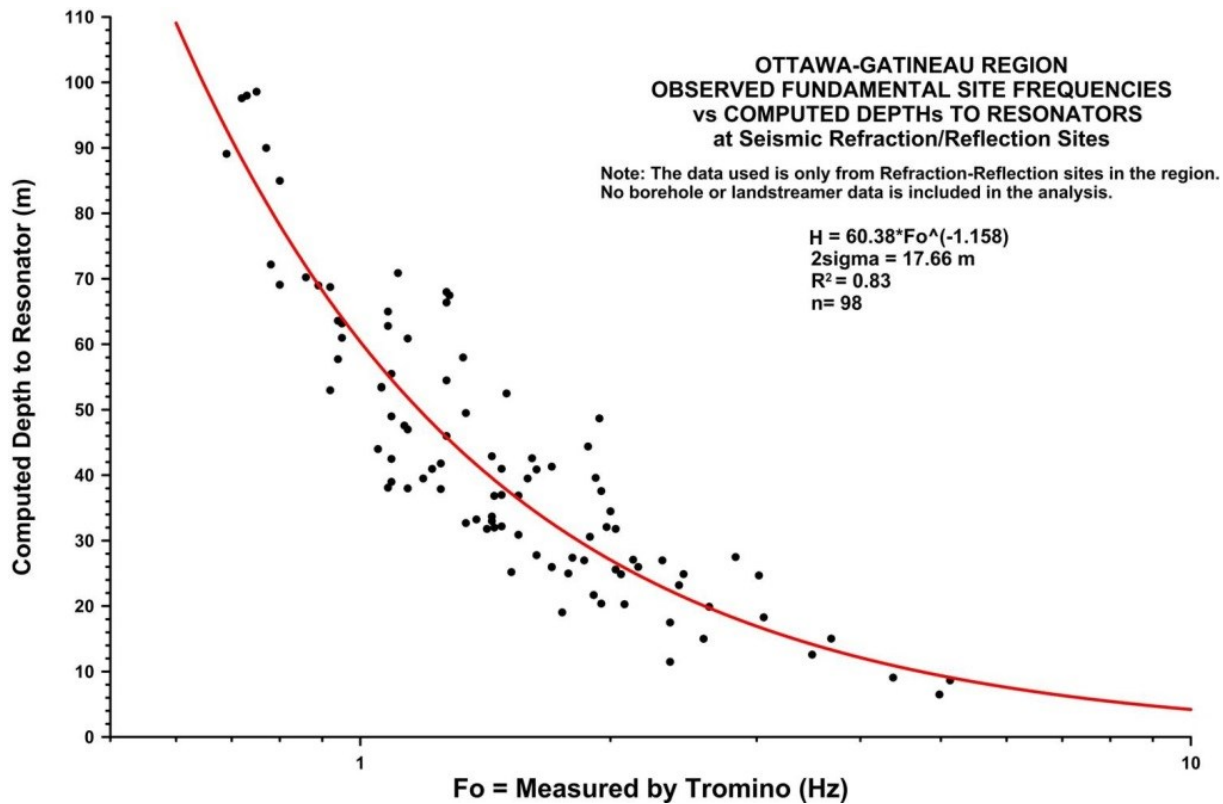


Fig. 3-11: Relation between fundamental site frequency and thickness of the soft soil sediment as determined empirically for the Ottawa region. Data collected and prepared by Dr. J. Hunter, GSC (pers.comm., 2015).

4. Data Observations

The goal of this study is to determine what effects the soil and its underlying bedrock have on the ground motions at the surface and in particular to examine the influences of basin-edge effects. These influences should be evident on the resulting recording. Hence, in this chapter we begin by examining the waveforms of the basin-site recordings from each of the three basins in order to find characteristics in both the time and the frequency domains which differ from expected – i.e. as compared to the reference rock site recordings.

There are many outstanding features that can be observed directly, while others require further digital processing before they become apparent. Patterns within the recordings should indicate how (or if) the basin is altering the resulting ground motions over the deepest part of the basin. We compare these characteristics with observations from previous studies at other basins around the world.

The list of earthquakes recorded and used for this study can be found in Appendix B. The original and processed data for the earthquake recordings used in this and subsequent chapters are included as an electronic supplement to this thesis, except for stations ORIO, ORHO and ALFO which are available on-line from the National Earthquake Database (Natural Resources Canada) at:
<http://www.earthquakescanada.nrcan.gc.ca/stndon/NEDB-BNDS/index-en.php>.

4.1 Time Domain Observations

Below are listed the characteristics of the time domain waveforms observed for each of the basins in the study area. Note that any analysis requiring absolute timing (e.g. particle motion plots) between the components of a station cannot be made on the stations JSSS, JSBS, and ALFS due to a timing misalignment problem prior to 2013/10/26. After that date the timing problem was solved with a software upgrade and by altering the routine used to download the data. See Appendix A for more details.

4.1.1 Large amplification

When comparing the recordings of local earthquakes from the basins in the Ottawa region, the signals from the soil sites are significantly amplified on all three components as compared to those of the nearby rock sites (see Fig. 4-1). For all earthquakes examined on the soil sites at all three basins, the horizontal components are always amplified considerably more than the vertical components.

If the theoretical broad band amplification due to the overburden-bedrock seismic impedance is calculated using Eqn. 2.3 (see Section 2.4.1), with constant bulk values for each layer of $V_{s_{soil}} = 150$ m/s and $V_{s_{rock}} = 2700$ m/s and densities of 2.5 g/cm³ for the rock and 1.61 g/cm³ for soil as a first approximation, we obtain an expected amplification of approximately 5 times for the soil site over that of the rock site recordings. Since there is a very strong seismic impedance contrast between the bedrock and the overlying soil, using Eqn. 2.6 (see S2.4.2) for resonance may be more appropriate. Using Eqn. 2.6 and the same values of V_s for rock and soil as mentioned above, the predicted amplification is around 28 times for the soil site over that of the rock site. Note that these amplification

estimates should be high, since the actual V_s over the entire depth of the clay profile of each of the basins is continuously changing and mostly higher than 150 m/s, as is the $V_{s_{avg}}$ which is based on the shear wave velocity calculated over the entire depth of the layer. In other words, in reality the velocity contrast between soil and rock is likely lower, which should lead to lower amplification. Furthermore, there is a till layer between the clay and rock, with an approximate V_s of 580 m/s. Including this layer would also further reduce the impedance contrast of the layers, and hence the calculated amplifications. However, for many of the recordings at all three basins, the amplification appears to be higher than either of these predicted values, at least on the horizontal components.

Fig. 4-1 shows the recordings (unfiltered) on all three basins of the m_N 3.6 2013/10/20 Barry's Bay, ON earthquake. The soil site data for all three components and all three basins is shown in black, and the rock site data in grey; the Lefaiivre basin pair (ALFS and ALFO) are plotted on the top, followed by the Kinburn basin pair (JSSS and JSBS) in the middle and the Orleans basin pair (ORHO and ORIO) on the bottom. This is plotted along with the corresponding rock site component for each basin shown in light grey. Qualitatively it can be observed that the amplification of the soil recordings (black) is much higher than that of the reference rock site, particularly on the horizontals, even though the two sites are within a couple of kilometres of each other, while the epicentral distance to the recording sites is between 100 and 200 km (depending on the basin). The vertical component is also amplified for all three soil sites as compared to the rock soil site counterpart, however the strength of this amplification varies and is not as strong as the amplification as that seen on the horizontal components.

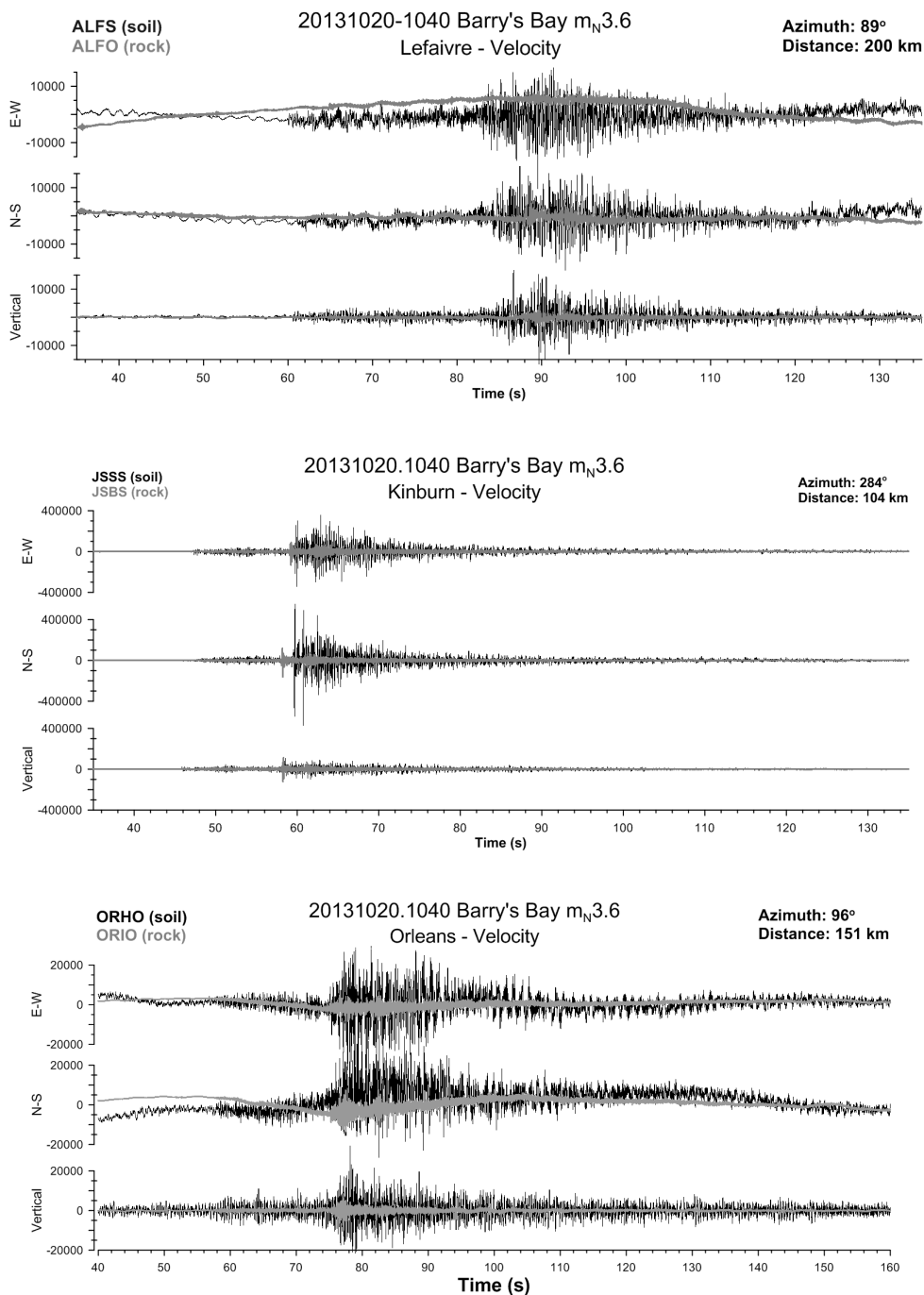


Fig. 4-1: Three-component recordings of the $m_N 3.6$ earthquake near Barry's Bay, ON on 2013/10/20 at 10:40 UT from all three basins (Lefaire basin pair on top, followed by the Kinburn pair in the middle, and the Orleans basin pair at the bottom), showing the soil site recordings in black, and the rock site recordings in grey. No filter was applied, hence some background low frequency signal is present in some of the plots that is unrelated to the local earthquake signal.

Large amplification effects have also been noted for other basins around the world, including the Mexico City basin (e.g., Singh and Ordaz, 1993), the Kanto basin in Japan (Kawase, 1996), and the Grenoble basin (Cornou and Bard, 2003). The observed amplifications computed using the spectra are presented in the following section (S4.2).

4.1.2 Duration

Following the recorded earthquake event, the three component channels take much longer to return to pre-event (background noise) levels on the soil site recordings of all three basins as compared to the station on the adjacent bedrock site. Fig. 4-2 is a typical example of a recorded local earthquake on the station pair ORHO (soil) and ORIO (rock) from the Orleans basin. It shows the recordings from the m_N 3.1 2012/09/22 Rockland, ON earthquake for all three components of the rock and soil site (rock site on top), passed through various filters to highlight the response of the basin at different frequencies. The top plot (A) shows the low frequency end, using a bandpass filter of 0.5 to 1.0 Hz on the data; the following plots (B) and (C) show the mid-frequency range with filters of 1.0 to 1.5 Hz and 2.0 to 3.0 Hz respectively used; and finally the last plot (D) is showing the high frequencies with the data filtered between 5.0 to 10.0 Hz. Note that the scale of the vertical axes is adjusted for each trace, in order to better see the data. Hence the amplitudes on this plot cannot be directly compared.

The soil recording shows significant signal to noise ratio long after the rock site recording has tapered back down to pre-earthquake levels, particularly in the lower frequencies. This longer duration of the signal (i.e. the amount of time the signal is above

the background noise), has been identified as an important factor in the damage potential of the ground motion (Beck and Hall, 1986). That is to say as the stronger shaking continues longer on the basin, there is more potential for damage. Note that when examining only the spectra or spectral amplification of the data, the information on the duration of the strong signal is not retained.

The long duration of these basin recordings has also proved to be one of the more difficult elements to account for and model (Chávez-García and Bard, 1994). Kawase and Aki (1989) proposed the long duration in the Mexico City basin might be due to the interference between body waves and surface waves diffracted from the basin-edge. This effect was later modelled by Kawase (1996) for the Kanto basin in Japan at which time he named it the “basin-edge” effect. This has been supported by more recent work by other researchers, including Narayan (2012).

4.1.3 Character of signal

Apart from the long duration, the frequency content of the soil site recordings all look markedly different from their counterpart rock site, with much lower frequency content being observed (see Fig. 4-2).

The results show the soil sites recordings of each basin are of consistently longer duration, even for the higher frequencies. However, the majority of this prolonged energy occurs in the lower frequency range, where the duration of the recordings greatly exceeds the duration of the rock site recording. This long duration, monochromatic coda is mentioned by numerous researchers (e.g. Flores et al., 1987; Singh and Ordaz, 1993;

Chávez-García and Bard, 1994; Ramos-Martínez et al., 1997) as a characteristic signal from various basins around the world, including the one in Kobe, Japan (Kawase, 1996) and in Texcoco, Mexico (Stephenson et al., 2006).

In the lower frequency range, late energetic arrivals or beats (see Fig. 4-2-A) are evident in the coda, as observed at other basins (e.g.; Singh and Ordaz, 1993; Chávez-García and Bard, 1994). Kato et al. (1993) postulated that these late arrivals were due to the reverberated SH waves and to Love waves, which is supported by later researchers, including Kawase (1996).

Some of the later energetic arrivals in the Mexico City basin have also been shown by Stephenson et al. (2006) to be due to later arriving phases probably converted near some basin boundary or feature.

4.1.4 Particle motion

As the focus of this study is the possible influence of basin-edge effects on surface ground motions, we specifically examined the data for signs of preferred orientations in both the time and frequency domains. One way to examine the basin-edge effect is to study the particle motion of the incoming wave along the azimuth for epicentres of different events and basin geometry. As mentioned in S3.3, only the station pair at Orleans had accurate timing until March 26, 2014. Not enough data has been acquired since that date on either the Kinburn or Lefavre basin, hence only the data from the Orleans basin will be examined using particle motion.

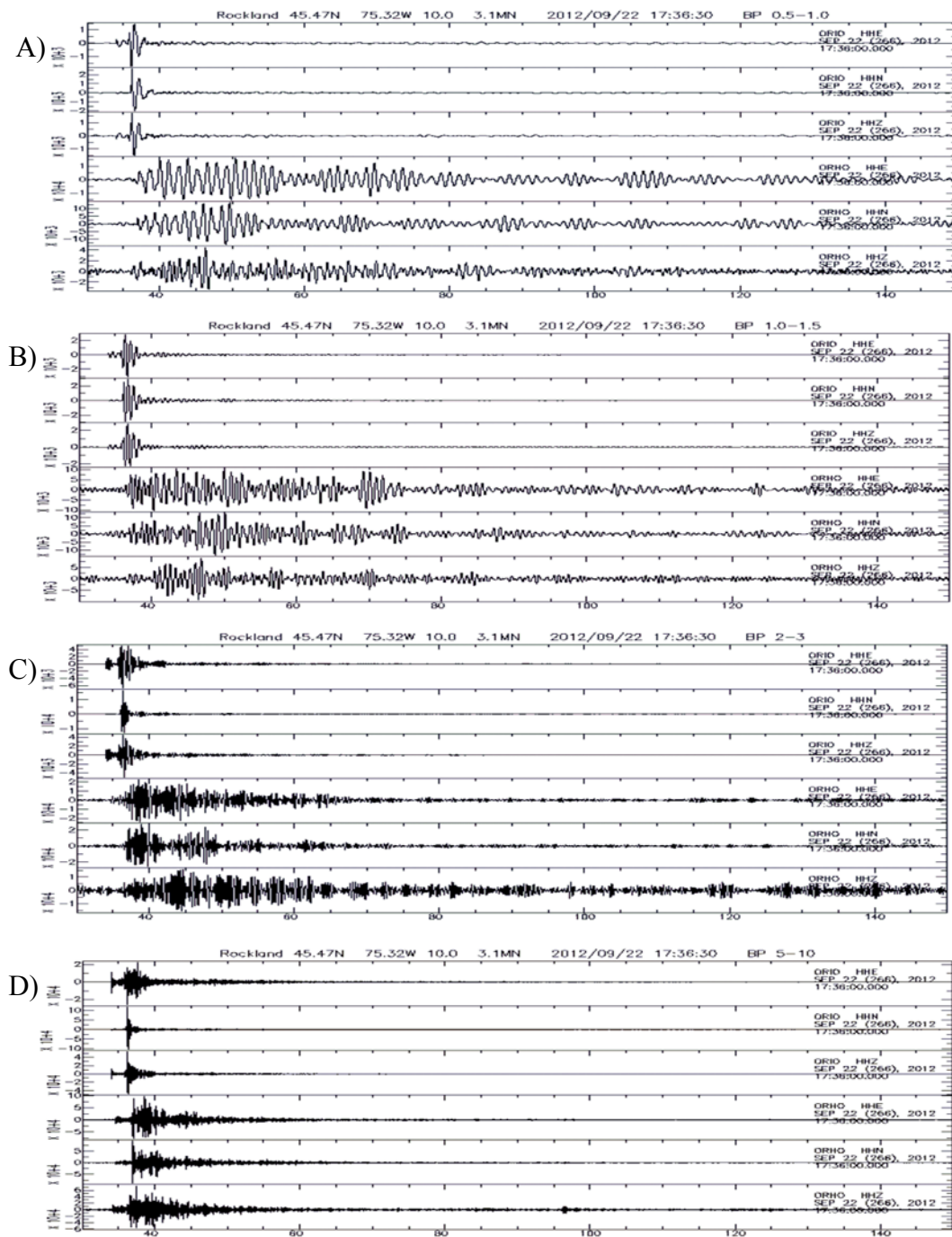


Fig. 4-2: Recordings of a local earthquake (Rockland, ON; M3.1; 2012/09/22 at 17:36 UT) from the Orleans basin comparing the three components (east, north and vertical) of the rock site ORIO and then the soil site ORHO recordings underneath at various pass bands: A) 0.5 to 1.0 Hz; B) 1.0 to 1.5 Hz; C) 2.0 to 3.0 Hz; and D) 5.0 to 10.0 Hz. Note the plots are fit to scale in order to better see the data, but in general the soil sites are of greater amplitude than their rock site counterparts.

Fig. 4-3 shows the recordings for the station pair ORHO (soil site in black) and ORIO (rock site in grey) for the $m_N 4.2$ Hawkesbury, ON earthquake which occurred on 2012/11/06 at 09:05 UT (Universal Time). The top three plots show the particle motion for (a) the East-West (E-W) component versus the Vertical (V) component; (b) the North-South (N-S) component versus the V component; and (c) the E-W versus the N-S components. The bottom portion of the plot shows the actual recordings on the three components (N-S, E-W and V), with the line above the time scale (in seconds) indicating the portion of the record that was used in the three particle motion plots above. By examining the overall particle motion for the entire duration of the event, it is evident that the motion has larger horizontal motion than vertical motion (see Fig. 4-3). This supports the observations in S4.1 with regard to the amplification of the components, wherein all the components from the soil recordings were amplified compared to the rock site, with the horizontal components significantly more so than the vertical.

By plotting the particle motions for various sections of the earthquake coda, we attempted to (a) identify the type of motion, particularly in the later sections of the recording where we observed the late energetic beats; and (b) isolate a preferred orientation or pattern that might be consistent between earthquakes. However, the high frequency nature of the local earthquakes is extremely chaotic; for example, within one second of data, the orientation of the motion may change multiple times. Fig. 4-4 shows the particle motion of horizontal components (E-W versus N-S) of the soil site ORHO for the $m_N 4.5$ Vercheres, QC earthquake that occurred on December 10, 2012. The 12 particle motion plots show various one second snapshots (except the top right plot which

is only 0.5 s of data), starting at approximately the start of shear wave arrival in the first plot, and moving progressively through the data. The original waveforms are shown below for reference.

It became evident that in order to determine if there is a prevalent orientation to the data, we could not examine the standard particle motion plots. Hence, another method was devised to examine the preferred particle motion orientation along the time series, as is described in Chapter 6, along with the results.

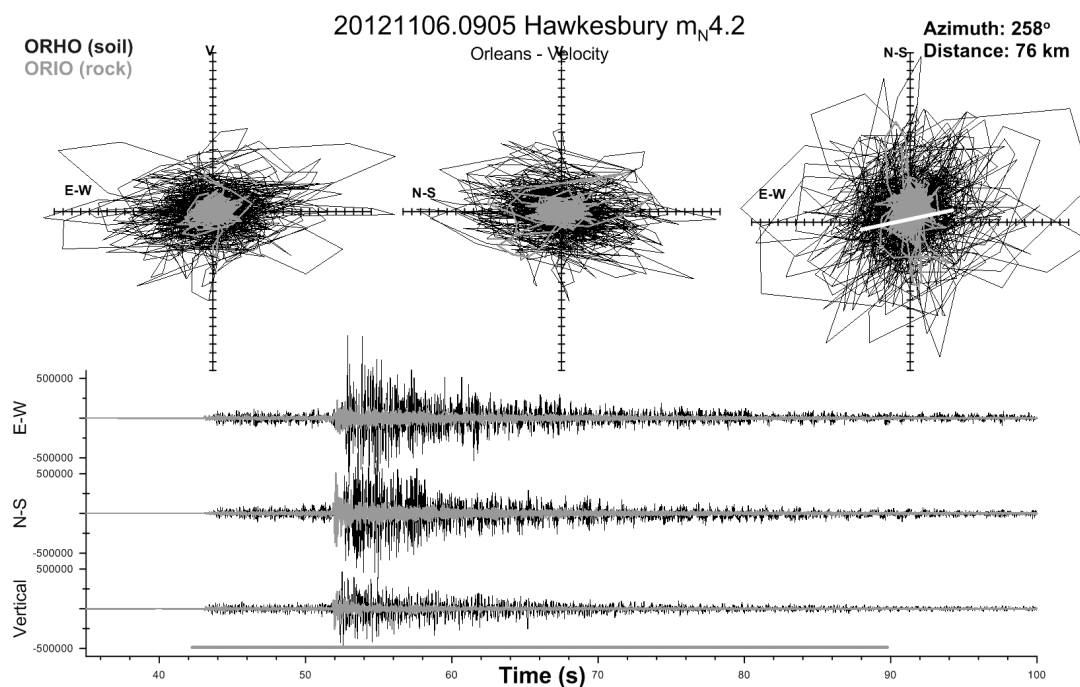


Fig. 4-3: Plot of seismograph data from the three components of the Orleans basin pair (ORHO: black; ORIO: grey) plotted on the bottom with time in seconds, with particle motion plots of E-W vs Vertical (V), N-S vs V, and E-W vs N-S. The long line above the time scale indicates the section of data used to produce the particle motion plots. The small white line on the E-W vs N-S particle motion plot shows the direction of the earthquake to the station.

We examined the first onset of the P-wave arrival, to determine the orientation of the particle motion alignment with respect to the azimuth of the earthquake. The P wave

is a compressional wave with particle motion in the direction of travel. The ray path will be from the earthquake hypocentre to the recording station. Due to the distance of most of the earthquakes from the site, the incoming ray will be mostly from below, meaning that the P wave should register most strongly on the vertical component, and a weaker horizontal component, that should be approximately in-line with the direction of the earthquake source. All the earthquakes with clear arrivals were examined for the Orleans station pair. The results showed the rock site always had the arrival orientation aligned to the earthquake azimuth (within a few degrees), whereas the orientation of the P-arrival on the soil site appeared random, with variances up to 90° , interpreted to result from multiple reflected and refracted waves from different sides of the irregular-shaped basin. Fig. 4-5 shows approximately 3s of data around the P-arrival on the Orleans station pair for the m_N 4.1 earthquake that occurred on 2013/05/17 near Shawville, QC. This event was clearly recorded by both the soil and rock sites. The short grey line on the E-W vs N-S particle motion plot (top right plot on Fig. 4-5) shows the direction of the earthquake from the station, and hence the expected direction of the P motion. As can be seen in this example, the rock site particle motion for the first P-arrival lines up approximately with this light grey line, whereas the soil site P-arrival motion does not. Note, that due to the larger background noise on the soil sites, it was often not possible to distinguish between azimuth and back azimuth in the actual recordings, hence the angles of arrivals may be greater than 90° from the expected arrival. However, it seems intuitively less likely that the initial motion would appear to be coming from the opposite side of the basin from the epicentre.

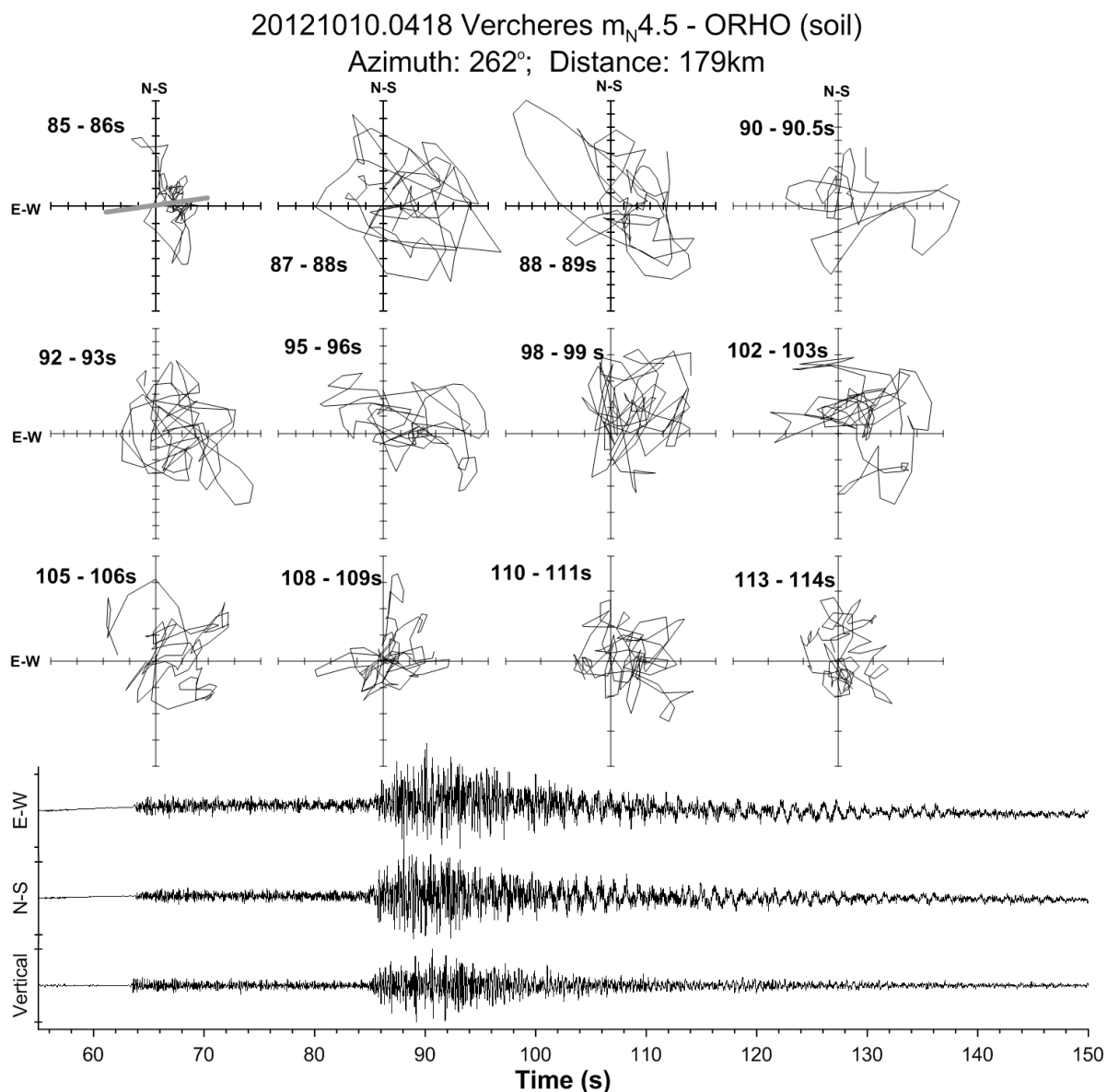


Fig. 4-4: Particle motion plots (top 12 plots) of horizontal components of ORHO (E-W vs N-S) for the 2012/10/10 Vercheres, QC 4.5mN earthquake (as seen below). The plots start at approximately the start of the shear wave arrival, and progress through time, with each plot showing the time segment used for that plot. The grey line on the first plot shows the expected orientation of the P arrival, given the azimuth of the earthquake.

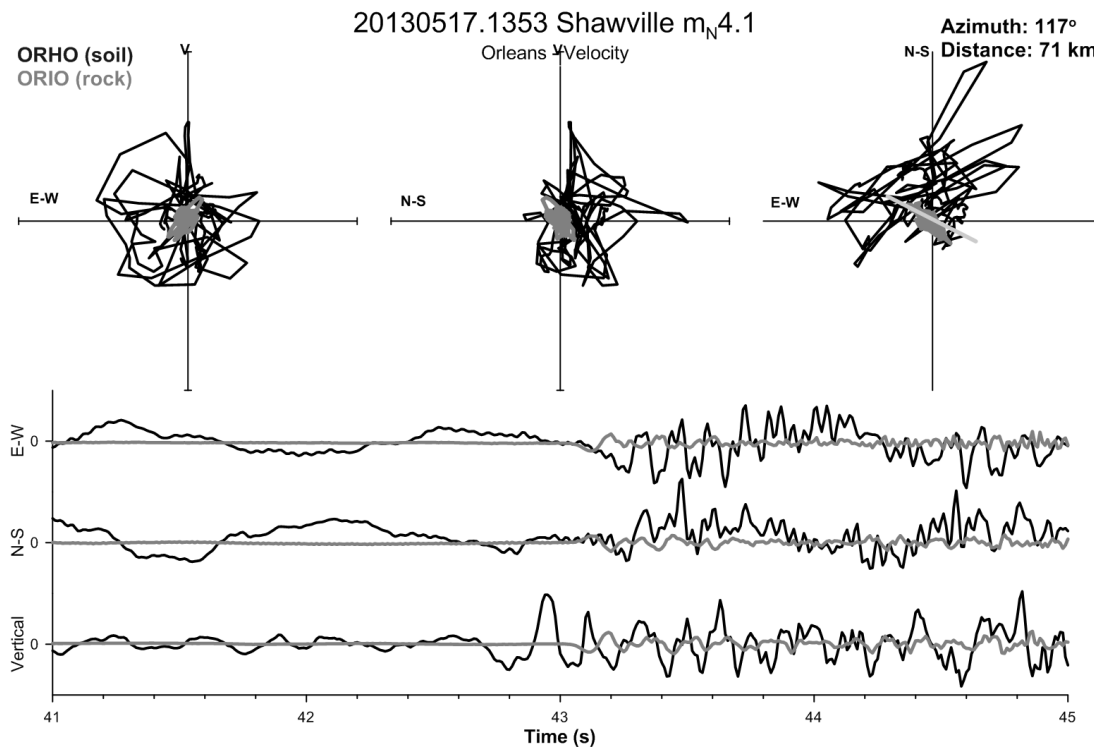


Fig. 4-5: Bottom shows the P-arrival on the 3-component data from ORHO (black) and ORIO (grey) for the 2013/05/17 $m_N 4.1$ earthquake near Shawville, QC. Top three plots are the particle motion plots (E vs Z; N vs Z; and E vs N) for the same time frame. The short light grey line on the third particle motion plot shows the azimuth of the earthquake to the station).

Bouaannani and Frasson-Botton (2013) examined the recordings of several soil sites around the Ottawa region from data from the 2010/06/23 Val-des-Bois, Québec earthquake. They also did not see any obvious correlation on the horizontal components with regards to the earthquake epicentre. Unfortunately the underlying bedrock topography is not known for their recording sites, so it is not possible to correlate the varying azimuthal deviations seen in that study to a particular subsurface feature.

Several studies from various regions around the world also note that the incoming surface waves are not aligned with the source, but rather to the basin-edges (e.g.; Field et

al., 2000; Somerville et al., 2002; Stephenson et al., 2006). In particular, Somerville et al. (2002) note that Love waves are predominately polarized parallel to the basin-edge, while the Rg waves were normal to the basin-edge. The attenuation of Rg waves was lower than that of the Love waves. Joyner (2000) accounted for this in his model for predicting ground motions over a basin, by using different ground motion prediction equations for vertical, parallel and perpendicular directions.

4.1.5 Delayed body wave arrivals on horizontals

For the Orleans station pair, where timing was known to be accurate and the components time-synchronized, it was noted on the soil site recordings that the P arrivals seemed to be delayed on the horizontals when compared to the vertical by around 0.3 to 0.4 seconds, whereas the P arrivals on the rock site appear to arrive concurrently on all components. This delay was noted for all the events where the P arrival was reasonably clear. Several of the earthquakes with the strongest arrivals were examined in detail. The m_N 4.2 Hawkesbury, ON earthquake that occurred on 2012/11/06 is shown as an example in Fig. 4-6. As can be seen in this figure where the first P-motion has been magnified, there is a much weaker P arrival on the horizontals that seems to arrive with, or just after the arrival on the vertical component, but well before the stronger arrival. This weak arrival is hidden in the noise in the weaker events. Hence, the strong arrival may not actually be the P-arrival, but is possibly the resonating waves from the P-arrival. If this is the case, then when measuring the direction of the ground motion with the “first-arrival” (as in S4.1.4), we would actually be measuring this resonant wave.

Another interpretation of this delay can be explained by the presence of the very low V_s soil within the basin overlying the very high V_s bedrock. As the P wave encounters the basin-edge, the incoming P wave will be refracted according to Snell's Law:

$$\frac{v_1}{v_2} = \frac{\sin \theta_1}{\sin \theta_2}$$

where v_1 and v_2 are the respective velocities of the rock and soil, and θ_1 and θ_2 are the angles of the P wave ray path with respect to the vertical in the rock and soil respectively.

The implication of this is that given the large velocity contrast, the incoming P-wave will become essentially vertical, with little to no energy in the horizontal direction. Hence why the P-wave is not visible on the horizontal components at the expected arrival time, but it is visible on the vertical component.

A similar magnified view of the S-arrival was not as conclusive as the P wave event. It is possible that there is a delay on one or more components. As well, the rock site signal has a delay from one horizontal to another, as is expected if the orientation of the earthquake to the station is such that one component is receiving mostly radial energy, with the other mostly receiving the transverse energy. However, for the soil site, in general the S arrival is not clear enough to judge the exact arrival times for even the larger earthquakes.

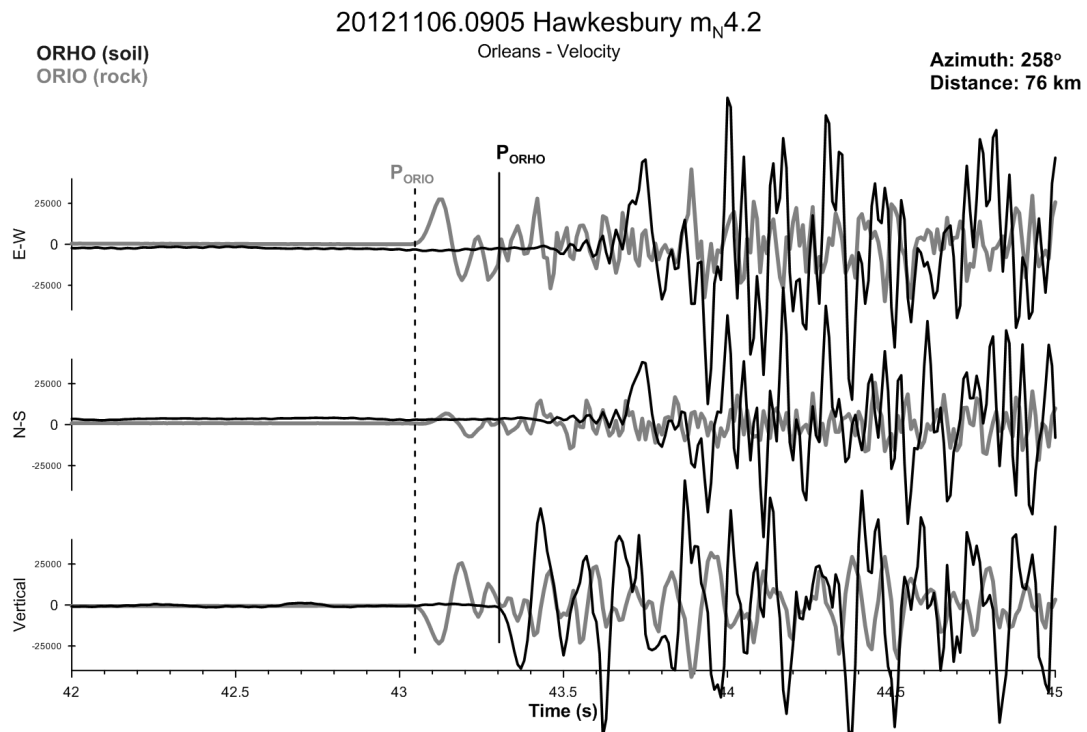


Fig. 4-6: Three seconds of data around the P-arrivals for ORHO (black) and ORIO (grey) for the E-W, N-S and Vertical components of data respectively. Data is from the 2012/11/06 Hawkesbury, ON $m_N 4.2$ earthquake. The approximate P-arrival is marked with a vertical black line, solid for ORHO and dashed for ORIO.

4.2 Frequency Domain Observations

During examination of the waveforms recorded over the basins in the time domain, we observed that the waveform frequency contents differed from those of the reference rock-site recordings (see section 4.1.3). In order to examine the change with respect to the frequency, a fast-Fourier transform (FFT) was taken, giving the amplitude of the signal versus frequency for any particular earthquake at a site. This was then smoothed (see sub-section below) and compared to the FFT calculated and smoothed for the rock site for the same earthquake and the same time window to determine the amount of amplification as a spectral ratio of soil versus rock (see Fig. 4-7).

Generally for engineering purposes, it is the horizontal forces that are of interest, as the vertical direction already needs to be engineered to account for the force of gravity. Theoretically we would rotate the horizontal components from N-S and E-W to be aligned with the earthquake, giving us the radial and tangential components which should have the maximum amplitude for the compressional and shear wave respectively. However, in this case the data from the soil site does not appear to be aligned as expected, likely due to the 2D and 3D effects of the basin, as discussed in the previous section (S4.1.4). Therefore, for the following calculations we will be considering the root mean square of the horizontal components, which is often used in earthquake engineering.

In Fig. 4-7, plots A to C show the spectra for the three components of JSSS (Kinburn soil site) and JSBS (rock site) for the $m_N4.2$ Hawkesbury, ON earthquake of 2012/11/06, without smoothing. Plot D shows the combined root mean-squared average of the horizontals, which was used for determining the horizontal to vertical ratio of plot E for each individual station, separately. Plot F also shows the ratio of mean-squared average of the soil horizontals to rock horizontals. As this figure shows, the spectra can be rather chaotic if no smoothing is applied and thus results in chaotic-looking amplifications. In order to see a more general pattern in the data, some smoothing was required. A triangular smoothing was applied to all the FFT results, prior to taking the ratio of soil to rock.

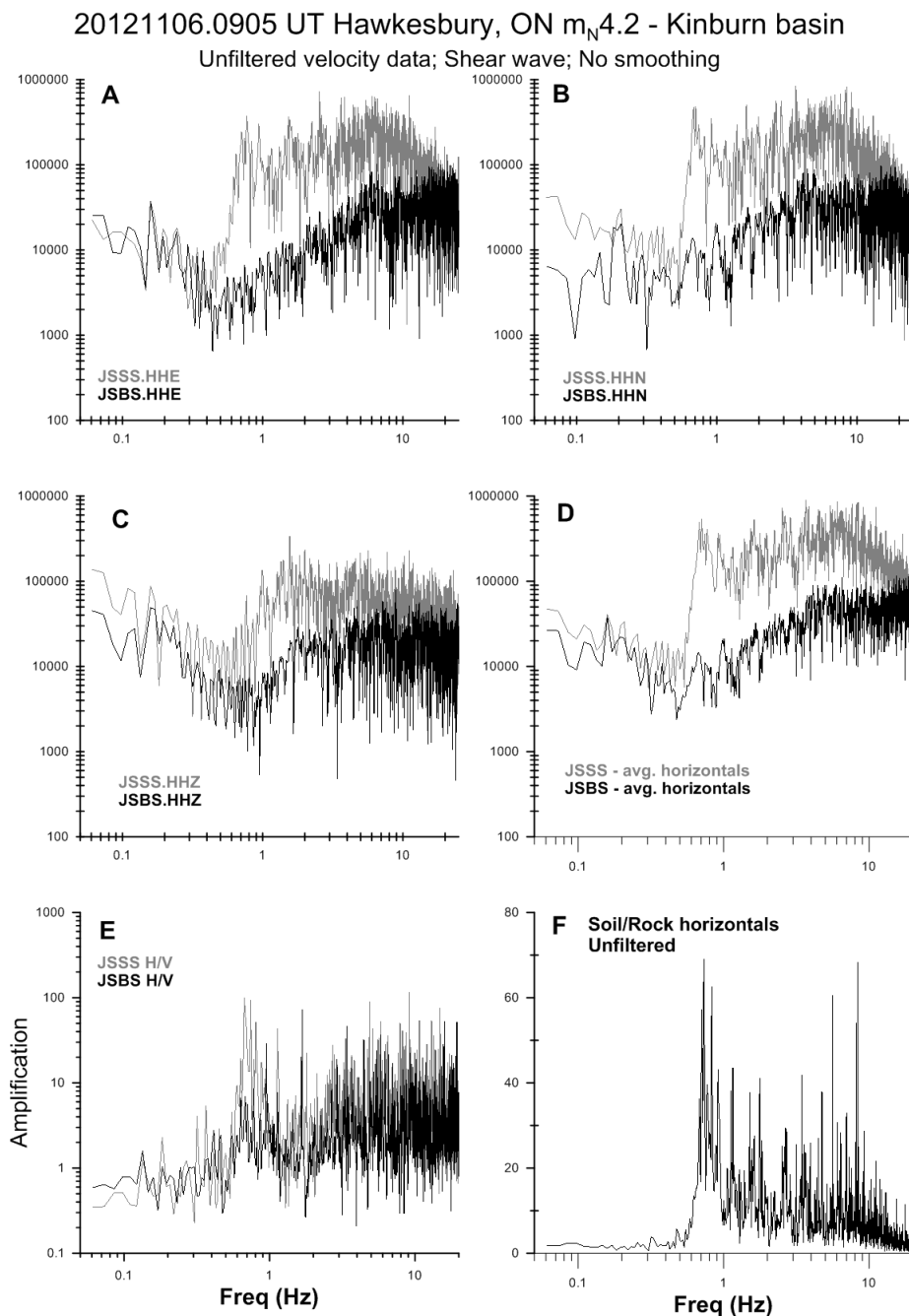


Fig. 4-7: Plots A-C show the frequency content (JSSS in green and JSBS in black) for the three components: E-W, N-S and Z (vertical) respectively. Plot D is the root mean-squared average of the horizontals. Plot E shows the ratio of the horizontal to vertical components. Plot F is the soil to rock spectral ratio. Both E and F use the averaged horizontals from C. Data from the 2012/11/06 $m_N 4.2$ Hawkesbury, ON earthquake. All of the data was unfiltered and no smoothing was applied for this plot.

Note that the National Building Code of Canada (NBCC) uses pseudo-spectral acceleration (PSA) based on the response spectrum with 5% damping, rather than the spectral ratio of the soil to bedrock. The response spectrum is the maximum response of a system with a single degree of freedom to an input motion and damping ratio (Kramer, p73). Using PSA produces a curve similar to the spectral ratios but appears slightly smoothed due to the restriction of the degrees of freedom. However in order to compare directly to what was recorded we are using the smoothed FFT's rather than PSA for our analysis.

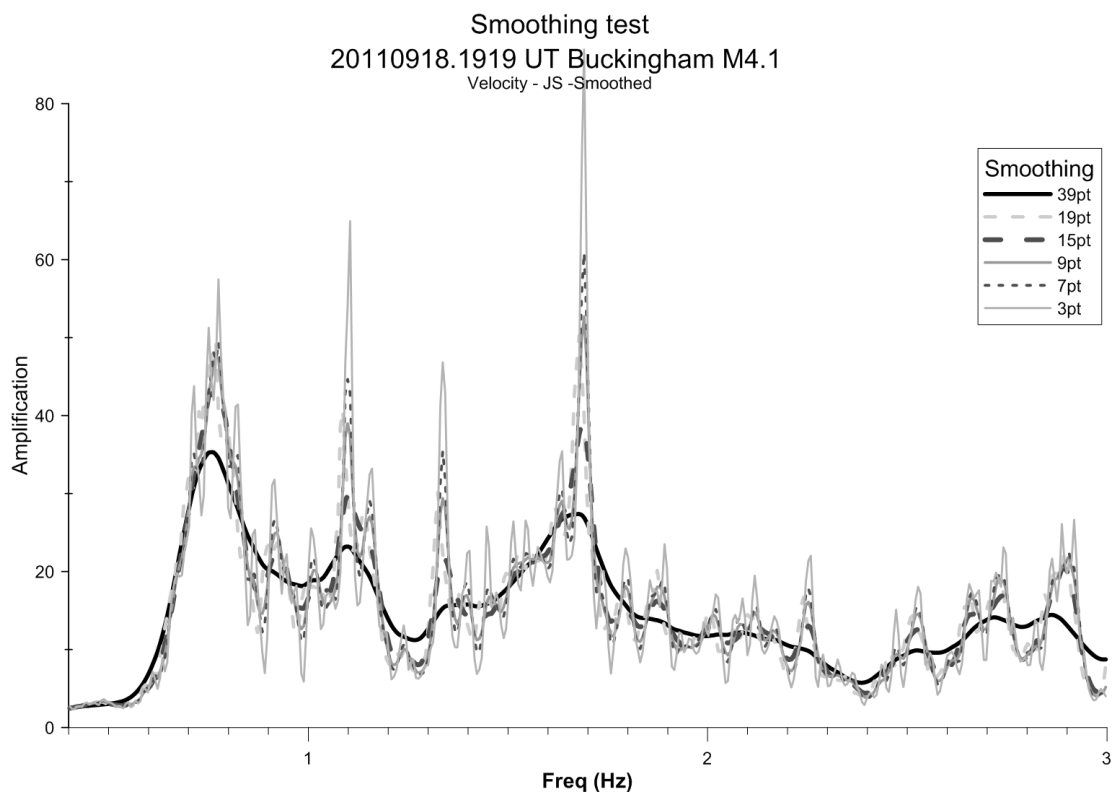


Fig. 4-8: Data for the Buckingham $m_N 4.1$ earthquake of 2011/09/18 using various degrees of smoothing of the FFT results, and then taking the soil to rock ratio.

4.2.1 Data processing and sensitivities

Smoothing

To determine to what degree the data should be smoothed, the smoothing functions were tested on several events. Each smoothing function is based on the same triangular smoothing function using an odd number of adjacent points. The point in the middle is the one being recalculated and is given full weight (i.e. weight of 1), while the adjacent points above and below are given progressively lower weight the further they are from the data point being calculated. For example, when calculating a 3-point smoothing function the middle point is weighted one, and the points above and below are each weighted only half: that is they are given a weight of $2/(3+1)$. For an n -point smoothing function, the weighting would decrease by $2/(n+1)$ for each step away from the middle. These weighted data points are then added together and averaged over the sum of the weights. For example, for a 3-point smoothing function the sum of the weights of the three points is $0.5+1+0.5 = 2$. For an n -point smoothing function it would be $(n+1)/2$.

Fig. 4-8 shows the results of the different filters tested on the 2011/09/18 Buckingham, QC earthquake as recorded on the Kinburn station pair. The smoothing is done on the FFT of each component prior to the calculation of the ratios. A 9-pt smoothing function was chosen as a compromise to bring out the general trends in the data while not losing too much information from the peaks. Hence, all the frequency analysis done on the data from the three pairs of seismograph stations used 9-point smoothing directly on the FFT data prior to any further data processing. To acquire

enough resolution in the resulting spectra, at least 30 seconds of shear data was used, beginning two seconds prior to the start of the shear wave arrival to avoid any effects of tapering on the results.

Shifting start times

Due to an error in the software used to retrieve the data from stations JSSS, JSBS, and ALFS, the data from these stations contain incorrect time labels. Hence, there may be a shift in start times from one component to another. An effort was made to cut each component 2s prior to the start of shear. However, this start time was not always very clear. Several earthquakes for each of the basins were investigated to determine the effects of shifting the start times several seconds, to before and to after the start of shear, on the resulting spectra.

Shifting to an earlier start time (such as -2 or -5 seconds), as it was expected, has a minimal effect on the resulting soil to rock ratio (see Fig. 4-9), whether we shift only the time used for the soil site, or both soil and rock sites. When we shifted the time forward (i.e., miss the beginning of the shear) by 5 seconds for only the soil site, again, there is very little difference in the result. This is because of the long duration of the signal on the soil site, which tapers away fairly slowly. So even if the beginning of shear is missed, there is still plenty of the event signal left in the later portion of the coda. When we shift the rock site by the same amount, however, the amplification of the soil:rock increases greatly. This is because the signal duration on the rock site is much shorter, hence any shift means significant data can be lost from the rock site resulting in what looks like an increased amplification of the soil.

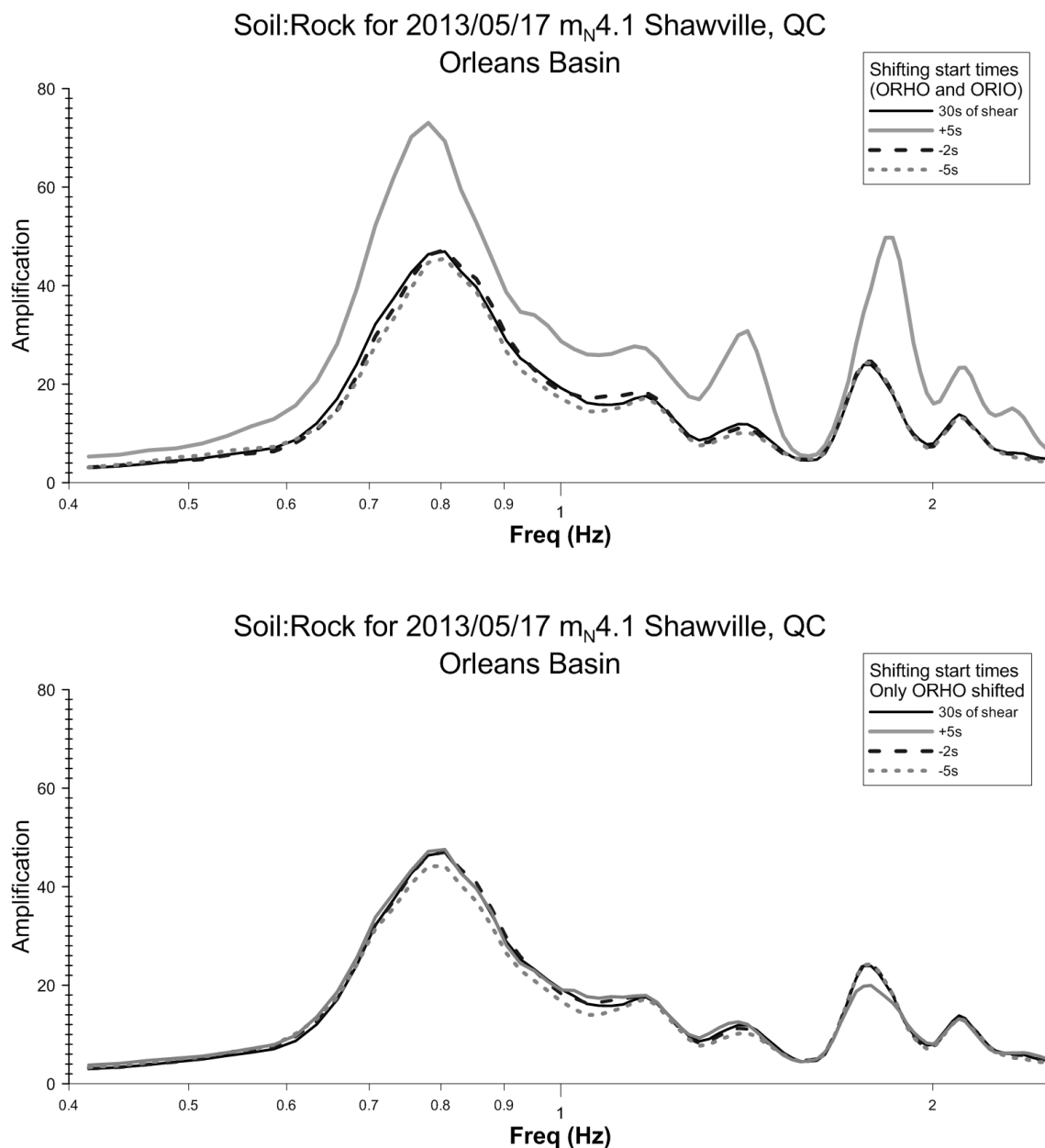


Fig. 4-9: Soil:Rock ratio of 30 s of shear wave data from the M4.1 Shawville, QC earthquake. Top figure shows when the start time of both rock and soil data is moved -2, -5 and +5 s from the original 30 s shear data. Bottom plot shows when only the start time of the soil data is moved -2, -5 and +5 s.

Further tests showed that if we cut the data too far before the start of shear, the data would slowly decrease in amplitude. But in general, the largest effect on the amplification always occurred when the beginning of shear was missed by more than 2s

for the rock site. This always resulted in an increase in amplification. Since all the data used for the following analysis was clear enough to allow the onset of shear to be estimated within less than 0.5s, and the rock site data tended to have clean, clear P-arrivals, we estimate that the lack of synched data should not have caused any appreciable bias in our processed data.

Time window of data used

To obtain a good representation of the frequency content of the data we need to use a time window containing the energy of interest (in this case the start of shear and including any generated surface waves that follow). However, we cannot get accurate information above the Nyquist frequency, which is half the sample rate of the initial data. In this case, since the sample rate of the seismic data is 100 samples/s, we cannot get resolution above 50 Hz (Telford et al., 1990). Taking the FFT of the data produces a series of data points at different frequencies that indicate the magnitude of the signal at that frequency. If the time window used is large enough (i.e. the number of samples used is large), the sample interval between the data points produced by the FFT becomes small, and the result can be approximated as a continuous series rather than discrete points (Hatton et al., 1986, p 12).

Typically, at least 30s of shear wave data was used for calculating the soil to rock ratios. That means both the soil site and the rock site needed to have at least 30s of data with a good signal to noise ratio. In general this required the use of only events of M3 or greater. Smaller events that were closer to the recording stations (i.e. with excellent first

arrival signal to noise) could not be used, as the duration of the signal above the background noise on the rock site was generally less than 30s.

Duration can be defined in many different ways. Some methods use power spectral density to measure duration, others use percent of total energy or rate of change of the root-mean-square of acceleration, etc. (Kramer, p80). However, by far the most common method is based on bracketed duration defined by Bolt (1969) as the time between the first and last exceedance of a particular threshold (e.g. 0.05g). For this study, we consider the duration of the S-wave to be from the beginning of the S-wave to the point in time where the S-wave approaches the background noise levels. Note that this definition, however, is still rather subjective.

A problem arises, however, when we want to examine and compare the spectra of the waveforms. For differing time windows of initial data, the resulting FFT will be resolvable to different frequencies, making it more difficult to compare and manipulate in a spreadsheet. For example the results from the FFT of 60s of data were resolvable to ~ 0.012 Hz, whereas the 30s data were resolvable to only ~ 0.024 Hz. Note that any time window less than 30s would not give enough resolution in the data; hence 30 s was chosen as the minimum amount of data required for this type of analysis.

For the larger events, large time windows were available with events where there was well over 100s of usable data. On the other hand the issue of analysis results from 30s of data comparable to 60s or 90s of data from the same event.

The data for a well-recorded event was sampled at different intervals, the FFT calculated and smoothed and the ratios calculated and plotted to determine whether the different sample rates in frequency made any difference in the amplification results. Fig. 4-10 shows how the different intervals of data affected the calculated spectral ratios for the 2012/10/10 $m_N4.5$ Vercheres, QC earthquake. The locations of the peaks do not change. However, the amplification recorded at the peaks increases with increased duration. Some of this increased amplification appears to be due to the lack of duration of the earthquake signal above the background noise on the rock site recording, as seen previously with the shifting start time. However, there are more details within the peaks, suggesting that the sample rate also has an effect. Hence, we used 45 or 60 s of data to generate all our plots, unless otherwise specified.

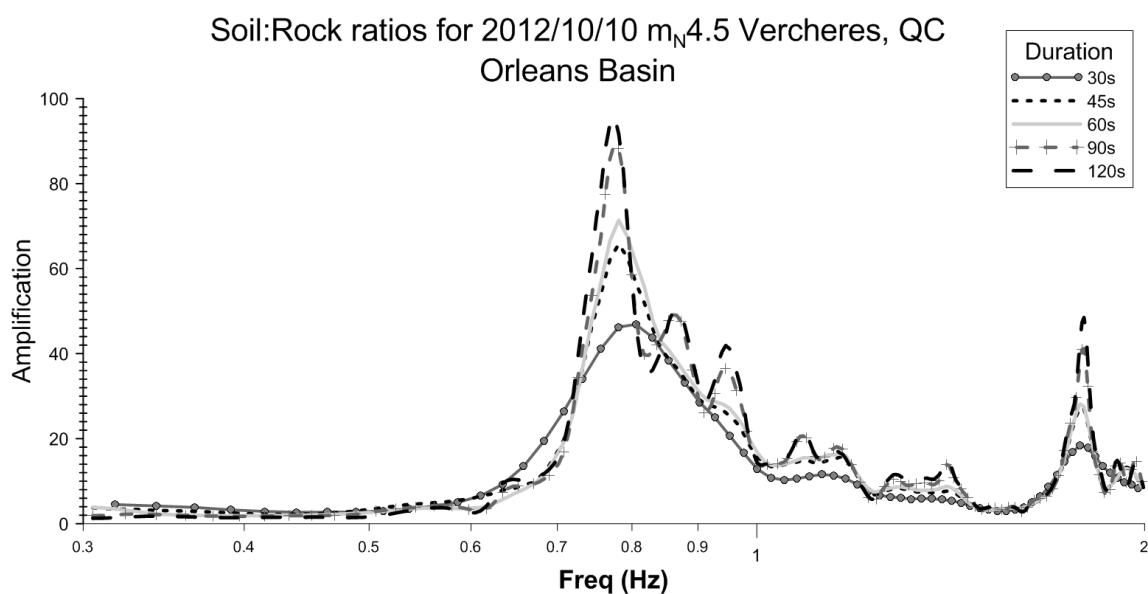


Fig. 4-10 Spectral ratios calculated for the $M4.5$ Vercheres, QC earthquake on the Orleans station pair for various durations of shear wave.

4.2.2 General shape of soil to rock spectral amplification curves

To examine the soil to rock amplification on each of the basins, we examined the larger earthquakes recorded by each station pair, generally of magnitude 3.5 or above, where the signal to noise on the station pair was well above the background noise and the duration of the signal was at least 45s for both the rock and the soil site. In general the resulting curves are similar to that found at other basins around the world with a peak at the fundamental frequency (f_0), followed by subsequent peaks at the higher harmonics. For our study basins, the f_0 is the highest peak, similar to what was found in some other basins including the alpine valley in Grenoble, France (Cornou and Bard, 2003).

The Orleans basin spectral ratio data included 11 well-recorded earthquakes, which are listed in Table 4-1. As seen in Fig. 4-11, the average soil to rock ratio for each individual earthquake (plotted in black) showed a set of distinct peaks in the frequency domain, starting with the largest peak at the lower frequency end, with each subsequent peak becoming smaller towards higher frequencies. This similar pattern is apparent for the curve of each individual earthquake (plotted in grey), although the amplitudes of the peaks are variable. The HVSR (horizontal to vertical spectral ratio), obtained from 30 s segments of a 30 minute recording of noise measurements (as described in S3.4), is plotted as a dashed black line using the scale on the right to allow for easier comparison of the frequency content recorded. Note that although the fundamental frequency recorded by HVSR is approximately equal to that calculated from the soil:rock ratios from the earthquake recordings, there is a large difference in the amplification found by these two methods. This is not surprising given that the HVSR is highly dependent on the

level of local noise present at the time of recording, which can vary with time of day and season, etc. Furthermore the HVSR reading is taken from the horizontal to vertical ratio from one recording site, whereas the soil:rock ratios are obtained using the combined horizontal recordings at two different sites.

Table 4-1: Orleans earthquake data used for spectral ratios

OR data	date.time (UT)	Mag (mN)	Dist. (km)	Azimuth	Duration (s)	
1	20131020.1040	3.6	151	96°	60	Barry's Bay, ON
2	20130530.0534	3.7	71	117°	60	Shawville, QC
3	20130517.1353	4.1	71	117°	60	Shawville, QC
4	20130517.1343	5.2	70	116°	60	Shawville, QC
5	20130116.0053	3.5	68	186°	60	Val-des-Bois, QC
6	20121212.1746	4.4	494	240°	60	La Malbaie, QC
7	20121106.0905	4.2	76	258°	60	Hawkesbury, ON
8	20121010.0419	4.5	179	262°	60	Vercheres, QC
9	20120204.0917	3.6	173	152°	60	Maniwaki, QC
10	20120122.0559	3.6	102	201°	60	L'Annonciation, QC
11	20110316.1736	4.3	78	260°	60	Hawkesbury, ON

The individual earthquake data from the Kinburn basin do not show a clearly defined spectral pattern on examination of the 9 spectral ratios (see Table 4-2 for list of events). As seen in Fig. 4-12, there is an initial peak, and then possibly a second one, but it is only on examination of the averaged data (plotted in black) that we observe a pattern similar to, but much less distinct than, that of the Orleans basin data. For each single peak on the Orleans basin data there appears to be a set of three closely spaced peaks on the Kinburn basin data, as shown on the averaged curve. This is repeated with the subsequent peaks at higher frequencies, with each set being lower in amplitude than the previous set. However, with the third set of peaks the amplitudes seem to flatten out, with

the peaks hovering around 10-15 times amplification. Again, the HVSR data (see S3.4) as recorded for the Kinburn basin is plotted as a dashed black line on Fig. 4-12, using the scale on the right, to use as a comparison of the peak frequencies recorded by this method as opposed to the spectral ratios from the earthquake data.

Like the Orleans basin data, the Lefaiivre data shows a more distinct first and second peak, with the first peak being much higher in amplitude than the second (see Fig. 4-13). However, the pattern for this basin only has two clear peaks, with a possible third peak, after which any pattern is lost, even for the averaged data curve. The data does suggest amplification after the second peak of the soil when compared to the rock, but at random frequencies, which changes from earthquake to earthquake. It is possible that there is a lack of data for this third basin. In order to get a reasonable number of events to create this plot, we examined lower magnitude events ($< m_N 3.5$) than we did for the other two basins. Altogether there were 9 events that showed good enough signal to noise for a long enough duration (at least 45s) to be used. See Table 4-3 for the list of the earthquakes used for the Lefaiivre basin spectral ratio analysis. The HVSR data for Lefaiivre is plotted for comparison of frequency content, using the scale on the right for amplification (black dashed line).

Apart from lack of data, 2D and 3D basin effects obviously also play a role. Each basin is reacting differently to the same or similar earthquakes. Although the surrounding bedrock and in-fill material is similar for each basin, the geometries of the basins are not. Furthermore, the sub-layering of the soil layer also varies (e.g. the Lefaiivre basin profile contains sand lenses – see Ch. 5), which also contributes to the variable results between

the basin. Although the system as a whole may have a distinct f_0 , each sub-layer will also have its own f_0 , which might cause the peaks to become more spread out and may be the cause of the multi-pointed peaks we see for the Kinburn data.

Table 4-2: Kinburn earthquake data used for spectral ratios

JS data	date.time (UT)	Mag (mN)	Dist. (km)	Azimuth	Duration	
1	20130530.0534	3.7	43	159°	60	Shawville, QC
2	20130517.1353	4.1	43	160°	60	Shawville, QC
3	20130116.0053	3.5	94	216°	60	Val-des-Bois, QC
4	20121212.1746	4.4	438	238°	60	La Malbaie, QC
5	20121106.0905	4.2	125	258°	60	Hawkesbury, ON
6	20121010.0419	4.5	230	260°	60	Vercheres, QC
7	20120122.0559	3.6	133	218°	60	L'Annonciation, QC
8	20110918.1919	4.1	77	254°	60	Buckingham, QC
9	20110316.1736	4.3	128	260°	60	Hawkesbury, ON

Table 4-3: Lefavre earthquake data used for spectral ratios

AL data	date.time (UT)	Mag (mN)	Dist. (km)	Azimuth	Duration (s)	
1	20131020.1040	3.6	201	89°	60	Barry's Bay, ON
2	20130521.2043	3.4	57	292°	60	Rigaud, QC
3	20130517.1343	5.2	114	96°	60	Shawville, QC
4	20130517.1353	4.1	115	96°	60	Shawville, QC
5	20130415.1332	3.1	39	244°	45	Brownsburg-Chatham, QC
6	20130219.0459	3.8	711	113°	60	Chapleau, ON
7	20130116.0053	3.5	65	138°	60	Val-des-Bois, QC
8	20121212.1746	4.4	441	239°	60	La Malbaie, QC
9	20121010.0419	4.5	126	267°	60	Vercheres, QC

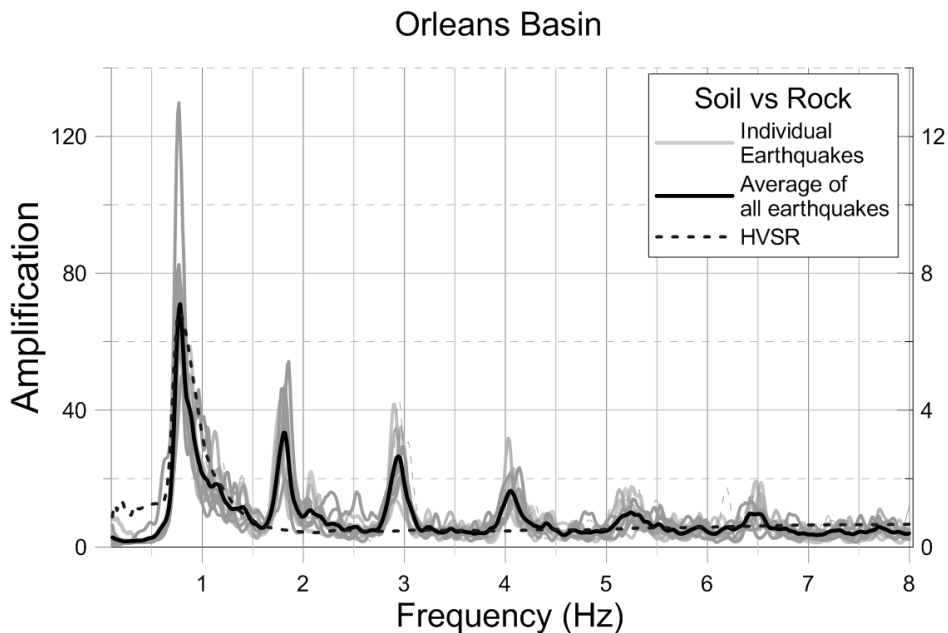


Fig. 4-11: Orleans basin plotting the root mean squared average horizontals of the soil:rock for 11 individual, well recorded earthquakes in grey, and their average in black. The HVSr is plotted (dashed black line) as recorded by a Tromino over 30 minutes of background noise. This line is plotted using the axis on the right, and hence is magnified by 10 times with respect to the earthquake data.

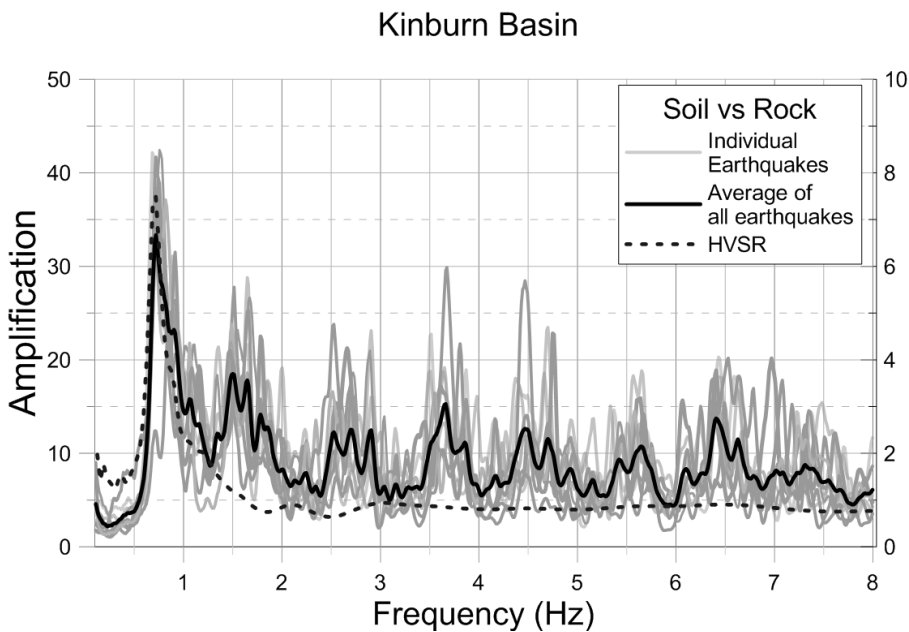


Fig. 4-12: Kinburn basin data plotting average horizontals soil:rock ratios for 9 individual earthquakes (grey) and their average (black). The dashed black line shows the HVSr using the amplification scale on the right (hence magnified 5 times with respect to the earthquake data).

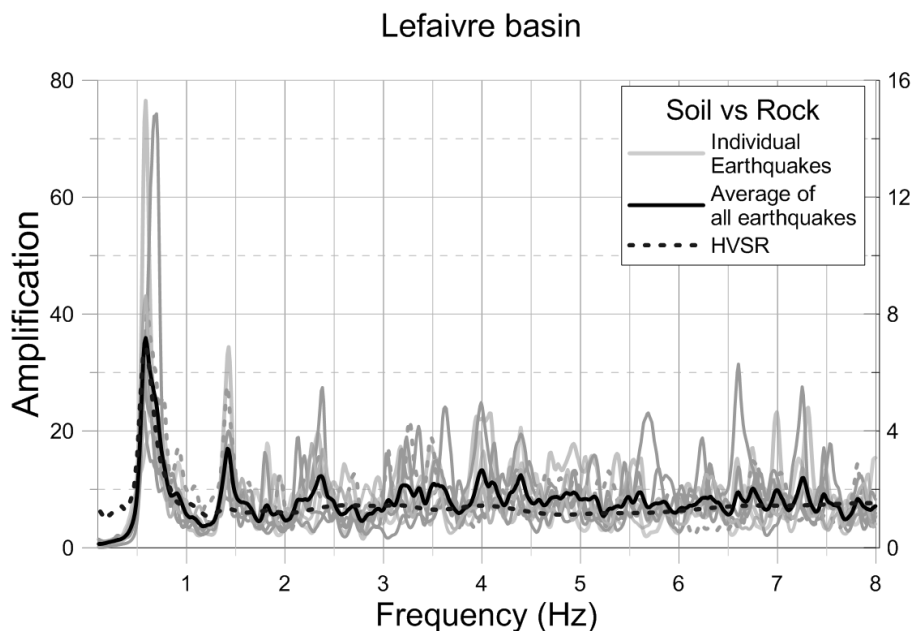


Fig. 4-13: Lefaiivre basin data plotting average horizontal soil:rock ratios for 9 individual earthquakes (grey) and their average (black). The dashed black line shows the HVSR using the amplification scale on the right (hence magnified 5 times with respect to the earthquake data).

4.2.3 Amplification

As calculated in S4.1.1, the amplification using the theoretical equation for seismic impedance (S2.4.1), with bulk values of $V_{s_{\text{soil}}} = 150$ m/s and $V_{s_{\text{rock}}} = 2700$ m/s, indicates 5 times amplification of the soil site as compared to the rock. Assuming resonance is the dominant effect for these sites due to the strong seismic impedance contrast, then the value of 28 times amplification from Equation 6 (S2.4.2) should be a better approximation of amplification at our sites.

However, the observed amplifications, based on a smoothed FFT, calculated from the data at Orleans show a range from ~40 to 130 times amplification of the soil site over the rock, with the average amplification of 70 times for the 11 earthquakes processed. This is much larger than the predicted value of 28 times due to resonance. The other two

basins show a more modest amplification with an average of ~35 times amplification. However, the Kinburn basin had a narrow range of ~23 to 42 times for the 9 earthquakes used for the calculation, while Lefaivre, like Orleans, had a much wider range of ~20 to 80 times for 8 earthquakes.

To see if the wider range for Orleans and Lefaivre was related to the data from any particular earthquake, we examined the individual spectral ratios for each basin. For Orleans, the Val-des-Bois M3.5 stood out to be well above the average, while the M4.3 Hawkesbury event was well below. Removing those two earthquakes from the averaging, the range becomes 56 to 82 times amplification, and the average remained approximately the same. No unusual noise or station problem was noted in the data that could have adversely skewed the results.

For the Lefaivre basin there were two events, M3.4 Rigaud and M4.5 Vercheres, QC, which had amplifications well above the other events at the fundamental frequency. Removing these two high values, and the lowest (M3.6 from Barry's Bay), we obtain a new range of 23-43 times amplification. Again, the average amplification does not change much for the basin with these values removed. And, as with the Orleans basin, there was nothing abnormal noted with this data suggesting it should be discounted.

On Fig. 4.11 to 4.13, the HVSR calculated for each basin is plotted using the vertical scale on the right. The HVSR amplifications, which will fluctuate depending on when the readings are taken but are roughly an order of magnitude lower than those from the spectral ratio, are approximately equal for all three basins (see Fig. 3-9). The spectral

ratios from the earthquake data, however, indicate that the Orleans basin has approximately twice the soil amplification as compared to the other two basins. Given that the bedrock and in-filling soil is similar for all three basins, 2- and 3-D effects (i.e. effects not related to resonance and seismic impedance) must be contributing to the differences recorded in the amplifications.

4.2.4 Fundamental Frequency, f_0

For all three basins, the highest amplification for the majority of the event data appears at the f_0 , as was recorded using the HVSR method (see Fig. 4-11 to 4-13). As mentioned in S3.4, the HVSR is calculated using 30 second segments from a recording of 30 minutes of ambient noise. The frequency at which the peak occurs has been shown to be related to the depth of the basin. Table 4-4 gives the values of the average recorded fundamental frequency for each basin, and the range (the lowest and highest frequency at which a peak was recorded) for the individual earthquakes used in the analysis.

For frequencies less than the f_0 , there is very little amplification shown in the basins; this mirrors the results of Cornou and Bard (2003), who also observe low soil to rock spectral ratios below f_0 recorded in their study basin in Grenoble, France, where direct energy is interpreted to be the main contributor at this frequency range as opposed to edge-generated surface waves. Their HVSR amplification measurements also showed lower values than those recorded from the earthquake data. As noted previously, however, the HVSR data is taken from only the soil site, and is highly dependent on when the measurements were taken.

Using a 45-60 s time window for the observed earthquake events, the lowest observable frequency component is in the range of 0.05 - 0.06 Hz. For the lowest frequency range, we observe a slight increase in amplification for a few earthquakes from both the Orleans and Kinburn basins, and particularly on the latter basin. These amplifications are still well below values recorded at the higher frequency ranges, where the curves level out. It is interesting to note, however, that the HVSR for Kinburn also has a similar slight upturn at these frequencies below the fundamental (< 0.8 Hz).

4.2.5 Higher harmonics

The main peak at the f_0 is followed by subsequent maxima that have progressively smaller less well defined peak amplitudes. The number of higher-frequency peaks varies from basin to basin but beyond these, at higher frequencies, there is a “leveling off” of the amplification plots with no additional defined peaks. This pattern was observed on all three basins and for every event recorded, with few exceptions. This observed pattern is similar to the pattern seen by other researchers including Kham et al. (2013), Semblat et al. (2000), Cornou and Bard (2003), etc.

Table 4-4: Observed frequencies for peaks in amplifications for the three basins.

Basin		f_0	1 st		2 nd		3 rd		4 th	
Orleans	Average	0.78	1.81		2.94		4.05		5.24	
	Range	0.77 0.81	1.76 1.86	2.83 2.99	3.97 4.14	5.1	5.3			
Lefaiivre	Average	0.59	1.4		... becomes indistinct					
	Range	0.56 0.70	1.3 1.5							
Kinburn	Average	0.72	1.5		2.7		... becomes indistinct			
	Range	0.68 0.85	1.3 1.7	2.5 2.9						

The subsequent peaks are interpreted as higher harmonics, although using Eqn. 2.5 (see S2.4.1) it is difficult to match the computed fundamental and harmonics V_s and soil thickness with the observations. There are several reasons for these observed differences. First and probably most importantly, the equation is only modelling 1D-effects, and does not take into account any 2 or 3D effects. Furthermore, the V_s is continuously changing with depth at all three of our sites, so there is uncertainty as to which V_s should be used within the equation (in the previous calculations one bulk V_s was assumed for an entire layer). Also, each sublayer also has its own f_0 , hence a few multiple layers can provide a wide range of differing f_0 s. Vrettos (2013) also showed how a continuously changing velocity profile (rather than discrete layers, as is used in the modelling programs) will also cause a shift in the location of the fundamental and harmonic peaks. For the higher harmonics, the recorded peaks become wider, so the actual frequency values for these harmonic peaks quickly become less clear.

For all three basins the fundamental peak is well defined for most earthquake events. However, depending on the earthquake, there are some cases where the peaks appear to shift from the average, causing a “smearing” of the peaks. On examination of the peaks interpreted to be the higher harmonics, the shift from a single peak becomes more pronounced. The amplitudes of the peaks are also of significantly lower value with each progressively higher harmonic, reaching a point where the peaks soon get lost in the noise and to this smearing effect.

The frequencies at which the peaks of the harmonics occur from the averaged curve are recorded in Table 4-4, as well as the range from the lowest and highest

frequency at which the peaks occur from the individual earthquakes. Note that for several individual earthquakes some peaks do not match well, so the accuracy of the recorded frequency for the higher harmonics in the Lefaiivre and Kinburn basins is not as great as that of the Orleans basin.

The harmonic peak amplitudes found in this study match fairly well with those peaks observed by Kolaj (2010) from an earlier study from the Orleans basin. Kolaj found peaks at 0.84 ± 0.05 Hz, 1.81 ± 0.06 Hz, 2.98 ± 0.05 Hz, 4.02 ± 0.07 Hz and 5.17 ± 0.12 Hz using the FFT and comparing ORHO to ORIO. Prior to the installation of ORIO, he used OTT and obtained values within ± 0.03 Hz of the frequencies listed above. Notably his fundamental frequency, when comparing to OTT was a lower value, of 0.81 ± 0.04 Hz, which is closer to the value found in this study.

In order to determine if adjusting the parameters used in the 1D equations would allow for the fundamental and harmonic peaks to be calculated, we calculated an “equivalent” shear wave velocity (V_{Sequiv}) to be used instead of our original estimated bulk V_s . Table 4-5 gives the V_{Sequiv} values determined for each of the basins assuming the relation in Eqn. 2.5 from S2.4.5 for 1-D effects, using the HVSR-determined f_0 and the known depth of the clay to the first major reflector (the till layer, in this case). Then, using these calculated V_{Sequiv} values, we estimated the expected harmonics in Table 4-6.

Table 4-5: Calculated V_{Sequiv} , using HVSR-determined f_0 and the thickness of the clay down to the first major reflector (till layer)

	Orleans	Lefaiivre	Kinburn
f_0 (Hz)	0.78	0.59	0.72
H (m)	83	108	97
V_s (m/s)	259	255	279

Then, instead of solving for the harmonics using a V_{Sequiv} , we use H_{equiv} as suggested by Dobry et al. (1976). For this calculation, Dobry et al.'s (1976) model using the following equation was chosen as the one that best fit the V_s data of the Ottawa Leda clay (J. Hunter, pers. com., 2016):

$$V_{S_{int}}(h) = V_0 * H^{\frac{p}{2}} \quad \dots [Eqn 4.1]$$

where $V_{S_{int}}(h)$ is the interval velocity data in terms of depth (h) in metres, V_0 is the reference (surface) shear wave velocity in m/s, and p is a constant. Note that $V_{S_{int}}$ represents the V_s at a particular depth and has been calculated from available geophysical data. This is in comparison to the $V_{S_{avg}}$ which represents the average V_s over the entire depth of the layer.

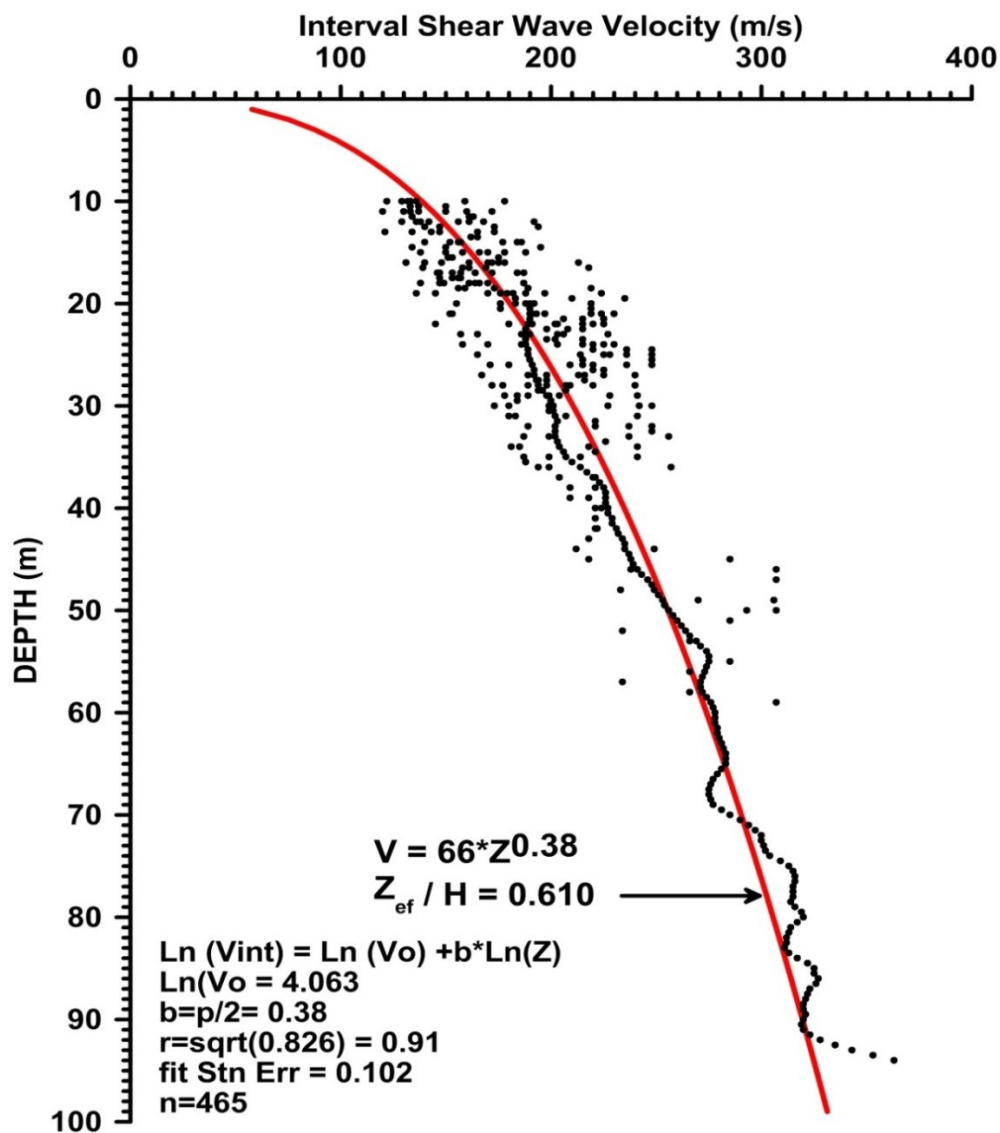
Results from Eqn 4.1 were then plotted and compared to the measured data collected and compiled from various boreholes around the Ottawa region. Then a p of 0.76 and H_{equiv}/H ratio of 0.61 were derived from the best fit plot (J. Hunter, pers. com., 2016; see Fig. 4-14). Using these values H_{equiv} , was derived and used to solve for V_s using Eqn 3.1, which in turn was used to solve for f_0 using Eqn 2.5. Results are shown in Table 4-7.

Table 4-6: Calculated frequency of higher harmonics (in Hz), using V_{Sequiv} calculated in Table 4-5

Basin and f_0		Harmonics		
		1	2	3
Orleans	0.78	2.34	3.9	5.46
Lefaiivre	0.59	1.77	2.95	4.13
Kinburn	0.72	2.16	3.6	5.04

Table 4-7: Calculated V_s and f_0 determined from using the H_{equiv} method of Dobry et al. (1976)

	Orleans	Lefavre	Kinburn
H_{equiv} (m)	50.63	65.88	59.17
V_s (m/s)	168.41	181.83	175.93
f_0 (Hz)	0.83	0.69	0.74



BHs: Anderson, JA-5, JA-6, LV96-1, LV96-2,
 LV97-1A, LV97-1B, LV97-1C, JSR

Fig. 4-14: Compilation of V_{int} data from various boreholes in the Ottawa region. A least-squares power law curve fit following the form of Dobry et al. (1976), using Chauvenet's rejection criterion to remove outliers. Data analyzed and prepared by J. Hunter (pers. com. 2016).

These values, however, do not compare well with the observed data in Table 4-4, which is likely largely due to the fact that the equation used does not account for 2- and 3-D effects. Also, as Vrettos (2013) showed, modelling a continuously changing V_s profile with distinct layers will also produce a slight shift in the data. For Orleans, for example, the 1st harmonic is calculated to be ~ 2.3 Hz. However the observed data has a peak at 1.81 Hz and then at 2.94 Hz, neither of which can be matched with the calculated table of harmonics. The results for Lefavre and Kinburn are similar, with the first harmonic peak in the data being at lower frequency than the calculated one. The same was found for the second harmonic peak, at least for the Kinburn basin data.

Note this issue of the theoretically calculated fundamental and harmonic peaks not coinciding with the recorded data is further discussed in Ch. 5 for the 1D models used in the ground motion modelling software.

4.2.6 Effects of source variables

To examine the source of the varying amplitudes and shifting in the fundamental frequencies and harmonics from earthquake to earthquake, several possible variables were investigated. The data were replotted in terms of time, magnitude, azimuth and distance to determine if any of these, may influence the recorded site data. The frequency content of the input ground motion also has an effect on the basin amplification, and this subject is discussed briefly at the end of this section. However, no direct analysis was done for the frequency content of each individual event as there was not enough variety of data for such an analysis at this time.

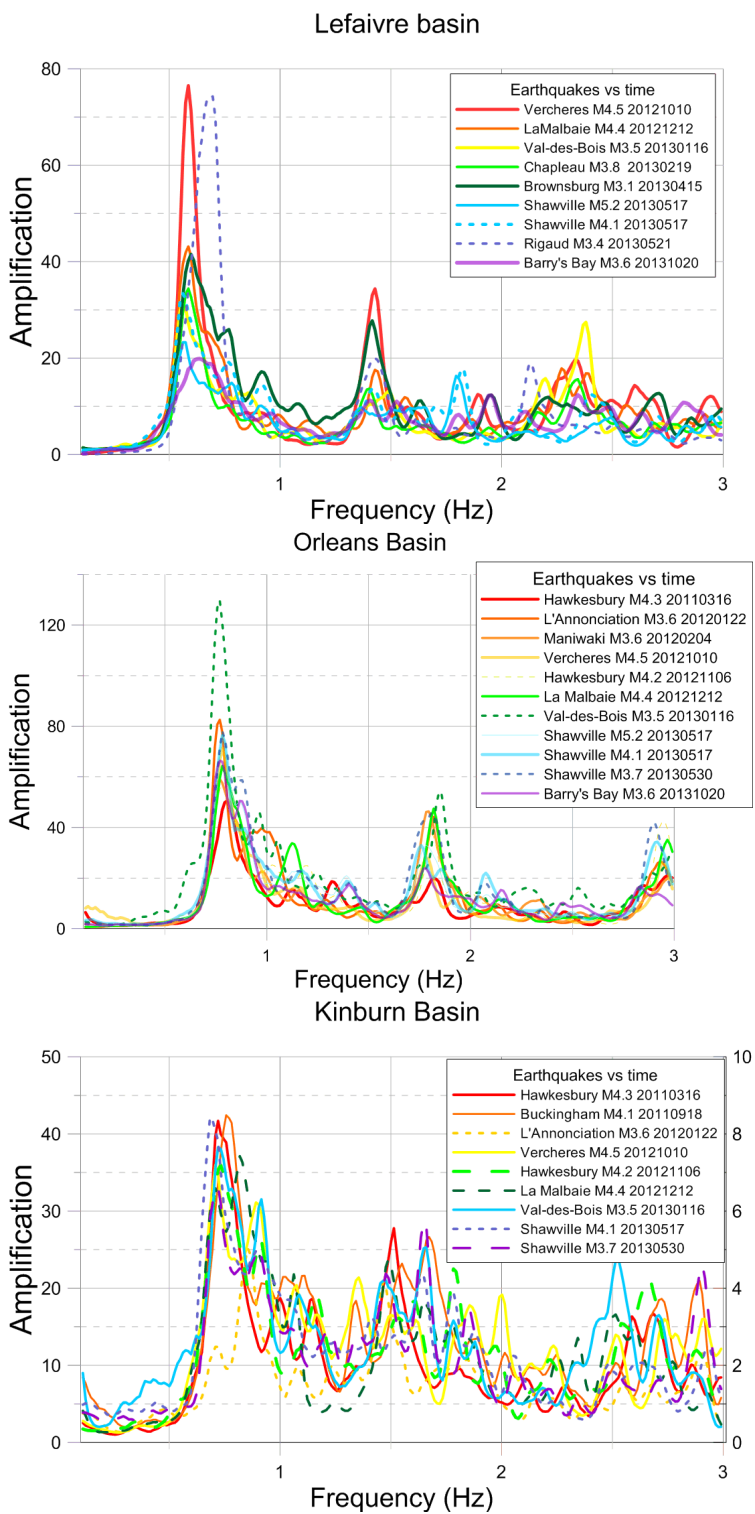


Fig. 4-15: Recorded spectral ratios with each earthquake colour-coded by time (red=oldest to purple=newest) for the Lefaivre basin data at top, followed by Orleans and Kinburn data.

Time

In Fig. 4-15, each of the individual earthquakes is plotted, each with a different colour, from oldest (red) to newest (purple). No dependence on time was noted for any of the three basins. Note that the Lefaiivre basin there is data only since late 2012, and so yields the least amount of information. But for all three basins, some of the earlier events commonly have similar amplifications or frequency content as some of the recent data. For example for the Kinburn basin, the 2011 Hawkesbury event shows similar amplification and f_0 as the 2013 Val-des-Bois earthquake. Conversely, events that occur close in time occasionally showed rather different amplifications and frequencies.

Magnitude

The magnitude of an earthquake also does not seem to have a direct relation to the amount of amplification or location of the peaks of the soil-to-rock spectral ratios that were recorded on each of the basins. For example the M4.2 Hawkesbury event (dashed dark-green line) has an approximate amplification of 35, while the M4.3 Hawkesbury (bright blue) and M4.1 Buckingham (bright green) events are closer to 40 times amplification (see Fig. 4.-15), even though all three events are in the same magnitude range. However the f_0 peak for the Buckingham event is slightly higher than those of the other two earthquakes. Although the results from only one basin are shown in Fig. 4-16, the results for the other two basins were similar. Note that the magnitude of an earthquake is related to the frequency content. A very small event contains significant higher frequencies, whereas a larger earthquake will contain significantly lower

frequencies. However, this is only one factor in the overall frequency content since epicentral distance will also play a role.

Distance

The earth acts as a high frequency filter, hence earthquakes that are more distant from the recording stations will have less high frequency. However, when the events were examined only with respect to distance for each of the basins, there was no indication of this being a significant parameter for differences in amplification or resonant frequency shifts for any of the basins.

The results for the Lefaiivre basin are shown in Fig. 4-17 where the two closest events, M3.4 Rigaud (in dashed orange) and M3.1 Brownsburg-Chatham at 39km (in solid red), have significantly different amplifications and frequencies. The most distant event, M3.8 Chapleau (in solid purple) has peaks at similar frequencies to the closest event (Brownsburg-Chatham, red), and has amplifications that are close to average, peaking at around 35.

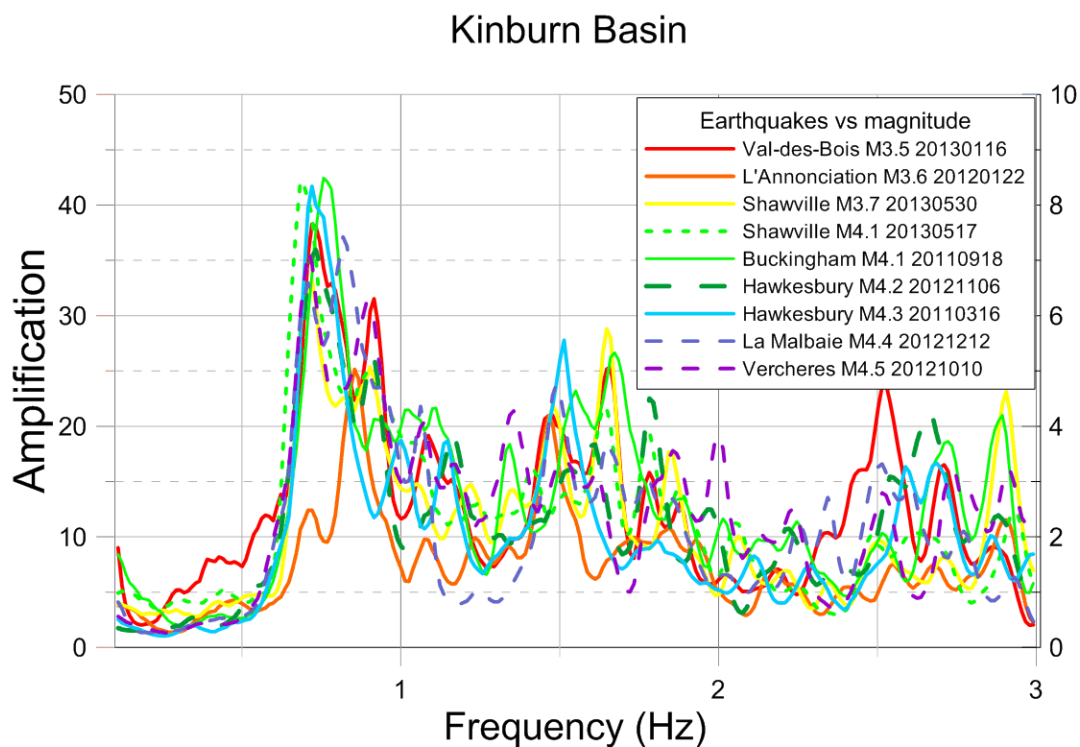


Fig. 4-16: Spectral ratios for earthquakes sorted by magnitude for the Kinburn basin.

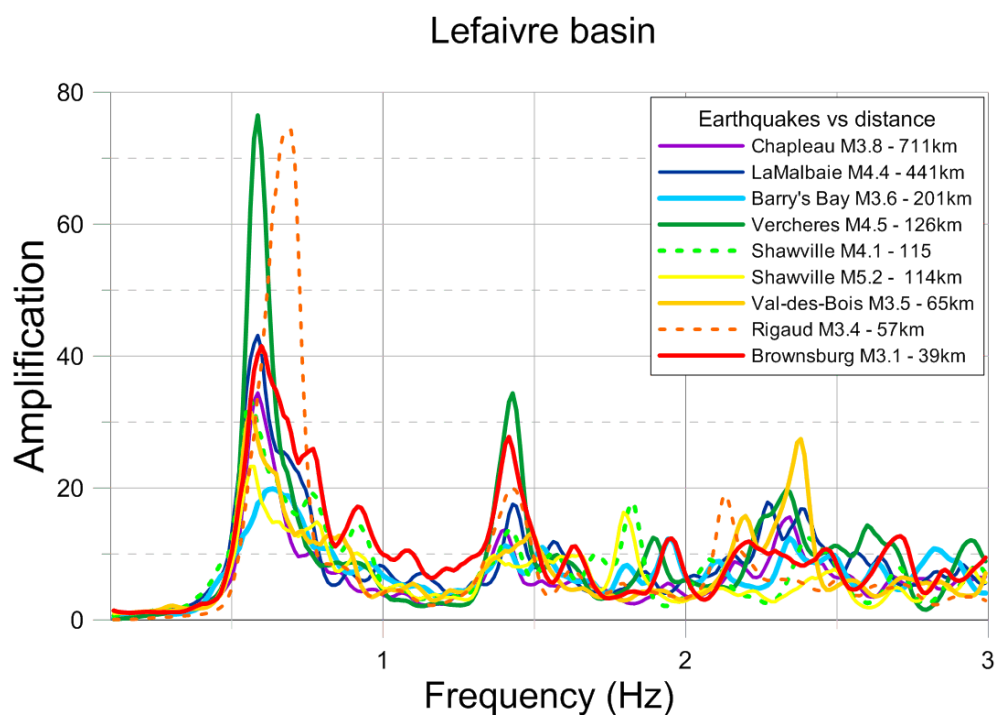


Fig. 4-17: Spectral ratios for earthquakes sorted by distance for the Lefaire basin.

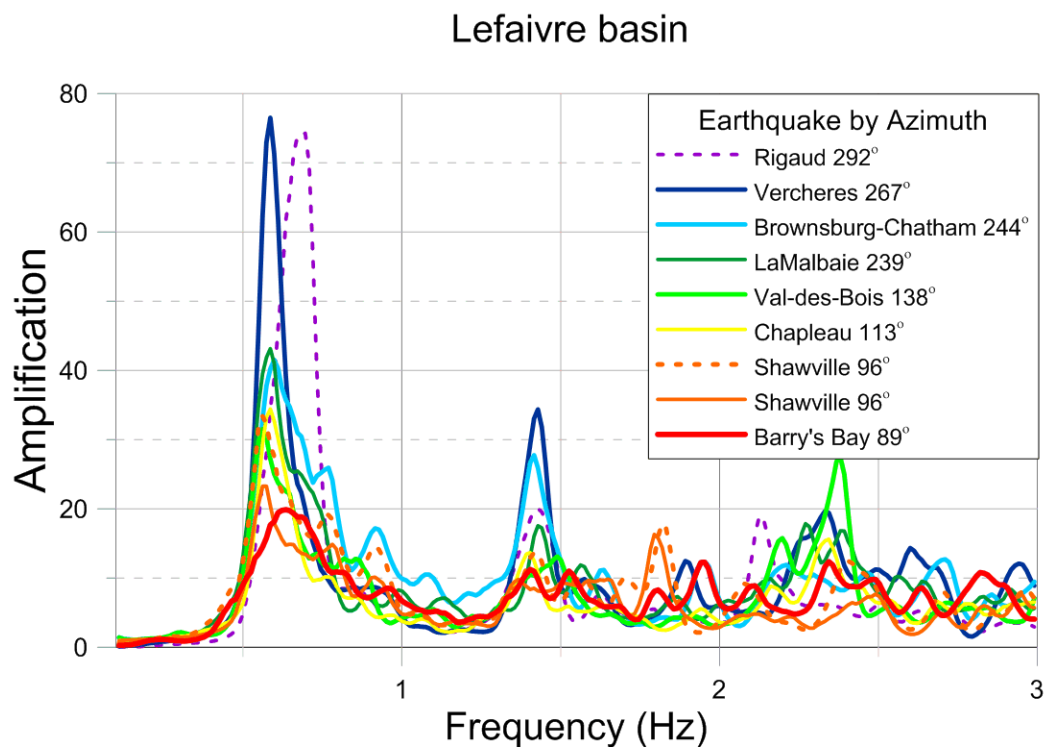


Fig. 4-18: Spectral ratios for earthquakes sorted by azimuth (from earthquake to seismic station) for the Lefaiivre basin.

Azimuth

A plot was created for each of the basins with earthquakes ordered by azimuth to observe if there was a preferred azimuth where the amplification might be stronger, or if the frequency peaks were shifted according to incoming azimuth. As shown in Fig. 4-18, for the Lefaiivre basin, there does appear to be a relation between the azimuth and the amplification, with the events from the south-east having the highest amplifications, the events from the east and north-east having intermediate values, and the events almost due north having the lowest. However, there is low confidence in this relation

given the relatively few number of events used for this analysis. There is no apparent relation between the azimuth and the shift in the location of the peaks.

Examining the results for the Orleans and the Kinburn basins (see Fig. 4-19 and 20), there is no obvious correlation between either the amplification or the frequency content to the earthquake epicentral azimuth. For example, on the Kinburn basin plot, the M3.5 Val-des-Bois, QC event and the M3.6 event from L'Annonciation, QC which are from approximately the same azimuth, have very different peak amplifications, and there is a significant shift in the recorded fundamental frequencies.

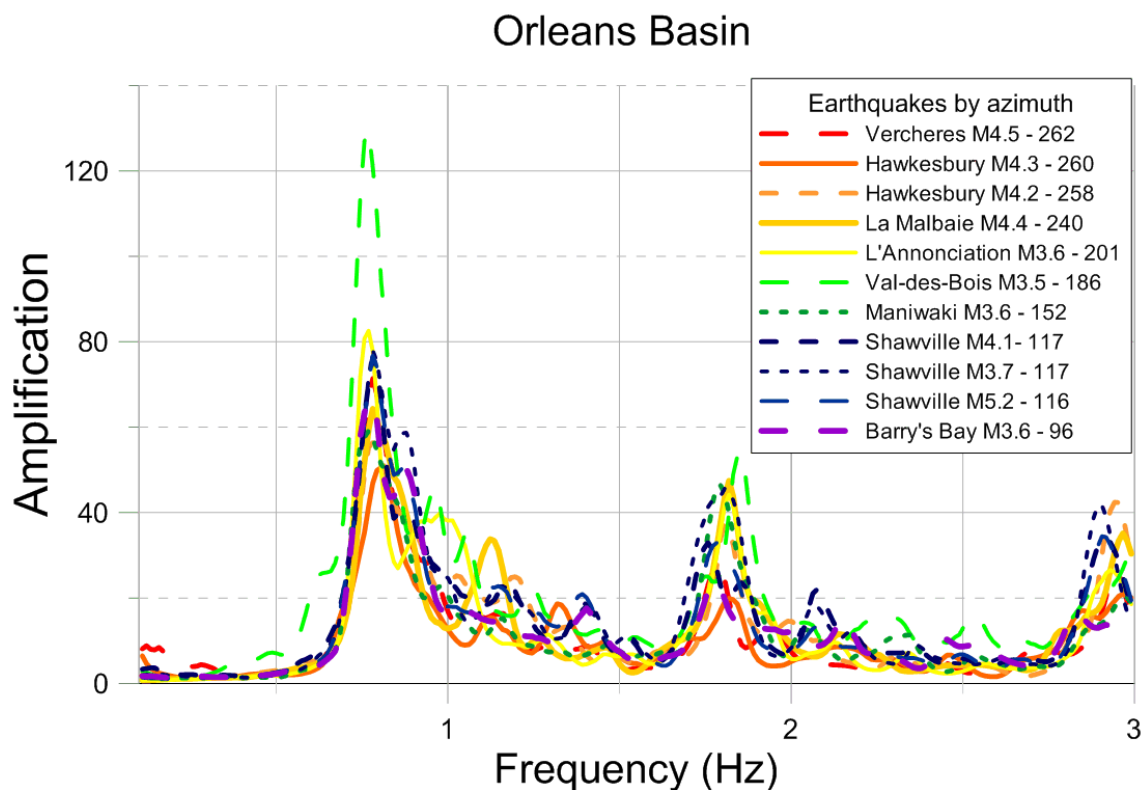


Fig. 4-19: Transfer functions for earthquakes sorted by azimuth (from earthquake to seismic station) for the Orleans basin.

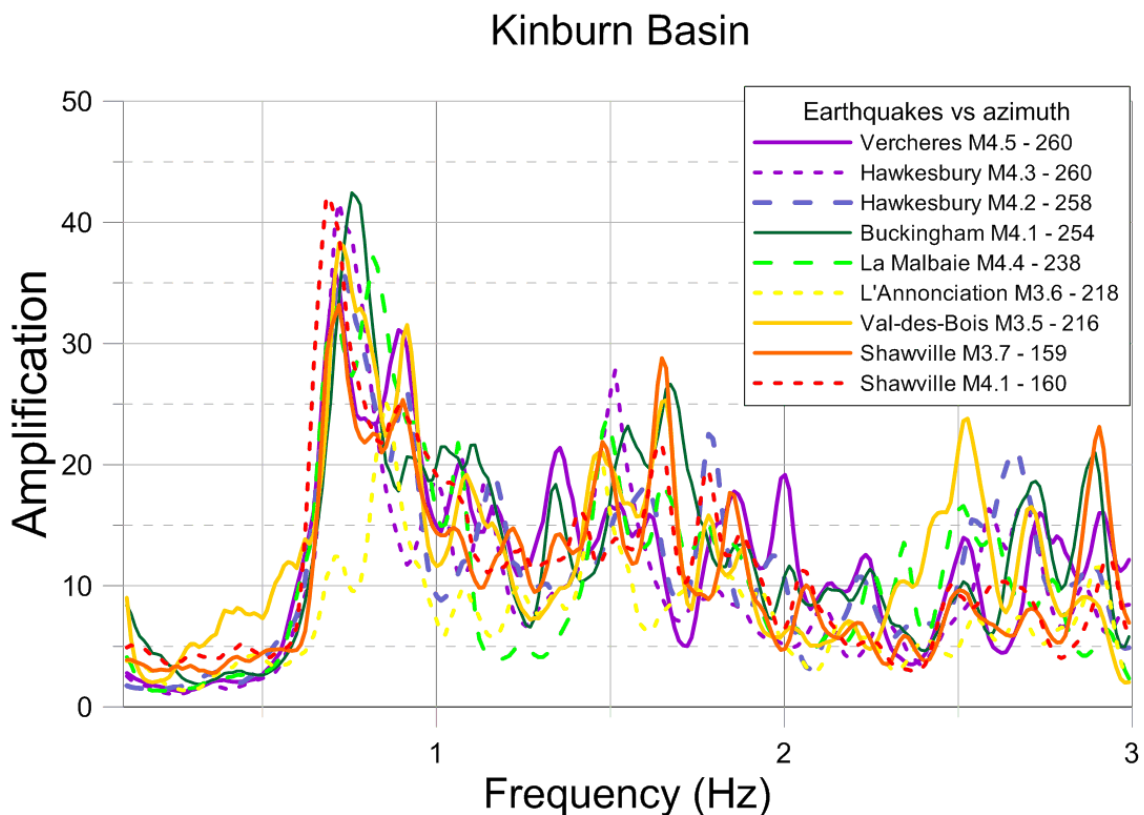


Fig. 4-20: Spectral ratios for earthquakes sorted by azimuth (from earthquake to seismic station) for the Kinburn basin.

Furthermore, the order of events in the first peak is not necessarily repeated in the following peaks. As shown in the plot with the clearest peaks (Fig. 4-19), the event with the highest amplification at the fundamental frequency is the M3.5 Val-des-Bois earthquake with average or even low frequency content. Examining the second peak event groups, the Val-des-Bois event maintains the highest amplification. As well, the frequency of the Val-des-Bois second peak is higher than that of most of the other events for this peak. However on examination of the third peak for this event, the amplification is significantly lower compared to that of the other earthquakes. Similar examples can be

found for the other two basins, although the peaks for the higher harmonics of other events are less clear, making interpretations more difficult.

The lack of a strong azimuthal dependence is likely due to the trapped seismic waves rebounding from the irregular basin-edges, with different frequencies being affected differently by the varying 2 and 3D structures.

Isolating variables

To isolate the cause of the amplification/ frequency shift further, we examined several series of events where one or more of the above mentioned variables were constant. For the Orleans basin, this was done for a series of earthquakes having epicentres near Shawville, QC (Fig. 4-21) as well as another series of earthquakes originating from the Val-des-Bois, QC region (Fig. 4-22). The Shawville series include three events: the main event m_N 5.2, and two aftershocks with m_N 4.1 and m_N 3.7, all occurring in May 2013. In other words, the time, distance and azimuth of the earthquakes were approximately constant.

The peak amplification at the fundamental frequency is the same for all three events, as is the frequency at which this peak occurs. Interestingly, there is a sub-peak (or “shoulder”) occurring between 0.8 and 0.9 Hz which has different amplifications for each event, as does the peak at the 1st harmonic (~1.8Hz) where the smallest event has the highest amplification.

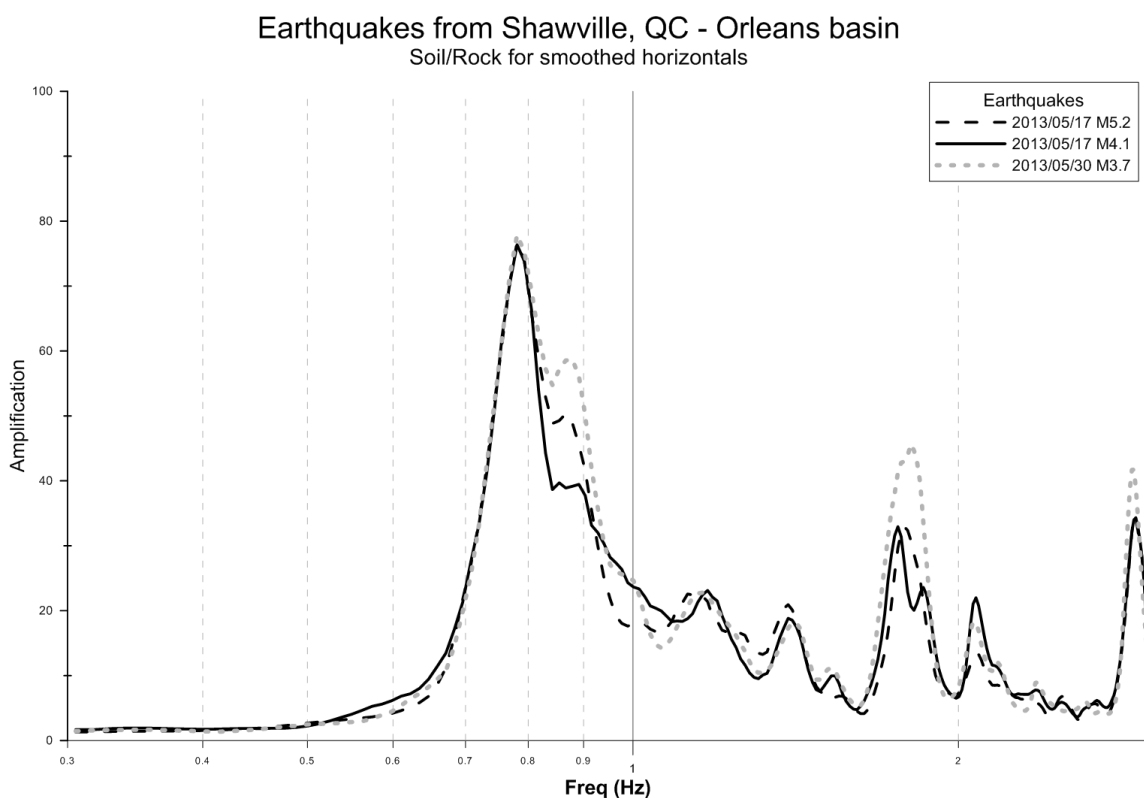


Fig. 4-21: Soil to rock ratios for 3 earthquakes occurring in May 2013 located near Shawville, QC as recorded on the Orleans station pair.

For the earthquakes located near Val-des-Bois, QC the events span a 4 year period, but the distance and azimuth are approximately equal. The magnitude ranges from m_N 3.5 to m_N 3.0, with the two middle events both being m_N 3.2. However, while the largest and the smallest events show the same amplification and have the same fundamental frequency, the two m_N 3.2 earthquakes have lower amplifications that are quite different from each other, and the one from 2012 also has the peak occurring at a higher frequency.

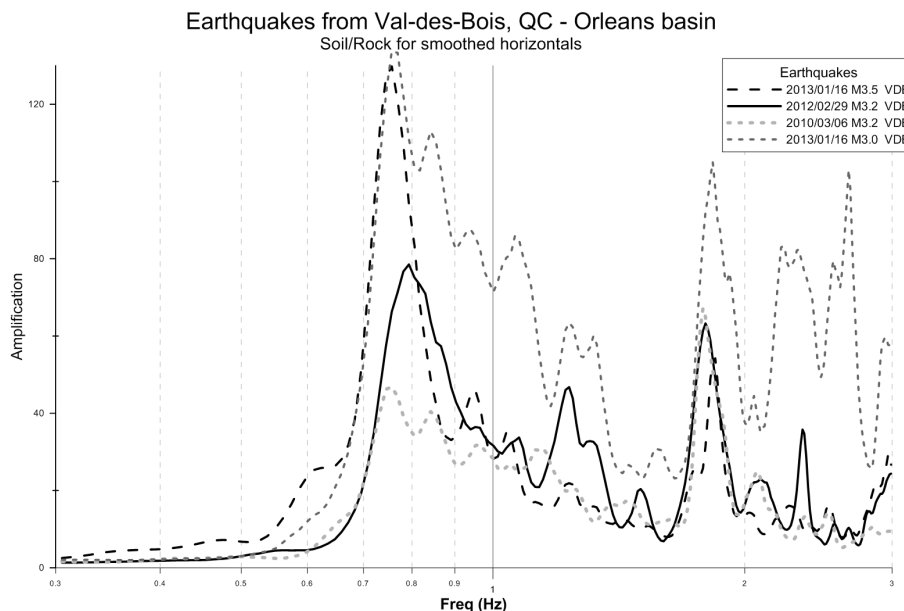


Fig. 4-22: Soil to rock ratios for 4 earthquakes occurring near Val-des-Bois, QC as recorded on the Orleans station pair.

Examining the data recorded by the Lefaiivre station pair for events from Shawville, QC (Fig. 4-23) we observe both differences in amplification and in the fundamental frequency. Hence, although the Orleans basin seems to have reacted similarly to this suite of events, the Lefaiivre basin did not. As with the Lefaiivre basin, the soil-to-rock ratios from the Kinburn basin recordings (Fig. 4-24) show varying amplifications and frequency contents.

2 and 3D structures must be affecting the resulting ground motions in order to account for the differing reactions of the basins to the different earthquakes. And since earthquakes with similar azimuths, distances and magnitudes result in varying responses within any one basin, the frequency content, and how these frequencies then interact with the 2 and 3D structures, must also be playing a role.

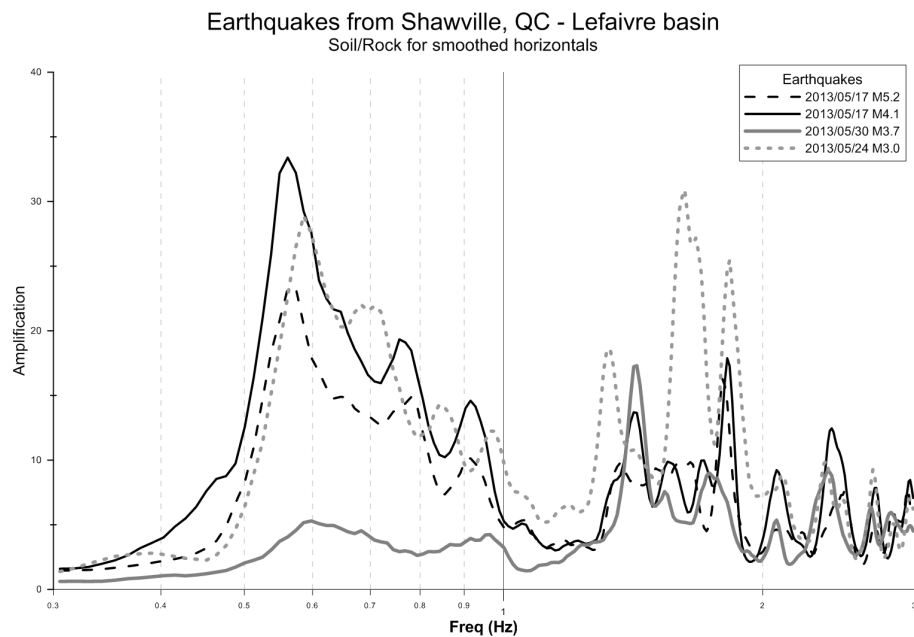


Fig. 4-23: Soil to rock ratios for 4 earthquakes occurring near Shawville, QC as recorded on the Lefavre station pair.

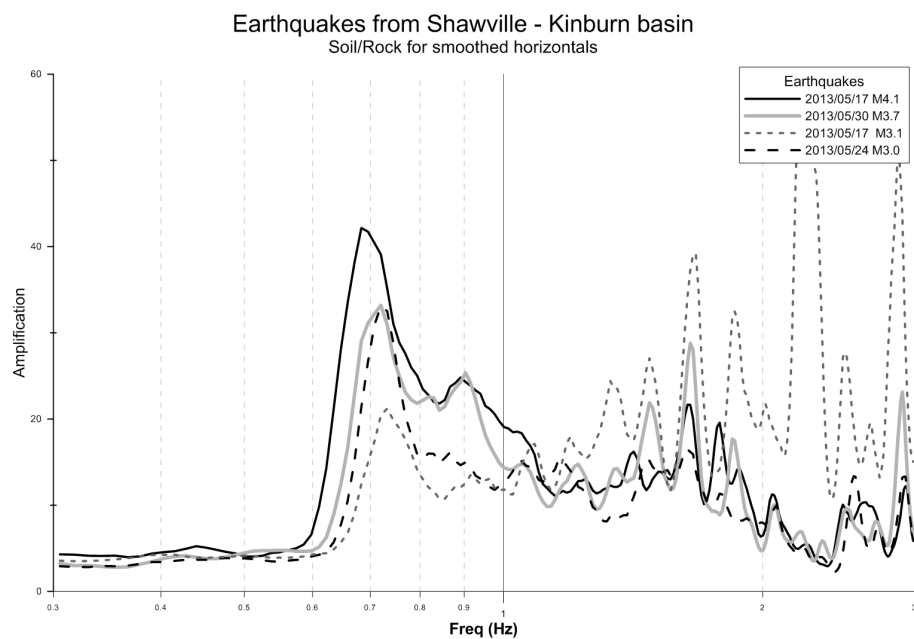


Fig. 4-24: Soil to rock ratios for 4 earthquakes occurring near Shawville, QC as recorded on the Kinburn station pair.

Input frequency: Teleseisms vs. Regional vs. Local Earthquakes

The frequency content can differ from one earthquake to another and depends in part on the magnitude, the distance of the earthquake to the recording station, and the source itself. Different frequency inputs may be affected quite differently by the 2 and 3D structures of a basin, leading to varying amplification results on any particular basin in response to one earthquake as compared to another. Rather than looking for small differences in frequency content between all these local earthquakes, we examine teleseismic and regional events and compare the results to those obtained for the smaller magnitude local earthquakes. Earthquakes in eastern North America tend to have a frequency-content relatively rich in high frequencies, and due to the small to moderate magnitudes of the events used in this study, poor in lower frequencies. In contrast, because the earth acts as a high frequency filter, the teleseisms recorded from large, distant events are depleted in high frequencies, but rich in low frequencies. The regional events are somewhere in between the local and teleseismic earthquakes.

Comparing the average soil to rock ratios from local recordings to the data recorded from the 2011/08/23 M5.8 Richmond, VA earthquake we find that the ratios calculated from 300s of shear wave arrivals and 200s of surface wave arrivals closely match each other (see Fig. 4-25). The ratio found from 90s of the P arrival from the same event is also quite similar, with the differences possibly being due to the different sample rates due to the longer intervals used for the shear and surface wave.

All three curves also match the average curve, but with more detail. Again, in part this may be due to sample interval of the resulting FFT being too widely spaced as the

time windows used from the local data were generally only 60s, sometimes less (see S.4.2.1), as well as the smoothing effect from averaging the curves of 11 events. The results for the teleseismic data are slightly different. The amplification data for the lowest frequencies, including the f_0 and the 1st harmonic appear, as with the regional data, to show similar amplifications at the same frequencies as was found with the local earthquake data, but however with more detail (see Fig. 4-26). And, as with the regional data, much of this effect is probably a result of the much larger time window taken for the FFT (360s for both the P and S arrivals, and 900s of surface waves). However, at frequencies near the 1st harmonic and at higher frequencies, the amplification level is generally increased up to ~8Hz, obscuring the peaks seen in the local and regional data.

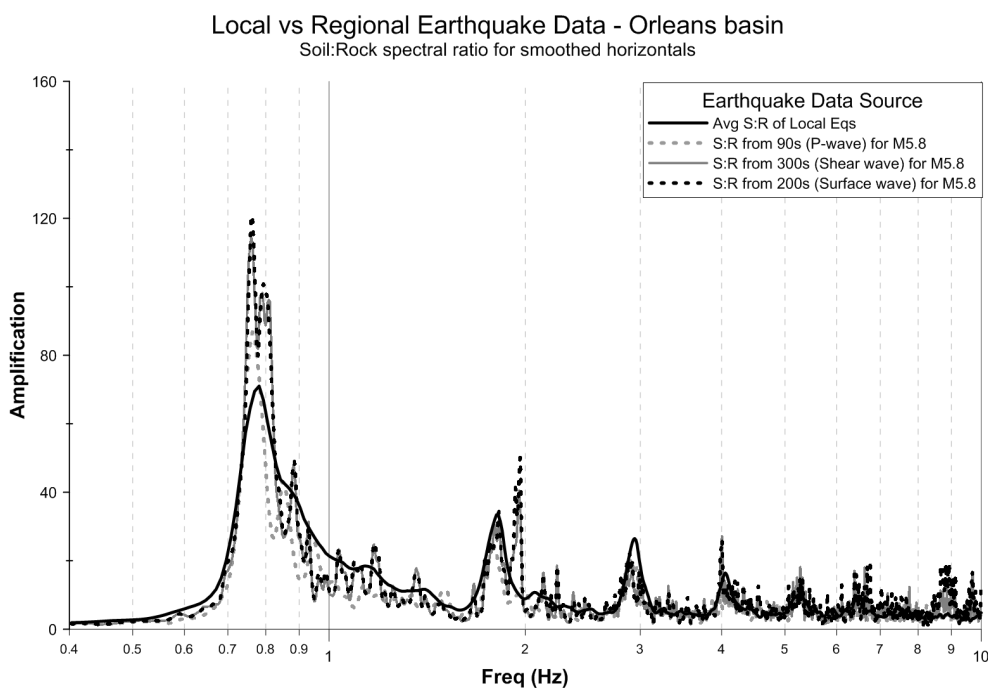


Fig. 4-25: Soil to rock ratios for the 2011/08/23 Richmond, VA M5.8 earthquake as recorded on the Orleans station pair compared with the average ratios recorded from local earthquake data.

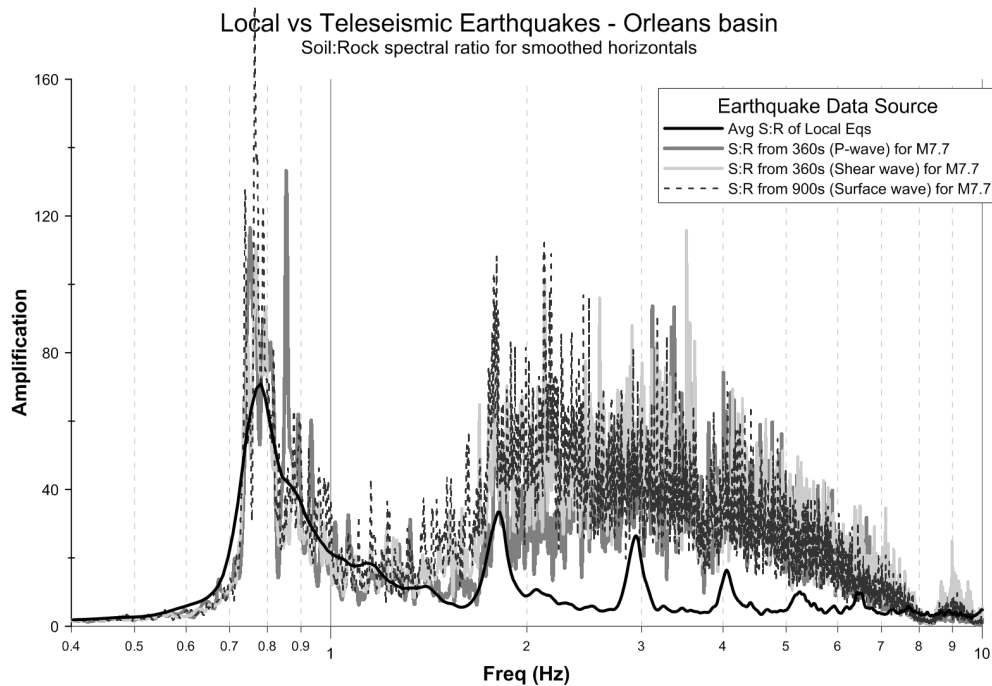


Fig. 4-26: Soil to rock ratios for the 2012/10/28 Haida Gwaii, B.C. Mw 7.7 earthquake as recorded on the Orleans station pair compared with the average ratios recorded from local earthquake data.

On inspection of the soil to rock ratios at the fundamental frequency, as before, we observe that the general location and shape of the average curve is similar to the teleseismic and regional curves. However, both the regional and teleseismic data show a sharper rise and fall off of amplification around the fundamental frequency, and show more details including several sub-peaks making up the main f_0 peak from the local averaged data.

As noted in S2.5.2, several studies showed that the angle of incidence influenced the amount of amplification in a basin; how it influenced the amplification depended on the geometry of the basin (e.g. Kham et al., 2013; Semblat et al., 2000). Regional and teleseismic waves will be approaching the basin approximately vertically, whereas the local waves will generally be coming in at an angle, depending on the location of the

epicenter. And as mentioned at the beginning of this section, the frequency content of the regional and teleseismic earthquakes will also have less high frequency content than that of the local events. The 2 and 3D geometries of the basin will also affect the varying incoming frequencies differently. Combined these two factors (incident angle and frequency content) explain the differences seen in the local versus the regional or teleseismic data. Despite this, the fundamental frequency is well defined for all three sources.

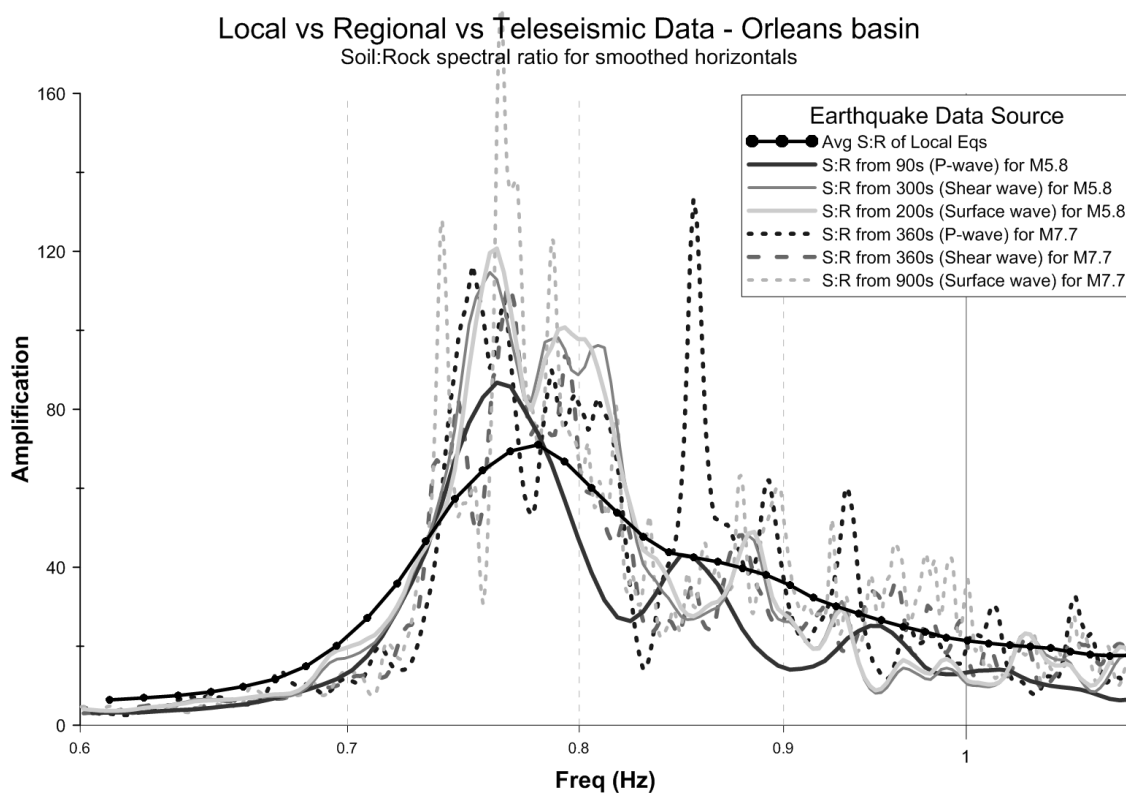


Fig. 4-27: Soil to rock ratios for the 2011/08/23 Richmond, VA M5.8 earthquake and the 2012/10/28 Haida Gwaii, B.C. Mw 7.7 earthquake as recorded on the Orleans station pair as compared with the average ratios recorded from local earthquake

4.2.7 Later “beats”

Additional features seen in the time series filtered with various pass bands (Fig. 4-2 of S4.1.3) are the later energetic “beats”. In studies done by Stephenson et al. (2006), it was demonstrated that some late energetic arrivals recorded on the Texcoco basin in Mexico were phases converted at the basin edges. However, the basin in that study was much larger, and hence the later signals were clearly separated from the earlier arrivals. As well, the signals were from larger, more distant earthquakes, and hence of much longer duration than the local signals recorded on basins in our current study. In order to obtain a reliable result from the FFT analysis the data must have a time window of at least 30s. However, due to the shorter duration of the high-frequency-rich local events that are used in this study, as well as the smaller size of the basins and the lack of array data, we cannot do a similar analysis to that of Stephenson et al. (2006).

However, to determine whether we could detect any change in frequency content throughout the recordings we compared the first 0-30 s of an event to the subsequent 30-60s, 60-90s and 90-120s. The 2012/10/10 $m_N4.5$ Vercheres, QC earthquake was chosen as it was well recorded, and the signal duration was of sufficient length on both the soil and the rock site to ensure reasonable results.

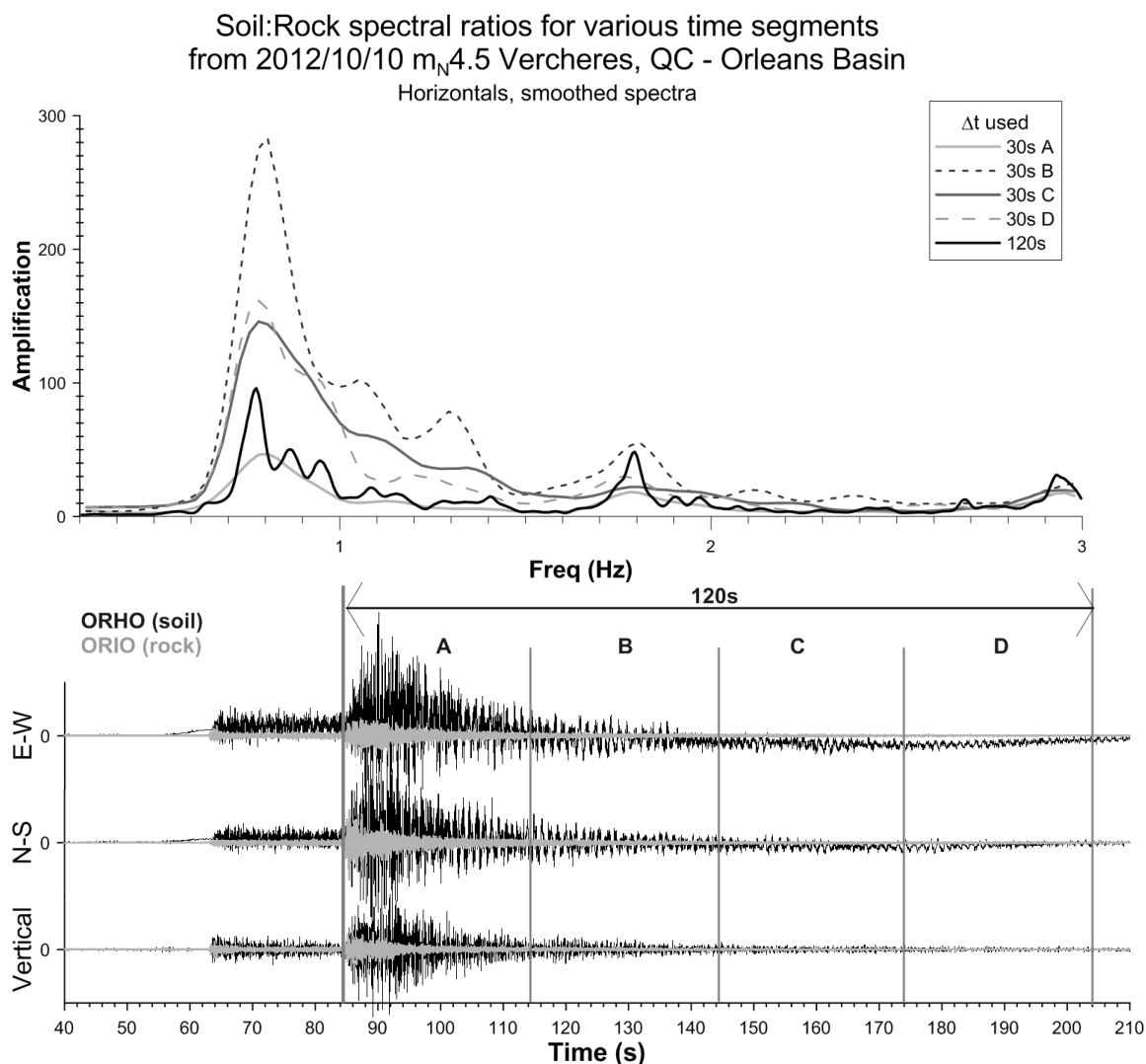


Fig. 4-28: Soil to rock ratios (mean-squared horizontals) for the 2012/10/10 $m_N 4.5$ Vercheres, QC earthquake as recorded on the Orleans basin pair. Time intervals are A) 0-30 s of shear; B) 30-60s of shear; C) 60-90s of shear; D) 90-120s of shear; and 0-120s of shear.

Fig. 4-28 shows the soil to rock ratios for each of the four 30s interval of data (A=0-30s of shear, B=30-60s of shear, C=60-90s of shear, and D=90-120s of shear). As well, the interval spanning all four of these 30s intervals, that is to say the data for 120s of shear, was also plotted.

As noted in the previous section, the amplifications are increased when comparing later data to the rock site, as the rock site signal attenuates more quickly than that of the soil site, meaning that further into the signal there is a greater difference between the recordings. Hence, the later 30s intervals (C and D) show higher amplification than the earlier ones (A and B). However, the general shape of each of the curves is quite similar, with the peaks occurring at the same frequency for each curve. Also, the longer the time interval used, the more detailed the curve, as seen when comparing any of the 30s interval calculated ratios to the 120s one.

4.3 Discussion

The effects of local earthquakes on ground motions over soft-sediment filled basins in the Ottawa region are similar to the effects recorded at other basins around the world, despite having different geometries and geophysical soil and rock parameters. The increase in amplification of particular frequencies has been seen in Mexico (Singh and Ordaz, 1993), California (Graves et al., 1998), Japan (Kawase, 1996), etc. Despite the high impedance contrast from the surrounding bedrock with high V_s versus the very soft-sediments with low V_s found in all three basins in the Ottawa region, these amplifications are larger than the general equations for 1D-effects alone predict (e.g. Cornou and Bard, 2003). The general shape of the soil-to-rock spectral ratio curves are similar, having the same pattern of a peak at the fundamental frequency followed by peaks at higher harmonics. The Ottawa basins show the highest amplification at the f_0 , like that of the Grenoble, France basin (Cornou and Bard, 2003). As well, the Ottawa basin sites also

show the long duration and late energetic arrivals (or beats) as seen on basins around the world (e.g. Stephenson et al., 2006; Graves, 1998; Kawase, 1996).

According to the relations in Eqn 2.3 and 2.6, the calculated 1D amplifications using the shear wave velocities and the densities of both the soil within the basin and the bedrock, all three basins should have approximately the same amplification due to seismic impedance or to resonance (S4.1.1), since the material infilling the basins and the surrounding bedrock is approximately the same for all three sites. However, these equations are only for 1D modelling and do not account for the 2D and 3D geometries, which likely account for some of the differences in amplification found between the 3 basins.

Soil to rock spectral ratio amplification results appear to be reasonably robust, for frequency content, and also are not very sensitive to start time, as long as the beginning of the shear on the rock site recording is not missed. Duration of the time window containing signals with high signal-to-noise affects the FFT sample rate and hence the amount of detail (i.e. variance in peak amplifications) one can see in the resulting curve. As seen in Fig. 4-10, shorter durations result in the FFT being discrete points, rather than approximately being a continuous curve. Details of peak amplification in between the sample intervals may be lost, but the general shape of the spectral ratio is preserved. Note that these amplification calculations are based on the smoothed FFT of the horizontals, whereas the NBCC is based on PSA.

It has been shown that comparable results can be achieved using more distant reference rock site (e.g. Cornou and Bard, 2003). In general our reference rock sites were immediately adjacent to the basin, 1-3 km from the soil sites (located at approximately the centres of the basins). Similar results were obtained in a previous study for the Orleans basin using a more distant site OTT, approximately 16km from the soil site (Kolaj, 2010). Note that for all the earthquakes used, the distance between the rock and soil site is considerably shorter than the epicentral distances of the earthquakes used in the analysis (generally in the 10's or 100's of kms).

Comparing the soil to rock spectral ratio curves recorded from one basin to another, shows that the Orleans basin has twice the spectral amplification than recorded for the other two basins. Although there is slight variation between individual earthquake recordings at a particular basin site, all local and regional events have soil-to-rock amplification ratios with the same general shape (the highest peak at f_0 , followed by subsequent harmonic peaks with lower amplitudes). Regional events are useful for amplification studies as they are generally of longer duration and hence a good spectral ratio can be achieved with even just one well recorded event. The same results are true for teleseisms, but only for the f_0 , since the dominant frequency ranges of these events are at or below the f_0 of the soil site and higher frequencies in the harmonic ranges are not present.

When examining the soil-to-rock spectral ratios in detail, it was noted that individual earthquakes showed highly varied amplifications. No particular earthquake shows the highest or the lowest amplification across all three basins consistently. In fact, even on a particular basin, one event may give the highest (or lowest) peak for the f_0 , but that pattern does not necessarily continue for any of the subsequent harmonic peaks. This is due in part to the random nature of earthquakes, but also seems to be a function of the input frequencies and how the incoming waves interact with the 2 and 3D bedrock geometries and soil structures. Even the frequencies at which the fundamental and harmonics occurred were found to shift between events. When trying to determine the cause of these differences, no convincing link was found in terms of time, magnitude, azimuth or distance, except on the Lefaiivre basin where the amplification showed a potential link to azimuth, but not the frequency at which f_0 occurred. Similarly no pattern was seen when looking at suites of events either from the same location (hence with distance and azimuth constant), and sometimes time (with all events occurring within a few days). There is the possibility that other source parameters (e.g. focal mechanism, frequency content) play a role in these observed differences. However, there is a lack of information on source parameters for the majority of these events and it is not currently possible to undertake such an investigation.

The HVSR measurements (as described in S3.4) taken from each of the sites are approximately equal, recording the fundamental frequencies with peak ratios of ~ 7 times of horizontal versus vertical recordings for all three basins soil sites. These peaks coincide exactly (in frequency, not amplification) with that of the soil-to-rock spectral

ratios from the local, regional and teleseismic data. However, the HVSR data shows only the fundamental peak. This peak can also be observed in soil to rock site ratios using just 30s of noise.

Note that since these amplifications are taken from the horizontal versus the vertical recordings at just the soil site, they cannot be directly compared with the soil to rock ratios which are taken from two different sites and actual earthquake recordings. Furthermore, HVSR readings are based on ambient noise measurements which may vary depending on time of day, presence of localized cultural noise, etc. Hence, the recorded amplifications for HVSR are highly dependent on when the readings are taken and can only be used as a guide to the location of the fundamental frequency. Nor does the HVSR measurement capture the peaks of the higher harmonics at higher frequencies which are evident in the soil-to-rock spectral ratios.

The f_0 can be determined using any one of the following equally well: HVSR; soil-to-rock ratios from noise, local, regional or teleseismic earthquake recordings. These data all show an initial peak at the same frequency for a particular basin, despite the differences in source parameters: local earthquakes recorded from the west Quebec seismic zone are smaller in magnitude, rich in high frequencies, and will enter the basin at an angle, whereas the teleseismic earthquakes recorded are depleted in high frequencies, while rich in lower frequencies, and will enter the basin from almost directly underneath (i.e. vertically). The HVSR readings are based solely on background noise. Note that 2 and 3D effect on amplification will be influenced by both the frequency content and the incident angle of the incoming wave.

The spectral ratios from the local and regional data also have subsequent peaks, assumed to be the higher harmonics as has been observed at other basins around the world (e.g. Semblat et al., 2000). For the Orleans basin, these peaks are similar to the ones reported from a previous study (Kolaj, 2010) who compared ORHO with both ORIO and a more distant rock site OTT.

Attempting to predict the location of these peaks using just the basic equation (Eqn 2.5) relating the frequency to the shear wave velocity (V_s) and the known depth of the soil layer (H) to the first major reflector proved difficult. Since the V_s changes continuously with depth it is not obvious which V_s should be used for the calculations. For example, one could use the average V_s ($V_{s_{avg}}$) calculated for the entire layer, or a V_s at a specific depth (e.g. $V_{s_{30}}$ being the V_s at 30 m depth). The interval velocity ($V_{s_{int}}$) calculated as a function of depth from the data collected at the sites is shown to be constantly changing over the profile.

Back-calculating a V_s from the measured f_0 , and using this to calculate the expected harmonics did not produce peaks at frequencies that matched the recorded ones for any of the basins. Neither did Dobry et al.'s (1967) method, which uses an equivalent depth ($H_{e_{quiv}}$); this method predicted values for f_0 which were higher than the actual f_0 for each basin. Both of these methods relied on simple 1D equations and did not take 2D and 3D effects into account.

Some of the discrepancy between the predicted and observed recorded signals may also be due to the details of the materials and their properties beneath the soil site

stations. An example is the glacial till layer, the thickness of which varies depending on location. This till layer typically has a shear wave velocity of approximately 580 m/s but with wide variance. Theoretically, however, this would decrease the seismic impedance contrast between the layers, and hence should lead to a *lower* amplification (not higher, as we see). However, depending on the thickness, only shorter wavelengths might be affected by this till layer, with no effect on the longer wavelengths.

Even without the till layer model, the soil profiles under each of the seismic stations located on the basins are quite complex, with continuously changing soil parameters (e.g. V_s and soil stiffness). Vrettos (2013) showed that a profile with continuously changing V_s with depth results in a shift the expected frequency peaks from that of a constant bulk V_s layer model. For this study a large amount of data is available for each of the soft-soil seismic sites, hence it is possible to build a detailed profile for each of the basins. This model may be used in a 1D ground motion analysis software program to obtain better model estimates of the amplifications and frequencies for 1D site effects, thus helping to focus on 2- and 3D geometry as Cornou and Bard (2003) suggest. This analysis will be done in Chapter 5.

A certain caution needs to be applied to any conclusions drawn from the results of the soil-to-rock spectral ratio analysis of this study as they rely on only a handful of local events for each basin. Signal to noise restrictions with smaller events precluded their use to obtain robust results, and hence the data set used was limited to events of $\sim M3$ and above. Possibly future work could include a stacking of the data to lower the magnitude threshold of events used.

There were also restrictions on the use of larger events. For example, the $m_N 5.2$ Shawville event was clipped on the JSSS (Kinburn basin seismic station), as was the regional event $M 5.8$ Richmond, VA. Likewise, the $M 5.0$ Val-des-Bois event of 2010/06/23 was clipped on ORHO on the Orleans basin. Hence, the results obtained were limited in their magnitude range, with very few events larger than $M 4$ for any of the basins. This was particularly a problem for obtaining data for the Lefaiivre basin, where the soil site has only been in operation since late summer, 2012. Continued recording for longer periods of time, and co-locating strong motion sensors with the seismograph sites will allow for a wider range of data to be collected, including more regional and teleseismic data. The continuous recording on ORHO and ORIO was helpful as it meant data could still be accessed later even if an event was first missed. And unlike the non-real time sites, we were able to retroactively access more data if the initial 180 s of downloaded data did not fully capture the event.

Note that the data from larger events would add valuable information. Most of the local events are weak motion events containing very high frequency, but little low frequency content. The regional data from the larger, more distant earthquakes will have more low frequency energy, but need to travel a longer path through the earth and hence are depleted of some of the higher frequencies. The teleseisms, being the largest magnitude and most distant earthquakes, have mostly low frequency content and are depleted of the high frequency content. Note that the incoming energy also arrives at different angles depending on the source, with teleseismic and regional earthquakes arriving approximately vertically from below the basin, while the local earthquake waves

will arrive at an angle. Large, local events would provide a new data set of events rich in both high and low frequencies, which would be an important addition as the basins' 2 and 3D structures respond differently to the varying frequencies and varying angles of incident.

Overall, the amplification is more significant in the horizontals than the vertical component, suggesting conversion of body waves into surface waves. Typically, Love waves have purely horizontal motion, while Rayleigh waves would have a vertical component. However, Konno and Ohmachi (1998) showed that at sites with a high acoustic impedance contrast, the Rayleigh wave may be purely horizontal. This would be consistent with other studies which have found a mix of Rayleigh and Love wave energies at other basins around the world (e.g. Cornou and Bard, 2003; Joyner, 2000; Somerville et al., 2002). In particular, Somerville et al. (2002) noted that in their Californian basin, the Love waves were polarized parallel to the basin-edge, while the Rayleigh waves were normal to it.

In order to sort out the various phases, it would be useful to analyze the wave energy direction, not just particle motion. However, this would require an array of stations on each basin. As there is only data from one 3-component station for this study, it is impossible to distinguish Love waves from Rayleigh waves. But the presence of both might help explain the chaotic particle motions recorded on all three basins.

Reverberations of other phases from non-uniform basin edges no doubt also contribute to the confused particle motion, a factor that is not aided by the small size of the basins being studied (Stephenson, 2007; Stephenson et al., 2006). In the future, an array may

allow for the tracking of wave energy, and not just wave motion, which might help future investigations.

Sommerville, et al. (2002) had noted that the attenuation of Rg was lower than that of Love waves. This suggests that it might be easier to identify patterns in the latter part of the recorded data. Stephenson et al. (2006) were able to isolate some of the late arriving energy on the Texcoco basin for large, regional earthquakes and show there was a distinct change of frequency content to that of the energy earlier in the recording. Using array processing they were even able to show the direction of the energy, and show convincing arguments that these are from body phases converted near the basin edge. For our basin study, using local, high frequency, quickly attenuated data, and with only a station pair, it was not possible to investigate these late arrivals in the same manner. The individual beats are not long enough in duration to measure reliable frequency content.

The long duration of the signals on the soil sites has been modelled by Kawase (1996) to be due to “basin-edge” effects. All three of the study basins recorded these long durations, with energies mostly in the horizontal components and particularly for the lower frequencies, suggesting surface wave generation at the basin-edges. We theorized that if this is the case, the direction of the wave energy might show an alignment that is consistent with a basin feature, as opposed to being aligned with the earthquake azimuth as seen on the rock sites, and hence the particle motions of the Orleans soil site was examined for evidence of preferred directions that might align with a basin feature. Note that as the data for this study consists of only one station on each of the basins, only the particle motion can be determined and not the direction of wave energy.

Traditional particle motion plots have not proved to be useful for these high frequency local earthquake recordings. Plots showed that motions could change direction even within one second. Trying to find patterns in the many plots generated for just one event was next to impossible. Furthermore, we were limited to looking at only the Orleans basin, due to a time stamp error in the Lefaivre and Kinburn basin data. The results for just the initial P-wave motion for the Orleans basin showed that the rock sites had an initial particle motion that was aligned with the azimuth of the earthquake, as is expected. However, the direction of the initial P-wave motion on the soil site appeared to be random, without any particular preferred azimuth, nor systematic offset.

Furthermore, the initial motion appeared to be delayed by ~ 0.3 s on the horizontal components as compared to the vertical on the soil sites. However, on closer inspection on some of the clearer events, it can be noted that there is a low energy arrival that does appear at the same time as the arrival on the vertical component, which is possibly the direct P arrival. Either the direct P-arrival is too weak to be visible, or more probably due to the impedance contrast across the basin boundary, the waves are directed almost purely vertically. The later, more visible arrival is likely the response of the basin to the P-arrival, with trapped waves being bounced around the basin in a manner dependent on the how frequency content and incident angle are affected by the 2 and 3D structures of the basin or the soil layers within. Note that this converted energy reaches the middle of the basin (i.e. the soil site) in ~ 0.3 s, highlighting how little separation there is between arrivals. Furthermore, it explains why these “P-arrivals” on the soil site do not have particle motions consistent with the epicentre. Hence, the basin is obviously affecting

both the direction and the amplification of the ground motions. However, there was no consistent preferred direction found, even from earthquakes with similar source azimuths, magnitudes or distances. This indicates that the relation between the 2 and 3D geometries of the basin and soil layers on the incoming frequencies is quite complex and not easily interpretable using data from just one station. Given the difficulty with determining patterns from the P wave, further analysis and comment on the S and surface wave particle motions is left to Chapter 6, where a different approach is taken to identify predominant particle motion azimuths for selected time spans within a recording.

5. 1D Ground Motion Modelling

In order to understand the effects of a bedrock basin on the resulting surface ground-motions of the infilling sediments (i.e. the 2 and 3D effects), we need to first have a good concept of what the effects of the soil column beneath the site would be if there were no buried bedrock basin (i.e. the 1D site effects only). In the previous chapter, it was determined that using the average shear wave velocities and densities for the soft sediments filling the basins and the surrounding rock, the estimated amplification due to impedance is expected to be around 5 times. For site resonance, which in the case of our basins is likely the more appropriate equation, the estimated amplification is approximately 28 times that of the soil over the rock site. However, when examining actual recordings of local earthquakes, the amplification was found to be closer to 35 times or more for the soil versus rock sites.

Furthermore, using the relation of soil height and V_s to frequency to determine the fundamental frequencies and the higher harmonics of the basins, the values calculated for the resonant frequencies did not exactly match the peaks determined from the recorded local earthquakes. This type of information is an important consideration for designing a building, to make sure the structures are built to withstand the amplifications expected, and that they are not susceptible to the frequencies most likely to be amplified during an earthquake.

However, the soil underneath the soil sites of each of the basins is not made of a single, homogeneous layer, but of multiple layers with varying shear wave velocities and densities, etc. Hence, to do a proper 1D analysis we will need to use a computer modelling program. There are several types of ground motion analysis software programs available, 1D analysis is commonly used (Kramer and Paulson, 2004) for scientific and engineering purposes, as detailed information on soil layers around any given site is often not available. These programs allow for the input of multiple horizontal layers to model the soil profile and will then determine the soil-to-rock transfer function; that is, the amount of expected amplification as a function of frequency.

Proshake (version 1.12, March 2003) was the software chosen for this project as it is based on the SHAKE algorithm (Schnabel et al., 1972) which forms the basis of many widely used ground motion analysis programs like Shake91, Shake2000, etc. (Destegul et al., 2007). Furthermore, Edushake is an educational version of the program, freely available. Its interface and underlying algorithms are the same as Proshake, but only allows the use of the provided input ground motions, modulus reduction and damping ratio curves (www.proshake.com). Some of the preliminary work and testing was done using Edushake.

This chapter will include the basics of Proshake, defines the soil profiles for each of the basins, the inputs used, and results of some test runs on simple profiles to determine the sensitivities of Proshake to particular variables. Finally we present the results from the detailed profiles for each basin, and discuss the results of the 1D amplification versus 3D amplification, as well as any limitations encountered.

5.1 1D modelling software

Proshake is a 1D ground-motion analysis software which uses an equivalent-linear model to approximate non-linear behavior in soils. (This approximation is commonly used in soil modelling (Kramer, p 275). It does not calculate porewater pressures and assumes no permanent deformation. Despite this, it is a widely used software and has been shown to give reasonable results. The program allows values to be entered in either metric or imperial units and the output files are simple text files that can be easily imported into a spreadsheet for further computations and analysis. For more information on data formats and files for Proshake see Appendix C.

The equivalent linear approach uses two general characteristics of the hysteresis loop (path of stress-strain behavior in a soil under cyclic loading) to describe its general shape: the inclination represented by the secant shear modulus (G_{sec}) and the area (A_{loop}) of the loop (Kramer, 1996; p231; see Fig. 5-1). The A_{loop} is a measure of energy dissipation and can be described by the equivalent damping ratio, ξ (Kramer, 1996; p231):

$$\xi = \frac{W_D}{4\pi W_S} = \frac{1}{2\pi} \frac{A_{loop}}{G_{sec} \gamma_a^2} \quad \dots \text{Eqn [5.1]}$$

where:

W_D is the dissipated energy; and
 W_S is the maximum strain energy.

The damping curve shows the relationship between equivalent damping ratio and the shear strain. The value of G_{sec} decreases as the shear strain increases. This

relationship is characterized by a modulus reduction curve. Note that Proshake assumes viscous soil damping (Proshake manual).

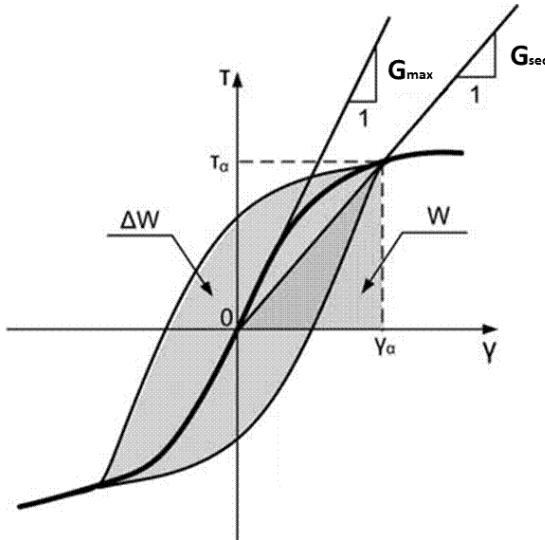


Fig. 5-1: Stress-strain curve illustrating the behavior of a typical soil undergoing cyclical loading. Graph shows the maximum shear modulus (G_{max}) and the general inclination of the hysteresis loop defined by G_{sec} . Figure modified from Assimaki et al., 2008.

In the equivalent linear model, G_{sec} and ξ must be constant for each soil layer, so the two variables are adjusted in iterations until the values are consistent with the level of strain induced in each layer (Kramer, p 270). Furthermore, there must be compatibility between layers: that is to say, the movement at the top of bedrock must equal the movement of the bottom of the layer of soil just above bedrock, and the movement at the top of that lowest soil layer must be equal to the movement at the bottom of the next layer of soil up, etc.

It is important to remember that this equivalent linear approach does not account for permanent strains or calculate porewater pressures. Although the water table can be

defined, this information is only used when vertical effective stresses are computed (Proshake manual). Proshake does total stress analysis.

To create a soil profile in Proshake, the thickness of the layer needs to be defined, as well as the bulk unit density of the material (γ_b), and either the shear wave velocity (V_s) or the maximum shear modulus (G_{max}). The latter two variables define the low-strain stiffness of the material (Proshake manual). For all three of our profiles the available data was such that we had either a measurement for, or were able calculate, V_s . Once either V_s or G_{max} is entered, the other variable will be automatically calculated, using the equation (Proshake manual):

$$G_{max} = \rho V_s^2 \quad \dots \text{Eqn [5.2]}$$

The layers are assumed to be flat-lying and infinite in the horizontal direction.

Furthermore, suitable modulus reduction and damping ratio curves must be chosen for each layer. Proshake has preprogrammed several well-known and widely used curves for rock, gravel, sand and clay. However, users can also define their own curves. These curves will be discussed in detail in S5.4.

To calculate the ground motion at a soil site, Proshake uses a frequency domain approach as outlined in Kramer (1996). First the rock motion is expressed as a Fourier series, and then the transfer function (amount of soil amplification to rock amplification) is calculated. The product of the Fourier series (for rock) and the transfer function are taken, and the inverse Fourier transform converts this back into the time domain

(www.proshake.com). To calculate the transfer function $F(\omega)$, the following algorithm is used:

$$F(\omega) = \frac{1}{\cos k_s^* H + i \alpha_z^* \sin k_s^* H} \quad \dots \text{ [Eqn 5.3]}$$

where:

ω is the circular frequency of the harmonic wave,

α_z^* is the complex impedance ratio; and

k_s^* is the complex wave number (subscript 's' refers to the soil layer).

5.2 1D profiles for each of the basins

The basic geology for the Ottawa region consists of Paleozoic or Precambrian bedrock with a high V_s , covered in parts with low V_s sediments known as Leda Clay. The clay is underlain in places by a till layer that varies in thickness, but has been found to be on average 5 m thick in the Ottawa region (Hunter et al., 2010). Details of these general layers are outlined in S3.1, and the damping ratios and modulus reduction curves used for these three layers is discussed in a later section (see S5.4). However, in order to build a detailed one-dimensional profile for each of the three basins, more site specific information is required. All the available geophysical data were gathered for each site, and the data required for the modeling were extracted to create a multi-layered profile.

Where the required data was not available, approximations, calculations or empirical approximations were made to fill in the blanks. In this way, a profile was built that represents the soil column at, or very close to, the soft-soil seismograph site for each of the three basins. Note that occasionally, if there were many measurements within less than a metre, the measurements would be combined into one layer, as the program would

not always compute a solution when too many layers were used. These details are summarized below for each basin.

5.2.1 *Lefaiivre basin, near Alfred, ON*

The Lefaiivre basin, the largest and deepest of the basins, is located east of Ottawa near Alfred, ON. The basin's general characteristics are outlined in Section 3.3.1. A high resolution profile shows the basin is filled with Holocene and Pleistocene glacio-fluvial sediments (Benjumea et al., 2003) with the top 50 m of soil being "disturbed" (Benjumea et al., 2003) and containing sand layers (Aylsworth et al, 2000).

Data for the detailed profile was obtained from JA02-4 located approximately 1.5 km to the NW of ALFS (see Appendix C for original data and calculations). The top of the Pleistocene unconformity was identified at 112 m depth and is associated with a significant shear wave seismic impedance contrast. Layers were mainly defined by moisture content readings. Bulk unit density (γ_b) was calculated assuming 100% saturation (Das, p32):

$$\gamma_b = \rho g = [(1+w)/(1-\Phi)] \times G_s \times g \quad \dots \text{ [Eqn 5.4]}$$

where:

ρ = density;

Φ = porosity; and

g = specific gravity = 9.81 m/s²

To determine ρ , the following equation was used:

$$\rho = \frac{(1+w)}{(1-e)} \times G_s \quad \dots \text{ [Eqn 5.5]}$$

where:

w = moisture content;

e = void ratio; and

G_s = specific gravity of the soil and is assumed to be 2.65 (H. Crow, pers.comm. 2012);

Void ratio is also defined as:

$$e = w \times G_s \quad \dots \text{ [Eqn 5.6]}$$

For sections where measurements were taken more than 5 m apart, these were divided into sub-layers and assigned the same γ_b . Many layers were less than 1 m thick, so these were sometimes combined, and an average bulk unit weight used for the soil layers. An average γ_b of 21.7 kN/m³ was obtained from the measurements from the till layer. This γ_b was also used for the other two profiles, as there are no other measurements or documentation on the γ_b of till in the Ottawa region. As there were no γ_b measurements available for rock at any of the basin sites, a γ_b of 26.0kN/m³ was assigned. This value was based on a literature search which produced values of G_s for quartz, sandstone, shale, etc. ranging from approximately 2.2 to 2.8, which translates to a γ_b of ~22 to 28kN/m³. As many of the values in the literature were generally at the higher end, an estimate of 26.0kN/m³ was used for the γ_b of rock at all three of our sites.

For V_s , the measured value closest to the depth of the layer was used. For thicker layers, a V_s obtained by averaging the V_s measurements contained within the thickness of that layer was used. The borehole extended through the glacial till. Some of the interpreted V_s data seem to be anomalously high through this layer, as noted by J. Hunter (pers. comm., 2013). According to the measurements from the borehole, the underlying bedrock is sandstone with V_s of 2567 m/s.

5.2.2 *Heritage Park basin, Orleans, ON*

The Orleans basin is a relatively small basin, with a maximum depth of around 100m, filled with sediments that are sensitive, and have a low V_s , commonly less than 180 m/s (e.g. Motazedian and Hunter 2008; Hunter et al., 2010). The V_s versus depth profile was re-interpreted using data from a 30 m deep borehole (see S3.3.2, Fig. 3-12) located 300 m from ORHO (Borehole: GSC OTT-07-02; see Appendix C for original information) and the integration of reflection data from shear wave surface sites in the basin within 1.5 km of the ORHO station (J. Hunter, pers. comm., 2014). As well, local borehole geological information adjacent to the ORHO site was used as a guide (J. Hunter, pers. comm., 2014)

For the till layer, the Ottawa average of 580 m/s for V_s was used, while for the bedrock the average velocity for shale ($2166 \text{ m/s} \pm 401 \text{ m/s}$). Shale is likely the rock-type underlying this site (J. Hunter, pers. comm., 2014). See S3.1 for table of V_s values for all rock types found in the Ottawa region.

For the Orleans basin, no γ_b measurements were available. All the readings identified to be from the till layer at Lefavre were averaged to obtain a γ_b of 21.7 kN/m^3 , which was used for the till in the Orleans profile as well, while the bedrock was assigned a γ_b of 26.0 kN/m^3 as noted previously (see 5.2.1 for more details).

For the soft sediment layer, γ_b estimates were calculated from V_s using Eqn 5.4 and 5.6 in conjunction with the relation from Hunter (2007):

$$\Phi = 1.422 - 0.1693 \times \ln(V_s); \quad 2\sigma = 0.13 \quad \dots \text{ [Eqn 5.7]}$$

$$e = \text{void ratio} = \frac{\Phi}{(1-\Phi)} \quad \dots \text{ [Eqn 5.8]}$$

See Appendix C for data spreadsheet which includes the original data from the borehole, as well as the calculations made to assign the thickness, V_s and γ_b for each layer. These data include notes on when layers were combined, the assumptions and calculations made, and any other notes with regard to the values assigned.

5.2.3 Kinburn Basin, Kinburn, ON

As mentioned in Section 3.3.3, the Kinburn basin is actually part of a set of interconnected basins, trending from north-west to south-east. The sub-basin which was instrumented with the seismograph sites lies just to the south-east of the hamlet of Kinburn, ON, is approximately 7 km long by 3 km wide, and is filled with low V_s , non-sensitive, Leda clay, underlain by a relatively thin layer of glacial till. The bedrock beneath the soil site JSSS is estimated to be Paleozoic (Hunter, pers. comm., 2012) based on high resolution seismic reflection interpretations and known fault structure in the area. The bedrock outcrop at the JSRS rock site is un-weathered granite gneiss of Precambrian age.

The soft soil seismic station JSSS is positioned roughly over this deepest portion of the sub-basin. Geophysical data was obtained from the borehole JSR-01 (Medioli et al., 2010), which is located approximately 330 m to the SSE of the seismograph site (see S3.3.3 for Fig. 3-14) and was drilled and logged down to 96.95 m, which is assumed to be to the top of the till layer. J. Hunter (pers. comm., 2012) noted that gravel came up with the last bit of core. The borehole information forms the basis of the profile.

The data was interpreted by H. Crow (pers. comm., 2013; see Appendix C for original data and calculations) using moisture content readings to define the layers. From the moisture content, and assuming 100% saturation, the γ_b was calculated using the formulas defined in S5.2.1.

For the Leda Clay layers (including the grey rhythmites, the massive marine clay, the upper red and grey rhythmites and the upper clay silt as described in Medioli et al. (2010), the plasticity index (PI) is generally assumed to be around 40 for the study region, although there are some recent suggestions it might be lower in certain areas around Ottawa (H. Crow, pers. comm., 2014). Vs data available is given for every 0.5 metre below 8 m depth, but the layer thicknesses were defined by the sparser moisture content readings, which were at irregular intervals. Hence, for the profile, the Vs readings at the depths closest to the layer's depth were used. For thicker layers, a calculated average from the Vs readings contained within that particular layer was used. For the top 8 m, Vs was estimated using bulk density by H. Crow (pers. comm., 2013).

As the borehole did not extend through the glacial till, no direct readings of thickness, Vs or γ_b are available for determining the physical properties of this layer or below. Hence, the mini-vibe section shot down John Shaw road was used to interpret the till thickness. The section in Fig. 3-8 (S3.3.3), interpreted by Pugin et al. (2013), shows the glacial till layer to have a thickness of ~26 m at the location of the borehole, down to the depth of 123 m. The velocity was assigned 580 m/s, the average found for till in the Ottawa region (see S3.1). No literature value for the ρ or γ_b of till in the Ottawa region

could be found, so as with the Orleans profile, we used the data collected in the glacial till layers of the Lefavre borehole to assign a γ_b of 21.7kN/m^3 .

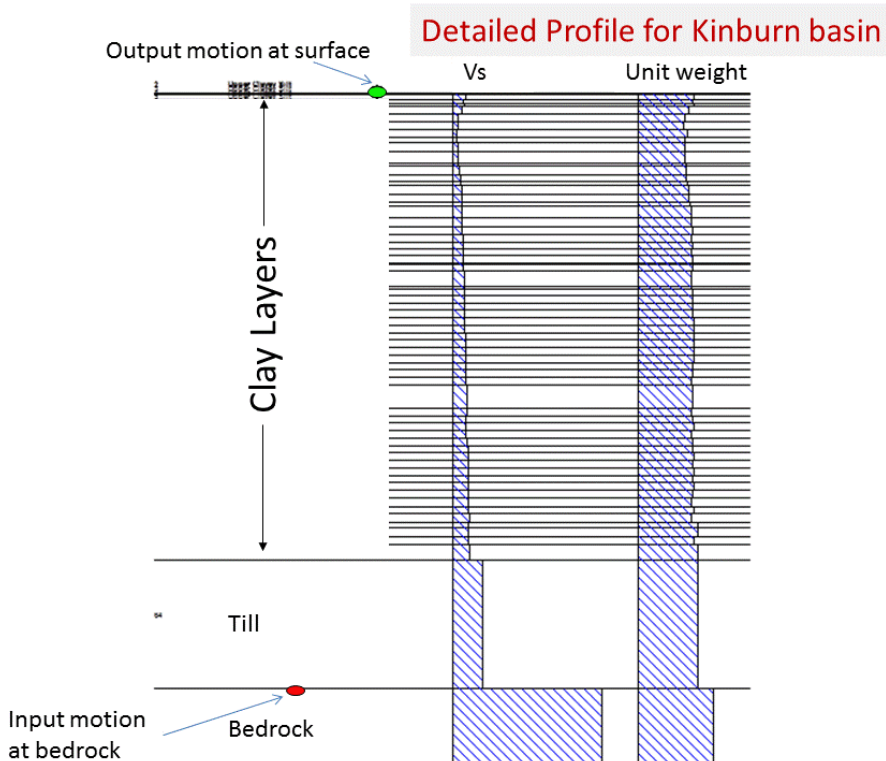


Fig. 5-2: Detailed profile as entered into Proshake of the Kinburn basin near the soft-soil site JSSS, using data from the borehole JSR-01 (Medioli et al. 2010) to estimate the depth, velocity and bulk unit weight of the soft-soil layers, and the mini-vibe section (Fig. 3-8, S3.3.3) as interpreted by Pugin et al. (2013) to estimate the depth of the till layer. Velocities for the bedrock and till layer were taken from averages found from samples of these layers throughout the Ottawa region (Hunter et al., 2010). Location of input motion at bedrock, and output on surface are shown.

The underlying bedrock is known to be Paleozoic (J. Hunter, pers. comm. 2012) as evidenced by the outcrop at the rock site, JSBS. Hence, for this profile, the average shear wave velocity found for Paleozoic Dolomite and Limestone in the Ottawa region was used: a velocity of $2890\text{ m/s} \pm 675\text{ m/s}$ (actual recordings ranging from 1172 m/s to 4786 m/s). And again, as there was no other information available on the γ_b of the rock, hence

we used the estimated value of 26.0kN/m^3 (see S5.2.1). See Fig. 5-2 for the detailed soil profile for the Kinburn soil site as it appears in Proshake.

5.3 Input motions

Proshake comes with strong motion recording samples that can be used as input (see Appendix C for file type descriptions) ground motion acceleration time series. Table 5-1 is a list of pre-included motions that were used for the tests described below (S 5.5). The table includes the basic information on the strong motion record as provided in Proshake, and additional information from <http://www.strongmotioncenter.org>. Note that all the strong motion records provided within the software are from Californian earthquakes, and are applied to the bedrock layer.

Table 5-1: Strong motion records available in Proshake that were used for testing various profiles, including the name of the seismic station, the date of the earthquake, the peak ground acceleration (PGA) in g's recorded at the site, and the approximate epicentral distance. Note that all the earthquakes and seismic stations are in California (* indicates a site known to be on rock).

	Motion	Seismic Station	Date of Eq	PGA (g)	Distance
1	M7.1 Loma Prieta	Gilroy1 *	1989/10/17	0.43	28.5 km
2	M7.2 Petrolia	Cape Mendocino*	1992/04/25	0.42	28.5 km
3	M6.7 Northridge	Topanga	1994/01/17	0.33	28.5 km
4	M7.1 Loma Prieta	Yerba Buena Isl.*	1989/10/17	0.07	28.5 km
5	M7.3 Kern County	Taft*	1952/07/21	0.19	28.5 km

Alternatively, we can input our own earthquake recordings into the software. To do this, we converted our velocity recordings to integer acceleration files, first removing instrument response using SAC (Seismic Analysis Code, developed by Lawrence Livermore National Laboratory and is copyrighted by the University of California distributed by IRIS: <http://ds.iris.edu/ds/nodes/dmc/software/downloads/>; see <http://ds.iris.edu/files/sac-manual/> for SAC manual). These files could then be entered directly using Proshake Utilities. See Appendix C for example of sac macros used to

convert the files to acceleration. Table 5-2 includes a list of all the local earthquake recordings used for the 1D ground motion modelling.

Table 5-2: Local earthquakes used in the 1D ground motion analysis. The table lists the town/city close to the earthquake, the Nuttli magnitude and the date of the event. All earthquakes are from the west Quebec seismic zone, except the La Malbaie event (Charlevoix region, ~400 km east).

	File name	Earthquake	Magnitude (m_N)	Date
1	AN36	L'Annonciation, QC	3.6	2012/01/22
2	BB36	Barry's Bay, ON	3.6	2013/10/20
3	BK41	Buckingham, QC	4.1	2011/09/18
4	DR35	Deep River, ON	3.5	2011/03/29
5	HN35	Huntington, QC	3.5	2011/08/24
6	HW42	Hawkesbury, ON	4.2	2012/11/06
7	HW43	Hawkesbury, ON	4.3	2011/03/16
8	LM44	La Malbaie, QC	4.4	2012/12/12
9	RG34	Rigaud, QC	3.4	2013/05/21
10	RL31	Rockland, ON	3.1	2012/09/22
11	SV37	Shawville, QC	3.7	2013/05/30
12	SV41	Shawville, QC	4.1	2013/05/17
13	SV52	Shawville, QC	5.2	2013/05/17
14	VB35	Val-des-Bois, QC	3.5	2013/01/16
15	VC45	Vercheres, QC	4.5	2012/10/10
16	VD32	Val-des-Bois, QC	3.2	2012/02/29
17	VD57	Val-des-Bois, QC	5.7	2010/06/23
18	WF35	Wakefield, QC	3.5	2011/07/21

5.4 Damping ratio and modulus reduction curves

To model the change in damping ratio and the shear modulus with change in stress, the damping ratio and modulus reduction curves as described in S5.1 were used. The damping ratio and modulus reduction change depending on the material properties, hence, a suitable modulus reduction curve and damping ratio must be chosen for each layer. Proshake provides several standard damping ratio and modulus reduction curves for rock, gravel, sand and clay. Note that the damping and modulus reduction curves tend

to be developed in pairs. When appropriate, Proshake will automatically choose the matching curve once one soil type is chosen. For example for clay, with the modulus reduction curve for Sun et al. (1988), PI=20-40 is chosen, the program will automatically assign the associated damping curve to be the Sun et al. (1988) , upper bound. Note, however, that the user could over-ride this selection and chose a different damping ratio. As these damping ratio and modulus reduction curves were generated together from similar datasets and were presumably intended by the authors to be used in conjunction with each other, we did not alter these pre-set values.

Linear “curves” are available, but as soil is not considered to behave linearly, we did not use this option. Note that in order to use the linear option a damping ratio % is required. Otherwise singularities occur at natural frequencies and this will lead to program execution errors (Proshake Manual). If the relation to strain was linear, the “curve” would just be a straight line.

A programming option is available to input custom damping ratio and modulus reduction curves. The predominant soft soil in our study area is a material deposited in the Champlain Sea known as Leda clay (see Ch. 3 for more details). Law et al. (1985) published a pair of damping ratio and modulus reduction curves for Leda clay at low to medium strains. These were added to Proshake and the outputs compared to those of the predefined damping ratio and modulus reduction curves. See Clay Damping ratio and modulus reduction curves below for more details.

Rock damping ratio and modulus reduction curves

Beginning with the basal rock layer in the model, there are two software parameter choices: the “Rock” curves defined by Schnabel et al. (1972); and the “Rock – Idriss” curves defined by Idriss (1990). There is no further information on our local rock types, hence both curves are tested for our model.

Gravel damping ratio and modulus reduction curves

Since the glacial till is a mix of sand, gravel, etc., we chose the modulus reduction and damping ratio curves that are associated with gravel (with similar V_s velocities as glacial till). These curves were defined by Seed et al. (1984) and are based on average behavior of 12-inch diameter cyclic triaxial tests on four different gravels. No curve is available specifically for till, and only the one “gravel” curve is available for this material in Proshake.

Sand damping ratio and modulus reduction curves

For the most part, our study basins are filled with fine grained silts and clays, which have a plasticity index. Hence, the sand damping ratio and modulus reduction curves would not be appropriate. However, the Lefavre profile does contain a few sand layers. For these sand layers there are two options: the damping ratio and modulus reduction curves defined by Seed and Idriss (1970) with “lower”, “average” and “upper” curves, or the sand curve by Idriss (1990). Note that for the Seed and Idriss (1970) curves, for our profile, we selected the Seed and Idriss “average” modulus reduction and damping ratio curves.

Clay damping ratio and modulus reduction curves

For clay, the available choices of curves are: Sun, Goesorkhi and Seed (1988); Seed and Sun (1989); Vucetic and Dobry (1991); and Ishibashi and Zhang (1993). Seed and Sun (1989) offer one set of damping ratio and modulus reduction curves for clay, whereas Sun et al. (1988) give a set of curves for varying plasticity indexes (PI). The modulus reduction curves for $PI < 5$ and $PI = 5-10$ are associated with the lower bound damping ratio curve. For the $PI=10-20$ modulus reduction curve there is an “average” damping ratio curve. And for $PI = 20-40$ there is an “upper” damping ratio curve. Presumably for the two higher PI modulus reduction curve options ($PI=40-80$ and $80+$), one would also use the upper damping ratio curve, although this is not automatically assigned.

The Vucetic and Dobry (1991) damping ratio and modulus reduction curves are based on work by Kokoshu (1980). They were examined the soil behavior that occurred during the 1985 Mexico City earthquake, and produced a family of damping ratio and modulus reduction curves for PI equal to 0, 15, 30, 50, 100 and 200. To apply the curves, the appropriate PI is selected for each layer, and Proshake linearly interpolates from the Vucetic and Dobry’s damping ratio and modulus reduction curves (Proshake manual).

The Ishibashi and Zhang (1993) damping ratio and modulus reduction curves are the only set which account for effective confining pressure; these values are computed assuming a pressure coefficient K_0 of 0.5 (Proshake manual). As with the Vucetic and Dobry curves, one assigns PI for the layers. Note that the Ishibashi-Zhang equations

predict $G/G_{\max} > 1$ at low strains, so in Proshake the value is set to 1.0 for these cases (Proshake manual).

Previous geotechnical work on the soils within the Ottawa region basins suggest the PI for Leda clay to be approximately 40, although there is a possibility that it is slightly lower than that (~ 20) at some sites (H. Crow, pers. comm. 2013). Hence, for the basins under study we do not use the Seed and Sun (1989) clay curves, but instead use either the Sun et al. (1988) modulus reduction curve with $PI = 40-80$ or with $PI = 20-40$, and we the upper bound damping ratio curve. We also use Ishibashi and Zhang's (1993) and Vucetic and Dobry's (1991) curves and set the PI to 40.

Note since Ishibashi and Zhang (1993) account for effective confining pressures, Ishibashi argues that it is the better curve for low-plasticity soils than Vucetic and Dobry's curves (Ishibashi, 1992). However, the Ishibashi-Zhang curves are not recommended for high plasticity soils (Proshake manual). Effective confining pressures have less of an effect on higher plasticity soils, and hence Vucetic and Dobry's curves may be more appropriate for the Leda clay at our sites with higher PI. Note that neither the study by Vucetic and Dobry (1991) nor the one by Ishibashi and Zhang (1993) included sensitive soil samples (Guerreiro et al., 2012). No reference could be found with regard to sensitivity for Sun et al.'s (1988) samples used, although it is highly probable they also did not use sensitive clay samples in their study.

Additionally, a Leda clay curve was created from the curve provided in Law et al. (1985), digitized by Dr. Hunter (NRCan, 2012), with one additional point at very low

strain as measured by H. Crow (NRCan, 2012). This partial curve has data only for strains below 0.2%. See Appendix C for the data for all the curves used. To compare the pair of Leda Clay curves to the other curves for clay, see Fig. 5-3. Currently there is research being conducted by the Civil Engineering department of Carleton University to define new curves for Leda Clay, but these curves were not yet available at the time of writing.

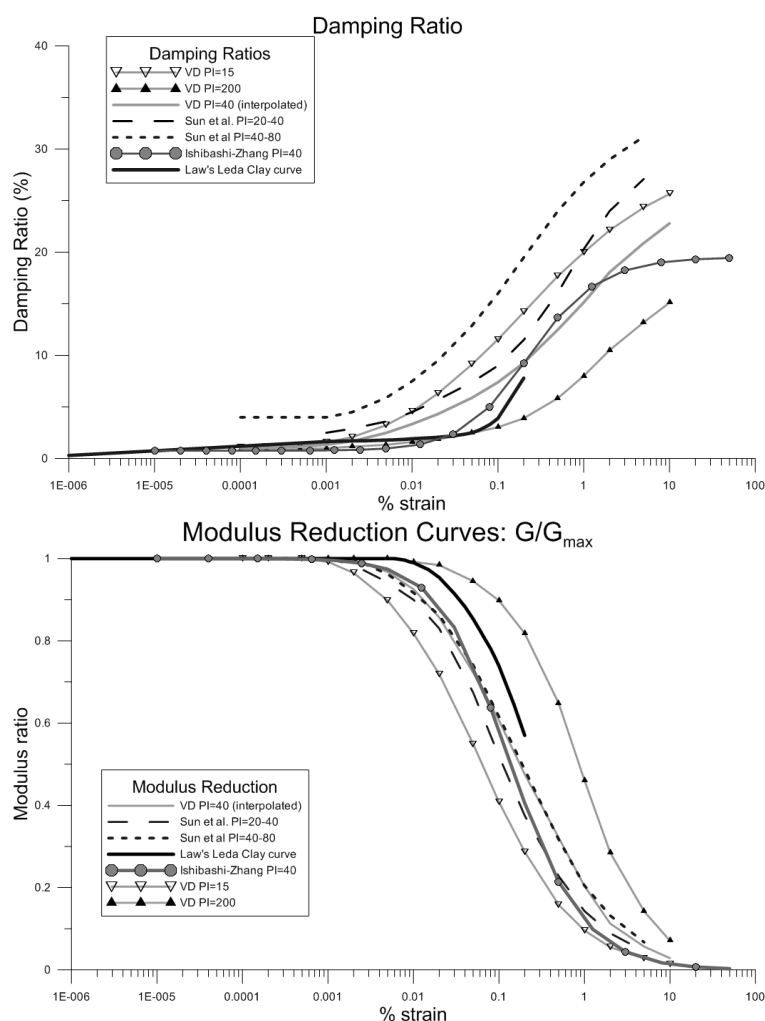


Fig. 5-3: Various relations of % damping ratio versus % strain for clays, including Vucetic-Dobry with plasticity index (PI) of 15, 40, and 200; Sun et al. for PI range of 20-40 and 40-80 with upper bound damping ratio; Ishibashi-Zhang with PI=40; and Law et al.'s (1985) damping ratio and modulus reduction curves for Leda clay.

5.5 Testing variable dependency and sensitivity

Although we were fortunate to have borehole information available from at or near to each of our basin sites, there are still many variables at the sites that might affect the outcome of the 1D modelling. From scientific point of view it is interesting to correlate the relative sensitivity of these variables with the model results. These variables are: the thickness (H), V_s , ρ (or γ_b) and the modulus reduction and damping ratio curves used for each layer.

Therefore, we have created a range of very basic, simple profiles to test the effects of each variable independently on the modelled ground motions and to determine any limitations. The input ground motions used for the tests were five of the Californian ground motions available in Proshake (see S5.3) as the actual predicted ground motions were not the purpose of these tests but rather the effects the change of a particular variable had on the results. Hence the transfer functions calculated for each test run were recorded and compared. The default setting for plotting the transfer functions in Proshake is 500 data points, with one data point every 0.1s, which is not adequate for capturing the peak amplifications (as noted in S4.2.1 with a similar issue in regards to the spectral ratios sample intervals). The plot settings were adjusted to 800 samples, with a data point at every 0.02s.

5.5.1 Test profiles

We began using two standard test profiles: the first being a two layer profile with homogeneous clay overlying bedrock; and secondly, a three layer profile with a layer of homogeneous layer of till added between the clay and bedrock (see Fig. 5-4). Note that for the purposes of the 1D ground motion modelling, all the layers are assumed by the program to be semi-infinite and flat-lying. Standard values used for the single clay layer model were: $V_s = 200\text{m/s}$; $\gamma_b = 17\text{kN/m}^3$; thickness of 97m. The V_s and γ_b are approximate averages from measured values and the thickness is that of the clay layer underneath the soft-soil seismograph site in the Kinburn basin. The Sun et al. (1998) modulus reduction curve for clay with $PI = 40-80$ and upper bound damping ratio curve were used to define the clay properties (as the plasticity index of the Leda Clay is generally assumed to be around 40 in the Ottawa region (H. Crow, pers. comm., 2013)).

The properties of the rock layer were: $V_s = 2700\text{m/s}$ and $\gamma_b = 26\text{kN/m}^3$. These values are based on average V_s found for bedrock in the Ottawa region from all bedrock types (Hunter et al., 2010), and the γ_b found from the measurements (averaged) at the Lefavre basin. The default curves used to define the properties of the bedrock layer are the “Rock” curves.

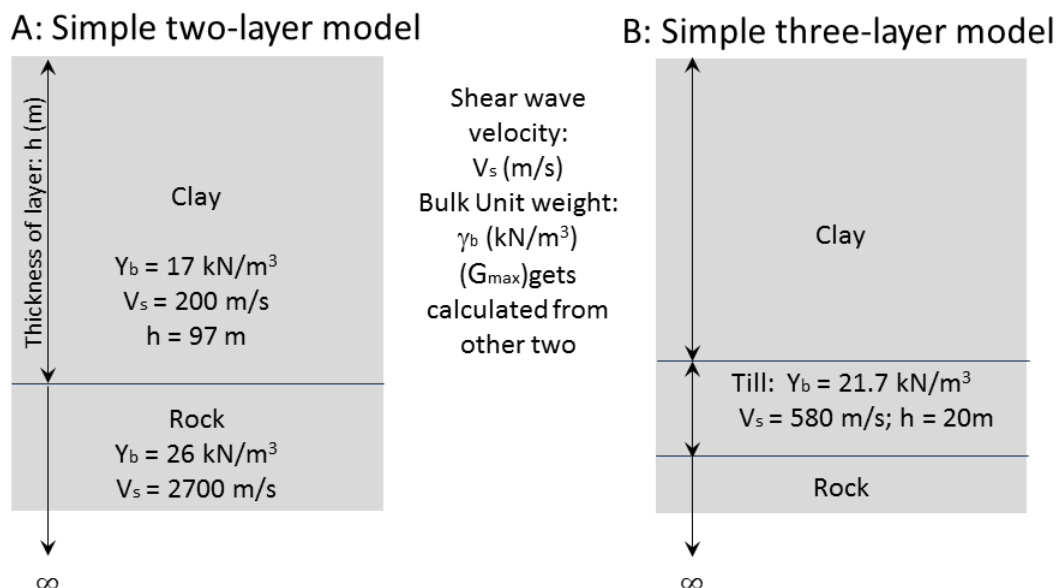


Fig. 5-4: Schematic showing the standard layout and values used for: A) the simple two layer model of clay over bedrock; and B) the simple three-layer model with clay overlying till and bedrock. These two profiles were used to test the sensitivity of the resulting transfer function to different variables.

For the three layer profile, the same standard properties were applied for the rock and clay layer. The till layer properties are assigned as follows: $V_s = 580 \text{ m/s}$, as taken from the average for the Ottawa region (Hunter et al., 2010); and $\gamma_b = 21.7 \text{ kN/m}^3$ as taken from the average of the measurements taken at the Lefaiivre basin from the till layers (see Appendix C for Lefaiivre data spreadsheet). The default thickness was chosen to be 20m, and the modulus reduction and damping curves used were the Gravel (Seed et al., 1984) curves in Proshake.

These standard values were used for all the test models, except for the variable being tested. For example, to see the effect of different values of V_s in clay, the γ_b , thickness and curves of our standard value for clay were used and only the clay V_s values altered between tests. The properties of the other layers were all from the standard model

described above. For each test, the resulting peaks in the transfer function were recorded (frequency and amplitude of peaks). These results can be seen in S.5.6 and Appendix C.

Although there are some sand layers present in the Lefaiivre basin, these are relatively thin compared to the overall profile and only present in the one basin. For the overall response of the basin they are not likely to have a large impact one way or the other on the overall response of the basin (although they may have very important implications in other ways, like potential for liquefaction). Hence they have not been included in our simple test models, and for our detailed profiles we used the measured or calculated properties of those layers, and for the curves we used the average Idriss (1990) sand curves.

Rock properties

For bedrock we began by changing the γ_b from the standard 26kN/m^3 , to a low of 24kN/m^3 , and a high of 28kN/m^3 . As we had very limited data as to what the range could be, these values are based on the measurements of the rock at the Lefaiivre basin, the general range for rock and quartz, as well as using the upper bound measurements from the till layer as a lower bound for the rock layer. The V_s range of 940 m/s to 4000 m/s with an average of 2700 m/s was based on the range of values found in the Ottawa region for bedrock (Hunter et al., 2010). Note that in reality measurements higher than 4000 m/s were found, but Proshake could not process any values higher than 4000 m/s for bedrock (see S5.7.3 to follow, in regards to the limitations of Proshake).

Till layer properties

Next we varied the properties of the till layer. Note that there is not much specific information for this layer at any of the sites and so this layer was assumed to be homogenous throughout. In any case, it is relatively thin as compared to the overlying soft-soil layer, being in the range of 0 to 35 m for the Ottawa region (Hunter et al., 2010) versus the 90+ m of soft sediments that we are profiling for each of the basins.

As there is only the one set of modulus reduction and damping curves available for gravel, the sand (Idriss, 1990) curves were used as a second set to test the effect of changing this property in the till layer. The γ_b was varied from 18 to 24kN/m³, as compared to the average value of 21.7kN/m³ (used for our standard model). This data is based on the measurements taken from the borehole within the Lefaivre basin.

For the Vs we used the information from Hunter et al. (2010) which has data from many till samples throughout the Ottawa region. The range of Vs values found are from 205 m/s to 931 m/s, with an average of 580 m/s, so these were the values we used for our tests. And finally, we checked for the effect of the till layer thickness, varying it from 0 to 40 m while keeping the clay layer constant at 97 m. Note that the maximum thickness for this layer found in the Ottawa region thus far is 35 m (Hunter et al., 2010). We did attempt to test thicker till layers, but Proshake would not process these (see S5.7.3 to follow, in regards to the limitations of Proshake).

Also tested was the variation in the thickness of the till with a constant total profile thickness of the profile constant – this was done by reducing the clay layer

thickness by the same amount as the till was increased. For this test we used the standard 97 m of clay with 20 m of till, then 77 m of clay and 40 m of till, 57 m of clay and 60 m of till and finally 37 m of clay with 80 m of till. Note that this last test is not very representative of our basins, since there is commonly a higher clay-to-till ratio, but these examples should highlight the importance of this ratio at other sites in Champlain Sea deposits, and the change in ground motion results.

Clay layer properties

The most detailed geotechnical information available is that of the clay layer. For γ_b , we tested values from 12.2kN/m³ to 19.3kN/m³. The average Leda Clay value was approximated to be 17kN/m³. The minimum and maximum values were chosen based on histograms of observed borehole data. This layer is much thicker than the till in all three of our profiles, and hence, probably has more of an effect on the resulting ground motions.

The average V_s of clay in this region is commonly 180 m/s or less (Hunter et al., 2010), but the lowest value set by Proshake was 190 m/s. We set our range from 190 m/s to 600 m/s with the maximum set much higher than measured anywhere in Champlain Sea sediments yet might be found in older Pleistocene fine grain units. Our standard V_s was set to 200m/s – this was estimated from Fig. 3-8 in S3.1, which shows a range of data from the Ottawa region for Leda clay, with most of the data being at or less than 200 m/s, even with depth. Again, these values were informed by the data available, but modified due to limitations. An exaggerated high-end value of V_s of 600 m/s was used (instead of a more realistic 416m/s, which was the maximum V_s readying for clay in the

boreholes associated with our basins) to highlight any differences in outcomes, as there was loss of range on the lower end.

All previous model profiles assume a homogeneous layer. In practice, however, the clay is not one homogenous layer, but rather V_s commonly increases with depth (except for near surface over-consolidation). At our basin sites, we do have some geophysical data yielding V_s information with depth from in-situ borehole data as well as surface shear wave refraction and reflection measurements. However, borehole data is not generally available down to bedrock near a site of interest, so it would be useful to see if a generic V_s -to-depth relation would be adequate to model the ground motion at a basin where perhaps only depth of the clay is known. For this we will use the relation described in S4.2.5, fitting Ottawa V_s versus depth for Leda clay to a power law (J. Hunter, pers. comm., 2016):

$$V_s = 66 \times Z^{0.38} \quad \dots \text{ [Eqn 5.9]}$$

where V_s is the shear wave velocity (m/s) of the Leda clay, and Z is the depth (m).

Clay typically is over-consolidated near the surface, forming a firm crust with higher V_s (S 3.1). This can be seen in Fig. 3-8 (S 3.1), where the V_s values found within the top 5 to 10 metres are more scattered, sometimes with values as high as 500 m/s, but with most values between 100 m/s to 240 m/s. Hence, a model test is done with a “crust” of 6 m clay, with varying values of V_s (200 and 600 m/s), to examine the effect on the overall results. Below 6 m depth the Eqn 5.9 is used to define the V_s of the clay layers

with depth. All other parameters remain the same. Finally, the results from the above model tests are compared to that of the multilayered profile, modelled from the actual measurements taken from the boreholes.

For clay, there are several options from the literature for modulus reduction and damping ratio curves. Furthermore, most of these are series of curves based on plasticity index (PI). We have good indication that the PI of the Leda clay at our sites is likely around 40, although there is some indications that values as low as 20 may occur in some areas around Ottawa (H. Crow, pers. comm., 2013). Hence, this yields a further variable whose effect on the results needs to be investigated.

The pairs of curves were introduced in S5.4, but there is little from their basic description that would allow us to decide which one is most appropriate for the basin sites. All the damping ratio and modulus reduction curves provided within Proshake seem to be widely used in various regions in the world. Law et al.'s (1985) curves are based solely on Leda clay samples from the Ottawa-Montreal region. However, these curves are only developed for low strains. Carleton University, Laval University and University of Waterloo in collaboration with GSC are doing work on developing more comprehensive curves for this material, but the results were not available to the author at the time of writing.

We chose to test all the various modulus reduction and damping ratio curves available for clay in Proshake, using the standard simple profile: Seed and Sun (1989)

with Idriss (1990), Ishibashi-Zhang's (1993) and Vucetic-Dobry's curves (1991) with $PI = 40$, and the Sun et al. curves (1988) with $PI=40-80$ and "Upper Bound" curve. Then the tests were run again using the detailed profile. The detailed profile was also used to test the curves from Law et al. (1985) for Leda clay.

Furthermore, we also tested the effect of changing the PI using Vucetic-Dobry's curves (1991) for which Proshake interpolates from a set of curves, and the Sun et al. curves (1988) for which the user chooses from a set of curves for defined ranges of PI . Note that the Leda clay curves from Law et al. (1985) do not have a PI parameter.

5.6 Input waveforms

One final variable that may affect the outcome of the 1D modelling is the input waveform. For testing the basic effects of the above profiles, we have used the available Californian ground motions as mentioned in S5.3. Five ground motions were included to ensure we were getting a reasonable average. And always the same five earthquakes were used so as not to skew the results due to different inputs.

However, for the final full profiles, the outputs using the Californian earthquakes are compared with the outputs using the data from local earthquakes. This helped us measure the importance of using earthquakes from the region of interest, or whether any generic earthquake data is sufficient.

5.7 Results

From all the data we had available, and the most appropriate estimates for any information we did not have, we came up with a detailed profile in S5.2 for each of the basins. Using these detailed profiles, we ran Proshake to determine the expected difference in ground motion between the rock and soil sites. This was then compared to the actual output that was recorded on the sites.

Some of the tests performed using the simple profiles were repeated with the detailed profile, and vice versa. The results, although shifted from the simple profile results, exhibit the same effects from the changing variables. So even though the actual frequencies and amplifications were different due to the different profiles, the effects of changing a particular parameter were similar regardless (i.e. shift of peaks to higher/lower frequencies; increase/decrease of amplification). See Appendix C for the full table of average amplification values found for each tests, as well as the maximum and minimum values found for individual earthquakes.

5.7.1 Test profiles

Rock

The results for the tests run varying the parameters of the bedrock are shown in Fig. 5-5 to 5-7, and Table 5-3 shows the modelling results versus the values calculated using the simple 1D equations for amplification due to impedance and resonance, and for the fundamental frequency and harmonics. As none of the changes to γ_b , V_s or the modulus reduction and damping curves in bedrock produced noticeable changes in the

resulting transfer functions that were modelled for any of the particular earthquake, and or in the average overall, there is only one line in Table 5-3 for the modelled results. Note that the standard values used in Fig. 5-4A are used for both the modelling and in the 1D equations for Table 5-3.

Table 5-3: Fundamental frequencies and amplifications determined through 1D modelling using a simple two-layer profile (clay over rock) versus the values calculated using the Eqn 2.5 for determining the harmonic frequencies and Eqn 2.6 for resonance amplification, A_{res} . Standard values are used for both: $H=97m$, V_s and γ_b for rock are $2700m/s$ and $26kN/m^3$; V_s and γ_b for clay are $200m/s$ and $17kN/m^3$.

	Amplification		f_0	Harmonics: $f_n = V_s/(4H) * (1+2n)$		
	A_{imp}	A_{res}	$V_s/(4H)$	1st	2nd	3rd
Eqns	4.5	20.6	0.51	1.5	2.6	3.6
Modelled	0.5		4.2	1.4	2.3	-

Transfer functions for 1D test profiles

Effects of different bedrock properties

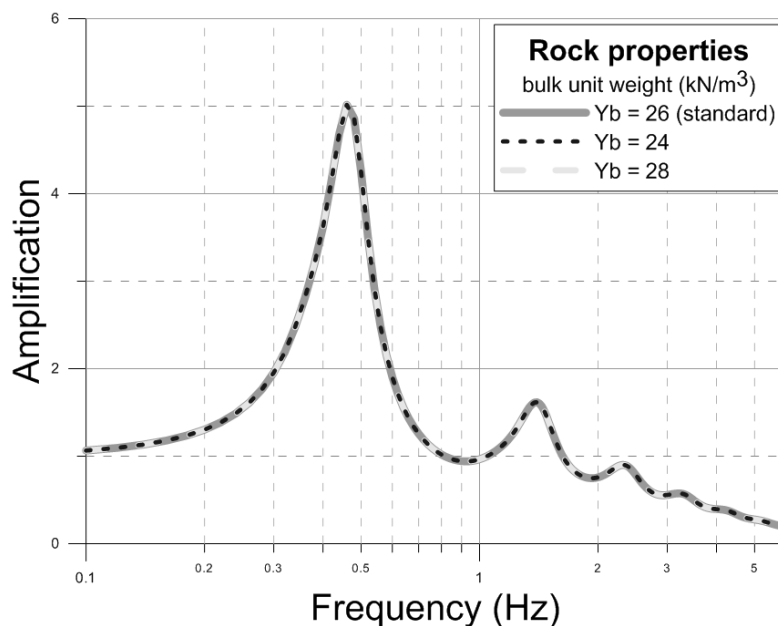


Fig. 5-5: Transfer functions as calculated with Proshake using the simple 2-layer profile (Fig. 5-4 A) with standard values, changing only the bulk unit weight of the rock layer from the standard value of $26 kN/m^3$ to $24 kN/m^3$ and $28 kN/m^3$.

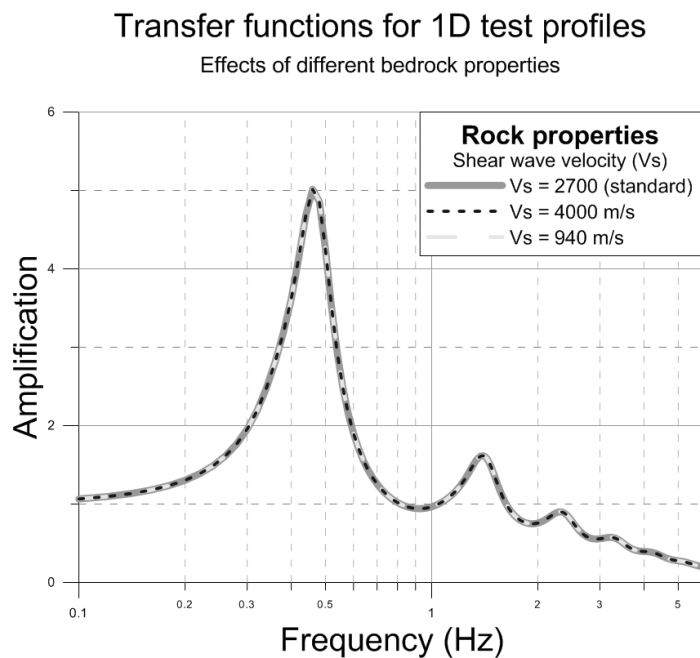


Fig. 5-6: Transfer functions as calculated with Proshake using the simple 2-layer profile (Fig. 5-4 A) with standard values, changing only the V_s of the rock layer from the standard value of 2700 m/s to 940 m/s and 4000 m/s.

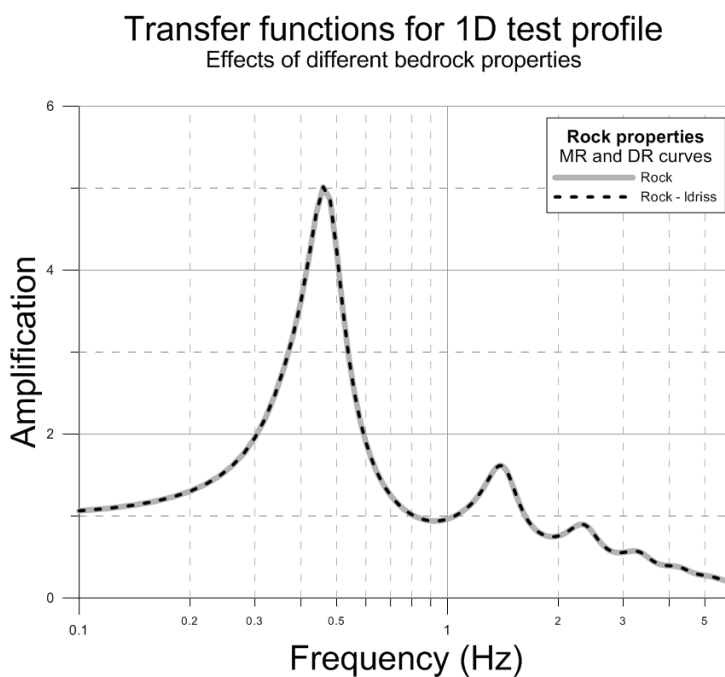


Fig. 5-7: Transfer functions as calculated with Proshake using the simple 2-layer profile (Fig. 5-4 A) with standard values, changing only the modulus reduction and damping curves that define the rock layer.

Till

The average results from all the earthquakes showed that the changing values of γ_b of the till layer, from a minimum of 17kN/m^3 and the maximum of 24kN/m^3 , showed very little effect on the final results (see Fig. 5-8). There was relatively little change in amplification except at the third and higher harmonics, with a slight decrease of less than 0.1 in amplification for the lower γ_b . No shift was seen in location of the peaks. The results from these tests are compared with the results testing the other till variables in Table 5-4.

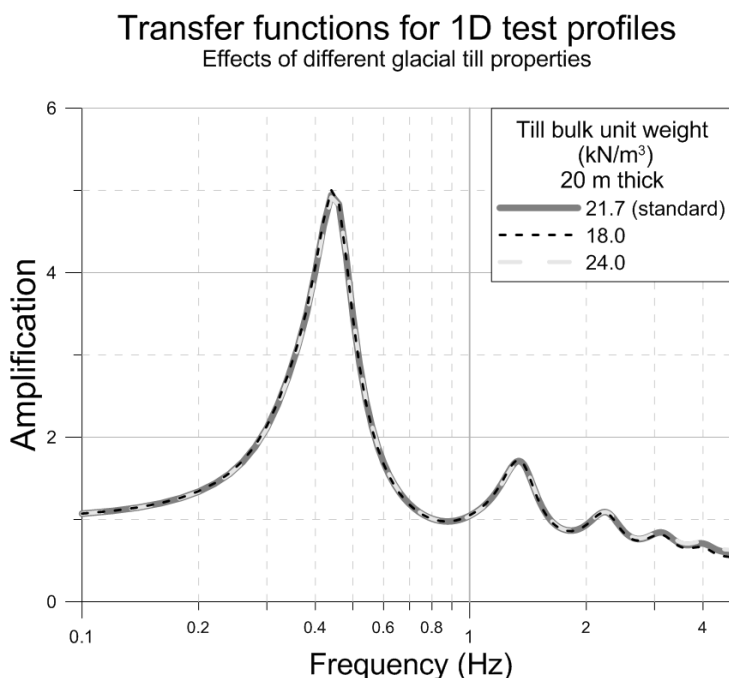


Fig. 5-8: Transfer functions as calculated with Proshake using the simple 3-layer profile (Fig. 5-4 B) with standard values, changing only the bulk unit weight of the till layer from the standard value of 21.7kN/m^3 to 18kN/m^3 and 24kN/m^3 . Vs of till was set to 580 m/s , and a thickness of 20m was used.

The higher Vs of the till layer, however, slightly shifted the location at which the peaks occurred towards higher frequencies (see Fig. 5-9). At the lower Vs for till, the peaks were shifted significantly to lower frequencies and the amplitudes of the peaks

were also decreased. To examine this phenomenon more closely, several additional, intermediate V_s values were chosen. These showed that within the range of the average V_s and higher, there were only minor differences in the resulting transfer functions. But as the value of V_s for till was decreased below the average of 580 m/s, the data shifted more towards lower frequency content. As the V_s value of the till layer approached that of the clay layer, an overall decreased amplification was noted.

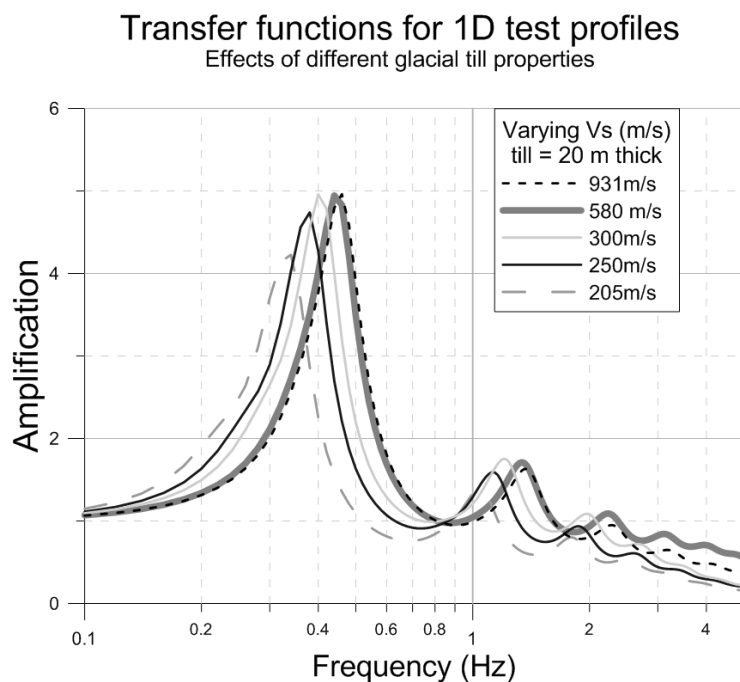


Fig. 5-9: Transfer functions as calculated with Proshake using the simple 3-layer profile (Fig. 5-4 B) with standard values, changing only the V_s of the till layer from the standard value of 580 m/s to values ranging from 205 m/s and 931 m/s.

A change in the modulus reduction and damping ratio curves of the till layer from “gravel” as defined by Seed et al. (1984) to “sand” (Idriss, 1990) showed equally little effect (see Fig. 5-10). There appears to be a very slight shift towards higher frequency for the sand curve, and at higher harmonics amplification of the sand curve is definitely less than the gravel curve; overall, these shifts are all very minor.

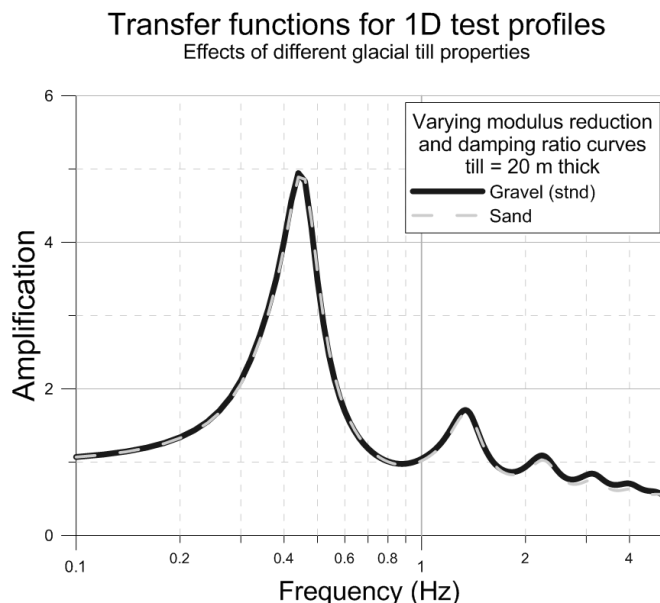


Fig. 5-10: Transfer functions as calculated with Proshake using the simple 3-layer profile (Fig. 5-4 B) with standard values, changing only the choice of modulus reduction and damping curves of the till layer from “Gravel” (Seed et al., 1984) to “Sand” (Idriss, 1990).

In our initial tests on variation of till thickness, we maintained the thickness of clay layer constant at 97 m and only varied the till layer thickness between 0 m and 40 m. Values greater than 40 m could not be processed by the ground motion analysis program (for additional comments see S5.7.3 with regard to Proshake limitations). From Hunter et al. (2010), the thickness of glacial till has not been found to exceed 35 m in the Ottawa region, so values as high as 40 m would adequately cover most site scenarios.

We found that in general the variation in till thickness did not make much amplitude difference in the fundamental peak amplification with only a slight decrease in frequency (~ 0.1 Hz) with increased thickness, and minimal increase in amplification (~ 0.4 times) for thickness variations between 0 m and 40 m (see Fig. 5-11). However, amplification variation effects are greater for the 1st harmonic peak, and even more so for the 2nd harmonic, but these peaks have much less amplification overall as compared to

the fundamental peak (the curves become less distinct for higher harmonics, and amplification approaches 1 after the 2nd harmonic). Note that this effect on the secondary peaks is only significant with till layers thicker than 20 m.

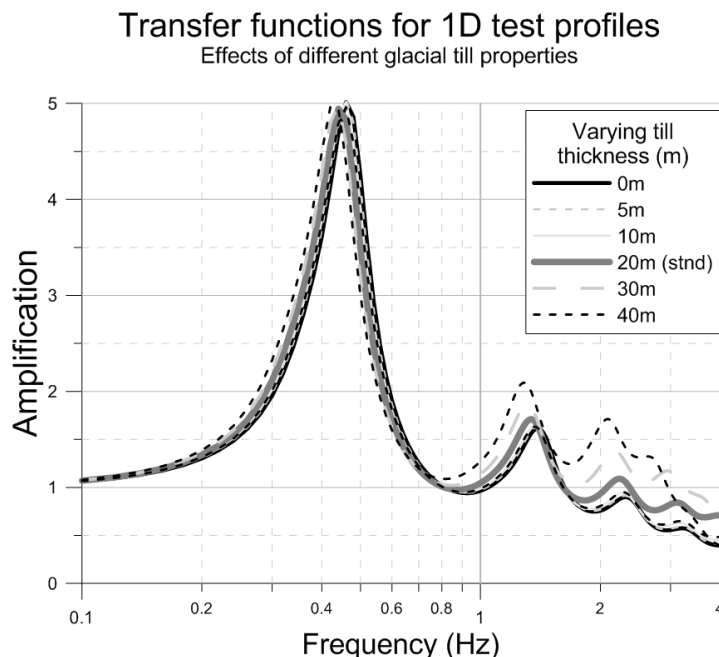


Fig. 5-11: Transfer functions as calculated with Proshake using the simple 3-layer profile (Fig. 5-4 B) with standard values, changing only the thickness of the till layer 0 m to 40 m.

We also tested the variation in the ratio of till thickness to clay thickness. The overall thickness of overburden was maintained constant, and the thickness of the clay was decreased as the till layer thickness increased in the models. As expected, this made a significant difference in amplification, with the fundamental frequency varying from around 0.44 Hz with a peak amplification of 4.9 for 97 m of clay with 20 m of till, to approximately 0.80 Hz and 7.2 times amplification for a 37 to 80 clay-to-till ratio of 37:80. See Fig. 5-12. Note that the amplification appears to significantly change as the ratio reaches about half till to half clay.

Transfer functions for 1D test profiles
Effects of different glacial till properties

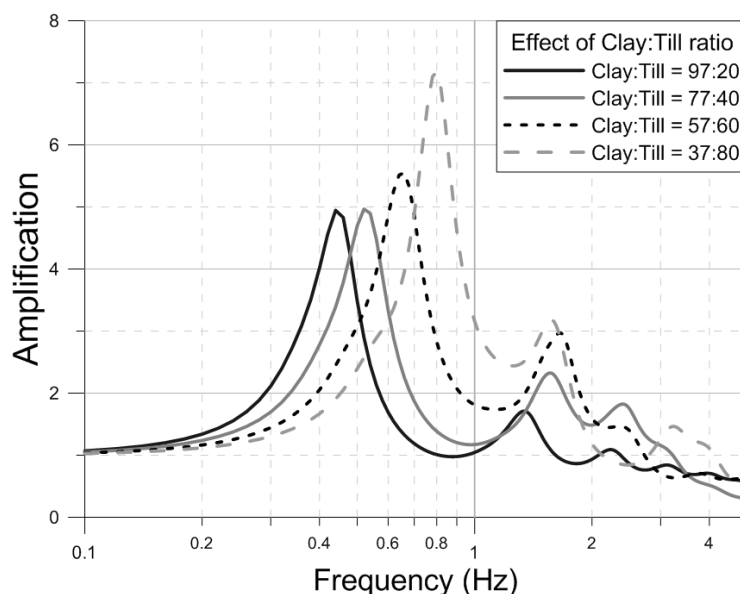


Fig. 5-12: Transfer functions as calculated with Proshake using the simple 3-layer profile (Fig. 5-4 B) with standard values, changing only the ratio of the clay and till layer thicknesses, while keeping the thickness of the overall profile the same.

Table 5-4: Results for the till layer tests using a simple 3-layer model as seen in Fig. 5-4B, varying the till thickness, V_s , γ_b , modulus reduction and damping ratio curves, and ratio of till:clay. Standard values used are a thickness of 20m of till, $V_s=580\text{m/s}$, $\gamma_b=17\text{kN/m}^3$, and the curves for gravel.

Till properties		f0		1st		2nd	
		amplif	freq	amplif	freq	amplif	freq
V_s	580	4.9	0.44	1.7	1.3	1.1	2.1
	205	4.2	0.34	1.4	1.1	<1	
	931	5.0	0.46	1.6	1.4	<1	
γ_b	21.7	4.9	0.44	1.7	1.3	1.1	2.2
MR/DR = sand		4.9	0.44	1.7	1.3	1.1	2.1
thickness	0m	5.0	0.46	1.6	1.4	<1	
	5m	5.0	0.46	1.6	1.4	<1	
	10m	5.0	0.46	1.6	1.4	<1	
	20m	4.9	0.44	1.7	1.3	1.1	2.1
	30m	5.0	0.44	1.9	1.3	1.4	2.2
	40m	4.3	0.50	2.1	1.3	1.7	2.2
clay:till	97 to 20	4.9	0.44	1.7	1.3	1.1	2.1
	77 to 40	5.0	0.52	2.3	1.5	1.8	2.4
	57 to 60	5.6	0.65	2.3	1.6	1.6	2.4
	37 to 80	7.2	0.80	3.2	1.7	1.5	3.3

Leda clay

For the clay, as with the rock and till, the value assigned to the γ_b of this layer had little to no effect on the resulting transfer functions (see Fig. 5-13). Increasing the thickness of the clay decreased the fundamental frequency slightly, while there was a slight increase in amplification (see Fig. 5-14).

For the simple 2D profile, the differences in amplification and frequency between the lower and higher values of V_s for clay were very pronounced (see Fig. 5-15). With the increased velocity there was a very noticeable shift in frequency, with the f_0 shifting from 0.44 HZ for the low V_s , up to 1.47 Hz for the high V_s (which is close to where the 1st harmonic was located for the lower V_s). The amplification increased from 5 to 7 times. This increase in amplification and shift in frequency was also noted in the higher harmonics.

Table 5-5 summarized these results for the simple 2-layer profiles using the standard values as shown in Fig. 5-4A, except for the clay-variable being tested. As can be seen, for the simple 2-layer model, the V_s of the clay affects the modelled amplification the most, while both the V_s and the depth of clay will both have an effect on the frequency.

Transfer functions for 1D test profiles Effects of varying Leda Clay properties

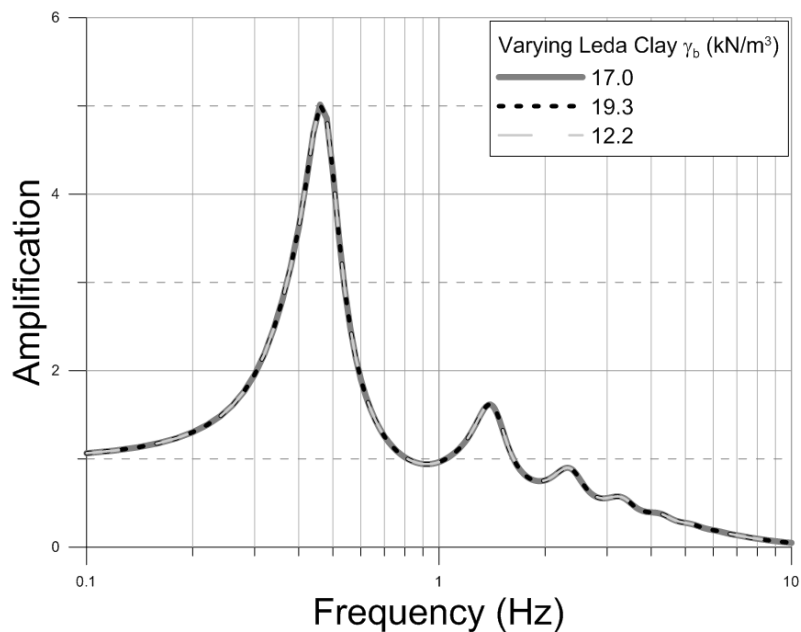


Fig. 5-13: Transfer functions as calculated with Proshake using the simple 2-layer profile (Fig. 5-4 A) with standard values, changing only the bulk unit weight of the clay for three models: 12.2, 17.0, and 19.3 kN/m³.

Transfer functions for 1D test profiles Effects of varying Leda Clay properties

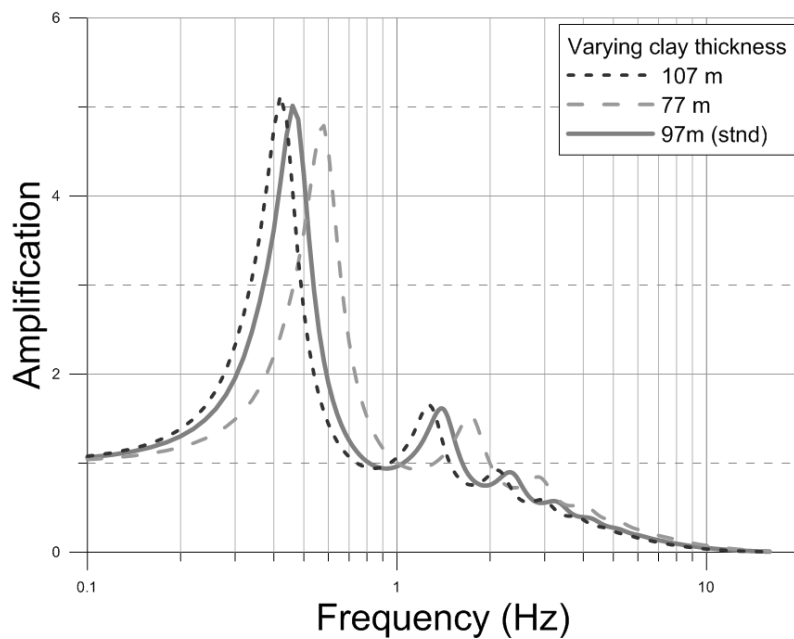


Fig. 5-14: Transfer functions as calculated with Proshake using simple 2-layer profile (see Fig. 5-4 A) with standard values, changing the thickness of the clay layer for three models: 77, 97, and 107 m.

Transfer functions of 1D test profiles

Effects of varying Leda Clay properties: simple 2-layer model

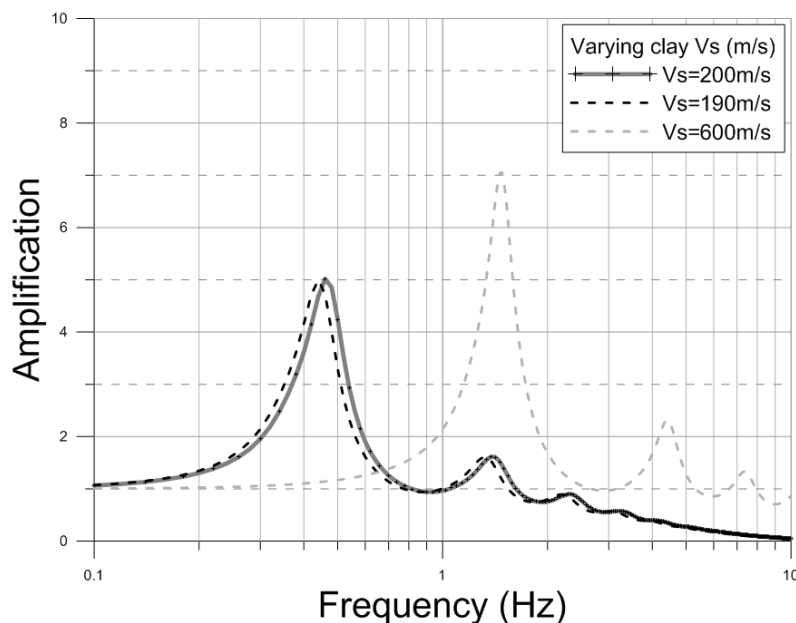


Fig. 5-15: Transfer functions as calculated with Proshake – comparing the results from the simple 2-layer profile (Fig. 5-4 A) with varying V_s .

Table 5-5: Results for the clay layer tests using a simple 2-layer model as seen in Fig. 5-4A, varying the clay γ_b , V_s and thickness. Standard values used for clay: $\gamma_b=17\text{kN/m}^3$; $V_s=200\text{m/s}$; and $H=97\text{m}$. Using the modulus reduction curve of Sun et al. (1988) with PI of 40-80 and the damping ratio “Upper bound” curve.

Variable		Average fo		1st		2nd	
		amplif	freq	amplif	freq	amplif	freq
γ_b (kN/m^3)	17	5.0	0.45	1.6	1.4	<1	
	12.2	5.0	0.45	1.6	1.4	<1	
	19.3	5.0	0.45	1.6	1.4	<1	
V_s (m/s)	200	5.0	0.45	1.6	1.4	<1	
	190	5.0	0.44	1.6	1.3	<1	
	600	7.1	1.47	2.3	4.4	1.4	7.4
H (m)	107	5.1	0.42	1.7	1.3	<1	
	77	4.8	0.58	1.5	1.7	<1	

Since the velocity profile of the clay layer tends to increase with depth, another test was done using the power equation Eqn 5.9 found in Ch 4 (see S4.2.5, Fig. 4-14).

The addition of a 6 m crust of either medium or high V_s clay did not alter the transfer

function results appreciably around the fundamental frequency, although the presence of the crust does seem to lower the amplification of the higher harmonics. These results are compared with the simple two-layer model results using the standard values, and the results using the profile created from the Kinburn borehole data (see Fig. 5-16), all using the same standard values for the bedrock and till (except for in the 2-layer model where no till is present). The modulus reduction curve used for the clay layers in all the profiles is Sun et al. (1988) for PI of 40 to 80 with the “upper bound” damping ratio curve.

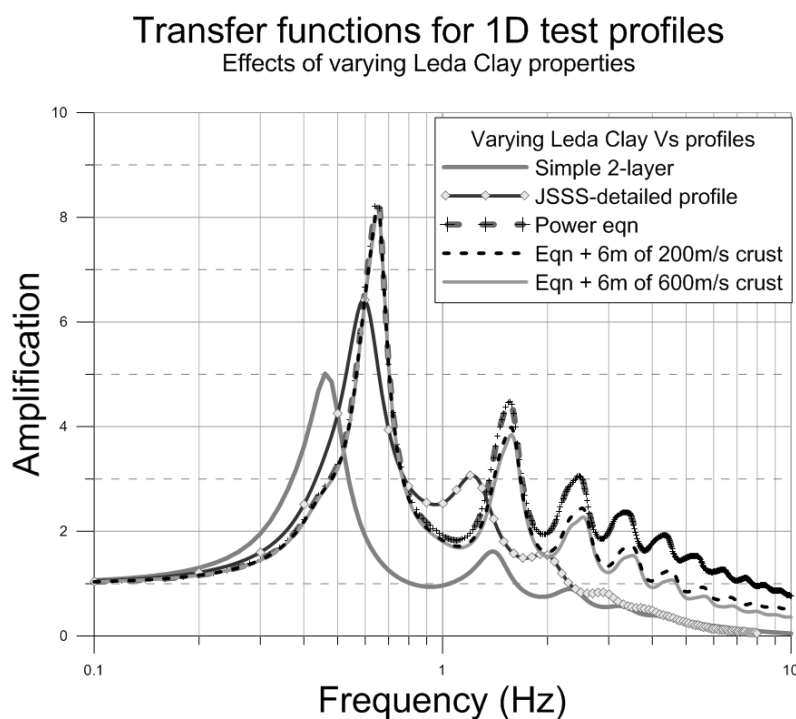


Fig. 5-16: Transfer functions as calculated with Proshake – comparing the results from the simple 2-layer profile (Fig. 5-4 A) with the results for increasing Vs with depth for the clay layer according to Eqn 5.9 power law, including 2 tests with a crust of 6 m with higher Vs.

Fig. 5-16, shows that for the two-layer model with a constant Vs of 200 m/s for the clay layer the amplification at 50 and fundamental peak at 0.45Hz is much lower than that from the detailed profile, which has a fundamental peak at 0.59 Hz with an

amplification of 6.4. On the other hand, the results using the power equation that has increasing V_s with depth, both the amplification at just above 8 and the f_0 peak at 0.66Hz are much higher than that of the detailed profile. These results are summarized in Table 5-6 below:

Table 5-6: Results comparing the simple 2-layer model with the detailed profile built from the Kinburn borehole data, and the varying V_s of clay using the power equation, with and without a 6m crust of higher V_s (200 and 600m/s).

	Average f_0		1st		2nd	
	amplif	freq	amplif	freq	amplif	freq
2-layer $V_s=200$	5.0	0.45	1.6	1.4	<1	
Power Eqn, no crust	8.2	0.65	4.5	1.6	3.1	2.5
6m crust $V_s = 200$	8.1	0.66	4.0	1.6	2.4	2.5
6m crust $V_s = 600$	8.1	0.66	3.9	1.6	2.3	2.5
Detailed profile	6.4	0.59	3.1	1.2	1.5	2.0

Modulus reduction and damping ratio curves for clay

The results from the tests using the simple profile show that each of the various sets of curves produce reasonably consistent transfer functions on average in terms of basic shape and of the location of the fundamental frequency and higher harmonics. The fundamental frequency is always the largest peak, and most curves produce only one or two higher harmonics above 1.0 times amplification, with the subsequent higher frequency low amplification peaks appearing indistinct.

The range for the fundamental frequency is 0.46 to 5.0 Hz, and that of the first harmonic is 1.3 to 1.5 Hz. However, when different modulus reduction and damping ratio curves were used, much more variation in the average modelled amplification was seen, from a low of 5 times amplification for the Sun et al. curves, to almost 20 times

amplification for Ishibashi-Zhang curves. See Fig. 5-17 and Table 5-7 for a summary of the results.

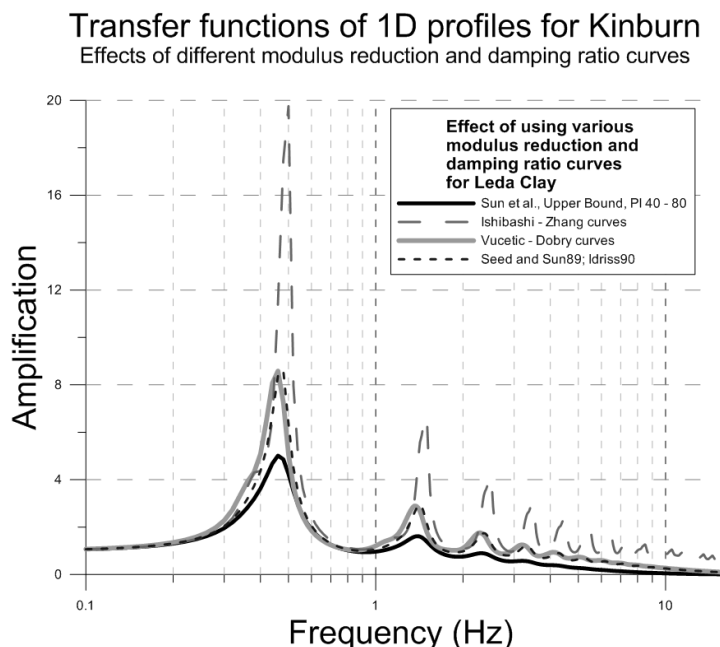


Fig. 5-17: Transfer functions as calculated with Proshake – comparing the results from the various modulus reduction and damping ratio curves as provided in Proshake. Using PI = 40 for Vucetic-Dobry and Ishibashi-Zhang curves.

Table 5-7: Results comparing the various modulus reduction (MR) and damping ratio (DR) curves for clay for simple 2-layer model. IZ = Ishibashi and Zhang (1993); VD = Vucetic and Dobry (1991); Sun = Sun et al. (1988); Seed/Sun = Seed and Sun (1989); and Idriss = Idriss (1990). The plasticity index (PI) was set to 40 (or equivalent) for the curves where that option is available.

Clay MR & DR Curves	Average f_0		1st		2nd	
	amplif	freq	amplif	freq	amplif	freq
IZ 40 IZ	19.8	0.50	6.6	1.5	4.1	2.5
VD 40 VD	8.6	0.46	2.9	1.4	1.8	2.3
Sun 40-80 clay upper	5.0	0.46	1.5	1.4	<1	
Seed/Sun Idriss90	8.6	0.48	2.9	1.4	1.7	2.4

For the above tests, we've been plotting the average transfer functions calculated in Proshake using the 5 Californian ground motions as described in S5.3, Table 5-1 with a simple two-layer profile as described in Fig. 5-4. Since the results show, however, that

the modelled outcomes depend mostly on the V_s profile used for the clay, we now examine the results obtained using the detailed profile (obtained from the borehole data at Kinburn) for the various modulus reduction and damping curves in detail, not just for the average ground motion, but also for each of the individual motions.

On examination of the results from the individual test ground motions it is noted that in general there is a range of frequencies for the fundamental peak of approximately 0.2 Hz from the lowest to the highest for all four of the modulus reduction and damping ratio curves. This is true for the Sun et al. (Fig. 5-18) and the Vucetic-Dobry (Fig. 5-19) curves even when the plasticity index was changed.

The amplification for each individual earthquake, however, can vary widely for each of the relations. The Sun et al. curves give the lowest modelled amplification, with a range of 3.5 to 7.2 times, whereas the Vucetic-Dobry curves give the highest amplification (apart from the Ishibashi-Zhang) with a range from 6.9 to 14.0 times, with the Seed and Sun/Idriss being mid-range. Note that all three of these curves approximately double from the lowest value to their highest.

The Ishibashi-Zhang (Fig. 5-20) transfer functions are by far the most varied, with amplifications as low as 9.4 times, all the way up to 50+ times, depending on the ground motion used. This set of curves also produces the highest number of higher harmonics above an amplification of 1.0 (see Fig. 5-20).

The results for the modelled transfer function using the various modulus reduction and damping ratio curves are given in Table 5-8. The models are based on the detailed

Kinburn profile and use the five Californian ground motions listed in Table 5-1. Note that the results from the earthquakes giving the lowest and the highest amplifications are given, as well as the average results for each set of curves. Fig. 5-18 to 5-20 show the results for all 5 ground motions as well as the average transfer function for the Sun et al., Vucetic-Dobry and Ishibashi-Zhang curves respectively.

Table 5-8: Results comparing the various MR and DR curves for clay for simple 2-layer model. IZ = Ishibashi and Zhang (1993); VD = Vucetic and Dobry (1991); Sun = Sun et al. (1988); Seed/Sun = Seed and Sun (1989); and Idriss = Idriss (1990). The plasticity index (PI) was set to 40 (or equivalent) for the curves where that option is available. The earthquake number refers to the Californian ground motion used and is listed in Table 5-1.

Clay MR & DR Curves		Eq with lowest amplif			Eq with highest amplif			Average fo	
		amplif	freq	eq	amplif	freq	eq	amplif	freq
IZ 40	IZ	9.4	0.38	2	51.0	0.50	3	19.8	0.50
VD 40	VD	6.9	0.36	2	14.0	0.48	3	8.6	0.46
Sun 40-80	upper	3.5	0.37	2	7.2	0.48	3	5.0	0.46
Seed-Sun	Idriss	5.0	0.38	2	14.5	0.48	3	8.6	0.48

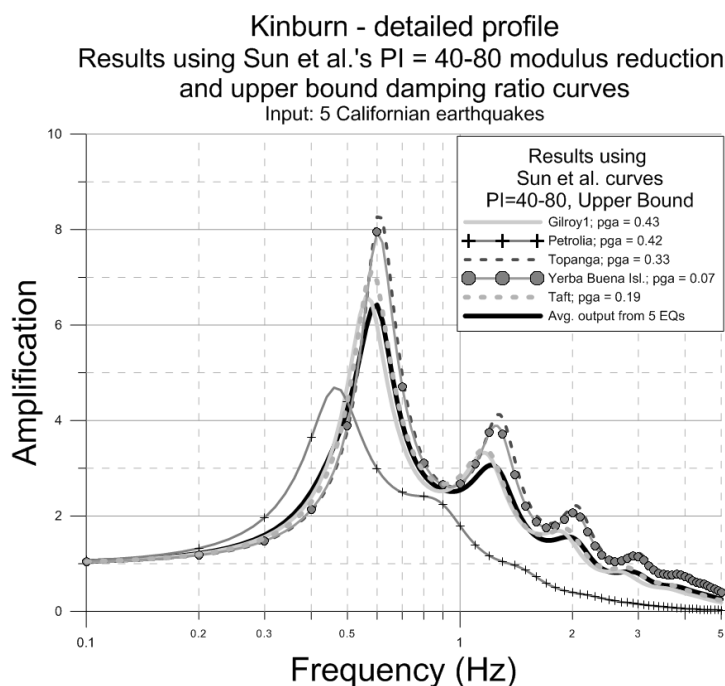


Fig. 5-18: Transfer functions as calculated with Proshake for 5 Californian strong motion recordings, as well as their average. Using Sun et al.'s modulus reduction curve for PI range of 40-80, with the upper bound damping ratio curve.

Kinburn - detailed profile
 Results using Vucetic & Dobry's modulus reduction and damping ratio curves
 Input: 5 Californian earthquakes

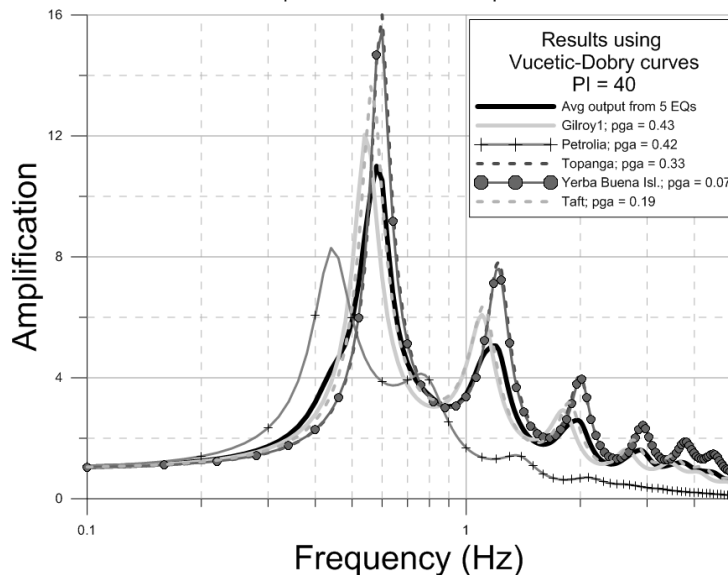


Fig. 5-19: Transfer functions as calculated with Proshake for 5 Californian strong motion recordings, as well as their average. Using Vucetic-Dobry's modulus reduction and damping ratio curves for PI of 40.

Kinburn - detailed profile
 Results using Ishibashi-Zhang's modulus reduction and damping ratio curves
 Input: 5 Californian earthquakes

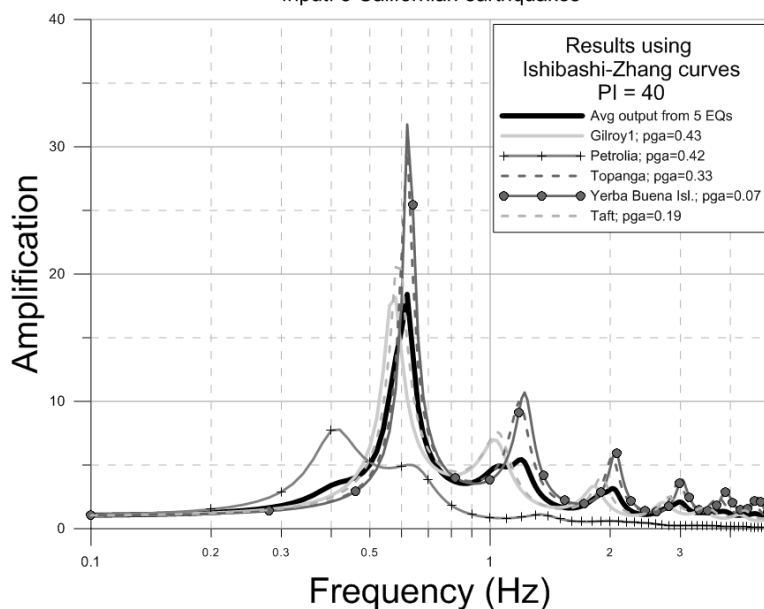


Fig. 5-20: Transfer functions as calculated with Proshake for 5 Californian strong motion recordings, as well as their average. Using Vucetic-Dobry's modulus reduction and damping ratio curves for PI of 40.

Plasticity index (PI)

To test the effects of changing plasticity index on the transfer functions, we examined two different sets of curves: that of Vucetic and Dobry which uses linear interpolation between a set of curves for varying PI; and Sun et al.'s curves which give various ranges of PI for which there are matching damping curves, which are user selectable. The detailed Kinburn basin profile was used with the Californian ground motions as input.

For the Vucetic-Dobry curves the effect of using increasing plasticity index (PI) is as expected; as the PI is increased, the frequency of the fundamental and harmonic frequencies increase slightly (e.g. from 0.54 to 0.62 Hz when PI is varied from 20 to 80). As well, the amplification increases significantly (from 8.4 to 14.4) over the same range of PI. These results are plotted in Fig. 5-21.

The results for the Sun et al. curves are less straight forward (see Fig. 5-22). The difference between the results for PI = 40-80 and those for PI = 80+, both using the Upper Bound damping ratio curve, are almost identical, while the 80+ curve shows a slight shift towards higher frequency (less than 0.1 Hz) and a slight increase in amplification at higher harmonics (0.2 or less).

Kinburn - detailed profile Effects of Plasticity Index using Vucetic-Dobry Curves

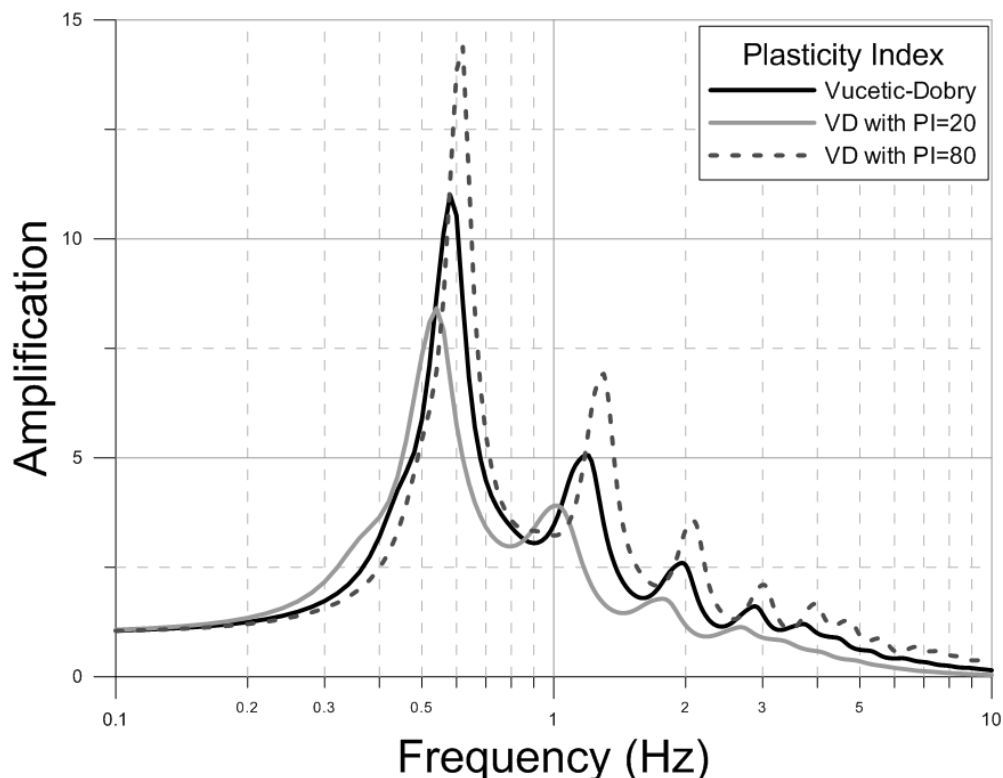


Fig. 5-21: Transfer functions as calculated with Proshake for 5 Californian strong motion recordings, as well as their average. Using Vucetic-Dobry's modulus reduction and damping ratio curves for PIs of 20, 40 and 80.

For the Sun et al. there are also various damping ratio curves from which we can choose. For the PI=40-80 modulus reduction curve with the average damping ratio (instead of the recommended Upper Bound) the resulting transfer function shows the peaks for the fundamental frequency and higher harmonics being essentially at the same frequencies, but with amplification greatly increased (9.4 times amplification modelled for the fundamental frequency, versus the 6.4 modelled with the Upper bound curve).

For the PI = 10-20 range with average damping ratio, the results show an amplification peak shift to lower frequencies by less than 0.1 Hz for the fundamental, but

by ~ 0.3 for the higher harmonics as compared to that for the two PI = 40-80 curves. The amplification for the lower plasticity index is higher by about 2.0 over that of the PI = 40-80 model with upper bound damping curve (but ~ 1.0 less than the results for the PI = 40 – 80 using the average curve).

The results for the PI tests described above for the Sun et al. curves are plotted in Fig. 5-22 and listed in Table 5-9 below:

Table 5-9: Results comparing the Sun et al. (1988) MR curves with varying PIs and damping ratio curves. Using simple 2-layer model with Californian earthquake ground motions.

Sun et al. (1988)	Eq with lowest amplification			Eq with highest amplification			Average f_0	
	amplif	freq	eq	amplif	freq	eq	amplif	freq
Sun et al. MR & DR Curves								
Sun 40-80 clay upper	3.5	0.37	2	7.2	0.48	3	5.0	0.46
Sun 40-80 clay avg.	5.7	0.36	2	11.4	0.48	3	7.4	0.46
Sun 10-20 clay avg.	5.4	0.26	2	10.4	0.46	5	6.3	0.42
Sun 80+ clay upper	3.5	0.41	2	7.0	0.49	3	5.2	0.48

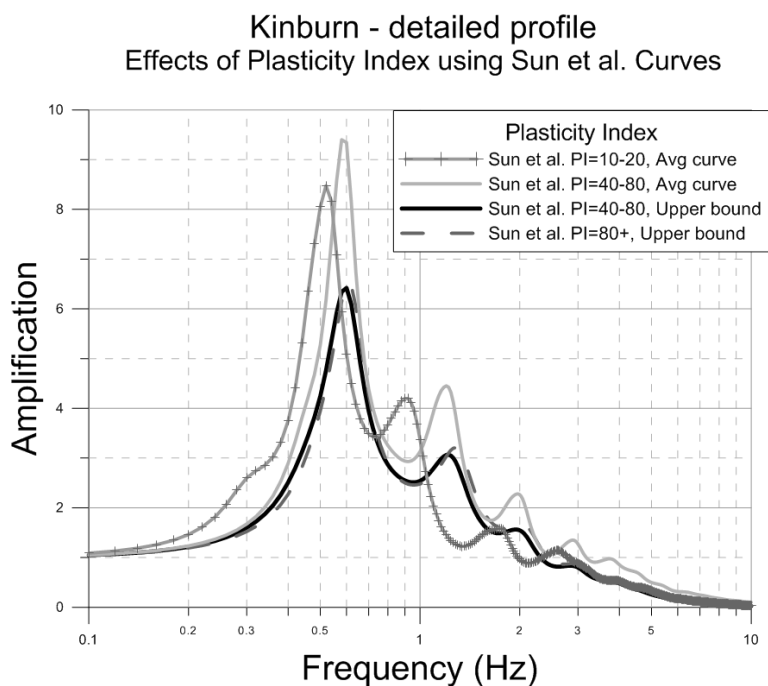


Fig. 5-22: Transfer functions as calculated with Proshake for 5 Californian strong motion recordings, as well as their average.; using Sun et al.'s modulus reduction for PI of 40-80 and upper bound damping ratio curve.

Leda clay curves

Finally, the results obtained using the preloaded curves in Proshake (that of Vucetic-Dobry PI=40 and of Sun et al. PI=40-80, upper bound results) are compared with those obtained using Law et al.'s (1985) curves that were specifically derived from Leda clay data. Again, the detailed Kinburn profile was used with Californian ground motions as input. The results for the average transfer functions are plotted in Fig. 5-23 for all three sets of curves.

The predicted peaks are all at similar frequencies for the three curves. However, the amplification for the Leda clay curve is predicted to be ~16 times, whereas for the Vucetic-Dobry clay curve it is approximately 11 and the Sun et al. clay curves predict only 6 times increase in amplification for the soil over the rock site (see Fig. 5-23).

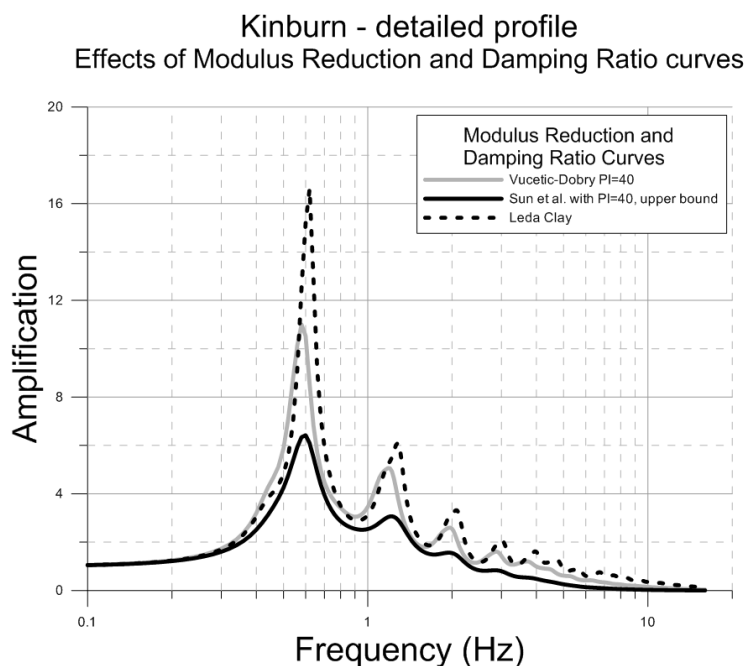


Fig. 5-23: Comparison of the modelled transfer functions as calculated with Proshake, using the average from 5 Californian strong motion recordings as input, for the modulus reduction and damping ratio curves of Vucetic-Dobry (PI=40), Sun et al. (PI=40-80, upper bound), and Law et al.'s Leda Clay.

5.7.2 *Input waveforms*

Although we have tested and compared all the variables in the parameters associated with the geological layers to create 1D profiles in Proshake, we have not yet examined how the input ground motions affect the resulting transfer functions. For the following set of tests the detailed profiles of the three basins were used. Three different sets of modulus reduction and damping curves were tested (Leda clay, Vucetic-Dobry for $PI=40$, and Sun et al. for $PI=40-80$, upper bound) using both the ground motions from California as well as those recorded locally on the study weak motion sites.

The modelled results for the Leda Clay curve using the west Quebec seismic zone recordings versus those from the Californian earthquakes are markedly different (see Fig. 5-24). There is a slight shift towards higher frequencies (from 0.62 Hz for the Californian ground motions, to 0.68 Hz for the local west Quebec ground motions), but also a dramatic increase in amplification, from ~18 to over 60 times.

When comparing the outputs from various modulus reduction and damping ratio for the west Quebec ground motions it is interesting to note that the frequencies at which the predicted peaks occur are identical (see Fig. 5-25). Furthermore, the Vucetic-Dobry curves predict an amplification of ~60, similar to that of the Leda clay curves. The Sun et al. curves predict lower amplifications (~20 times) for the west Quebec earthquakes, although this is still well above that which was found using the Californian ground motions (6.4 times). Similar results were obtained for the other two basins when using the local earthquakes as input ground motions.

Transfer functions for 1D detailed Kinburn basin profile
using Law et al.'s curve for Leda Clay
California earthquakes vs local earthquake recordings

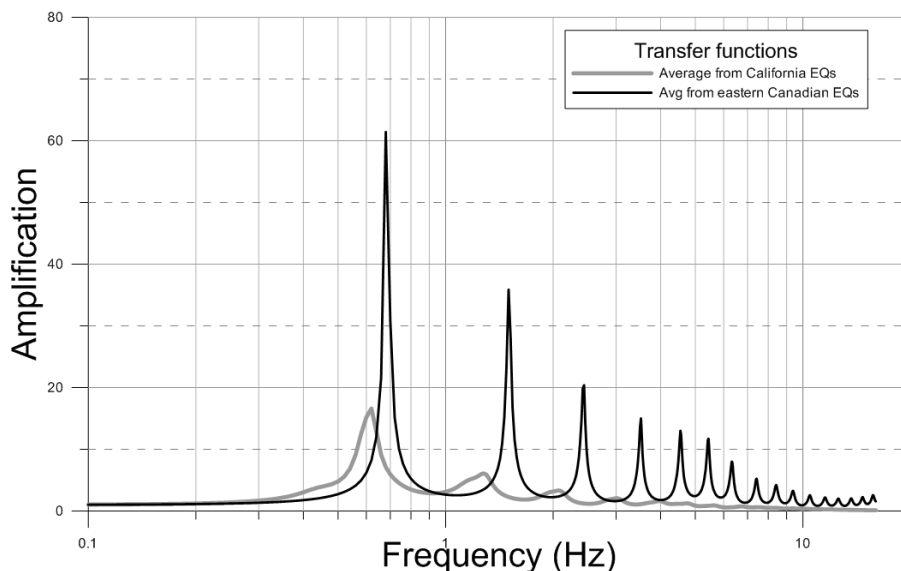


Fig. 5-24: Comparison of the modelled transfer functions as calculated with Proshake, using the Leda Clay curves (Law et al., 1985) for the average from 5 Californian strong motion recordings as input versus the average from 12 local recordings from the weak motion seismograph site at the Kinburn basin rock site.

Transfer functions of 1D profiles for Kinburn
Effects of various Modulus Reduction & Damping ratio curves using local recordings

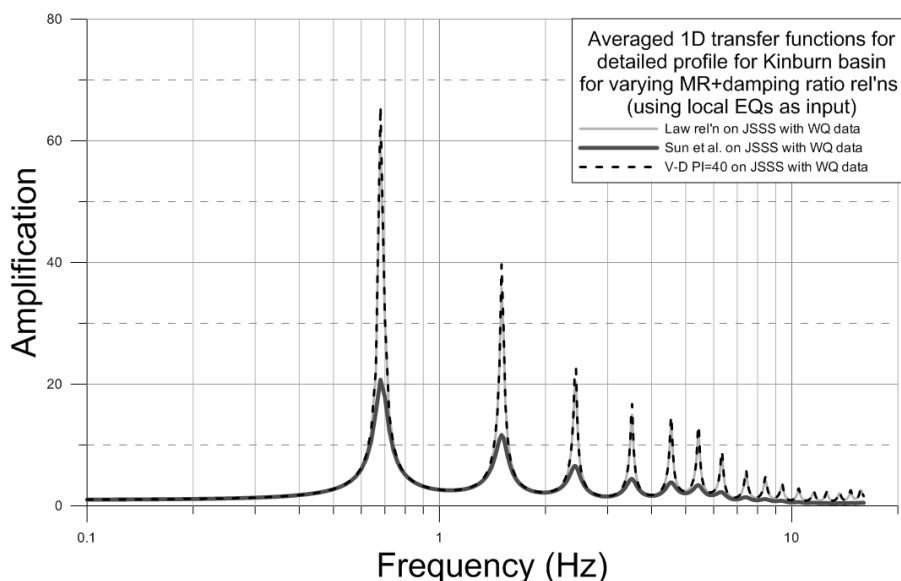


Fig. 5-25: Comparison of the modelled transfer functions as calculated with Proshake, using the average from 12 local recordings from the weak motion seismograph site at the Kinburn basin rock site for the modulus reduction and damping ratio curves of Vucetic-Dobry (PI=40), Sun et al. (PI=40-80, upper bound), and Law et al.'s Leda Clay.

It should be noted although many of the ground motions used are to the same as those used to obtain the average soil-to-rock spectral ratio for each basin, there are a few differences. For example, we used the rock recording from the $m_N5.2$ Shawville earthquake as recorded on JSBS and the $m_N5.7$ Val-des-Bois earthquake as recorded on OTT as input for all three basins for the 1D modelling, as these two were the two strongest ground motions recorded on our sites thus far. Also some earthquakes were well recorded on a particular rock site so provided great input for our modelling, but were not recorded on the corresponding soil site and hence could not be used for the spectral ratios. See Tables 5-10, 5-11 and 5-12 for the list of earthquake ground motions used for each of the three basin profiles, Kinburn, Lefavre and Orleans respectively. See Tables 4-1, 4-2 and 4-3 in for the lists of earthquakes used for each of the basin soil-to-rock spectral ratios.

Table 5-10: List of recordings used for modelling the Kinburn basin, including the date, location and magnitude of the earthquake, the seismograph station on which it was recorded, and the PGA, and the Proshake filename.

EQ	Proshake filename	date	location	mag (m_N)	recording station	PGA (g)
1	SV41JZ	20130517	Shawville, QC	4.1	JSBS.HHZ	6.8E-03
2	SV37JZ	20130530	Shawville, QC	3.7	JSBS.HHZ	2.2E-03
3	BB36JZ	20131020	Barry's Bay, ON	3.6	JSBS.HHZ	1.3E-03
4	HW43JZ	20110316	Hawkesbury, ON	4.3	JSBS.HHZ	4.6E-03
5	SV52JZ	20130517	Shawville, QC	5.2	JSBS.HHZ	4.4E-02
6	HW42JZ	20121106	Hawkesbury, ON	4.2	JSBS.HHZ	1.9E-03
7	VC45JZ	20121010	Vercheres, QC	4.5	JSBS.HHZ	9.3E-04
8	HN35JZ	20110824	Huntingdon, QC	3.5	JSBS.HHZ	2.1E-04
9	VB35JZ	20130116	Val-des-Bois, QC	3.5	JSBS.HHZ	7.2E-04
10	VD57OTZ	20100623	Val-des-Bois, QC	5.7	OTT.HHZ	1.9E-02
11	LM44JZ	20121212	La Malbaie, QC	4.4	JSBS.HHZ	6.0E-05
12	RG34JZ	20130521	Rigaud, QC	3.4	JSBS.HHZ	2.3E-04

Table 5-11: List of recordings used for modelling the Lefavre basin, including the date, location and magnitude of the earthquake, the seismograph station on which it was recorded, and the peak ground acceleration (PGA). The Proshake file name is also included.

EQ	Proshake filename	date	location	mag (mN)	recording station	PGA (g)
1	SV41AZ	20130517	Shawville, QC	4.1	ALFO.HHZ	3.5E-04
2	SV37AZ	20130530	Shawville, QC	3.7	ALFO.HHZ	7.8E-05
3	BB36AZ	20131020	Barry's Bay, ON	3.6	ALFO.HHZ	2.6E-05
4	HW43OZ	20110316	Hawkesbury, ON	4.3	ORIO.HHZ	1.6E-03
5	SV52AZ	20130517	Shawville, QC	5.2	ALFO.HHZ	8.1E-04
6	RL31AZ	20120122	Rockland, ON	3.1	ALFO.HHZ	1.5E-04
7	VC45AZ	20121010	Vercheres, QC	4.5	ALFO.HHZ	6.8E-04
8	SV52JZ	20130517	Shawville, QC	5.2	JSBS.HHZ	4.4E-02
9	VB35AZ	20130116	Val-des-Bois, QC	3.5	ALFO.HHZ	1.5E-04
10	VD57OTZ	20100623	Val-des-Bois, QC	5.7	OTT.HHZ	1.9E-02
11	LM44AZ	20121212	La Malbaie, QC	4.4	ALFO.HHZ	3.0E-05
12	RG34AZ	20130521	Rigaud, QC	3.4	ALFO.HHZ	1.7E-04

Table 5-12: List of recordings used for modelling the Orleans basin, including the date, location and magnitude of the earthquake, the seismograph station on which it was recorded, and the peak ground acceleration (PGA). The Proshake file name is also included.

EQ	Proshake filename	date	location	mag (mN)	recording station	PGA (g)
1	SV41OZ	20130517	Shawville, QC	4.1	ORIO.HHZ	8.4E-04
2	SV37OZ	20130530	Shawville, QC	3.7	ORIO.HHZ	1.9E-04
3	BB36OZ	20131020	Barry's Bay, ON	3.6	ORIO.HHZ	7.8E-05
4	HW43OZ	20110316	Hawkesbury, ON	4.3	ORIO.HHZ	1.6E-03
5	SV52OZ	20130517	Shawville, QC	5.2	ORIO.HHZ	2.3E-03
6	HW42OZ	20121106	Hawkesbury, ON	4.2	ORIO.HHZ	1.7E-03
7	VC45OZ	20121010	Vercheres, QC	4.5	ORIO.HHZ	4.7E-04
8	HN35OZ	20110824	Huntingdon, QC	3.5	ORIO.HHZ	4.8E-05
9	VB35OZ	20130116	Val-des-Bois, QC	3.5	ORIO.HHZ	1.4E-04
10	VD57OTZ	20100623	Val-des-Bois, QC	5.7	OTT.HHZ	1.9E-02
11	LM44OZ	20121212	La Malbaie, QC	4.4	ORIO.HHZ	3.9E-05
12	SV52JZ	20130517	Shawville, QC	5.2	JSBS.HHZ	4.4E-02

Fig. 5-26 shows the results for the Kinburn basin from all the individual local earthquakes (with the transfer function with highest and lowest amplification marked in dark grey dashed lines), as well as the average transfer function (in black). The

differences in the results from the various input earthquakes are mainly that of amplification. The modelled peaks occur at essentially the same frequencies, regardless of the local earthquakes used. This was found even for the more distant La Malbaie, QC earthquake which is located at approximately 400 km from the basins, as compared to the local earthquakes which are generally less than 200 km away from our basin sites. Similar results were found for the Orleans and Lefavre basins.

Transfer functions for detailed Kinburn profile and Leda clay curves
Using west Quebec ground motions as input motions

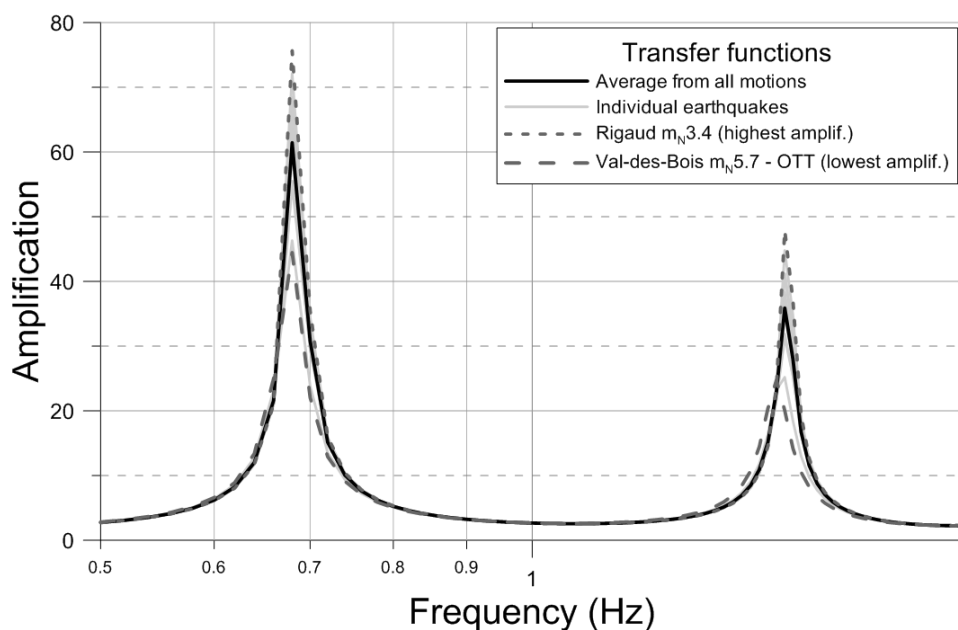


Fig. 5-26: Comparison of the modelled transfer functions for various earthquakes using the detailed profile for Kinburn and Law et al.'s (1985) Leda clay curves as calculated with Proshake. See Table 5-10 for list of earthquakes ground motions used.

5.7.3 1D modelling results compared to the recorded spectral ratios

In this section we examine the results of the modelled soil amplifications for all three basins using local earthquakes as input and the detailed profile built from the

borehole logs and other available geophysical data. These transfer functions are compared to the actual soil-to-rock spectral ratios as found in S4.2 from the local earthquake recordings.

The average modelled transfer functions using Leda clay curves (black line) with local earthquakes as inputs are compared to the actual recorded spectral ratios (thick grey line) for all three basins in Fig. 5-27 to 5-29. The results show that for two of the basins, Kinburn (Fig. 5-27) and Orleans (Fig. 5-29), the predicted transfer function has the fundamental frequency as the highest peak, and the following peaks decrease in amplitude with each subsequent harmonic. For the Lefaivre basin (Fig. 5-28) it is the 1st harmonic that is predicted to be highest, with the fundamental and the 2nd harmonic being lower in amplification, and each subsequent higher harmonic decreasing as well. The actual soil-to-rock spectral ratios, however, show the fundamental being the highest for all three basins (Fig. 5-27 to 5-29). Furthermore, the peaks for all three basins are predicted to be at a lower frequency than the spectral ratios calculated from the actual recordings from soil and rock sites, although this is most pronounced in the Lefaivre basin results.

When comparing these modelled results using Leda clay curves versus the two pre-defined modulus reduction and damping ratio curves in Proshake (Sun et al. and Vucetic-Dobry), the Vucetic-Dobry results (dashed grey line) are comparable to the results from the Leda clay (black line), whereas the Sun et al. results (dashed grey) are vastly lower in amplification and predict the peaks at much lower frequencies for all three basins (Fig. 5-27 to 5-29).

For the Kinburn basin (see Fig. 5-27) we observe a lower average amplitude for the recorded ratios than the average of the modelled transfer functions. The overestimation of the model is the largest at the f_0 , which predicts an amplification of ~ 75 , but the soil-to-rock spectral ratios are closer to 35 times amplification. By the 2nd harmonic, however, the modelled data almost matches the recordings. Higher harmonics are lost in the noise. The f_0 occurs at a frequency just slightly higher than what is predicted, but with each higher harmonic this difference is larger.

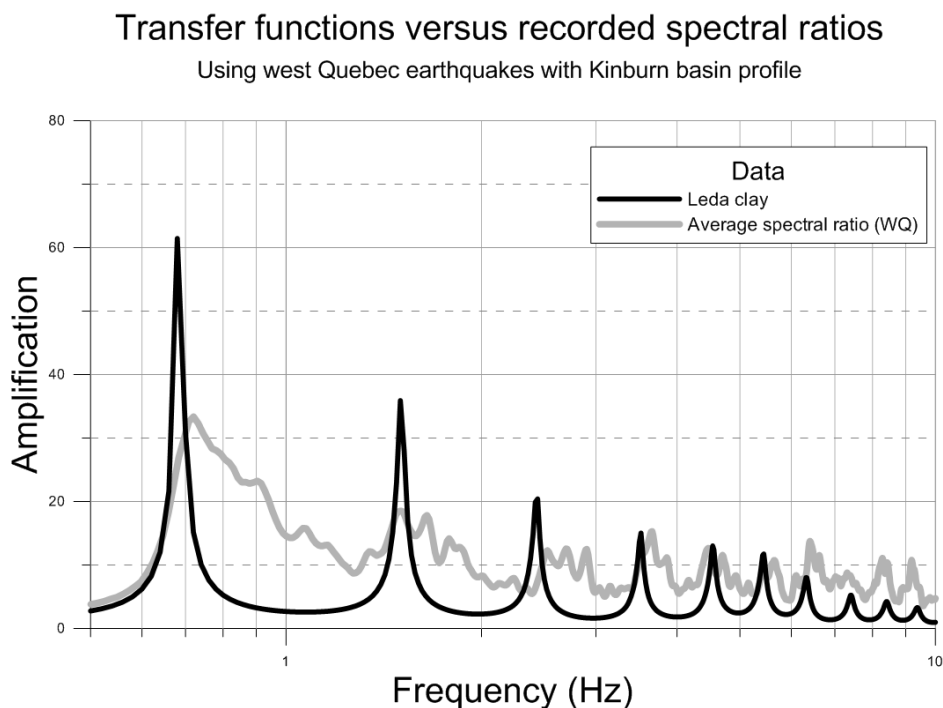


Fig. 5-27: Comparison of the soil:rock ratios from actual recordings of 9 M3.5+ earthquakes at the Kinburn basin, versus the modelled transfer function for the detailed profile as calculated with Proshake. Plotting the average results from 12 local recordings from the weak motion seismograph site at the Kinburn basin rock site, and Law et al.'s Leda clay modulus reduction and damping ratio curves.

The results for the Lefavre basin modelling (Fig. 5-28) are more complicated.

They show that the expected peak for the first harmonic should have higher amplification

then that at the f_0 , and then decreasing again with each higher harmonic. The actual recordings, however, show the f_0 as the strongest peak, just like we see at the other two basins. As we see on the Kinburn basin, the Lefaiivre models show sharp, distinct peaks, while the recorded data is much broader. In the case of the Lefaiivre basin, the amplification of the f_0 appears to match that which is predicted. However, since the f_0 is the highest peak on the recorded data, the amplifications of the higher harmonics are all very over-predicted by the model. The location of the peaks is shifted slightly to higher frequencies, and any data after the 2nd harmonic is lost in the noise on the recorded data, as was the case for Kinburn basin data.

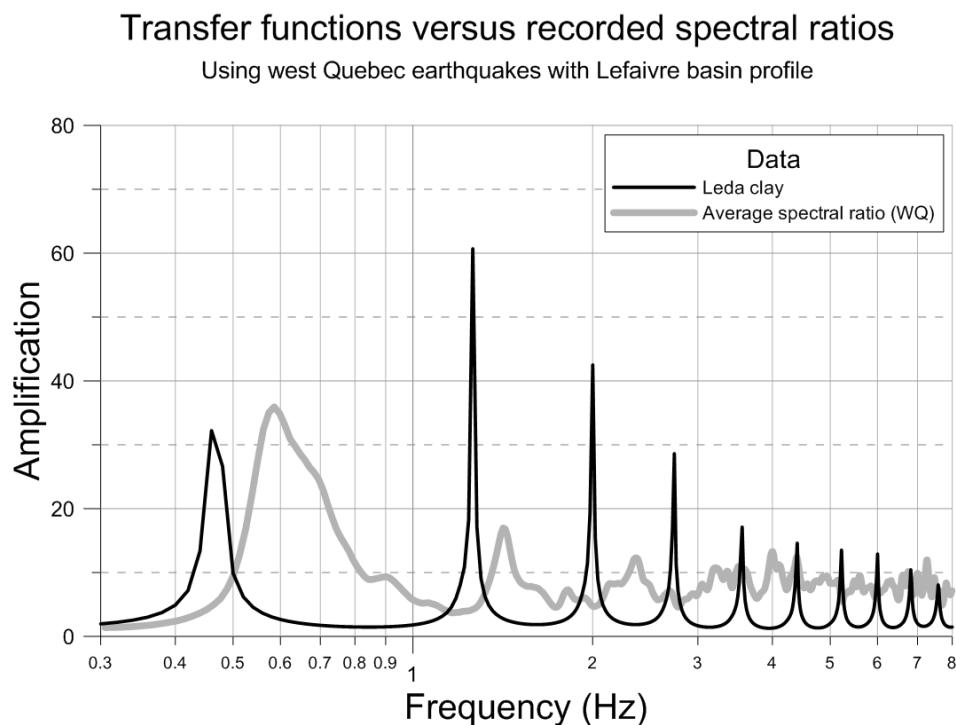


Fig. 5-28: Comparison of the soil:rock spectral ratios from averages of recordings of 9 M3.0+ earthquakes at the Lefaiivre basin, versus the modelled transfer function for the detailed profile as calculated with Proshake, plotting the average result from 12 local recordings from the weak motion seismograph site at the Lefaiivre basin rock site as input, and Law et al.'s Leda clay modulus reduction and damping ratio curves.

For the Orleans basin, the location of the peaks modelled for the Orleans basin is also shifted towards slightly lower than those of the recorded data, but much less than for the Lefavre basin. The average observed amplification found from spectral ratios of earthquake recordings is much higher than the modelled one at the f_0 (~80 times, versus the modelled ~50 times). The observed average harmonic peaks are much closer in amplification to the model: the 1st harmonic is just below the modelled amplification (see Fig. 5-29), whereas the 2nd and 3rd harmonics are slightly over-predicted by the model.

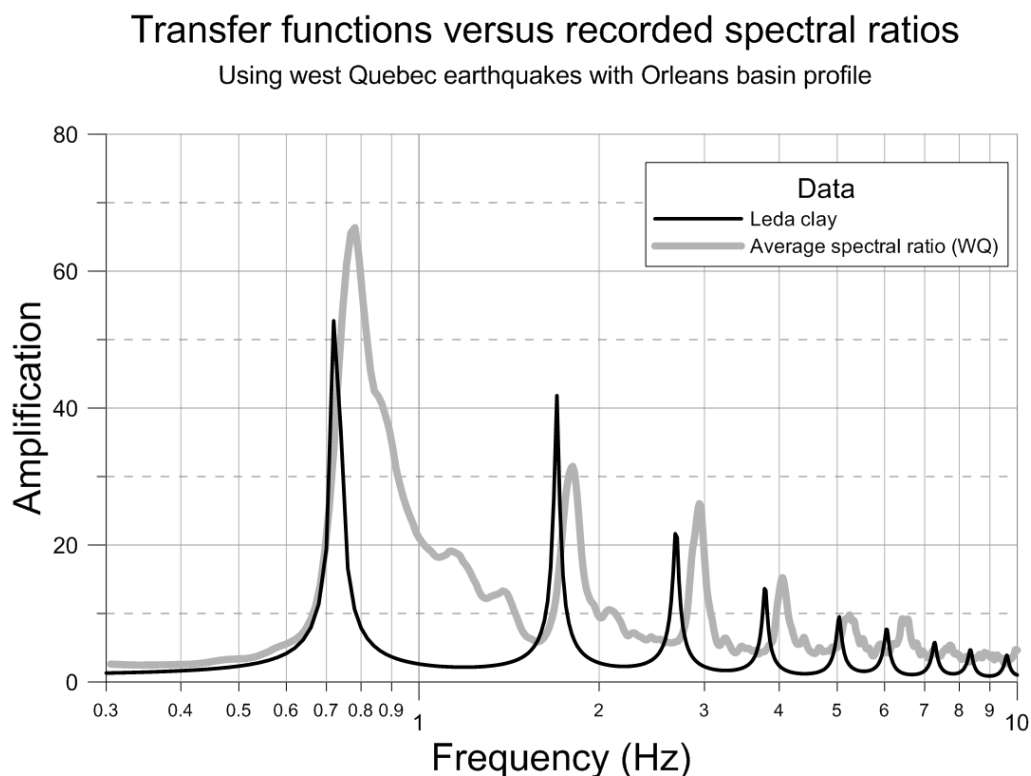


Fig. 5-29: Comparison of the soil:rock ratios from actual recordings of 11 M3.5+ earthquakes at the Orleans basin, versus the modelled transfer function for the detailed profile as calculated with Proshake, plotting the average results from 12 local recordings from the weak motion seismograph site at the Orleans rock site and Law et al.'s Leda clay modulus reduction and damping ratio curves.

5.7.4 Note about Proshake assumptions and limitations

As noted in the Proshake manual, this program is based on an equivalent-linear model, and as such no permanent deformation can be modelled. Furthermore, it does not calculate porewater pressures. Viscous damping is assumed. Despite these assumptions, the algorithm has proven to give realistic results (Kramer, p231). However, the user should always remember these basic limitations, and make sure they are reasonable assumptions for the site being considered.

Previous authors have found certain limitations with programs based on the SHAKE algorithm. For example, Destegül et al. (2007) found that when modelling stiff, thick soils with ground motions of high acceleration ($\sim 0.48g$ or more), that the spectral accelerations calculated by the program they were using (in this case Shake2000) became less reliable.

While using the Proshake we did encounter several limitations. For the simple profiles, it was found that the profile would not be processed when V_s for bedrock was greater than 4000 m/s, nor when V_s for clay was less than 190 m/s. In order to test whether this was a limit due to the contrast or the actual V_s value, we ran some tests for the bedrock with clay at higher values, and found that indeed the bedrock V_s could be increased slightly as the V_s of clay was increased. For the clay, however, even with bedrock below 1000 m/s, Proshake does not appear to be able to process any profiles with the clay layer below 190 m/s.

For the detailed profiles, no such problems arose, even with model layers with lower Vs than 190 m/s. Of course for the detailed profiles, these layers were thin, and the contrast between layers was much less due to the gradual increase of Vs for clay with depth. Hence, it is likely that this limit has to do with the amplification computed from the combination of properties for the layers.

Another limitation seemed to be the depth. For example, our maximum till thickness was 40 m with 97 m of overlying clay. However, there was no issue with increasing the till layer thickness, as long as the clay thickness was also reduced. This, again, may be a function of the layer properties and the resulting calculations causing large outputs (i.e. very high amplifications or singularities), and possibly profiles with different properties could have greater overall thickness and still be processed within Proshake. This is supported by the fact that there seemed to be no issue with the detailed Lefaiivre profile, our deepest profile.

Furthermore, there seemed to be a limitation of layers at around 100, sometimes more or less depending on the profile. Again, it is possible this was due to the layer properties and not an actual hard limit on the number of layers. Further testing would be required. We were able to get around this limitation by combining some of the thinner layers together, which worked fine for the scale of our three profiles.

Hence, there may be issues for sites that are very deep and have large contrasts between layers, and extreme values (e.g. very low Vs) for material properties. These limitations, as well as the basic, underlying assumptions for equivalent linear modelling,

should be kept in mind when choosing a 1D ground-motion modelling program that is suitable for a site.

5.8 Discussion of 1D modelling results

5.8.1 Test profile results – sensitivities to variables

Rock

In general it was found that the profiles were not very sensitive to the properties assigned to the rock within the expected range of material properties at our study sites. It is likely this is due to the extreme difference in properties between the rock and the overlying sediments in this region. Hence, specifics about the rock type underlying the site are not required. It should be sufficient for our sites to use the average V_s for rock collected for the Ottawa region for 1D modelling, and any γ_b within usual range for rock.

Till

The γ_b did not seem to have much of an effect for any layer, including the till. It would be useful to have some measured values appropriate for each layer, but if the user were lacking this data, using an estimate would be unlikely to have any real effect on the 1D modelling results.

Also for the till layer, the change in modulus reduction and damping ratio curves from gravel to sand made very little difference. This suggests that the lack of data in the literature regarding curves for till layers might not be too significant to obtain good results. However, as we have no data on how close either the gravel or the sand curves

model the actual behavior of the till layer, this test may not have covered the entire range of possibilities. Hence, it would be beneficial to obtain some data for future testing.

Unfortunately, judging from the data gathered from the Lefaivre borehole, it can be seen that there are very large fluctuations within this layer, and it may not be possible to get a representative set of curves for this material.

The thickness of the till had only a minimal effect on the fundamental frequency peak, but had moderate effects on the higher harmonics, with both amplitude and frequency being affected. The frequency shift is likely associated with the increase in the depth of the overall soil profile (see Eqn 2.5; S2.4.2). Note that the increased thickness seemed to make an appreciable difference once the model thickness of till was 30 or 40 m. The changes between thicknesses of 0 and 5 m were minimal and suggest that a layer with thickness less than 5 m can be ignored in models.

We observed much different results when we increased the till layer thickness in our models, while in turn reducing the clay thickness to keep the overall soil profile at the same thickness. In these tests we observe significant increase of amplification and frequency as the till layer thickness increases and the corresponding clay layer is thinner. These results are in line with that expected from Eqn 2.5 (S2.4.2), as the dominant material becomes the one with higher Vs. However, although this test highlights the importance of knowing the clay-to-till thickness ratio at a site, it is not realistic for any of our basins, as we have very good estimates of clay depth at each of our sites from various geophysical data (e.g. Tromino measurements, borehole data, landstreamer profiles).

For the more realistic test profiles, the biggest difference in results for the till layer were caused by changing the V_s . When V_s is set to 580 m/s or higher (larger contrast between clay and till, smaller between till and rock), there were only slight changes in the transfer functions. But as the V_s is decreased, both the frequency and the amplitude decreased, the latter quite significantly as the V_s approached that of the clay. Thus, it is important for modelling purposes to have a reasonable estimate of the V_s of the till layer. Unfortunately, this layer is known to have a wide range in V_s , as is seen in the measurements taken at the Lefaivre borehole.

Clay

Overall, the most important layer to detail correctly is the clay layer. This is due in large part to its thickness, as well as the extremely low V_s of the layer. As with the till and rock layers, changing the γ_b did not have any large effect on the final results. Hence, a specific value does not need to be determined for each layer, but a general value for the clay is probably sufficient. However, both the variation of V_s and the modulus reduction and damping ratio curves can significantly affect the outcome, as can the overall thickness, as seen in the clay to till ratio tests. Eqns 3-2 and 3-3 show how the thickness of the layer will determine the f_0 .

For our sites, the thickness of the clay layer was well determined by various geophysical measurements. For most sites, however, where boreholes or other seismic data are likely to be unavailable, simple Tromino measurements (see Chapter 3), or any seismic recordings from earthquakes or noise from a site (see Chapter 4) could provide a measurement of the f_0 . This in turn can be correlated to depth for the Ottawa region by

Eqn 3.3 found by Hunter et al. (2010). This measurement is considered to be representative of the soft sediments above the first major reflector, which in the case of the seismic sites at our basins would likely be the till layer. Hence, the thickness of the clay layer is relatively easy to determine (to within a few metres) compared to that of the till.

Not as easy to obtain are V_s measurements down the length of the clay profile. With this variable, it is also a matter of the rate of change with depth. Using the simple profiles, there was a significant shift up in frequency of the peaks and increase in amplification in the transfer function of the model with higher V_s . Of course, as the V_s range was over-exaggerated, one would expect that any error in V_s would be much less than seen between these two curves.

A power equation (S4.2.5, Eqn 5-9), derived from the borehole data at the Kinburn site, was also tested to see if this would adequately model the detailed profiles. It produced results with higher frequency peaks than the simple 2-layer or the actual detailed profile. As Leda clay often has an over-consolidated layer near the surface, a 6 m crust of higher V_s , was tested but found to have no effect. It is suggested that this crust can likely be ignored in models without affecting results.

It is evident from the results obtained using the detailed profile, that a simple 2 or 3 layer profile is not sufficient to model either the expected frequencies or amplitudes that will be recorded on the basins. Even the results using the power equation while producing a fundamental peak closer to that of the detailed model, it was still slightly

shifted, this time to a higher frequency. The harmonic peaks were increasingly poorly modelled, and the predicted amplitudes were all too high from the model using the power equation. With the current data, we conclude that there is no easy way to approximate the results obtained from the detailed model.

Modulus reduction and damping curves for Leda clay

The various modulus reduction and damping ratio curves were introduced in S5.4, but there is little from their basic description that would allow us to decide whether one is more appropriate than the other, and all the curves provided within Proshake seem to be widely used in various regions in the world. Hence, all the curves available for clay were tested, along with the curves specifically for Leda clay by Law et al. (1985).

As noted in S5.4, the Ishibashi-Zhang curves may be considered better at lower PI's as compared to Vucetic-Dobry because they take effective confining pressures into account (Ishibasi and Zhang, 1993), but there is a question about the stability of their outcomes for higher PIs. In our tests, the Ishibasi-Zhang curves also showed a highly variable output from the test profiles. Since effective confining pressure is less important at higher PIs, likely the Vucetic-Dobry would be the better choice for our sites. Note, however that neither of these curves were derived using sensitive clay samples (Guerreiro et al., 2012), and likely neither did the Sun et al. (1988) curves. Law et al.'s (1985) curve is the only one based specifically on Leda clay samples from the Ottawa-Montreal region. However, this curve is only developed for low strains.

For testing the effect of PI we eliminated the Ishibashi-Zhang curves, and tested just the Sun et al., and Vucetic-Dobry curves. The Leda clay curves do not have a PI component. It is more important to use the correct PI for the Sun et al. curves, as there is a large variation between the results (mostly in amplification) produced by that, for example, of the lower PI curve, versus that produced by the higher PI levels. This difference becomes less at the higher PI's, but is still significant between PI = 10-20 and PI = 40-80. This is important as the clay at the study sites may have a PI as low as 20 or up to 40. Hence, either of the two curves, or the intermediate of PI=20-40 might apply. Furthermore, the selection of damping ratio curves is also important, which can cause further significant changes in amplification if an inappropriate curve were to be selected. In general Proshake will automatically select the appropriate damping ratio curve once the modulus reduction curve has been selected. However, this is not always the case when changing from one curve to another. So care should be taken to select the correct accompanying curve.

Plasticity index is also important for the Vucetic-Dobry curves. However, in this case, as the curves predictably increase with increased PI, and there is interpolation between the curves, there is not the same quantized variation that comes with using predefined curves for specific ranges. It also removes the ambiguity of whether to use the 20-40 curve or the 40-80 curve for a PI of 40.

The results from the Vucetic-Dobry curves were much closer to those obtained from the Leda clay curves than the Sun et al. curves. Although this suggests that the Vucetic-Dobry could be used instead of the Leda clay ones, it is important to keep in

mind that these results were only for low strain and the relation may not hold true for stronger ground motions.

To date, very few studies have used Leda clay measured samples to define modulus reduction and damping ratio curves. We used the Law et al. (1985) curves that were produced for low strains (up to 0.2), which are sufficient for the weak motion data we currently have available, but yield no information for stronger ground motions. There are currently studies being done at Carleton University, Laval University and University of Waterloo in collaboration with GSC, to define new curves for Leda clay for higher strains as well. These data, however, were not available at the time of testing.

For future investigations an appropriate curve for Leda clay that includes higher strains should be used. When using the local earthquake data (which has a much higher frequency content, and much lower strain than the Californian ground motions used), the results using the Vucetic-Dobry (PI40) curves give similar results, especially in terms of frequency, as the Leda Clay curves used in this study. This suggests that the Vucetic-Dobry curve might be adequate, but we note that as we did not have data for the behaviour of Leda clay at higher strains, we are not sure that these curves are appropriate for higher strains.

Ground motion inputs

The final important variable to address is the input motions used. It was shown that there was a significant shift in the frequency of the resonant peaks when using the high frequency content earthquakes of the local recordings, as compared to the results

obtained when using the Californian earthquakes with much lower frequency content. Note, as well, that the Californian earthquakes had much higher PGA, which would utilize a different part of the modulus reduction and damping ratio curves, subsequently affecting the results in terms of amplification as well. Hence, appropriate ground motions must be used to obtain reasonable models for the basins.

It is important to recall that although the ground motions are represented by one curve, in reality there are three components, one vertical and two horizontals, and hence three ground motion curves to consider. Joyner (2000) accounted for this in his model for predicting ground motions over a basin, by having different ground motion prediction equations for vertical, parallel and perpendicular directions. However, Proshake (as with similar ground motion modelling software) only provides one transfer function, with no possibility of assigning a particular component.

As mentioned in Ch. 4, for engineering purposes the horizontal motion is of most interest, as vertical forces are already taken into account due to gravity. Furthermore, as shown in S4.1.1, the horizontal amplifications over the basins are much higher than the vertical ones. Hence, our modelling is concerned with predicting the *horizontal* motions. Further, the two horizontals will have differing ground motions. Typically in seismological analysis, the horizontals would be rotated towards the source azimuth to give a radial and a transverse component (rather than N-S and E-W components), which would produce the maximum and minimum ground motion from that earthquake. However, as shown in S4.1.4, the particle motions are not as expected (i.e. when rotated the maximum shear energy is not necessarily in the transverse direction), making it

difficult to reduce the horizontals into one component of interest. To avoid azimuthal problems we used the root mean squared average of the horizontals for our soil-to-rock spectral ratios which is easy to calculate and often used in the engineering community.

Furthermore, whether we used either a horizontal or the vertical component from the rock site as input did not seem to have a significant effect on the resulting transfer function. Hence, for the test we chose the vertical component for best signal-to-noise conditions.

It is important to note that each individual earthquake showed slightly different values of frequencies and amplification, due to the highly random nature of earthquakes. For the modelled data in general, the smaller earthquakes tended to have larger amplifications than the larger earthquakes, as expected due to the non-linear nature of soil. However, occasionally a stronger earthquake exceeded a slightly weaker one in amplification. This underlines the fact that even for a 1D model the source parameters (other than just peak ground acceleration) do play a role in the soil amplification. For the soil-to-rock spectral ratios calculated from the recorded data, the individual earthquakes often do not follow a pattern in terms of amplification or frequency content being related to PGA, distance, magnitude, azimuth, etc. The range of amplifications is large, even for earthquakes of similar strengths. And whereas the models for the ground motions with the largest amplification for the f_0 also had the largest amplification at the higher harmonics, this was not the case with the recorded ratios.

5.8.2 1D modelling results versus the recorded spectral ratios

Overall, for all three basins, the prediction of the location of the peaks of the transfer functions seems to be shifted slightly to lower frequencies as compared to the actual recorded soil-to-rock spectral ratios. This is most pronounced for the Lefaivre basin. Although none of the observed peaks perfectly match the modelled data, the patterns are similar enough to validate that we are observing the fundamental frequency and higher harmonics. The amplification predictions for the fundamental frequency were over-estimated for Kinburn basin, but underestimated for Lefaivre and Orleans. In general, the amplifications did not match well between the modelled data and the recorded data. Our basic assumptions are that the linear equivalent ground motion modelling should be reasonable for our site conditions, and that the Leda clay curves derived by Law et al. (1985) are appropriate for the clay at our sites, and that the ground motions used are within the low levels of strain given by the Leda clay data.

According to the results of our tests on sensitivity of model variables, the difference between the locations of the predicted peaks to recorded ones could be due to inaccuracies in the profile parameters. The mostly likely source of this shift would be inaccuracies in modelling of the clay layer, in particular the V_s versus depth profile or the modulus reduction and damping ratio curve. As Vrettos (2013) showed, even the difference between V_s changing continuously with depth versus discrete layers can shift the frequencies of the fundamental and harmonics modelled for a profile. Hence a simple model for this layer is not adequate for modelling purposes.

Inaccurate modelling of the till layer Vs might also have introduced some error, however in general the effect of this layer should be minimal. In fact, the direction of the shift of amplification peaks to higher frequencies would require the till to have a higher Vs than that used, but with increased Vs the effect on peak location was greatly decreased. Inaccurate modelling of the rock layer is unlikely to be a factor in these models.

The Vs profile of the clay layer would have the greatest effect on the modelled outcome. Our detailed profiles were based on much more geophysical data than is usually available at a site, including boreholes and seismic reflection, which characterized the shear wave velocity and surficial geology for all seismograph sites; hence most of the errors in the model itself should be minimized. Thus it is more likely that the differences we see between the modelled and the recorded data is due to the 2 and 3D effects of the basin geometry.

From previous studies we know that the accuracy of the basin model geometry is important, particularly for investigating the higher frequencies (Semblat et al., 2005). The frequency content of the local earthquakes at our sites is high. We noted in Ch. 4 the differences in the frequency of the peaks from the soil-to-rock spectral ratios of the individual earthquakes recorded, suggesting that potentially source parameters and/or basin interactions (likely on a small scale given the frequencies involved) may play a role in the resulting ground motions over the basin.

In terms of amplification, we obtained three different results from the three basins. All the soil-to-rock ratios from the basin recordings show that the f_0 is the most amplified peak, with peaks of lower amplitude for each subsequent higher harmonic. This is what the models for Kinburn and Orleans predict as well. However, the model for the Lefaiivre basin predicts that for this basin the first harmonic should be the one with the highest peak.

The Lefaiivre basin has the lowest f_0 of the three basins, being the deepest, while the frequency content of the sources used is relatively high. When using the Californian earthquakes with lower frequency content as input, the modelled transfer function shows the f_0 peak is the highest. Hence, it is probable that for higher magnitude earthquakes with more low frequency content, the fundamental frequency would likely be modelled as the strongest peak. Note that the actual recordings show the f_0 at a higher value than the predicted from our model studies.

Part of the difference between spectral ratios observed at Orleans versus the spectral ratios observed at the other two basins may lie in the shape of the peaks, which are much more tightly defined for Orleans, with all the energy being concentrated within a much smaller frequency range, whereas the Lefaiivre basin has much broader peaks, and the Kinburn basin has almost a series of three smaller peaks for the fundamental and each harmonic. There is less data for Kinburn and Lefaiivre, however this does suggest the role of basin shape in not just the location of the peaks, but also the resulting amplification. These 2 and 3D effects are not modelled by Proshake which is based on 1D modelling,

and hence the complexities in the shape of the spectral ratio curves are not reflected in the modelled transfer functions.

5.9 Conclusions

For successful modeling of a soft-sediment basin for the Ottawa region, the most important detailed information to gather is that on the clay layer. Specifically, the depth of the clay layer, the V_s profile with depth and the modulus reduction and damping ratio curves appropriate for Leda clay are required. While the depth of the layer is relatively easily estimated from Tromino measurements or seismograph records at the site (relating the recorded f_0 to depth to the first major reflector, likely the till layer, using the predefined equation for the Ottawa region), the V_s profile with depth is not easily obtained without other geophysical data (e.g. a borehole or landstreamer data). Although a non-linear power law approximation of interval V_s versus depth gives a more realistic result as compared to the simple 2 or 3 layer models, it still does not match the transfer functions calculated from a detailed profile based on borehole and other geophysical data.

The appropriate modulus reduction and damping ratio curves make a big difference in terms of predicted amplification and location of the fundamental and higher harmonic frequencies. The plasticity index and the source of data used for creating the curves need to be considered. There is not enough data to show whether there is a difference between the sites with sensitive clays versus the non-sensitive clay sites, but the Vucetic-Dobry with $PI=40$ (1991) and Leda clay (Law et al., 1985) curves give a result much closer in frequency and amplification to the recorded data than the other

available curves. Note, however, that these were only tested for low strain events, and a Leda clay curve valid for higher strains should be used in future studies.

It is very important to use ground motions appropriate to the site under investigation. The lower frequency and higher PGA of the Californian events gave a much lower estimate of the amplification and f_0 and higher harmonic frequency peaks than the local west Quebec earthquakes. Note that the recorded results are still quite variable and more good quality data with a larger range of distance, magnitude, PGA, azimuth would be useful to get a more robust average for comparison with the models.

With the proper profile data and inputs in our models, although the peaks are still shifted slightly to lower frequencies, they begin to give a reasonable estimated compared to the recorded data from local and regional earthquake events. However, the amount of amplification is not generally well predicted by the modelled results. Assuming that equivalent linear modelling is valid for our site and that the profile details are accurate, it is likely that 3D effects from both the soil layering and the buried bedrock basin are contributing to the differences in the amplification and frequency results of the models versus the actual recorded data. For example, while the models over predict the amplification at the fundamental frequency of the Kinburn basin, for the Orleans it is underestimated. The location of the peaks of the Lefavre basin are poorly predicted, whereas those for the Kinburn and Orleans basins are only slightly shifted from those recorded on the soil-to-rock ratios. (See Fig. 5-27 to 5-29). Even the shapes of the peaks show the influence of the 2 and 3D geometries: the modelled transfer functions for all three basins show simple sharp peaks at the fundamental and harmonic frequencies, with

a reasonably steady decrease in the height of the peaks for the higher harmonics (the predicted fundamental peak for Lefaiivre being the exception when the input motions don't contain enough energy at the predicted f_0). Conversely the recorded spectral ratios all have much broader peaks, and the shape of the peaks seems to be unique for each of the basins. For example the Kinburn basin has multiple sub-peaks, whereas Orleans has one sharp peak, which drops off more slowly on the higher frequency side.

These differences cannot be explained simply by possible inaccuracies in the models, but clearly show that there are 2 and 3D effects that cannot be modelled by a 1D modelling program, even with the most detailed profiles and accurate parameters. Furthermore, this demonstrates that these effects make the modelling of the resulting ground motions over these basins impossible with just 1D modelling.

6. Particle motion analysis

In order to determine if the underlying bedrock basin geometry affects the ground motion over the basin, we can examine the particle motion of the recorded waveforms at the soft soil sites. However, as noted in Chapter 4, due to the high frequency content in the local recordings the particle motion can appear to be going in several different directions within just one second of data. This high frequency data is naturally more chaotic than longer period data as it will be affected by the smaller scale structures, while the longer period data will pass right through these local, small scale variations without any effect. Our interest is in whether the presence of the basin is affecting the incoming waveforms in a specific way. Hence, we are looking for trends in the data recorded over the basin which point to basin-edge generated waves.

In this chapter we will introduce the method devised to process and plot the data, the results from the analysis with this method and what we see or don't see in terms of trends. As mentioned in Ch. 4, the particle motion analysis could only be performed on the Orleans station pair due to a software error which caused a timing error in the components of ALFS, JSBS and JSSS. (See Appendix A for more details).

6.1 Background

To examine the particle motion from the waves recorded at the seismograph site of interest, we must determine the wave motions expected to be present in the data. The P wave is a compressional wave, travelling outward from the epicentre towards the receiver

(see Fig. 6-1). When determining the particle motion of a P arrival, one would expect to see horizontal motion in the direction of the azimuth/back-azimuth of the earthquake. If the source is further than a few tens of kilometres from the receiver, there should also be vertical motion, showing larger amplitudes the further the source is from the station.

The S wave is a shear wave, with the main motion perpendicular to the direction of the direction of travel and can have both a horizontal (SH) and a vertical (SV) component (in Fig. 6-1 the particle motion of the shear wave is shown polarized in the vertical direction). This motion is expected to show larger horizontal amplitude than vertical amplitude. For this arrival we would expect to see the horizontals to show motion that is approximately 90 degrees from that of the P arrival (and hence 90 degrees from the epicentre azimuth/back-azimuth), with the reference rock site being used to confirm exactly which orientation is expected at the site.

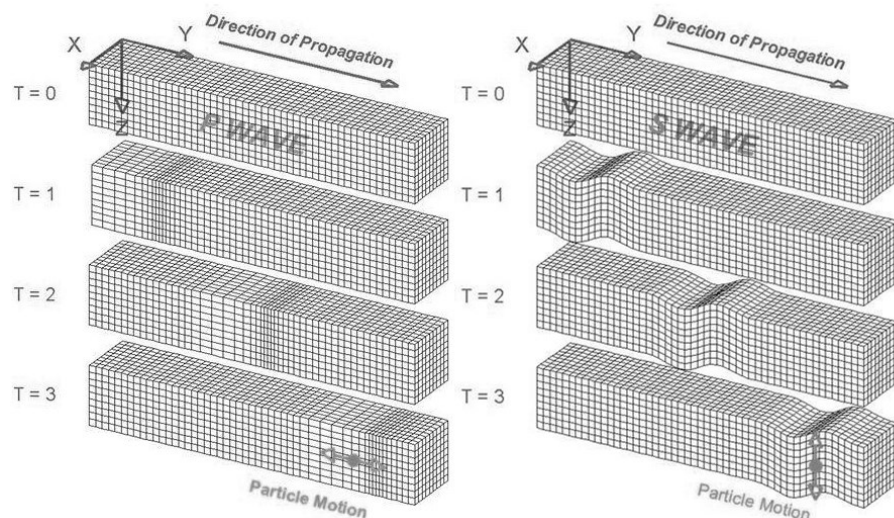


Fig. 6-1: Graphical representation of the two body waves, P and S, showing the direction of travel and the direction of particle motion. Image source: <http://www.geo.mtu.edu/UPSeis/waves.html> (accessed February 2016).

There are two main types of waves that are confined to the earth's surface: Rayleigh waves and Love waves (see Fig. 6-2). Rayleigh waves (Rg) generally show retrograde elliptical motion, in the direction of travel. Hence they contain vertical motion, and the horizontals should appear to be moving in the same direction as the P wave (azimuth/backazimuth of the earthquake to the recording station). Love waves show only horizontal motion, and like the S wave the motion is 90 degrees to the direction of travel (see Fig. 6-2).

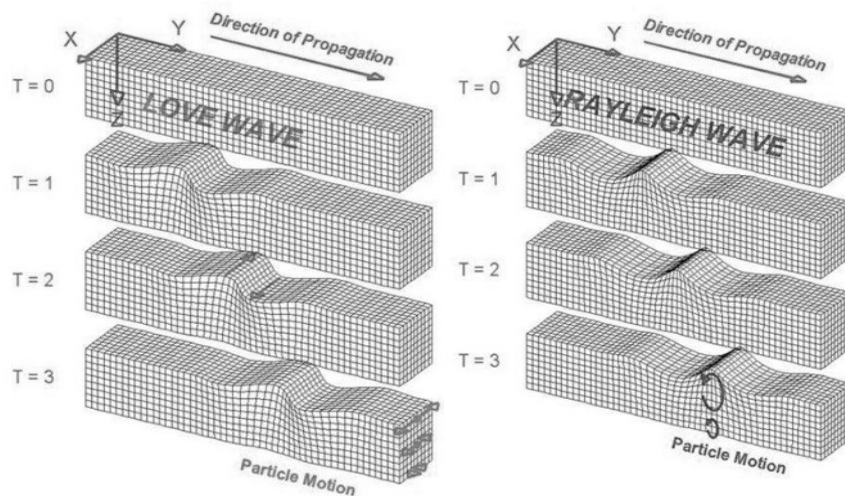


Fig. 6-2: Graphical representation of the two types of surface waves, Love and Rayleigh waves, showing the direction of travel and the direction of particle motion.

Image source: <http://www.geo.mtu.edu/UPSeis/waves.html> (accessed February 2016).

For the recordings of our local earthquakes, on a rock site we would normally expect to see just the two body wave arrivals: P and S. The earthquake sources in the west Quebec seismic zone and the nearby Charlevoix seismic zone tend to be of small to moderate magnitudes (M2-5) and generally more than 5 km deep, precluding the generation of significant surface waves (Ma, 2006; Lamontagne, 1999).

6.2 Particle motion plots

Typically the particle motion is represented in three plots: east-west versus vertical; north-south versus vertical; and east-west versus north-south. Fig. 6-3 and shows what a typical particle motion plot would look like for a P wave arrival, as captured by the rock site ORIO.

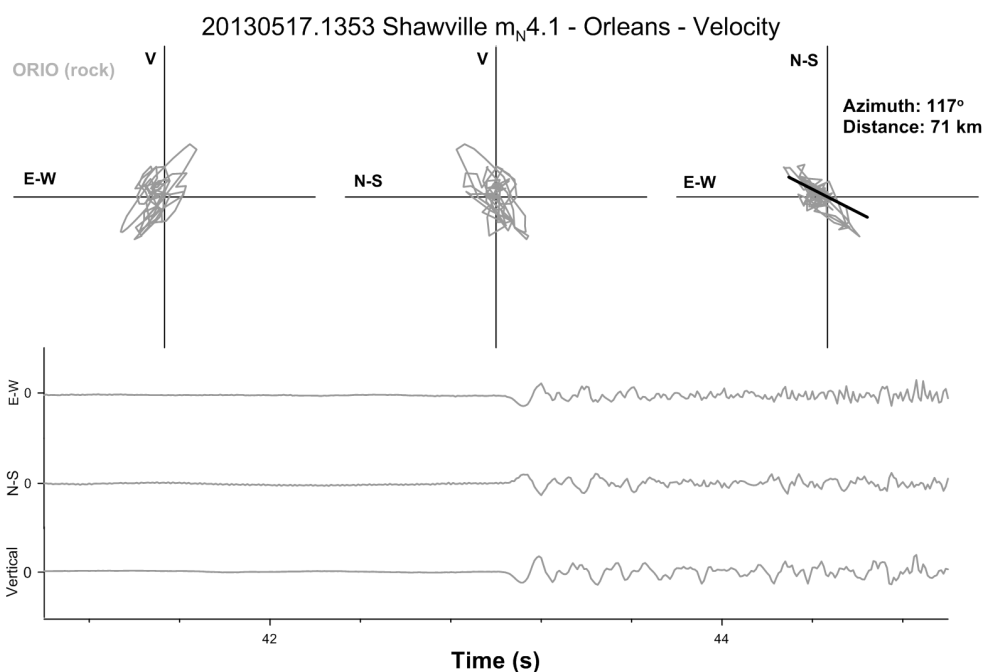


Fig. 6-3: Bottom shows the P-arrival on the 3 component data for the rock site (ORIO in light grey) for the 2013/05/17 $m_N 4.1$ earthquake near Shawville, QC. Top three plots are the particle motion plots (E vs Z; N vs Z; and E vs N) for the same time frame. The short black line on the third particle motion plot shows the azimuth of the earthquake to the station.

For basin-edge generated events, we expect to see shear waves converted at the basin-edge to surface waves which radiate within the basin. If these surface waves are Love waves, the plots should show the particles moving transverse in the horizontal plane only. For Rg waves, the plots should show the particles moving in the direction of the energy (from source to recording site) in a retrograde elliptical motion (energy in the

vertical direction, but none in the transverse). However, this can become more complicated, as shown in the paper by Konno and Ohmachi (1998). Their studies showed that the Rg wave motion depends on the velocity contrast of the rock and overlying soil. When there is a high impedance contrast ($V_{S_{\text{rock}}}:V_{S_{\text{soil}}} \geq 2.5$), like at our sites, the Rg wave motion transitions between normal retrograde motion at short periods, transitioning to prograde motion at medium periods, and back to retrograde at longer periods. At the transition point from retrograde to prograde (at lower periods), Konno and Ohmachi (1998) modelled the motion to be purely vertical, whereas the second transition from prograde back to retrograde was modelled to have purely horizontal motion (see Fig. 2-5, Ch. 2).

The original interest in examining the particle motion plots was to examine the long duration signal which occurs after the onset of the shear wave on soil sites within the basin, as this is the section of the coda most likely to contain basin-generated surface waves. If the wave energies are travelling in the direction that is not in line with the azimuth of the earthquake source, but systematically altered to a particular direction (perhaps in relation to a basin-edge), then we may surmise that this is due to the influence of the basin. However, as discussed in S4.1.4, due to the high frequency nature of the recordings, the direction of the motion changed often, sometimes several times within one second of recording time, making it difficult to detect any trend, even in the body wave coda at the sampling interval used. Hence an alternative way of representing the particle motion is required. As the preliminary particle motion results show that the

motion is predominantly horizontal (see Fig. 4-3, Ch. 4), we focus on the plots showing the two horizontal components.

Rose diagrams were tested as a means of highlighting the predominant direction recorded over a selected portion of the waveforms. To create a rose diagram, the particle motion angles are calculated for each sample over a chosen time window and then binned: in our case we are using 10 degree bins. The number of samples within a bin is then summed up and displayed on a circle as a 10 degree wedge at the corresponding angle. Hence, each rose diagram is a snapshot of the directions of particle motions over the entire chosen time frame. Fig. 6-4 shows results for the 2013/05/17 $m_N4.1$ Shawville, QC earthquake as recorded on the Orleans soil site, ORHO. The three component recording is shown under the rose plots as reference. The four rose plots show the results for the following time windows: 40-95s; 41-51s; 51-65s and 65-95s. The time segment of the first rose plot (top-left) was chosen to include the entire event, including the P-, S- and surface waves. As can be seen, this overall plot is not very useful, showing motions from all directions almost equally. However, that is expected when mixing several different types of arrivals together. Hence, the next three plots attempt to separate the incoming phases, with the chosen time window (41-51s) encompassing most of the P-wave, the next window (51-65s) including mostly the shear wave, and finally the last window (65-95s) containing what is interpreted as the basin-generated surface waves. However, the resulting rose plots even for these narrower time windows focussing on what should be just one type of energy, there is still no apparent preferred direction visible. A short pale grey line on the overall (top left) rose plot would indicate the

azimuth of the earthquake, and hence the expected direction of motion for the P-arrival.

To see if there's a pattern within a particular arrival, we need to break the time windows into even smaller segments.

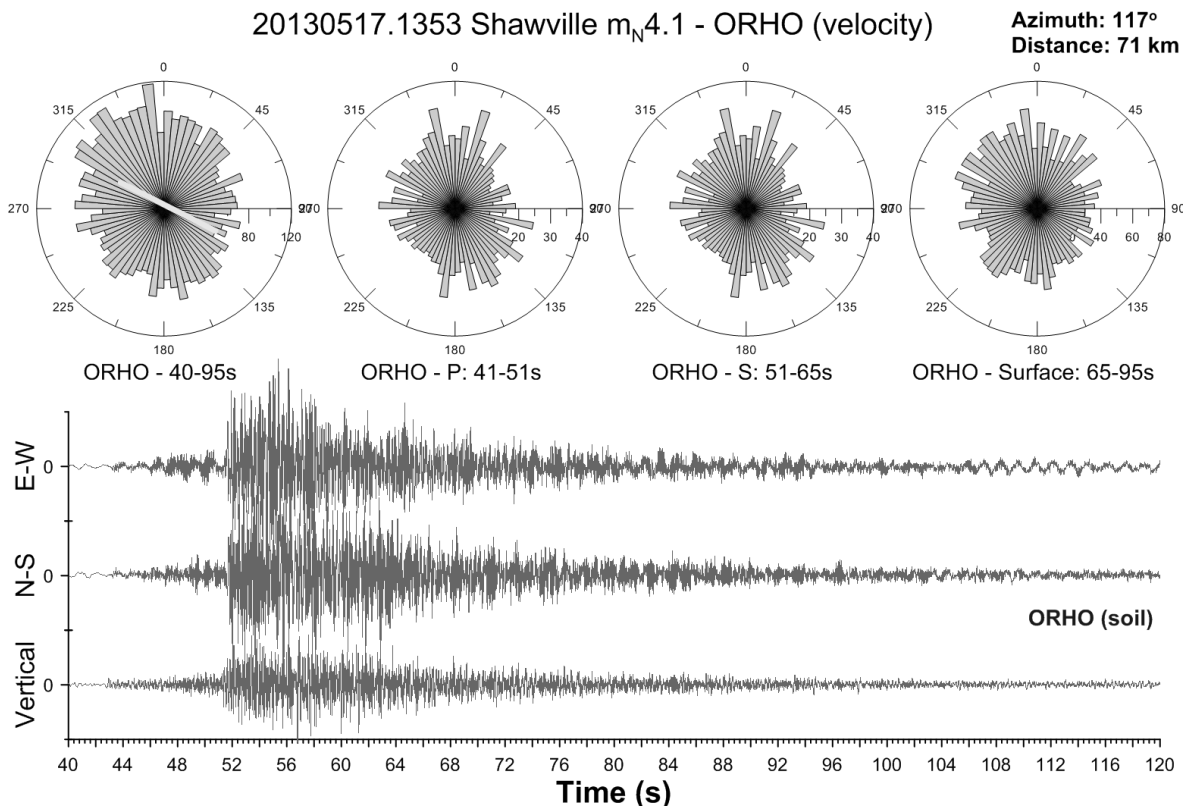


Fig. 6-4: ORHO data for the $m_N 4.1$ 2013/05/17 Shawville, QC earthquake. The lower plot shows the 3-component waveform as recorded on the soil site. The rose plots at the top show the particle motion direction on ORHO for the following time segments: 40-95s (P, S and surface waves included), 41-51s (P wave only), 51-65s (mostly S wave), and 65-95s (mostly surface wave energy). A pale grey line superimposed on the top-left rose plot indicates the azimuth of the earthquake (117°) to the station.

By examining the waveforms in shorter time intervals it is found that certain parts of the waveform do have distinct directions. Fig. 6-5 shows various rose diagrams from just the P arrival, one second at a time for each of the plot. However, the number of plots required quickly becomes overwhelming, even for just one phase. Furthermore, it is not easy to co-relate the results with the section of coda being examined. Hence, this

approach is also not adequate for capturing the changes in direction of motion, particularly in the latter part of the waveform.

Another option would be a plot similar to a spectrogram but showing density of particle motion directions as they vary in time. This will allow us to see not only which azimuths are prevalent in a waveform, but how these change with time throughout the recording. As well, all the information will be contained within one plot, making it easier to make interpretations within one recorded event, and to compare those results from one earthquake to another. A program, which we called “Azigram” was written to produce these types of plots and is described in the section below.

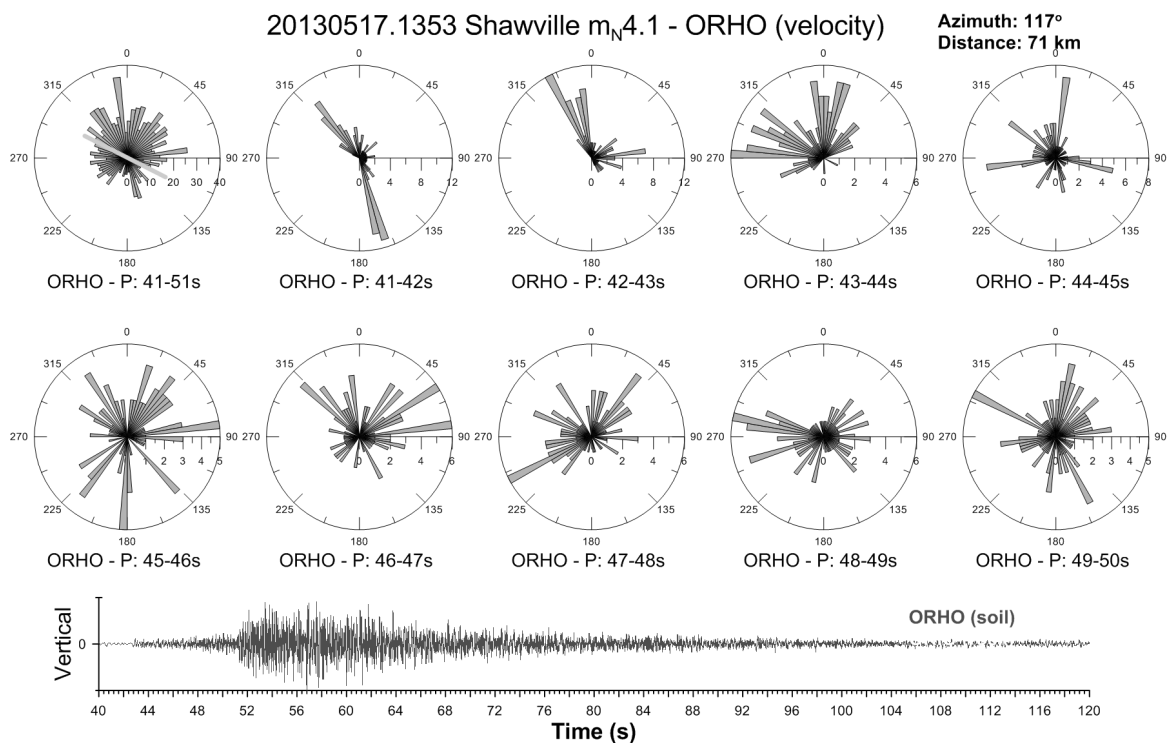


Fig. 6-5: ORHO (Orleans soil site) data for the m_N 4.1 2013/05/17 Shawville, QC earthquake. The lower plot shows the vertical component as recorded on the soil site. The rose plots at the top show the corresponding particle motion directions from ORHO for the entire P wave coda, and followed by 1s time windows throughout the P phase arrival (from 41-50s).

6.3 Azigram

Azigram is written in Python programming language (www.python.org) using Obspy (www.obspy.org), a set of modules specifically designed for processing seismological data. The direction and amplitude of particle motion was calculated along the time-series using the following two lines of code (for the complete Python code see Appendix D):

```
amplitude = [sqrt(n**2+e**2) for n,e in zip(trace_n.data, trace_e.data)]
pm_angle = [atan2(e,n)*180/pi for e,n in zip(trace_e.data, trace_n.data)]
```

The earthquake events being investigated are local, weak motion events that are rich in high frequency. In addition, background noise can be another obstacle for examination of local and small earthquakes. These may make the direction of the particle motion chaotic and difficult to interpret. Hence, the direction data was binned over a specific time span and range of direction and plotted in time along with the time series plotted below it, much like a spectrogram (see the caption of Fig. 6-6 for more information). A further plot weighted by amplitude was also produced. These plots were made for both the soil and the reference rock site, and the results compared.

The procedure outlined above was repeated with the data bandpass filtered from 0.3 Hz to 5 Hz. This helped reduce the random chatter of the higher frequencies, as well as the bias from very low frequencies. It was then repeated again for several narrow bandpass filters. The frequencies chosen were the ones that showed the highest amplifications in the calculated transfer functions for the earthquakes examined (see Fig. 4-12 in Ch. 4), and are interpreted to represent the fundamental frequency (f_0) and the

three higher harmonics (1st, 2nd and 3rd) of the Orleans basin: 0.8 Hz \pm 0.3 Hz, 1.8 Hz \pm 0.3 Hz, 2.9 Hz \pm 0.3 Hz, and 4.1 Hz \pm 0.5 Hz.

2011/07/21 Wakefield, QC m_N3.5

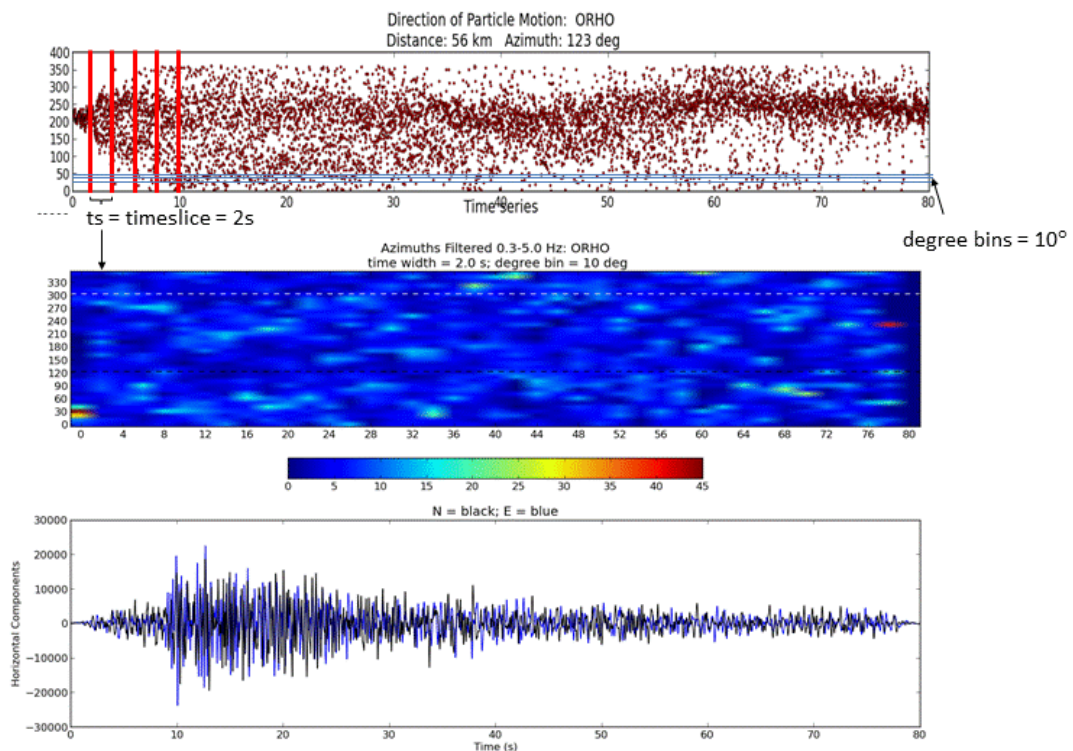


Fig. 6-6: The angle of particle motion for each sample of the two horizontal components (shown in the bottom plot: east in blue and north in black), is calculated and plotted in the top plot. This is then divided into 2s timeslices, and the number of samples within each 10 degree bins is counted and plotted in the middle plot. Data is from the 2011/07/21 m_N3.5 earthquake centred near Wakefield, QC.

After some testing of plot parameters, it was decided that a range of 10° bins over a 2 second time-slice allowed for sufficient samples within a bin-time step to highlight correlative sections along the time series where certain azimuths were preferred, without losing precision in direction or time of occurrence. It was noted, as it was expected, that

for signals with a lower frequency content such as in regional or teleseismic earthquake data, an increased time-step gave better results. In other words, the lower the frequency content of the data, the larger the ideal time-slice.

Furthermore, to avoid missing preferred directions that occur over a time-step boundary, an approach using overlapping bins was adopted. After some testing it was decided a 20% overlap could optimally be used. The difference between the plots for 10%, 20%, 30% and 40% were slight, but at 50% it was noted that significant smearing between time-step had occurred and precision was lost without gaining any new information.

Note that the stations/components and variables mentioned above (time-span, degree-bin size) are hard-coded into the program, but are easily changed in the code. We examine only the horizontal components of the soil and rock sites, as this is where the majority of the amplification was observed.

For the complete Python code used see Appendix D.

6.4 Tests to determine program settings

Azigram was found to perform best on earthquakes that were recorded on the soil site (ORHO) with high signal-to-noise, generally those magnitudes of around M3.5 or greater within the west Quebec seismic zone. Although some earthquakes of smaller magnitude produced interpretable results, in general there was not enough signal to noise to show strong preferred orientations. A dotted black line was added to the plot to show the azimuth of the earthquake (and a dotted white line for the back-azimuth) as an aid in the interpretation of the data.

6.4.1 Filtering and Weighting

Applying Azigram on unfiltered data produced no obvious pattern due to the high frequency scatter. Furthermore, the presence of very low frequency content unrelated to the local events of interest occasionally would result in the data to plot off-centre; in turn this resulted in spurious preferred azimuth over the entire length of the trace. Band pass filtering the data may eliminate or reduce these effects at either end of the frequency spectrum and allow preferred azimuths to appear in the data as shown in Fig. 6-7. The amplitude-weighted data approach helps to bring out details in some of the more energetic arrivals (i.e. the S wave arrival, and some later energy bursts), however some information from lower energy arrivals is lost.

6.4.2 Displacement versus Velocity Plots

Converting the data to displacement before plotting the results did not generally improve the resolution of the results. For the smaller events and unfiltered data, the quality of the displacement plots was significantly poorer. Hence, to simplify the processing, velocity data were used throughout for the particle motion analysis.

6.4.3 Response of rock site

The results from Azigram on the rock site (ORIO) show for the P arrivals a preferred azimuth in the direction of the azimuth/back-azimuth of the earthquake. The S arrivals are 90° from the direction shown for the P arrivals. These results from the rock site confirm the program works as expected. Note that the particle motion will move first in the direction it is pushed, and then back again in the opposite direction (e.g. azimuth/back-azimuth for the P arrival), hence there will always appear to be two

preferred directions for an arrival. Fig. 6-7 shows the results as seen on the rock site (ORIO) for the 2013/05/17 $m_N5.2$ earthquake centred near Shawville, QC. Note that a broadband filter of 0.3-5.0 Hz was used on the data prior to processing the particle motion directions. The top plot (a) shows the just the particle motion directions with time, while the plot underneath (b) shows the same data but multiplied by the amplitude of particle motion. The black and white dashed lines represent the azimuth and back-azimuth respectively. The earthquake trace as recorded by the ORIO horizontals is plotted underneath for reference (N-S in black; E-W in blue). The plot of horizontal particle motions clearly shows a preferred direction along the azimuth/backazimuth for the P arrivals (at around 10s in Fig. 6-7) while the S arrivals (at around 20s) appear perpendicular to it. In general, there is no further strong azimuthal preference after the S arrival.

6.4.4 Noise

When plotting noise before an event, the diagrams generally showed random patterns. However, occasionally a preferred azimuth could also be detected, if a polarized noise exists around the station, which was found to be the case for most of seismic stations close to urban areas. Usually, the polarized noise is amplified by local soil, thus, this tended to occur more frequently on the soil site than the rock, and was not always consistent across the different frequency bands. As the stations are located within the residential area, it is probable that these occasional patterns were due to local noise, or perhaps a more distant background low frequency signal. However, the pattern from the

noise is much lower amplitude than an earthquake event, and with a good signal to noise ratio, background noise should not influence the results.

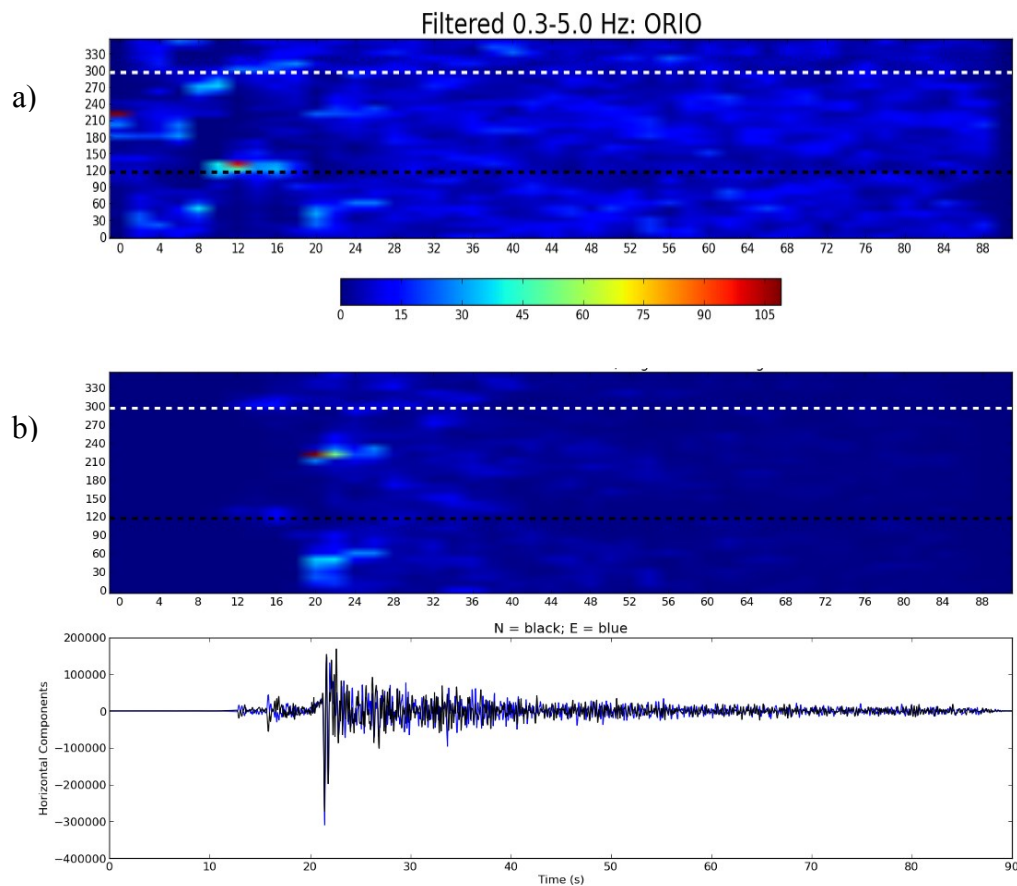


Fig. 6-7 - Particle motion analysis versus time for the bedrock site ORIO, showing the azimuth (black horizontal dashed line) and the backazimuth (white dashed line) for the 2013/05/17 m_N 5.2 Ladysmith, QC earthquake: a) broadband filtered from 0.3 – 5.0 Hz; and b) same filter but number of counts in bin multiplied by the amplitude; the two horizontal components (north-south = black; east-west = blue) are shown below at the same time scale for reference.

6.4.5 *Deconvolving rock from soil*

An attempt was made to remove the rock site response from the soil site. The assumption here is that both stations are recording the same energy from an earthquake, and the only difference between the two sites is the additional response from the basin on the soil site. Since the sets of two stations at each basin are relatively close to each other

(in the order of 1 or 2 kms), and the epicentral distance under consideration is generally quite large (often 100+ kms), this assumption is reasonable. However, the results obtained did not seem reasonable, most likely this was due to an error in processing. The error seems to occur when attempting to rotate the traces to the epicentre. Perhaps this is because the motion recorded on the soil sites do not behave as a normal rock site would (with the majority of the P-wave energy aligned along the azimuth of the earthquake, and the majority of the S-wave at 90° from the azimuth); or perhaps there is too much high frequency content which is not coherent between the two sites. High frequency energy is affected by much smaller scaled structures and can hence be quite localized. This problem has been seen in other basin experiments (e.g. Cornou and Bard, 2003; Stephenson, 2007). However, more likely there was an error in processing, which caused an artifact in the data. In any case, the results were not deemed to be trustworthy, and hence not used.

6.5 Seismic particle motions on ORHO

In contrast to the results from the rock site (ORIO), the azimuthal plots for the soil site (ORHO) show P-wave arrivals that almost never align with that of the earthquake, and in some cases are shifted a full 90° , as seen for the P phase arrival in Fig. 6-8 at around 16s. For the S wave arrivals (early high amplitude arrivals 25-32s) in Fig. 6-8, the direction of motion occurs at the earthquake azimuth (at 24-28s) and then “drifts” or migrates towards perpendicular directions (28-36s), possibly due to the arrival of surface waves combining with the shear wave. This “drifting” of the arrival appears as a “smearing” over several azimuthal bins, resulting in poor determination of the angle of

arrival. This same effect is visible within the P phase, and can best be seen for more distant events where there is more separation between the phases. When the same data is filtered around the fundamental frequency (see Fig. 6-9), the initial P phase arrival is clearer, but S wave arrivals appear weaker, with the change of the particle motion from one azimuth to another appearing more pronounced and of longer duration.

The data filtered around a narrow frequency band tend to have cleaner arrivals and less variation of azimuths along the time series. Commonly, filters centred around the 1st and 2nd harmonics show the clearest particle motions associated with arrivals for most events. The filter centred around f_0 commonly showed the azimuth of the particle motion “rolling” back and forth, as seen in Fig. 6-9. The exception is the 2012/10/10 M4.5 Vercheres, QC earthquake where, for the soil site, the particle motions analysed with this filter had a nearly constant direction of motion for both the P and S wave arrivals. The P wave showed azimuths to be slightly shifted from the direction of the earthquake, and the S wave arrivals showed orientations perpendicular to that of the P wave. Note, however, that this result was not typical for any of the other earthquakes analysed.

The recorded azimuths for any particular earthquake and the arriving phase did not always match between the different frequency bands. That is to say, the particle motion recorded for the P phase when applying a band-pass filter around the fundamental frequency could be different than that recorded when band-pass filtering around the dominant frequencies of the 1st or 2nd harmonic.

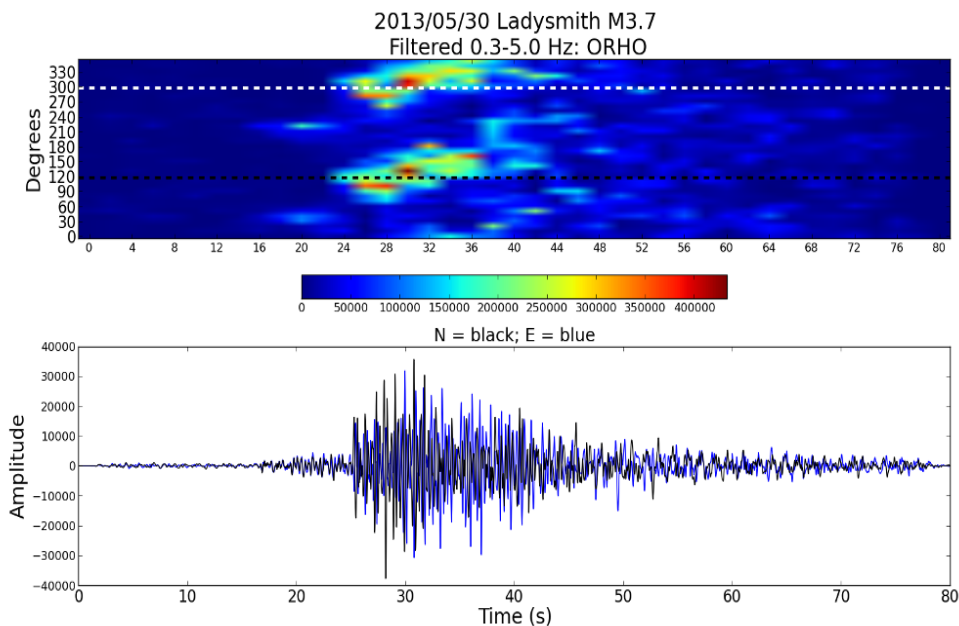


Fig. 6-8: Particle motion with respect to time for the soil site ORHO (dashed black line representing the event azimuth; backazimuth in white) for the 2013/05/30 $m_N 3.7$ Ladysmith, QC earthquake. The data is filtered from 0.3-5.0 Hz and weighted by amplitude.

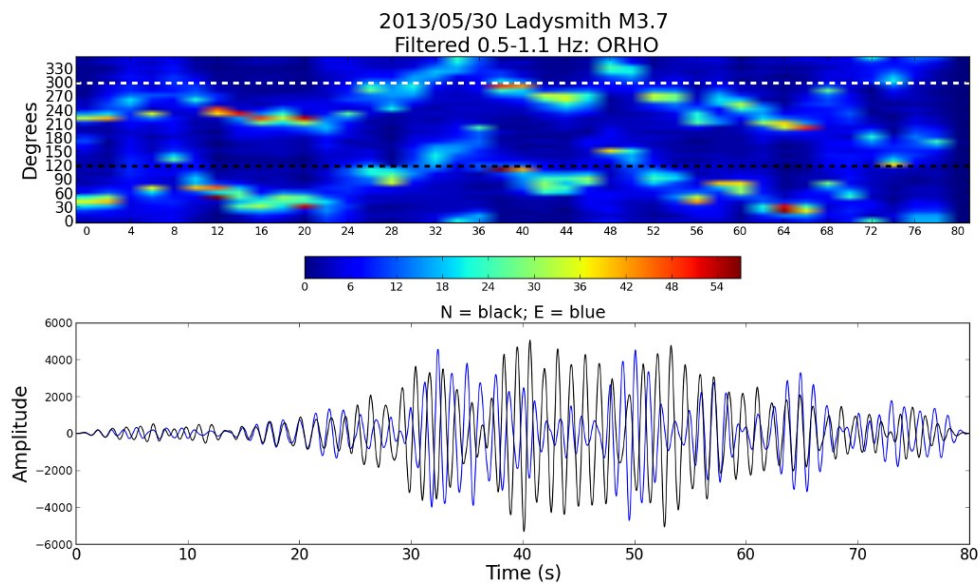


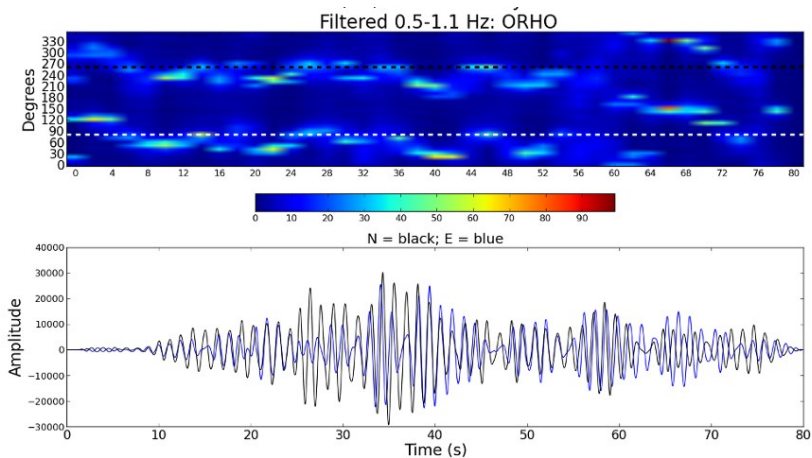
Fig. 6-9: Particle motion analysis with respect to time for the soil site ORHO (event azimuth in black, backazimuth in white) for the 2013/05/30 $m_N 3.7$ Shawville, QC earthquake, with data filtered around the fundamental frequency (0.8 ± 0.3 Hz) of the basin.

Even events from the same epicentral region (similar backazimuth and distance to source) do not show consistent results. Fig. 6-10 shows three events from the same azimuth: M4.3 2011/03/16 Hawkesbury, M4.5 2012/10/10 Vercheres, and M4.2 2012/11/06 Hawkesbury. Although there is some consistency for the P arrival on all three events, the first Hawkesbury event displayed a completely different azimuth for the S phases. The second Hawkesbury event and the Vercheres event are more consistent with each other, despite the differences in epicentral distances.

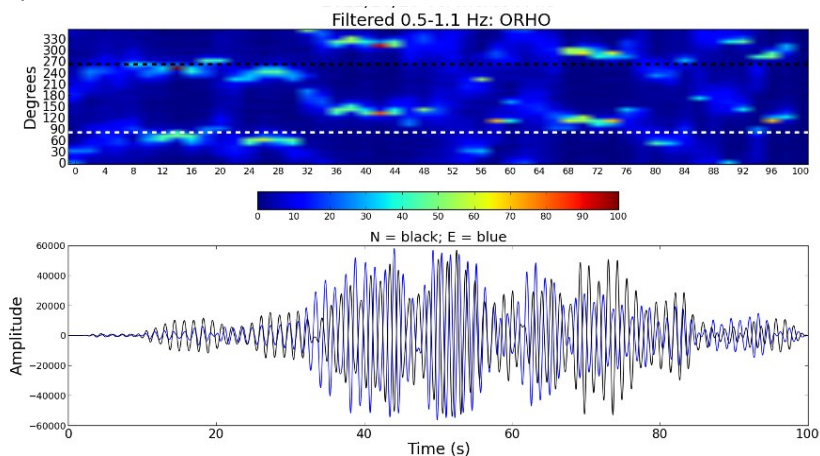
6.6 Interpretation

The particle motions for the P and S phase are as predicted for the nearby rock site. However, over the soil basin, the P and S arrivals are seemingly random. Both ORIO and ORHO were processed in the same manner, and processing errors can be ruled out. A systems error, such as the components being accidentally misnamed or switched, was also ruled out as the calculated predominant angles are not offset by a consistent amount. This was confirmed by Dr. Allison Bent of Natural Resources Canada (email communication, 2014), who had found no issues with this particular station during her checks of the network stations. Hence, the variation in the arrival azimuths may be due to the presence of the 3D geometry from either the bedrock basin or the soil layers within that basin.

a) 2011/03/16 Hawkesbury M4.3: azimuth = 260° , distance = 78 km



b) 2012/10/10 Vercheres M4.5: azimuth = 262° , distance = 178 km



c) 2012/11/06 Hawkesbury M4.2: azimuth = 258° , distance = 75 km

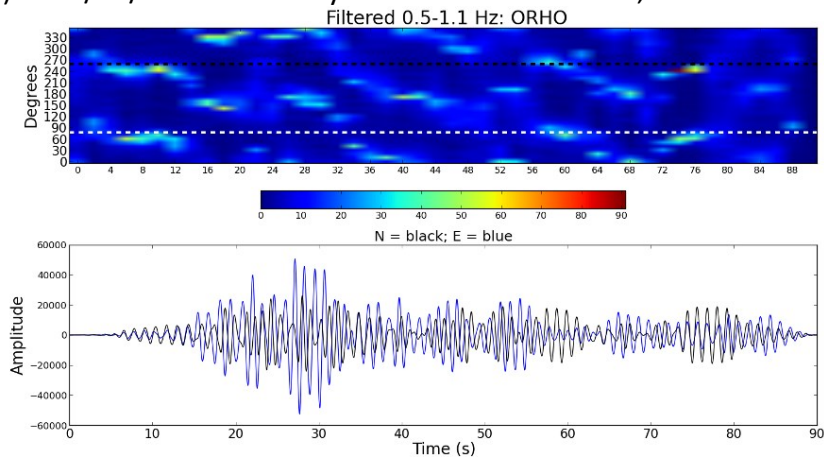


Fig. 6-10: Particle motion analysis on soil site ORHO for three earthquakes from similar azimuths, narrowband filtered around the fundamental frequency from 0.5 – 1.1 Hz.

Note that the conversion of one phase to another could also be occurring at the basin boundary. For example, as a P-wave encounters a basin boundary, it can be converted to an S-phase. And this would also lead to changes in the particle motion that is observed.

The azimuths of the particle motion do not seem to be related to the earthquake itself. There is no relation or systematic offset from the direction of the earthquake to the recorded incoming phases. As events similar in magnitude, azimuth and distance produced different resulting plots, frequency content, radiation pattern and/or other source parameters could play a role in the final effect of the basin on the redirection of the energy, as evidenced by the events shown in Fig. 6-10. However, lack of data (number of events, and information on their focal mechanisms) does not allow us to come to any definite conclusion.

The reduction of the “drifting” effect in the narrow band filtered data versus the more broadly filtered data suggests that the drifting and smearing of arrivals may be due to waves of various frequencies each being affected differently by the basin.

The occasional variation of particle motion azimuth for a phase from a particular earthquake filtered at different narrow bandpass ranges, also suggest that the initial frequency content of the earthquake may play a role in the basin response modifications to the final ground motion at the soil site. Plots from more distant events commonly showed the “migrating” of direction of motion occurring several seconds into the P phase already.

6.7 Discussion

The initial focus of this study was to determine whether the basin played a role in the recorded ground motions. In Ch. 5 it was determined that the amplifications for the Orleans basin appear to differ from that which is calculated using a 1D ground motion modelling software. Furthermore, although the surrounding bedrock and in-fill soil material is similar for all three basins, the amplification results varied from basin to basin, suggesting the 3D bedrock basin affects the ground motion over the basin. However, the examination of the particle motions could not constrain any preferred orientations of surface waves that would be related to the 2D and 3D basin geometry. It should be noted that the shape of the Orleans basin is somewhat complicated and small in size, which may play a role in the lack of obvious relation between the ground motions, with possible reflections at basin edges from multiple directions.

The particle motion of the soil site recording also did not seem to be related to the azimuth of the earthquake, unlike the nearby rock site that clearly showed expected particle motions for both the P and S phases. Hence, although not predictable or repeatable, the basin is nonetheless affecting the resulting direction of the particle motions. Filtering the data at several narrow frequency bands helped to isolate the motions of various frequencies, but did not help determine any pattern to the data with respect to either the earthquake location or local 2D and 3D geometry.

As only one soil station is available per basin, the difference between the azimuth and backazimuth cannot be sorted out using this method of displaying the recorded

motion. This is not a problem on the rock site on which the motions are oriented as expected, or even on the soil site when the angle is not too far removed from the original (as the wave is unlikely to be travelling from the far end of the basin back to the source). However, at more extreme deviations from the expected arrival angle, it becomes impossible to determine which angle is the azimuth of the motion, which is deleterious to any interpretation of a possible pattern. The installation of an array would eliminate this ambiguity and allow tracking of coherent energy across the basin.

The other two basins have also been instrumented: Lefaiivre with a station pair, and Kinburn which initially had only one station pair but has since been upgraded to a six-station array (see Crane et al., 2015). Now that the manufacturer has fixed the data-downloading software bug, in the future, the data from these basins can also be analyzed and compared with the results obtained from Orleans. It will take time, however, to collect a significant number of events with sufficient signal to noise with which to do this type of analysis for these two basins.

7. Discussion

7.1 Discussion of results of this study

For this study, we examined data recorded over three different soft-sediment filled basins in the Ottawa, Ontario region and determined that the buried bedrock geometries generated 3D site effects that were visible in both the frequency content and the particle motion of the surface ground motions at the basins. Although the three basins are all relatively small (varying in size from 3 km by 5 km and 100 m deep, to 10 km by 18 km and 140 m deep) and contain similar low velocity material, known locally as Leda clay, overlying a thin layer of glacial till and bedrock with relatively high Vs (~2700 m/s on average), the three basins reacted quite differently to similar ground motion inputs. 1D modelling for all three basins was able to predict some, but not all of the features of the recorded soil to rock ratios.

Site conditions over buried basins have been found to have a significant impact on the resulting surface ground motions. Kawase (1996) noted that the surface waves impinging on much lower velocity soft sediments will be greatly amplified, and that this could have significant implications for higher seismic hazard over these local basins. Since the local Leda clay has such an extremely low velocity, and is contrasted by high velocity bedrock, these 3D site effects may play a very important role in local seismic hazard of the Ottawa, Canada region.

The earthquake sources are mainly from the adjacent west Quebec seismic zone which experiences mostly weak motion events, with approximately 50 M2+ events per year. For much of our analysis we studied mainly weak motion events of M3+ that were well recorded by both the rock and the soil sites at a particular basin. The seismograph sites had been operational on the Orleans, Kinburn and Lefavre basins since 2007, 2010 and 2012 respectively, and earthquake data until late 2013 was used for this study. Unfortunately due to a manufacturer software bug, the data downloaded from the latter two basins did not have accurate timing until the beginning of 2014, and hence could not be used in the particle motion analysis portion of this work.

The earthquake data available for this study were obtained from three station pairs, with one seismograph site roughly over the centre of the basin, and the second site on nearby bedrock acting as a reference. Thus, since the source of the recorded motions was at least 10's of kms distant, the path of the motion to the soil and rock site were mostly identical except for the last couple of kms. In other words, the difference between the rock and soil site recordings should reflect the difference in the site conditions.

The data were examined to verify whether the presence of the basin caused 3D effects such as focusing-defocusing, resonance and/or basin-edge effects and whether these made an important contribution to the overall ground motion within the basin. Certainly 1D effects alone did not account for the recorded data, hence the presence of 2- and 3-D effects due to the buried bedrock basin and/or the in-filling soil layer were found to influence the ground motions in terms of frequency, amplification and particle motion, although the exact nature of this influence is less clear. Note that smaller scale structures

will have an influence on the higher frequencies, while larger scale structures will influence the lower frequencies.

From comparing the motions and the original time series of the basin recordings versus those on rock, it is immediately evident that the duration of the coda is much longer on the soil site, particularly at the lower frequencies, and that there are later energetic beats evident on the soil sites that are not present on the reference rock sites. This has been noted in other basins (e.g. Chávez-García and Bard, 1994) and was attributed to 3D effects, possibly due to either resonance (e.g. Bard and Bouchon, 1985), or to the conversion of late-arriving phases at the basin-edge (Stephenson et al., 2006), or basin-edge effects in general (Kawase and Aki, 1989).

From examination of the soil stations the first arrival of the P-wave on the horizontal component of motion is followed 0.3 s later by a highly amplified arrival, with low-frequency content. It appears that the basin “reacts” to the first P-arrival by producing basin-generated waves (whether through resonance or through generation of surface waves at the basin boundary) with an amplified wave of frequencies particular to the fundamental and harmonics of the soil site within the basin. Another possibility is that due to the large contrast in velocities from the rock to the soil, that all the P wave energy is directed purely vertically, accounting for the lack of arrivals noted at the expected P-wave arrival time. Furthermore, the P wave energy (which travels along the ray path) could also be converted to S wave energy at the basin boundary, which is a slower wave, which would then arrive later than the expected P wave on the horizontals. The S wave particle motion is perpendicular to the ray path, with both horizontal (SH) and vertical

(SV) components. However, the arrivals noted on the horizontal components of the recording station on the Orleans basin were chaotic for both the P and the S arrival, and followed no systematic pattern.

Examining the long duration coda within the basin in detail, we see a pattern of changing particle motion directions along the trace; the motions are mostly amplified in the horizontal directions, supporting concept that these are surface waves which have been recorded on the soil sites. Although generally Love waves show only horizontal motion, while Rayleigh waves display both a horizontal and a vertical component, the modelling work done by Konno and Ohmachi (1999) does predict that for sites with high impedance contrast, Rayleigh waves may contain mainly horizontal motion as well. Hence, one could only distinguish between the two wave-types solely based on the direction of particle motion. Unfortunately as no clear pattern in terms of direction was visible for any of the phases, including the body waves, there was neither a way to discern the types of surface waves recorded, nor the location(s) where they might be being generated.

From measured soil to rock seismic parameters, 1D ground motion modelling was able to predict the general shape of the spectral amplification observed from the measured spectra of the earthquake recordings for the Orleans and Kinburn basin. There is a consistent pattern of highest soil-rock amplification at the fundamental frequency f_0 , and with the subsequent diminishing harmonic peak amplitudes. Very little or no amplification was observed at frequencies less than the f_0 ; the exception was the Lefaiivre basin transfer function which in contrary predicted the 1st harmonic as the highest peak.

A similar pattern of amplifications at the fundamental and higher harmonic frequencies was also found by Cornou and Bard (2003) for the Grenoble basin, which is also small in size, but filled with alluvial sediments which are deeper than any of our Ottawa area basins. Cornou and Bard (2003) suggested that any amplification above the predicted 1D amplification must be due to 3D effects.

For all models, the predicted peaks are sharply defined, with narrow peaks with virtually no amplification in between these maxima. These amplification peaks in the models studied are “shifted” to slightly lower frequencies than shown by the field observations of earthquake events (based on the smoothed FFT ratios of the recorded data). For the Lefaivre basin, the modelled transfer function showed a similar shift to lower frequencies than the recorded soil-to-rock ratios, with the 1st harmonic being modelled as the largest peak rather than the f_0 , a feature which is not reflected in the actual data. This underestimation of the f_0 peak likely occurred due to the “shift”, since the frequency content of the observed earthquake data from the west Quebec seismic zone which was used as the input ground motion is quite rich in high frequencies. For models where we used lower frequency input events (the Californian earthquakes), the f_0 was once again predicted to be the highest peak. This demonstrated the importance of using appropriate ground motion inputs with the expected frequency content in order to correctly model the basin response.

The modelling results demonstrated that the basin response can be modelled to a certain level using a 1D ground motion modelling software, but with important differences. For one, as previously mentioned, the peaks are slightly “shifted” to lower

frequencies. This is likely a result of the V_s profile for clay, which is approximated with discrete interval velocity $V_{s_{int}}$ layers and taken from discrete readings along the profile. As noted by Vrettos (2013), however, that by substituting discrete approximate layers with a continuous V_s -versus-depth profile will result in a shifting of the peaks.

An HVSR reading or local recording can be used to easily calculate the actual fundamental frequency (and for the local recordings, one can also obtain the peaks for the higher harmonics), which can be used to verify the modelling results, and adjust them if necessary. Note that the HVSR readings, however, neither correctly predict the absolute amplification recorded from the spectral ratios of the shear and surface waves of the weak motion events for each basin, nor do they show the relative amplification between the basins from the spectral ratios (based on the smoothed FFT ratios of the recorded data): e.g. the amplification at the fundamental frequency for the Orleans basin is almost twice that of the other two basins, ~ 70 times versus ~ 35 times respectively. The HVSR readings instead show similar amplifications ranging from between 5 times to 12 times for all three of the basins.

In order for a 1D model to yield a reasonable transfer function, it was found that it was important to have several key pieces of information: a reasonably accurate V_s profile for the clay (as mentioned above); an appropriate modulus reduction and damping ratio set of curves for the material being examined; and finally, in order to compare results obtained from the modelled transfer functions to the actual soil-to-rock spectral ratios, the appropriate ground motion inputs are required. In other words, earthquake recordings with the correct magnitude and frequency content must be used. Hence, recordings from

other areas of the world may not be appropriate. This is important as there are relatively few strong motion recordings for eastern Canada, and in particular for eastern Ontario/western Quebec.

Although there was a general agreement in shapes of the transfer functions as modelled by Proshake (see Eqn 5.3) and the spectral ratios based on the smoothed FFT soil-to-rock ratios of the recorded data, the comparison of the models and the observations showed different results for the three basins. These results differed despite the fact that all three basins are reasonably similar in depth (100 m, 120 m and 140 m for the Orleans, Kinburn and Lefaivre basins respectively), and that all three are filled with similar soft-sediments and underlain by a till layer and bedrock of similar material properties. Hence the differences must come from the variations in the 3D geometric properties of the three basins.

For Orleans, the peak amplification for the fundamental resonant frequency is under-predicted while the amplifications of the higher harmonics are almost equal to that predicted. The amplification peaks from the observed soil to rock ratios, while being the most narrow, and well defined of the three basins, were much wider than the peaks modelled by the software. Hence, even after accounting for the higher frequency content of the local earthquakes, the particular nature of the Leda clay with modulus reduction and damping curves data specifically obtained from this material, and a very detailed $V_{s_{int}}$ profile based partly on borehole data, there are yet more amplification effects than can be accounted for using a 1D model. As suggested by Cornou and Bard (2003), this additional amplification must be due to 3D effects due to the basin.

The Kinburn basin, on the other hand, showed much less amplification for each of the resonant peaks, with the fundamental f_0 amplification over-predicted to the observed soil-to-rock spectral ratios. The amplification peaks in the modelled ratios are much wider than those from the Orleans basin, with each peak made up of three closely spaced peaks for the fundamental as well as for each of the subsequent higher harmonics. This is not reflected in the modelled transfer function peaks, which are shown as sharp and narrow and well defined for this basin as they are for the other two. This phenomenon suggests a possible effect of the 3D geometry of the bedrock basin.

The modelled transfer function for the Lefavre basin is different from the other two basins, since the 1st harmonic is indicated to be the highest predicted peak, instead of the fundamental. As discussed above, this is likely due to the modelling “shifting” the peaks to lower frequencies, and the local earthquakes having more energy in the higher frequencies. However, the observed soil to rock spectral amplification ratios are similar to the ones found at Kinburn, being shifted slightly towards lower frequencies (due to the slightly deeper soft soil layer), and less well defined. The latter characteristic might also be due to the lack of data for this basin, as it was only recently instrumented and hence had the least number of recorded events over all from which to choose; hence we were forced to use smaller earthquakes to obtain our ratios.

Examining the soil to rock spectral amplification ratios for each of the basins individually, it was noted that in comparing earthquake events there is sometimes a slight shifts of peak amplification frequencies from one earthquake to another. Using earthquakes from one source (a series of main shock and aftershocks) we can see this

phenomenon for events occurring close to the same time, and of similar distance and azimuth. Examining events of similar magnitude also showed a shift. But no pattern was discernable in terms of any of these variables, hence no connection of the location of the fundamental peak with azimuth, distance, magnitude or time. Hence it is probable that focal mechanisms may play a role, as well as possibly combinations of the variables mentioned above.

Overall, there is plenty of suggestion of basin effects in all of the following: the character of the signals, the particle motions, the amplifications and the spectral ratios. It has been shown in both the particle motion analysis results and the spectral analysis that the incoming frequencies play an important role in the subsequent interaction with the basin. Although without array studies within a basin it is difficult to come to a definite conclusion, Kawase (1996) suggested that if the amplification is due to focussing, then the location of the highest amplification of the motion at the surface of the basin does not change from one earthquake event to another, whereas the location of highest amplitude is frequency dependent for basin-edge effects. Since this study contained only rock-soil station pairs we cannot observe other locations in the basin; however Kawase's work does suggest that the basin-edge may play a larger role than basin shape focussing at our sites.

Given the pattern that amplification is mostly found at the fundamental frequency and higher harmonics, we can also firmly state that resonance plays a major role in the amplifications seen at all three sites. However, the much higher amplification than predicted for the Orleans basin, and the wider peaks with possible sub-peaks at the f_0 and

harmonics for the other two basins shows that at all three basins there are effects beyond 1D amplification that are making significant contributions, and that the geometries of buried-bedrock basins' may be significant factors as well.

7.2 Future work

An array of five soft soil seismograph sites, along with one reference rock site have been installed on the Kinburn basin, across the width of the basin, with one extra station along the length in the middle (Crane et al., 2015). This will allow for the comparison of amplification of the ground motion at sites with different depths and proximities to the basin-edges. For example, 1D analysis may be less appropriate at the basin edges (Gvirtzman and Louie, 2010). The array data will also allow ray processing techniques to be used to map the direction of the energies of the waves over the basin and may help define the type of wave energies that are prevalent (Chávez-García et al., 2002), as well as identifying the origins of these wave energies (Stephenson et al., 2006).

More data has been collected on both the Kinburn and Lefaiivre basin since 2014, with no timing issues, allowing for particle motion analysis to be performed for any new earthquakes that are well recorded by these basins. The new data will add to the ranges of azimuths, distances, and magnitudes, which may help develop any patterns or dependencies of the results to these variables where they exist. Focal mechanism data could also be added, at least for the medium sized events to verify whether this affects particle motions and/or ratios over the basin. Once such data have been collected and analyzed for all three basins, it might also be possible to compare the results between the

basins to compare similarities or differences. This might help to determine the contribution of the shape of the basins (e.g. larger, solitary, elongated bowl shape versus elongated, interconnected basin, with one sharp edge, etc.) to the ground motion responses over the basins.

In terms of the modelling work, the data collected for 1D profiling is comprehensive in terms of the depths and shear wave velocity profiles for the clay layer. More data on the till layer would be useful, but generally the variation in till properties in the Ottawa region has only minor effects on the results.

The quality, Q , of the bedrock and soil which make up the basins, determines the amount of damping on the recorded ground motion. As was noted by Ramos-Martínez et al., (1997), Q has an important influence on the amplitude and duration of the soil response. The surface waves, guided by shallow layers, can attenuate quickly. Therefore, knowing Q can help determine the placement of the soil sites on the basin. For larger basins, Ramos-Martínez et al. (1997) speculate that the stations need to be relatively close to the basin-edge to capture the surface waves. The Q for the soft sediments is not very well determined yet, and is work that is currently on-going.

The newest curves for Leda clay from the current studies by Carleton University, Laval University and University of Waterloo in collaboration with GSC should be used to help predict what will occur at higher strain levels. To do this, strong motion data (synthetic or real) with similar frequency content and higher PGA's must be used in the simulations.

The results from the 1D modelling in this study should also be compared to results from other 1D modelling programs (e.g. non SHAKE-based programs) to ensure consistency and highlight any limitations or biases from the SHAKE equivalent-linear algorithms. Furthermore, 3D modelling on these basins needs to be completed, and the outcomes compared to the actual recordings. The differences seen between the recordings and the 1D models should be accounted for by the 3D models, and the 3D modelling should help identify the nature of the sources of amplification.

Finally, the “disturbed” Lefaiivre basin shows various levels of surface topographic upheaval (from 3-8 m) over the entire basin (Aylsworth et al., 2000). It might be interesting to map this upheaval to see if any patterns emerge in terms of the amount of upheaval versus the location on the basin. If this were the case, it would provide a guide as to the changing amplitudes of the ground motions over this particular basin. Note that neither of the other two basins being investigated have this “disturbed” ground feature, although there are other basins in the Ottawa region that do show interpreted earthquake triggered “disturbed” surface features (e.g. Brooks, 2013).

7.3 Requirements for further study

The prime limiting factor in this study was the amount of recorded earthquake data. In order to do a much more thorough analysis on the various parameters affecting the particle motion and the soil to rock ratios on the three basins, a much larger data set is required which would sample more distances, azimuths, magnitudes, etc. First, the rate of earthquakes from the west Quebec seismic zone is on average 50 M2+ per year. For

much of our analysis we preferred the higher signal-to-noise events of M3+, hence only a handful of events were available for the Kinburn and Lefaiivre basins, since the stations were installed in 2010 and 2012 respectively. This paucity of data was further exacerbated for the particle motion analysis due to a data collection software bug, which meant that the timing between components for the Kinburn and Lefaiivre basin data were not in synch (See Appendix A). This problem was fixed in early 2014, but unfortunately for this study we only looked at data until the end of 2013. Hence no particle motion analysis could be done for either of these basins.

We did perform particle motion analyses for the Orleans basin, which had been installed in 2007 and had no timing issues. But for this basin, the events used were mostly limited to the west Quebec seismic zone, with a range of a few kilometres around ~200 km and with back-azimuths generally between 270° and 90° to the north (~180° of azimuth coverage only). Some azimuths were more prevalent than others. From the more distant earthquakes, only one Charlevoix event (~400 km) was of large enough magnitude to be well recorded, while only two regional events (M5.4 Illinois and M5.8 from Richmond, VA) were captured.

Note that our basins are located in or close to urban areas, and hence polarized noise from cultural sources may also hinder the determination of the dominant particle motion directions on earthquake ground motions. This is particularly true for the Orleans basin which is located within a residential area, and the Kinburn basin which is located in an active farming area.

The earthquakes in this study were all weak motion events that were large enough to be well recorded on the soil sites ($\sim M3.0+$; possibly smaller if very close to recording site). Hence the magnitude and PGA (peak ground acceleration) range is limited. Unfortunately, it is difficult to record strong motion events as they are rare in this region. The largest magnitude and strongest PGA events (due to its proximity to the study area) were the $m_N5.7$ (**M5.0**) Val-des-Bois, QC event of 2010/06/23 earthquake, with a PGA of ~ 0.02 on calculated from the OTT seismograph, and the $m_N5.1$ Shawville, QC event with a PGA of 0.04 on JSBS. This was also the largest ever recorded earthquake in the Ottawa region, although the magnitude for an earthquake that might have caused the ground disturbance at the Lefaivre basin is estimated to exceed $M6.5$ (Aylsworth et al., 2000).

The above suggests that the determination of distance, magnitude, PGA, and time effects on the particle motion or frequency content of the soil to rock spectral amplification ratios is limited in scope. Note that there was little to no information available on the focal mechanisms of most of the earthquakes used, so no analysis on the effect of this variable was possible.

The lack of observational data affected the scope of 1D modelling as well. Theoretically, due to soil non-linearity, we would expect that a larger PGA event should have less amplification than smaller events. The frequency content of a larger magnitude event would also be significantly different than the smaller earthquakes which are limited to mostly high frequencies. However, due to both a lack of modulus reduction and damping curves for Leda clay, and local data, the non-linear behaviour of our basins for larger PGA events could not be modelled.

Finally, all of the work thus far has been based on one single soil station located at the middle of the basin. This yields the earthquake response at only one point in the basin, but does not give us any areal or regional infra-basin response. Furthermore, it also limits the particle motion analysis, as we can only observe the onset of wave motion but not the direction of the wave energy; this limits the conclusions that can be drawn from our analysis. Although 1D modelling has been shown to provide some reasonable estimates of the resulting ground motion over the basins, there were some obvious differences from the 1D model and the actually observed data. These differences have been attributed to the 3D effects from the bedrock basin. In order to model these effects a 3D model would be required, as well as 3D modelling software.

8. Conclusions

In examining the time series data recorded on our three basins has shown that the Ottawa region basins have ground motions with many of the same features as seen in other basins around the world to be related to 2- and 3D effects, including strong horizontal amplification, extended duration of the signal, with mono-frequency and late energetic beats. In particular the strongly horizontal motion and long durations point to the generation of surface waves generated by the basin-edge.

The soil-to-rock spectral ratios for all three basins are similar in terms of general shape, with the highest amplification recorded at the fundamental frequency, f_0 . This frequency was similarly recorded in the spectral ratios of teleseismic, regional and local earthquake data; however, the higher harmonics were only captured in the local and regional data, due to the lower frequency content of the teleseismic source. The HVSR noise recordings also can be used to determine the f_0 , but since these readings are done only on the soil site, they do not reflect the amplification seen on soil versus rock, nor do they record the higher harmonics.

Despite general similarities in the spectral ratio curves, there are differences in terms of the peaks, with fundamental and harmonics being narrower for the Orleans basin, while the other two had much broader peaks. The Kinburn basin even had multiple peaks. Given that all three basins are surrounded by the same or similar bedrock and are

filled with soft-soil with similar geophysical properties, the difference was determined to be due to the basin geometry at each site.

Although the spectral ratios for each basin were in general found to be quite robust, they did shift slightly in terms of frequency, and sometimes quite a lot in amplification, from earthquake to earthquake. However, no predictable relationship was found in terms of azimuth, distance, magnitude or time.

When attempting to model the transfer function for a particular site profile using ground motion modelling software, it was found that the results were most sensitive to the material properties of the soft soil layer. In particular, the outputs depended mostly on the Vs, as well as which modulus reduction and damping ratio curves used for each layer. Furthermore, input motions were found to be equally important, as the frequency content of the small to moderate earthquakes from the local west Quebec seismic zone differed greatly to the standard strong motions from California.

When using the most detailed profile, with the appropriate Leda clay curves, all three sites had resulting transfer functions which showed sharp peaks at a fundamental frequency and higher harmonics. However, these curves were still slightly shifted from the actual recorded spectral ratios for each basin. Furthermore the recorded peaks were either broader or significantly higher than the predicted amplifications from the calculated transfer functions, suggesting the contribution of 2 and 3-D effects.

The particle motions recorded on the soil site ORHO were found to be changing with time and dependant on frequency. Hence 2 and 3-D structures in the basin's bedrock

geometry, and/or in the soil layers are influencing the incoming waves, with larger scale structures influencing the lower frequencies, while the smaller scale structures are influencing the higher frequencies.

References

Chapter 1.

Aylsworth, J.M., Lawrence, D.E., and Guertin, J. (2000). Did two massive earthquakes in the Holocene induce widespread landsliding and near-surface deformation in part of the Ottawa Valley, Canada? *Geology*, **28**, 903-906.

Benjumea B., Hunter J. A., Aylsworth J. M. and Pullan S. E. (2003). Application of high-resolution seismic techniques in the evaluation of earthquake site response, Ottawa Valley, Canada. *Tectonophysics* 368, 193–209.

Hunter, J.A., Crow, H.L., Brooks, G.R., Pyne, M., Motazedian, D., Lamontagne, M., Pugin, A.J.-M., Pullan, S.E., Cartwright, T., Douma, M., Burns, R.A., Good, R.L., Kaheshi-Banab, K., Caron, R., Kolaj, M., Folahan, I., Dixon, L., Dion, K., Duxbury, A., Landriault, A., Ter-Emmanuel, V., Jones, A., Plastow, G., and Muir, D. (2010). Seismic Site Classification and Site Period Mapping in the Ottawa Area Using Geophysical Methods. *Geological Survey of Canada, Open File 6273*.

Kawase, H. (1996). The cause of the damage belt in Kobe: “The basin-edge effect,” constructive interference of the direct S-wave with the basin induced diffracted/Rayleigh waves, *Seismological Research Letters*, **67**, 25-41.

Microzonation in the Ottawa Region: Vs30 map and borehole information, Carleton University, Ottawa, Canada; [Accessed: April 2015]: <http://http-server.carleton.ca/~dariush/Microzonation/main.html>

Chapter 2.

Bard, P.-Y. and Bouchon, M. (1980a). The seismic response of sediment-filled valleys. Part I. The case of incident *SH* waves, *Bull Seismol Soc Am*, **70**, 1263-1286.

Bard, P.-Y. and Bouchon, M. (1980b). The seismic response of sediment-filled valleys. Part II. The case of incident *P* and *SV* waves, *Bull Seismol Soc Am*, **70**, 1921-1941.

- Bard, P.-Y. and Bouchon, M. (1985). The two-dimensional resonance of sediment-filled valleys, *Bull Seismol Soc Am*, **75**, 519-541.
- Beck, J.L., and Hall, J.F. (1986). Factors contributing to the catastrophe in Mexico City during the earthquake of September 19. 1985. *Geophysical Research Letters*, **13**, 593-596.
- Boore, D.M. and W.B. Joyner (1997). Site amplifications for generic rock sites. *Bulletin of the Seismological Society of America*, **87**, 327-341.
- Borcherdt, R.D. (1970). Effects of Local Geology on Ground Motion near San Francisco Bay. *Bull Seismol Soc Am*, **60**, 29-61.
- Chávez-García, F.J. and Bard, P.-Y. (1993 a). Gravity Waves in Mexico City? –I. Gravity Perturbed Waves in an Elastic Solid. *Bull Seismol Soc Am*, **83**, 1637 – 1655.
- Chávez-García, F.J. and Bard, P.-Y. (1993 b). Gravity Waves in Mexico City? –II. Coupling Between an Anelastic Solid and a Fluid Layer. *Bull Seismol Soc Am*, **83**, 1656 – 1675.
- Chávez-García, F.J. and Bard, P.-Y. (1994). Site effects in Mexico City eight years after the September 1985 Michoacán earthquakes. *Soil Dynamics Earthquake Engineering*, **13**, 229-247.
- Chávez-García, F.J., Castillo, J., and Stephenson, W.R. (2002). 3D Site-Effects: A Thorough Analysis of a High-Quality Dataset, *Bull Seismol Soc Am*, **92**, 1941-1951.
- Cornou, C., and Bard, P.-Y. (2003). Site-to-bedrock over 1D transfer function ratio: An indicator of the proportion of edge-generated surface waves? *Geophysical Research Letters*, **30**, 1453-1456.
- Day, S.M., D. Roten, and K.B. Olsen (2012). Adjoint analysis of the source and path sensitivities of basin-guided waves, *Geophys. J. Int.*, Vol 189, pp. 1103-1124.
- Delépine, N., and Semblat, J.-F. (2012). Site effects in an alpine valley with strong velocity gradient: Interest and limitations of the ‘classical’ BEM, *Soil Dynamics and Earthquake Eng.*, **38**, 15-24.
- Field, E.H. and SCEC Phase III Working Group. (2000). Accounting for Site Effects in Probabilistic Seismic Hazard Analyses of Southern California: Overview of the SCEC Phase III Report, *Bull Seismol Soc Am*, **90**, no. **6B**, S1-S31.

- Field, E. H. (1996). Spectral amplification in a sediment-filled valley exhibiting clear basin-edge induced waves. *Bull. Seism. Soc. Am.*, **86**, 991-1005.
- Flores, J., Novaro, O., and Seligman, T.H. (1987). Possible resonance effect in the distribution of earthquake damage in Mexico City. *Nature*, **326**, 783-785.
- Foda, M.A., and Chang, Y.H. (1996). Faraday resonance in thin sedimentary layers, *Eleventh World Conference on Earthquake Engineering*, **Paper No. 86**.
- Furumura, T. and Kennett, B.L.N. (1998). On the nature of regional seismic phases -III. The influence of crustal heterogeneity on the wavefield for subduction earthquakes: the 1985 Michoacan and 1995 Copala, Guerrero, Mexico earthquakes, *Geophys. J. Int.*, **135**, 1060-1084.
- Gilbert, F. (1967). Gravitationally perturbed Rayleigh waves, *Bull Seismol Soc Am*, **57**, 783-794.
- Graves, R.W., Pitarka, A., and Somerville, P.G. (1998). Ground-Motion Amplification in the Santa Monica Area: Effects of Shallow Basin-Edge Structure, *Bull Seismol Soc Am*, **88**, 1224-1242.
- Hunter, J.A., Crow, H.L., Brooks, G.R., Pyne, M., Motazedian, D., Lamontagne, M., Pugin, A.J.-M., Pullan, S.E., Cartwright, T., Douma, M., Burns, R.A., Good., R.L., Kaheshi-Banab, K., Caron, R., Kolaj, M., Folahan, I., Dixon, L., Dion, K., Duxbury, A., Landriault, A., Ter-Emmanuel, V., Jones, A., Plastow, G., and Muir, D. (2010). Seismic Site Classification and Site Period Mapping in the Ottawa Area Using Geophysical Methods. *Geological Survey of Canada, Open File 6273*.
- IASPEI Standard Seismic Phase List*. (2003). International Seismological Centre, Thatcham, U.K. [Accessed: May 2015]. <http://www.isc.ac.uk/standards/phases/>
- Joyner, W.B. (2000). Strong motion from surface waves in deep sedimentary basins, *Bull. Seism. Soc. Am.*, **90**, no. **6B**, S95-S112.
- Kato, K., Aki, K., and Teng, T-L. (1993). 3-D Simulations of surface wave propagation in the Kanto Sedimentary Basin, Japan – Part 1: Application of the Surface Wave Gaussian Beam Method. *Bull Seismol Soc Am*, **83**, 1676 – 1699.
- Kawase, H. and Aki, K. (1989). A study on the response of a soft soil basin for incident S, P, and Rayleigh waves with special reference to the long duration observed in Mexico City, *Bull Seismol Soc Am*, **79**, 1361-1382.

- Kawase, H. (2008). Seismic Responses of Irregular Ground – Four Decades of Development from Theory to Observation. *In proceedings of the 14th World Conference on Earthquake Engineering*. Beijing, China.
- Kawase, H. (1996). The cause of the damage belt in Kobe: “The basin-edge effect,” constructive interference of the direct S-wave with the basin induced diffracted/Rayleigh waves, *Seismological Research Letters*, **67**, 25-41.
- Kham, M., Semblat, J.-F., and Bouden-Romdhane, N. (2013). Amplification of seismic ground motion in the Tunis basin: Numerical BEM simulations vs experimental evidences.
- Kolaj, M. (2010). Ottawa bedrock shear wave classification and weak motion earthquake site amplifications for the Orleans buried valley. Bachelor of Science, Honours thesis, Carleton University.
- Konno, K., and Ohmachi, T. (1998). Ground-motion Characteristics Estimated from Spectral Ratio between Horizontal and Vertical Components of Microtremor, *Bull. Of the Seismological Society of America*, **88**, 228-241.
- Kramer, S.L. (1996). *Geotechnical Earthquake Engineering*, Prentice Hall, New Jersey, p. 653.
- Liu, H.-L., and Heaton, T.H. (1984). Array analysis of the ground velocities and accelerations from the 1971 San Fernando, California, earthquake, *Bull. Seism. Soc. Am.* **74**, 1951-1968.
- Lomnitz, C. (1990). Mexico 1985: the case for gravity waves. *Geophys. J. Int.*, **102**, 569-572.
- Lomnitz, C. (1996). The gravilastic Equation and the Emergence of Gravity Waves in Large Earthquakes, *Bull. Seismological Society of America*, **86**, 1220-1228.
- Malischewsky Auning, P.G., Lomnitz, C., Wuttke, F., and Saragoni, R. (2006). Prograde Rayleigh-wave motion in the valley of Mexico, *Geofisica Internacional*, **45**, 149-162.
- Pal, J.D. and Atkinson, G.M. (2012). Scenario ShakeMaps for Ottawa, Canada. *Bull Seismol Soc Am*, **102**, 650-660.
- Pedley, T.J. (1997). *Introduction to Fluid Dynamics*, Scientia Marina, **61**, 7-24.

- Pugin, A.J.-M., Brewer, K., Cartwright, T., Pullan, S.E., Perret, D., Crow, H., and Hunter, J.A. (2013). Near surface S-wave seismic reflection profiling – new approaches and insights, *First Break*, **31**, 49 – 60.
- Olsen, K.B., Pechmann, J.C., and Schuster, G.T. (1995). Simulation of 3D elastic wave propagation in the Salt Lake Basin, *Bull. Seism. Soc. Am.* **85**, 1688-1710.
- Olsen, K.B., and Schuster, G.T. (1995). Causes of low-frequency ground motion amplification in the Salt Lake Basin: the case of the vertically-incident *P* wave. *Geophys. J. Int.* **122**, 1045-1061.
- Olsen, K. B. (2000). Site amplification in the Los Angeles basin from three-dimensional modeling of ground motion. *Bull. Seism. Soc. Am.*, **90**, S77 –S94.
- Ramos-Martínez, J. Chávez-García, F. J. Romero-Jiménez, E. Rodríguez-Zúñiga, J. L. Gómez-González, J. M. (1997). Site effects in Mexico City: Constraints from surface wave inversion of shallow refraction data, *J. Appl. Geophys.*, **36**, 157-165.
- Rial, J.A., Saltzman, N.G., and Ling, H. (1992). Earthquake-Induced Resonance in Sedimentary Basins, *American Scientist*, **80**, 566-578.
- Sanchez-Sesma, F., Chavez-Perez, S., Suarez, M., Bravo, M.A., and Perez-Rocha, L.E. (1988). On the seismic response of the Valley of Mexico, *Earthquake Spectra*, **4**, 569-589.
- Semblat, J.F., Kham, M., and Bard, P.Y. (2008). Seismic-Wave Propagation in Alluvial Basins and Influence of Site-City Interaction. *Bull Seismol Soc Am*, **98**, 2665 – 2678.
- Semblat, J.F., Kham, M., Parara, E., Bard, P.Y., Pitilakis, K., Makra, K., and Raptakis, D. (2005). Seismic wave amplification: Basin geometry vs soil layering, *Soil Dynamics and Earthquake Engineering*, **25**, 529-538.
- Semblat, J.F., Dangla, P., and Kham, M. (2002). Seismic Site Effects for Shallow and Deep Alluvial Basins: In-Depth Motion and Focusing Effect, *Soil Dynamics and Earthquake Engineering*, **22**, 849-854.
- Shearer, P.M., and Orcutt, J.A. (1987). Surface and near-surface effects on seismic waves – theory and borehole seismometer results, *Bull Seismol Soc Am*, **77**, 1168 – 1196.
- Singh, S.K., Mena, E., and Castro, R. (1988). Some Aspects of Source Characteristics of the 19 September 1985 Michoacan Earthquake and Ground Motion Amplification in and near Mexico City from Strong Motion Data. *Bull Seismol Soc Am*, **78**, 451-477.

- Singh, S.K. and Ordaz, M. (1993). On the Origin of Long-Coda Observed in the Lake-bed Strong-Motion Records of Mexico City. *Bull Seismol Soc Am*, **83**, 1298-1306.
- Somerville, Paul, Nancy Collins, Robert Graves, and Arben Pitarka (2002). *Development of an Engineering Model of the Amplitude and Duration Effects of Basin Generated Surface Waves*. SMIP02 Seminar on Utilization of Strong-Motion Data, p. 127 - 146.
- Stephenson, W.R. (2007). Visualisation of resonant basin response at the Parkway array, New Zealand. *Soil Dynamics and Earthquake Engineering*, **27**, 487 – 496.
- Stephenson, W.R., Lomnitz, C., and Flores, H. (2006). Late resonant response at Texcoco, Valley of Mexico, during distant earthquakes. *Soil Dynamics and Earthquake Engineering*, **26**, 791-798.
- U.S. Geological Survey, Department of the Interior/USGS. (July 2012). Boulder Colorado, USA. [Accessed: October 2015]: <http://earthquake.usgs.gov/learn/glossary/>
- Vidale, J. E., and D. V. Helmberger (1988). Elastic finite-difference modeling of the 1971 San Fernando, California earthquake. *Bull. Seism. Soc. Am.* **78**, 122-141.
- Vrettos, C. (2013). Dynamic response of soil deposits to vertical SH waves for different rigidity depth-gradients, *Soil Dynamics and Earthquake Engineering*, **47**, 41-50.

Chapter 3.

- Adam, J., and Basham, P. (1989). The seismicity and seismotectonics of Canada, east of the Cordillera, *Geosci. Can.*, **16**, 3 – 16.
- Adam, J., and Basham, P. (1991). The seismicity and seismotectonics of eastern Canada. In *Neotectonics of North America*, edited by D.B. Slemmons et al., pp. 261-276, Geol. Soc. Of Am., Boulder, Colorado.
- Aylsworth, J.M., Lawrence, D.E., and Evans, S.G. (1997). Landslide and settlement problems in sensitive marine clay, Ottawa Valley. Geological Association of Canada, Mineralogical Association of Canada, Joint Annual Meeting, 1997, Ottawa, Field Trip b1, 63 p. (fieldbook)
- Aylsworth, J.M., Lawrence, D.E., and Guertin, J. (2000). Did two massive earthquakes in the Holocene induce widespread landsliding and near-surface deformation in part of the Ottawa Valley, Canada? *Geology*, **28**, 903-906.

- Aylsworth, J.M. and Hunter, J.A. (2004). A geophysical investigation of the geologic controls on landsliding and soil deformation in sensitive marine clay near Ottawa; *in* Proceedings of Geo-Engineering for the Society and its Environment. 57th Canadian Geotechnical Conference and the 5th joint CGS-IAH Conference. Quebec, Quebec. October 24-27, 2004.
- Baird, A.F., McKinnon, S.D., and Godin, L. (2010). Relationship between structures, stress and seismicity in the Charlevoix seismic zone revealed by 3-D geomechanical models: Implications for the seismotectonics of continental interiors, *J. of Geophys. Research*, **115**,
- Bard, P.-Y. and Bouchon, M. (1985). The two-dimensional resonance of sediment-filled valleys, *Bull Seismol Soc Am*, **75**, 519-541.
- Basham, P.W., Weichert, D.H., and Berry, M.J. (1979). Regional assessment of seismic risk in eastern Canada. *Bull. Seism. Soc. Am.* **69**, 1567-1602
- Benjumea B., Hunter, J. A., Aylsworth J. M. and Pullan S. E. (2003). Application of high-resolution seismic techniques in the evaluation of earthquake site response, Ottawa Valley, Canada. *Tectonophysics* 368, 193–209.
- Bent, A.L. and Perry, C. (2002). Depths of eastern Canadian earthquakes from region data, *Seism. Res. Letters.* **73**, 273 – 284.
- Bent, A.L, Drysdale, J. and Perry, C. (2003). Focal Mechanisms for Eastern Canadian Earthquakes, 1994 – 2000, *Seism. Res. Letters.* **74**, 452 – 468.
- Brooks GR (2013). A massive sensitive clay landslide, Quyon Valley, southwestern Québec, Canada, and evidence for a paleoearthquake triggering mechanism. *Quaternary Research*. Retrieved from <http://dx.doi.org/10.1016/j.yqres.2013.07.008>.
- Brooks GR (2014). Prehistoric sensitive clay landslides and paleoseismicity in the Ottawa Valley, Canada. In "Landslides in sensitive clays: from geosciences to risk management." 119-131. L'Heureux, et al. (Eds.), *Advances in Natural and Technological Hazards Research* 36, Dordrecht. Springer Science+Business Media.
- Cassidy, J.F. Rogers, G.C., Lamontagne, M., Halchuk, S., and Adams, J. (2010). Canada's Earthquakes : 'The Good, the Bad, and the Ugly'. *Geoscience Canada.* **37** (1), 1-16.

- Crane, S. (2016). *Numerical Modelling of Seismic wave propagation through a soft soil basin: Kinburn, Ontario*, PhD thesis - in progress, Earth Sciences Department, Carleton University, Ottawa, Canada.
- Crow, H. Pyne, M., Hunter, J.A., Pullan, S.E., Motazedian, D., Pugin, A.J-M. (2007). Shear wave measurements for earthquake response evaluation in Orleans, Ontario. Geological Survey of Canada, Open File 5579, 29 pages 1 CD-ROM
- Dineva, S., Eaton, D., Ma, S., and Mereu, R. (2007). The October 2005 Georgian Bay (Canada) earthquake sequence: Mafic dykes and their role in the mechanical heterogeneity of Precambrian crust, *Bull. Seismol. Soc. Am.* **97**, 457 – 473.
- Eden, W.J., and Crawford, J.B. (1957). Geotechnical properties of Leda clay in the Ottawa area. National Research Council of Canada, Research paper no. 37 of the Division of Building Research, Ottawa, ON
- Forsyth, D.A. (1981). Characteristics of the western Quebec seismic zone, *Can. J. Earth Sci.* **18**, 103-119.
- Gadd, N.R. (1986). Lithofacies of Leda clay in the Ottawa Basin of the Champlain Sea. Geological Survey of Canada, Paper 85-21, 44 p.
- Graves, R.W., Pitarka, A., and Somerville, P.G. (1998). Ground-Motion Amplification in the Santa Monica Area: Effects of Shallow Basin-Edge Structure, *Bull Seismol Soc Am*, **88**, 1224-1242.
- Guralp Systems Ltd. (c 2016). Reading, U.K. [Accessed January 2016]: <http://www.guralp.com>
- Harrison, J.E., and MacDonald, G. (1979). Generalized bedrock geology, Ottawa-Hull, Ontario and Quebec, available from Geogratis (<http://geogratis.gc.ca/api/en/nrcan-nrcan/ess-sst/92ba532f-7ad7-50e6-b12c-757c24c930f1.html>): Geological Survey of Canada, "A" Series Map, **Issue 1508A** (Licence: <http://open.canada.ca/en/open-government-licence-canada>)
- Hunter, J.A. Research Scientist, Geological Survey of Canada, Natural Resources Canada.
- Hunter, J.A., Burns, R.A., Good, R.L., Aylsworth, J.M., Pullan, S.E., Perret, D., and Douma, M. (2007). Borehole shear wave velocity measurements of Champlain Sea sediments in the Ottawa-Montreal region, *Geological Survey of Canada, Open File 5345*.

- Hunter, J.A., Crow, H.L., Brooks, G.R., Pyne, M., Motazedian, D., Lamontagne, M., Pugin, A.J.-M., Pullan, S.E., Cartwright, T., Douma, M., Burns, R.A., Good, R.L., Kaheshi-Banab, K., Caron, R., Kolaj, M., Folahan, I., Dixon, L., Dion, K., Duxbury, A., Landriault, A., Ter-Emmanuil, V., Jones, A., Plastow, G., and Muir, D. (2010). Seismic Site Classification and Site Period Mapping in the Ottawa Area Using Geophysical Methods. *Geological Survey of Canada, Open File 6273*.
- Kao, H., Shan, S.-J., Bent, A., Woodgold, C., Rogers, G., Cassidy, J.F., and Ristau, J. (2012). Regional Centroid-Moment-Tensor Analysis for Earthquakes in Canada and Adjacent Regions: An Update, *Seism. Res. Letters*. **83**, 505 – 515.
- Kinematics Inc. (c. 2015). Pasadena, CA, USA. [Accessed January 2016]: <http://www.kinematics.com>
- Kolaj, M. (2010). Ottawa bedrock shear wave classification and weak motion earthquake site amplifications for the Orleans buried valley. Bachelor of Science, Honours thesis, Carleton University.
- Kramer, S.L. (1996). Geotechnical Earthquake Engineering, Prentice Hall, New Jersey, p. 653.
- Lamontagne, M. and Ranalli, G. (2014). Earthquakes and geological structures of the St. Lawrence Rift System. In: Intraplate earthquakes, by Talwani, P (ed.) p1-25, Cambridge University Press.
- Lamontagne, M. (1987). Seismic activity and structural features in the Charlevoix region, Quebec, *Can. Journal of Earth Sciences*, **24**(11), 2118-2129.
- Lin, L., and Adams, J. (2010). Strong Motion Records of the Val-des-Bois, Québec, Earthquake of June 23, 2010. Canadian Hazards Information Service Internal Report 2010-1.1, 20 pages plus digital appendix.
- Ma, S. and Atkinson, G. (2006). Focal depth distribution for earthquakes with $m_N \geq 2.8$ in western Quebec, southern Ontario, and northern New York, *Bull. Seismol. Soc. Am.*, **96**, 609 – 623.
- Ma, S. and Eaton, D. (2007). The western Quebec seismic zone (Canada): clustered, mid-crustal seismicity along a Mesozoic hot spot track, *J. of Geophys. Research*, **112**, B06305. Doi 10.1029/2006JB004827
- Medioli, B.E., Alpay, S., Crow, H.L., Cummings, D.I., Hinton, M.J., Knight, R.D., Logan, C., Pugin, A.J.-M., Russell, H.A.J., and Sharpe. (2012). Integrated datasets

from a buried valley borehole, Champlain Sea basin, Kinburn Ontario; Geological Survey of Canada Current Research 2012-13.

- Microzonation in the Ottawa Region: Vs30 map and borehole information, Carleton University, Ottawa, Canada; [Accessed: April 2015]: <http://http-server.carleton.ca/~dariush/Microzonation/main.html>
- Motazedian, D., Khaheshi Banab, K., Hunter, J.A., Sivathayalan, S., Crow, H. and Brooks, G. (2011). Comparison of Site Periods Derived from Different Evaluation Methods, BSSA, v 101, pp2942-2954.
- Motazedian, D; and Hunter, J.A. (2008). Development of a NEHRP map for the Orleans suburb of Ottawa, Ontario. *Canadian Geotechnical Journal*, **45**(8);1180-1188.
- Motazedian , D., J.A. Hunter, A. Pugin, K. Khaheshi Banab, H.L. Crow (2011). Development of a Vs30 (NEHRP) Map for the City of Ottawa, Ontario, Canada”, *Canadian Geotechnical Engineering Journal*. doi:10.1139/T10-081. [NSERC and GSC].
- Nakamura, Y. (1989). A Method for Dynamic Characteristics Estimation of Subsurface Using Microtremor on the Ground Surface. Quarterly Report of RTRI, **30 (1)**, 25-33.
- Nanometrics Inc. (c. 2016). Kanata, ON, Canada. [Accessed January 2016]: <http://www.nanometrics.com>
- National Building Code of Canada. (2005). Canadian commission on building and fire codes, National Research Council Canada, NRCC 47666, 1167 pp., <http://www.nrc-cnrc.gc.ca/eng/ibp/irc/codes/05-national-building-code.html>.
- Earthquakes Canada. Natural Resources Canada (NRCan), Ottawa, Canada. [Accessed 2012/10]: www.earthquakescanada.nrcan.gc.ca
- Rial, J.A., Saltzman, N.G., and Ling, H. (1992). Earthquake-Induced Resonance in Sedimentary Basins, *American Scientist*, **80**, 566-578.
- Williams, D.A. (1991). Paleozoic geology of the Ottawa – St. Lawrence Lowland, southern Ontario. Ontario Geological Survey, Open File Report 5770, 292p.

Chapter 4.

- Beck, J.L., and Hall, J.F. (1986). Factors contributing to the catastrophe in Mexico City during the earthquake of September 19, 1985. *Geophysical Research Letters*, **13**, 593-596.
- Bolt, B.A. (1969). Duration of strong motion, Proceedings of the 4th World Conference on Earthquake Engineering, Santiago, Chile, pp. 1304 - 1315.
- Bouaanani, N. and Frasson-Botton, C. (2013). Correlations of three-component ground motions from the 23 June 2010 Val-des-Bois, Quebec, earthquake. *J. Seismol.*, **v17**, pp 861-881.
- Chávez-García, F.J. and Bard, P.-Y. (1994). Site effects in Mexico City eight years after the September 1985 Michoacán earthquakes. *Soil Dynamics Earthquake Eng.*, **13**, 229-247.
- Cornou, C., and Bard, P.-Y. (2003). Site-to-bedrock over 1D transfer function ratio: An indicator of the proportion of edge-generated surface waves? *Geophysical Research Letters*, **30**, 1453-1456.
- Dobry, R., Oweis, I., and Urzua, A. (1976). Simplified procedures for estimating the fundamental period of a soil profile, *Bull Seismol Soc Am*, **66**, 1293-1321.
- Field, E.H. and SCEC Phase III Working Group. (2000). Accounting for Site Effects in Probabilistic Seismic Hazard Analyses of Southern California: Overview of the SCEC Phase III Report, *Bull Seismol Soc Am*, **90**, no. **6B**, S1-S31.
- Flores, J., Novaro, O., and Seligman, T.H. (1987). Possible resonance effect in the distribution of earthquake damage in Mexico City. *Nature*, **326**, 783-785.
- Graves, R.W., Pitarka, A., and Somerville, P.G. (1998). Ground-Motion Amplification in the Santa Monica Area: Effects of Shallow Basin-Edge Structure, *Bull Seismol Soc Am*, **88**, 1224-1242.
- Hatton, L., Worthington, M.H., and Makin, J. (1986). *Seismic Data Processing*, Blackwell Scientific Publications, London, U.K.
- Joyner, W.B. (2000). Strong motion from surface waves in deep sedimentary basins, *Bull. Seism. Soc. Am.*, **90**, no. **6B**, S95-S112.

- Kato, K., Aki, K., and Teng, T-L. (1993). 3-D Simulations of surface wave propagation in the Kanto Sedimentary Basin, Japan – Part 1: Application of the Surface Wave Gaussian Beam Method. *Bull Seismol Soc Am*, **83**, 1676 – 1699.
- Kawase, H. and Aki, K. (1989). A study on the response of a soft soil basin for incident S, P, and Rayleigh waves with special reference to the long duration observed in Mexico City, *Bull Seismol Soc Am*, **79**, 1361-1382.
- Kawase, H. (1996). The cause of the damage belt in Kobe: “The basin-edge effect,” constructive interference of the direct S-wave with the basin induced diffracted/Rayleigh waves, *Seismological Research Letters*, **67**, 25-41.
- Kham, M., Semblat, J.-F., and Bouden-Romdhane, N. (2013). Amplification of seismic ground motion in the Tunis basin: Numerical BEM simulations vs experimental evidences.
- Kolaj, M. (2010). Ottawa bedrock shear wave classification and weak motion earthquake site amplifications for the Orleans buried valley. Bachelor of Science, Honours thesis, Carleton University.
- Konno, K., and Ohmachi, T. (1998). Ground-motion Characteristics Estimated from Spectral Ratio between Horizontal and Vertical Components of Microtremor, *Bull. Of the Seismological Society of America*, **88**, 228-241.
- Kramer, S.L. (1996). Geotechnical Earthquake Engineering, Prentice Hall, New Jersey, U.S.A., p. 80.
- Narayan, J.P., (2012). Effects of P-Wave and S-Wave Impedance Contrast on the Characteristics of Basin Transduced Rayleigh Waves, *Pure and Applied Geophys.*, **169**, 693-709.
- Ramos-Martínez, J. Chávez-García, F. J. Romero-Jiménez, E. Rodríguez-Zúñiga, J. L. Gómez-González, J. M. (1997). Site effects in Mexico City: Constraints from surface wave inversion of shallow refraction data, *J. Appl. Geophys.*, **36**, 157-165.
- Semblat, J-F, Duval, A-M., and Dangla, P. (2000). Numerical analysis of seismic wave amplification in Nice (France) and comparisons with experiments, *Soil Dynamics Earthquake Eng.*, **19**, 347-362.
- Singh, S.K. and Ordaz, M. (1993). On the Origin of Long-Coda Observed in the Lake-bed Strong-Motion Records of Mexico City. *Bull Seismol Soc Am*, **83**, 1298-1306.

- Somerville, Paul, Nancy Collins, Robert Graves, and Arben Pitarka (2002). *Development of an Engineering Model of the Amplitude and Duration Effects of Basin Generated Surface Waves*. SMIP02 Seminar on Utilization of Strong-Motion Data, p. 127 - 146.
- Stephenson, W.R. (2007). Visualisation of resonant basin response at the Parkway array, New Zealand. *Soil Dynamics and Earthquake Engineering*, **27**, 487 – 496.
- Stephenson, W.R., Lomnitz, C., and Flores, H. (2006). Late resonant response at Texcoco, Valley of Mexico, during distant earthquakes. *Soil Dynamics and Earthquake Engineering*, **26**, 791-798.
- Telford, W.M., Geldart, L.P, and Sheriff, R.E. (1990). *Applied Geophysics*, 2nd ed., Cambridge University Press, New York, N.Y., U.S.A. p218
- Vrettos, C. (2013). Dynamic response of soil deposits to vertical SH waves for different rigidity depth-gradients, *Soil Dynamics and Earthquake Engineering*, **47**, 41-50.

Chapter 5.

- Assimaki, D., Li, W., Steidle, J., and Schmedes, J. (2008). Quantifying nonlinearity susceptibility via site-response modeling uncertainty at three sites in the Los Angeles basin. *Bull. Seism. Soc. Am.* **98**, 2364-2390.
- Aylsworth, J.M., Lawrence, D.E., and Guertin, J. (2000). Did two massive earthquakes in the Holocene induce widespread landsliding and near-surface deformation in part of the Ottawa Valley, Canada? *Geology*, **28**, 903-906.
- Benjumea B., Hunter, J. A., Aylsworth J. M. and Pullan S. E. 2003. Application of high-resolution seismic techniques in the evaluation of earthquake site response, Ottawa Valley, Canada. *Tectonophysics* 368, 193–209.
- Centre for Engineering Strong Motion Data; Data provided by the California Strong Motion Instrumentation Program (CSMIP) and the USGS National Strong Motion Project (NSMP). [Accessed: October 2014]: www.strongmotioncenter.org
- Crow, H.L., Hunter, J.A., Pugin, A.J.M., Pullan, S.E., Alpay, S. and Hinton, M. (2014). Empirical Geophysical/Geotechnical Relationships in the Champlain Sea Sediments of Eastern Ontario. Chapter 20 pp253-264 From: J.-S. L'Heureux et al. (eds.), *Landslides in Sensitive Clays: From Geosciences to Risk Management*, Advances in

- Natural and Technological Hazards Research 36, doi 10.1007/978-94-007-7079-9_20, Springer Science+Business Media Dordrecht 2014
- Crow, H., Hunter, J.A., Pugin, A., Brooks, G., Motazedian, D., and Khareshi-Banab, K. (2007). Shear Wave Measurements for Earthquake Response Evaluation in Orleans, Ontario. The Diamond Jubilee, Ottawa, ON
- Crow, H. Pyne, M., Hunter, J.A., Pullan, S.E., Motazedian, D., Pugin, A.J-M. (2007). Shear wave measurements for earthquake response evaluation in Orleans, Ontario. Geological Survey of Canada, Open File 5579, 29 pages 1 CD-ROM
- Das, B.M. (2008). Advanced Soil Mechanics – Third Edition, Taylor and Francis, New York, NY.
- Destegül, U., van Westen, C.J., and Slob, S. (2007). Sensitivity analysis of SHAKE based soil site response modelling. Presented at the 2007 annual New Zealand Society of Earthquake Engineering Conference, Palmerston North, March-April 2007. 10 p.
- Dobry, R. and Vucetic, M. (1987). "Dynamic properties and seismic response of soft clay deposits," *Proceedings*, International Symposium on Geotechnical Engineering of Soft Soils, Mexico City, Vol. 2, pp. 51-87.
- Guerreiro, P. Kontoe, S. and Taborok, D. (2012). Comparative study of stiffness reduction and damping curves. *Proceedings*, 15WCEE, Lisbon, Portugal, 2012.
- Hunter, JA. (2007). Measurements of compressional and shear wave velocities and formation porosities in Quaternary sediments. Presented: OttawaGeo2007, Ottawa, ON.
- Hunter, J.A., Crow, H.L., Brooks, G.R., Pyne, M., Motazedian, D., Lamontagne, M., Pugin, A.J.-M., Pullan, S.E., Cartwright, T., Douma, M., Burns, R.A., Good., R.L., Kaheshi-Banab, K., Caron, R., Kolaj, M., Folahan, I., Dixon, L., Dion, K., Duxbury, A., Landriault, A., Ter-Emmanuil, V., Jones, A., Plastow, G., and Muir, D. (2010). Seismic Site Classification and Site Period Mapping in the Ottawa Area Using Geophysical Methods. *Geological Survey of Canada, Open File 6273*.
- Ishibashi, I. and Zhang, X. (1993). "Unified dynamic shear moduli and damping ratios of sand and clay," *Soils and Foundations*, Vol. 33, No. 1, pp. 182-191.
- Ishibashi, I. (1992). Discussion to "Effect of soil plasticity on cyclic response," by M. Vucetic and R. Dobry, *Journal of Geotechnical Engineering*, ASCE, Vol. 118, No. 5, pp. 830-832.
- Kokoshu, T. (1980). Cyclic triaxial test of dynamic soil properties for wide strain range, *Soils and Foundations*, **22 (2)**, pp. 45-60.

- Kramer, S.L. (1996). *Geotechnical Earthquake Engineering*, Prentice Hall, New Jersey.
- Kramer, S.L., and Paulsen, S.B.. (2004). Practical use of geotechnical site response models. International Workshop on Uncertainties in Nonlinear Soil Properties and their impact on Modeling Dynamic Soil Response. UC Berkley, USA, PEER.
- Law, K.T., Cragg, CBH, Lee, C.F. (1985). Seismic Soil Behaviour under an Earth Dyke. *In proceedings of XIth International Conference on Soil Mechanics and Foundation Engineering*, Paper No. 1327 v4, pp1853-1860, San Francisco, CA, August 1985.
- Medioli, B.E., Alpay, S., Crow, H.L., Cummings, D.I., Hinton, M.J., Knight, R.D., Logan, C., Pugin, A.J-M., Russell, H.A.J., and Sharpe. Integrated datasets from a buried valley borehole, Champlain Sea basin, Kinburn Ontario; Geological Survey of Canada Current Research 2012-13.
- Motazedian, D; and Hunter, J.A. (2008). Development of a NEHRP map for the Orleans suburb of Ottawa, Ontario. *Canadian Geotechnical Journal*, **45**(8);1180-1188.
- Proshake: EduPro products; EduPro Civil Systems, Inc., Sammamish, WA, USA. [Updated: August 2013]: <http://www.proshake.com/>
- Pugin, A.J.-M., Brewer, K., Cartwright, T., Pullan, S.E., Perret, D., Crow, H., and Hunter, J.A. (2013). Near surface S-wave seismic reflection profiling – new approaches and insights, *First Break*, **31**, 49 – 60.
- Rollins, K.M., Evans, M.D., Diehl, N.B., Daily, W.D. (1988) Shear modulus damping relationships for gravels. *J. of Geotech.and Geoenviron. Eng.*, **124**, 396-405.
- SAC: Seismic Analysis Code, developed by Lawrence Livermore National Laboratory; copyrighted by the University of California distributed by IRIS (Incorporated Research Institutions for Seismology), Washington, DC, USA. [Accessed: August 2012]:IRIS: <http://ds.iris.edu/ds/nodes/dmc/software/downloads/>
- SAC User Manual - developed by Lawrence Livermore National Laboratory; copyrighted by the University of California distributed by IRIS (Incorporated Research Institutions for Seismology), Washington, DC, USA. [Accessed: August 2012]: <http://ds.iris.edu/files/sac-manual/>
- Schnabel, P.B., Lysmer, J., and Seed, H.B. (1972). "SHAKE: A computer program for earthquake response analysis of horizontally layered sites," *Report No. EERC 72-12*, Earthquake Engineering Research Center, University of California, Berkeley, California.

- Seed, H.B. and Idriss, I.M. (1970). "Soil moduli and damping factors for dynamic response analyses," *Report No. EERC 70-10*, Earthquake Engineering Research Center, University of California, Berkeley.
- Sun, J.I., Golesorkhi, R., and Seed, H.B. (1988). "Dynamic moduli and damping ratios for cohesive soils," *Report No. EERC-88/15*, Earthquake Engineering Research Center, University of California, Berkeley.
- Vrettos, C. (2013). Dynamic response of soil deposits to vertical SH waves for different rigidity depth-gradients, *Soil Dynamics and Earthquake Engineering*, **47**, 41-50.
- Vucetic, M. and Dobry, R. (1991). "Effect of soil plasticity on cyclic response," *Journal of Geotechnical Engineering*, ASCE, Vol. 117, No. 1, pp. 89-107.

Chapter 6.

- Crane, S., Motazedian, D. and Hunter, J. (2015). 2D Modelling of Seismic Wave Propagation through a Soft Soil Basin: Kinburn, Canada, *In Proceedings of the 11th Canadian Conference on Earthquake Engineering*, 2015 – in press.
- Konno, K., and Ohmachi, T. (1998). Ground-motion Characteristics Estimated from Spectral Ratio between Horizontal and Vertical Components of Microtremor, *Bull. Of the Seismological Society of America*, **88**, 228-241.
- Lamontagne, M. (1999). Rheological and Geological Constraints on the Earthquake Distribution in the Charlevoix Seismic Zone, Québec, Canada. *PhD Thesis submitted to the Graduate Studies and Research, Department of Earth Sciences, Carleton University*, Ottawa, Ontario.
- Ma, S. and Atkinson, G. (2006). Focal depths for small to moderate earthquakes ($m_N = 2.8$) in western Quebec, southern Ontario, and northern New York, *Bull Seismol Soc Am*, **96**, 609-623.
- Obspy – A Python Framework for Seismology. [Accessed: February 2014]: www.obspy.org.
- Python Programming Language – Python Software Foundation (PSF), Beaverton, OR, USA. [Accessed: February 2014]: www.python.org
- UPSeis – an educational site for budding seismologists; Michigan Technological University, Houghton, MI, USA; [Accessed: December 2015]: <http://www.geo.mtu.edu/UPSeis/waves.htm>

Chapter 7.

- Aylsworth, J.M., Lawrence, D.E., and Guertin, J. (2000). Did two massive earthquakes in the Holocene induce widespread landsliding and near-surface deformation in part of the Ottawa Valley, Canada? *Geology*, **28**, 903-906.
- Bard, P.-Y. and Bouchon, M. (1985). The two-dimensional resonance of sediment-filled valleys, *Bull Seismol Soc Am*, **75**, 519-541.
- Brooks, G.R. (2013). A massive sensitive clay landslide, Quyon Valley, southwestern Quebec, Canada, and evidence for a paleoearthquake triggering mechanism, *Quaternary Research*, **80**, 425–434.
- Crane, S., Motazedian, D. and Hunter, J. (2015). 2D Modelling of Seismic Wave Propagation through a Soft Soil Basin: Kinburn, Canada. *In Proceedings of the 11th Canadian Conference on Earthquake Engineering*, 2015, Victoria, Canada.
- Chávez-García, F.J. and Bard, P.-Y. (1994). Site effects in Mexico City eight years after the September 1985 Michoacán earthquakes. *Soil Dynamics Earthquake Engineering*, **13**, 229-247.
- Chávez-García, F.J., Castillo, J., and Stephenson, W.R. (2002). 3D Site-Effects: A Thorough Analysis of a High-Quality Dataset, *Bull Seismol Soc Am*, **92**, 1941-1951.
- Cornou, C., and Bard, P.-Y. 2003. Site-to-bedrock over 1D transfer function ratio: An indicator of the proportion of edge-generated surface waves? *Geophysical Research Letters*, **30**, 1453-1456.
- Gvirtsman, Z. and Louie, J.N. (2010). 2D Analysis of Earthquake Ground Motion in Haifa Bay, Israel, *Bull Seismol Soc Am*, **100**, 733-750
- Kawase, H. and Aki, K. (1989). A study on the response of a soft soil basin for incident S, P, and Rayleigh waves with special reference to the long duration observed in Mexico City, *Bull Seismol Soc Am*, **79**, 1361-1382.
- Kawase, H. (1996). The cause of the damage belt in Kobe: “The basin-edge effect,” constructive interference of the direct S-wave with the basin induced diffracted/Rayleigh waves, *Seismological Research Letters*, **67**, 25-41.

- Konno, K., and Ohmachi, T. (1998). Ground-motion Characteristics Estimated from Spectral Ratio between Horizontal and Vertical Components of Microtremor, *Bull. Of the Seismological Society of America*, **88**, 228-241.
- Mazzotti, S., and Adams, J.(2005). Rates and uncertainties on seismic moment and deformation in eastern Canada, *J. Geophys. Res.*, 110, B09301, doi:[10.1029/2004JB003510](https://doi.org/10.1029/2004JB003510).
- Stephenson, W.R., Lomnitz, C., and Flores, H. (2006). Late resonant response at Texcoco, Valley of Mexico, during distant earthquakes. *Soil Dynamics and Earthquake Engineering*, **26**, 791-798.
- Vrettos, C. (2013). Dynamic response of soil deposits to vertical SH waves for different rigidity depth-gradients, *Soil Dynamics and Earthquake Engineering*, **47**, 41-50.

Appendix A: Instrumentation

I. Station information

A pair of three-component, broadband, 100 samples/s seismometers are located on each of the three basins. Due to a problem with the software used to download and convert the event data for the non-continuous stations (ALFS, JSBS and JSSS), the start-time stamp for each component can be off by several milliseconds, so the timing for these stations is not considered reliable, making particle motion comparisons impossible for these sites. The error causing this problem was identified in late 2013 to be due to the downloading software. The issue was addressed and fixed by 2013/10/26, but the solution could not be applied retroactively to the earlier downloaded data.

Furthermore, a software upgrade on JSBS and JSSS at the beginning of July 2012 caused the EW and vertical component to be switched. This error was caught and corrected by mid-August 2012. For the affected data, the labels on the files were simply renamed to reflect the actual recordings.

Table A-1 contains the basic information for all the seismograph sites used in this study, including the station name, the seismometer and digitizer used, the coordinates and elevation of the site, and the dates of operation.

Table A-1: Station information for sites used in study, including site name, coordinates, equipment type and dates of operation.

Stn name	Digitizer	Seismo	Coordinates		Elev. (m)	Dates of Operation ¹	
			Lat (N)	Lon (W)		Open	Close
ALFO	Trident	CMG-3ESP	45.6283	-74.8842	46 ²	2009/05/29	-
ALFS	Taurus	CMG-3T	45.6197	-74.8434	46 ²	2012/09/06	-
JSBS	Taurus	Trillium 120p	45.3979	-76.1773	69	2010/06/15	2013/10
JSSS	Taurus	Trillium 120p	45.3859	-76.1562	61	2010/11/01	2013/10
ORHO	Taurus	CMG-3ESP	45.4563	-75.5367	51	2007/06/27	2013/11/08
ORIO	Taurus	CMG-3ESP	45.4515	-75.5111	74	2008/06/19	2013/11/08

¹ Dates of operation are taken as the date of the last change made to the station set-up, and in the case of the Kinburn stations, the date of the first available data.

² Elevation measured taken from Google Earth.

Additional information on the equipment used can be found at the manufacturers' websites listed below:

Seismometres and Accelerometres:

Weak motion sites:

CMG-3 from Guralp: see <http://www.guralp.com/products/instruments/cm-g-3>

Trillium 120p from Nanometrics: see
<http://www.nanometrics.ca/seismology/products/trillium-120-ppa>

Strong motion sites at Kinburn:

Etna recorders from Kinometrics: see <http://www.kinometrics.com/p-76-Etna.aspx>

Digitizers:

From Nanometrics:

Trident: see <http://www.nanometrics.ca/seismology/products/trident>

Taurus: see <http://www.nanometrics.ca/seismology/products/taurus>

For H/V spectral ratios:

Grilla Tromino: see <http://www.tromino.eu/>

II. Sac Displacement Instrument Response Files

ALFO

ZEROS 3
POLES 5
-502.654800 0.000000
-1005.309600 0.000000
-1130.973400 0.000000
-0.044420 0.044420
-0.044420 -0.044420
CONSTANT 4.543230e+17

ALFS

ZEROS 3
POLES 5
-502.654800 0.000000
-1005.309600 0.000000
-1130.973400 0.000000
-0.044420 0.044420
-0.044420 -0.044420
CONSTANT 4.572000e+17

ORHO

ZEROS 3
POLES 5
-502.654800 0.000000
-1005.309600 0.000000
-1130.973400 0.000000
-0.044420 0.044420
-0.044420 -0.044420
CONSTANT 4.572000e+17

ORIO

ZEROS 3
POLES 5
-502.654800 0.000000
-1005.309600 0.000000
-1130.973400 0.000000
-0.044420 0.044420
-0.044420 -0.044420
CONSTANT 4.572000e+17

JSBS

ZEROS 5

-106.0000 0.0000

-158.0000 0.0000

POLES 7

-0.0386 0.0365

-0.0386 -0.0365

-190.0000 0.0000

-158.0000 193.0000

-158.0000 -193.0000

-639.0000 1418.0000

-639.0000 -1418.0000

CONSTANT 8.177712e+17

JSSS

ZEROS 5

-106.0000 0.0000

-158.0000 0.0000

POLES 7

-0.0386 0.0365

-0.0386 -0.0365

-190.0000 0.0000

-158.0000 193.0000

-158.0000 -193.0000

-639.0000 1418.0000

-639.0000 -1418.0000

CONSTANT 8.177712e+17

OTT.HHZ

ZEROS 5

867.080000 904.779000

867.080000 -904.779000

POLES 4

-0.148096 0.148096

-0.148096 -0.148096

-314.159270 202.319000

-314.159270 -202.319000

CONSTANT 7.458530e+07

Appendix B: Seismic Data

I. List of strong motion recordings

Acceleration data available for Kinburn basin until end of 2013:

20110316-173655-Hawkesbury4M3
 20110823-175104-RichmondVA5M8
 20130517-134323-Shawville5M2

These strong motion data were recorded by the ETNA strong motion instrument co-located with the seismograph sites at JSBS and JSSS (see Appendix A for seismograph site coordinates).

II. List of weak motion recordings

See spreadsheet below for list of weak motion earthquakes, and on which stations they were recorded.

Event	Alfred		Orleans		OTT	Kinburn		Notes
	ALFS	ALFO	ORHO	ORIO		JSSS	JSBS	
20061207-KapuskingCochrane4M2			X		X			> 400 km away
20080418-093659-Illinois5M4			X		X			Regional event
20100101-005250-Maniwaki2M2			X	X	X			
20100101-032158-MontLaurier1M8			X	X	X			
20100101-154525-Pembroke1M3			X	X	X			
20100104-002044-Huntingdon1M8			X	X	X			
20100106-152859-Huntingdon2M0			X	X	X			
20100109-174946-FortCoulange1M8			X	X	X			
20100110-200044-Salaberry1M3			X	X	X			
20100111-225251-Maniwaki1M7			X	X	X			
20100113-192939-MontLaurier1M7			X	X	X			
20100117-084816-Kazabazua2M0			X	X	X			
20100201-171806-SaintJean2M8			X	X	X			
20100205-014843-Thurso1M5			X	X	X			
20100208-161912-FermeNeuve2M2			X	X	X			
20100211-222820-			X	X	X			

Morrisburg1M9								
20100212-044621-Kingston2M0			X	X	X			
20100212-055703-Maniwaki2M5			X	X	X			
20100214-031411-Hawkesbury1M8			X	X	X			
20100223-203106-Ste-Agathe1M9			X	X	X			
20100227-060156-VDB1M6			X	X	X			
20100228-014452-Thurso2M8			X	X	X			
20100305-023759-Maniwaki2M1			X	X	X			
20100306-150924-VDB3M2			X	X	X			
20100309-231212-Russell1M8			X	X	X			
20100312-024940-VDB2M0			X	X	X			
20100324-053427-Thurso2M0			X	X	X			
20100511-151545-LAnnonciation2M1			X		X			
20100518-125557-Huntingdon2M2			X	X	X			
20100518-230501-StJovite2M6			X	X	X			
20100615-145948-Ste-Julienne3M3			X		X	X		
20100623-154327-VDB						X		
20100623-VDB-5M0			X	X	X			
20100623-VDB-AftershocksM2						X		
20100706-041527-VDB2M3			X	X	X	X		JSSS - N ?
20100707-010100-Maniwaki2M1			X	X	X			
20100709-215025-VDB2M4			X	X	X	X		JSSS - N ?
20100715-004013-VDB2M0			X	X	X	X		JSSS - N ?
20100724-071111-VDB2M3			X	X	X	X		JSSS - N ?
20100803-063544-VDB2M1			X	X	X	X		JSSS - N ?
20100820-113224-Gananoque2M0			X	X				
20100823-053130-Kemptville1M5			X	X		X		JSSS - N?
20100902-142108-StAndreAvellin2M6			X	X		X		JSSS - N?
20100909-093111-FermeNeuve2M1			X	X		EZ		JSSS - N missing
20100909-122621-Shawville2M3			X	X		EZ		JSSS - N missing
20100912-234850-DeepRiver2M1			X	X		EZ		JSSS - N missing
20100919-164729-Labelle3M3			X			EZ		JSSS - N missing

20100919-165707-Labelle3M3			X			EZ		JSSS - N missing
20100920-100243-Labelle1M6			X			X		JSSS - N?
20100927-195239-VDB2M0			X	X				
20100930-180912-Maniwaki1M9			X	X		EZ		JSSS - N missing
20101012-054346-VDB2M1			X	X		EZ		JSSS - N missing
20101015-221615-Rockland2M2			X	X		EZ		JSSS - N missing
20101021-132343-FermeNeuve2M2			X	X		EZ		JSSS - N missing
20101101-065903-SteAdele2M1			X	X		X	X	JSSS - N?
20101101-074733-Pembroke2M6			X	X		X	X	JSSS - N?
20101113-065758-FermeNeuve2M0			X	X		X	EZ	JSBS - N missing
20101119-215118-VDB2M0			X	X		X	EZ	JSBS - N missing
20101213-083425-VDB2M2			X	X		X	X	
20101220-012337-MontLaurier2M2			X	X		X	X	
20101222-150436-VDB2M4			X	X		X	X	
20101225-072814-Renfrew1M6			X	X		X	X	
20101229-084037-VDB1M9			X	X		X	X	
20110109-154135-FortCoulonge1M9			X	X		X		
20110112-105144-FortCoulonge1M9			X	X		X		
20110113-123220-Kazabazua2M8			X	X				
20110129-130736-Maniwaki2M0			X	X				
20110206-233327-VDB2M1			X	X		X	X	
20110207-224336-MontLaurier2M0			X	X		X	X	
20110220-211851-LEpiphanie2M1			X	X		X	X	
20110222-190633-Petawawa2M9			X	X		X	X	
20110305-233845-Labelle2M0			X	X	X	X	X	
20110310-223853-Maniwaki2M7			X	X	X	X	X	
20110316-173655-Hawkesbury4M3			X	X	X	X	X	
20110321-093048-Maniwaki2M4			X	X	X	X	X	
20110329-160435-DeepRiver3M5			X	X	X	X	X	
20110406-142230-Wakefield2M5			X	X	X	X	X	
20110417-012233-			X	X	X	X	X	

StAndreAvellin2M2								
20110419-032841-DeepRiver2M1			X	X	X	X	X	
20110424-033718-Labelle2M2			X	X	X	X	X	
20110424-034514-Labelle2M2			X	X	X	X	X	
20110428-195718-StJovite2M4			X	X	X	X	X	
20110501-182522-MontLaurier2M2			X	X	X	X	X	
20110507-064510-Huntingdon2M7			X	X	X	X	X	
20110509-144643-LAnnonciation3M1			X	X	X	X	X	
20110511-054942-LAnnonciation3M0			X	X	X	X	X	
20110512-040748-Embrum2M5			X	X	X	X	X	
20110523-111832-Shawville1M7			X	X	X	X	X	
20110524-071332-Papineauville2M4			X	X	X	X	X	
20110616-040316-Huntingdon2M6			X	X	X	X	X	
20110721-230552-Wakefield3M5			X	X	X	X	X	
20110727-230257-Maniwaki2M7			X	X	X	X	X	
20110823-162259-Maniwaki2M6			X	X	X	X	X	
20110823-162403-Maniwaki2M0			X	X	X	X	X	
20110823-175104-RichmondVA5M8			X	X		X	X	Regional event
20110824-171432-Huntingdon3M5			X	X	X	X	X	
20110824-184408-Huntingdon2M3			X	X	X	X	X	
20110918-191913-Buckingham4M1						X	X	
20110922-220430-Rockland1M8			X	X	X	X	X	
20110929-124956-StJovite2M0						X	X	
20111009-092926-FortCoulonge2M1						X	X	
20111011-183859-Maniwaki3M0						X	X	
20111016-034409-Thurso2M8						X	X	
20111018-051039-LAnnonciation2M8			X	X	X	X	X	
20111020-174646-Vankleek2M1			X	X	X	X	X	
20111022-023945-LOrignal2M8			X	X	X	X	X	
20111103-160247-FortCoulonge2M6			X	X	X	X	X	
20111105-174148-VDB2M3			X	X	X	X	X	

20111105-200613-Arnrior2M0			X	X	X	X	X	
20111110-015253-LAnnonciation2M3			X	X	X			
20111111-141102-Maniwaki2M2			X	X	X	X	X	
20111121-071650-Cornwall2M6			X	X	X	X	X	
20111221-191754-FermeNeuve2M0			X	X	X	X	X	
20111226-150953-Petawawa2M1			X	X	X	X	X	
20111227-172103-Chesterville1M9			X	X	X	X	X	
20120106-052256-FermeNeuve2M5			X	X	X	X	X	
20120107-023322-Cornwall2M6			X	X	X	X	X	
20120107-125656-Cornwall2M4			X	X	X	X	X	
20120109-090536-FermeNeuve2M2			X	X	X	X	X	
20120110-111022-ConstanceBay2M0			X	X	X	X	X	
20120120-135253-FermeNeuve2M3			X	X	X			
20120122-055946-LAnnonciation3M6			X	X	X	X	X	
20120129-034301-MontLaurier2M0			X		X	X	X	
20120204-091702-Maniwaki3M6			X	X	X	X	X	
20120208-222427-Thurso2M3			X	X	X	X	X	
20120213-000152-Pembroke2M0			X	X	X	X	X	
20120221-001549-LAnnonciation2M0			X	X	X	X	X	
20120226-080356-Maniwaki2M3			X	X	X	X	X	
20120229-000927-VDB3M2			X	X	X	X	X	
20120229-031227-VDB2M0			X	X	X	X	X	
20120406-022516-Hawkesbury2M2			X	X	X	X	X	
20120407-214728-Wakefield3M1			X	X	X	X	X	
20120502-000340-Moosonee4M2			X	X	X	X	X	>400km
20120511-030232-Petawawa2M1			X	X	X	X	X	
20120515-171215-GatineauBLAST1M7			X	X	X			Quarry blast
20120610-052339-StJovite2M3			X	X	X	X	X	
20120613-035436-Hawkesbury2M5			X		X	X	X	

20120708-111338-HappyValleyGooseBay4M4-ZE_swap_JS			X	X	X	X	X	Too small to see on soil sites. On JS sites, swap Z and E comps.
20120721-070114-FermeNeuve2M7			X	X	X	X	X	On JS sites, swap Z and E comps.
20120723-112158-StAndreAvellin2M3			X	X		X	X	On JS sites, swap Z and E comps.
20120804-182749-StJeanPortJoli3M8			X	X	X			>400km; On JS sites, swap Z and E comps.
20120808-141343-Gracefield2M0			X	X	X	X	X	On JS sites, swap Z and E comps.
20120826-213251-MontLaurier3M0			X	X		X	X	
20120920-141116-BuckinghamBlast2M3	X	X	X	X	X	X	X	Quarry blast
20120922-173630-Rockland3M1	X	X	X	X	X	X	X	
20120922-185304-Rockland2M3	X	X	X	X	X	X	X	
20120927-091302-FermeNeuve2M1	X	X	X	X	X			
20121001-225008-StJerome2M1	X	X	X	X	X			
20121003-050159-Morrisburg2M0	X	X	X	X	X			
20121004-182747-Huntingdon3M0	X	X	X	X	X	X	X	
20121009-185251-StMichelDesSaints2M1	X	EZ	X	X	X			ALFO.HHN missing
20121010-041928-Vercheres4M5	X	X	X	X	X	X	X	
20121014-005539-Hawkesbury1M3	X	X						
20121015-102135-FermeNeuve2M5	X	X	X	X	X	X	X	
20121015-102400-FermeNeuve2M3	X	X	X	X	X	X	X	
20121028-HaidaGwaii7M7			X	X				Teleseism
20121031-064200-Thurso1M2			X	X				
20121106-090527-Hawkesbury4M2			X	X	X	X	X	
20121106-094225-Hawkesbury2M2			X	X	X	X	X	
20121106-101240-			X	X	X	X	X	

Papineauville2M5								
20121114-173133-ValDesBois2M0	X	X	X	X	X	X	X	
20121127-075556-Matane4M2	X	X	X	X				>400km
20121129-233953-FermeNeuve2M6	X	X	X	X		X	X	
20121207-081824-Japan7M3	X	X	X	X		X	X	Teleseism
20121212-174605-LaMalbaie4M4	X	X	X	X		X	X	>400km
20121214-103602-Baja6M4	X		X	X		X	X?	Teleseism; JSBS issue?
20121231-041240-ValDesBois2M4			X	X	X			
20130105-085819-Alaska7M7	X		X	X	X			Teleseism
20130112-073437-Alfred2M5	X	X	X	X	X	X	X	
20130116-005304-VDB3M5	X	X	X	X	X	X	X	
20130116-010148-VDB3M0	X	X	X	X	X	X	X	
20130116-134636-Huntingdon2M7	X	X	X	X	X	X	X	
20130202-235638-LOriginal2M3	X	X	X	X	X			
20130203-082700-LOriginal1M9	X	X	X	X	X			
20130206.011223-SantaCruzIslands8M0	X	X	X		X			Teleseism
20130219-045943-Chapleau3M8	X	X	X	X	X		X	>600km
20130225-194032-Gatineau1M5Blast	X	X	X	X	X	X	X	Quarry blast
20130226-103134-Cornwall2M3	X	X	X	X	X	X	X	
20130304-084153-LOriginal1M2	X	X	X	X	X			
20130306-022428-Rigaud1M8	X	X	X	X	X			
20130306-181158-LOriginal1M9Blast	X	X	X	X	X			Quarry blast
20130313-203221-Hawkesbury2M7	X	X	X	X	X	X	X	
20130314-102725-Maniwaki2M6	X	X	X	X	X	X	X	
20130323-201912-BarrysBay2M6			X	X	X	X	X	
20130324-030728-Kingston2M0			X	X	X	X	X	
20130415-133225-Brownsburg3M1	X	X	X	X	X	X	X	
20130415-9-5Blasts						X	X	Local Kinburn blasts. Continuous recording 9am-5pm.
20130418-051836-LAnnoiation2M6	X	X	X	X	X	X	X	

20130512-202832-StAndreAvelin2M3	X	X	X	X		X	X	
20130515-191314-ConstanceBay2M7	X	X	X	X	X	X	X	
20130517-134323-Shawville5M2	X	X	X	X	X	X	X	Strong motion data available for Kinburn
20130517-135355-Shawville4M1	X	X	X	X	X	X	X	
20130517-201517-Shawville3M1			X	X	X	X	X	
20130519-051422-Metcalfe2M2	X	X	X	X	X	X	X	
20130521-204302-Rigaud3M4	X	X	X	X	X	X	X	
20130524-054449-Okhotsk8M3	X	X	X	X	X	X	X	Teleseism
20130524-070831-Maniwaki3M6	X	X	X	X	X	X	X	
20130524-194808-Shawville3M0	X	X	X	X	X	X	X	
20130530-053458-Shawville3M7	X	X	X	X	X	X	X	
20130613-130040-CrystalBeach2M1	X		X	X	X	X	X	
20130615-155831-Shawville2M5	X		X	X	X	X	X	
20130616-054722-Russell2M6	X		X	X	X	X	X	
20130813-1142-Columbia6M6	X	X	X	X	X			Teleseism
20130904-015212-FermeNeuve3M1	X	X	X	X	X	X	X	
20130925-142434-CrystalBeach2M5	X	X	X	X	X	X	X	
20131020-104033-BarrysBay3M6	X	X	X	X	X	X	X	
20131105-170254-Alfred1M6	X	X	X	X				

III. SAC macros

Below are included some examples of the SAC macros used for the data processing for the current study. Actual macros used for any particular event are included within the data directory for that event in the digital Supplementary Material.

SAC macros for calculating FFTs:

e.g.

```
qdp off
r orio.hhe orio.hhn orio.hhz orho.hhe orho.hhn orho.hhz
cut 49.4 94.4
r
```

```

p1
w prepend cut45-
cut off
r cut45-*
p1
taper
fft
keepam
write append -fft
write alpha append -fft.i
q

```

SAC macros for converting data files from velocity to acceleration:

The SAC macro below is an example of how data was converted from velocity to acceleration data, so that it could be imported into Proshake.

e.g.

```

r jsbs.hhe
rmean
taper
transfer from polezero subtype SACPZs_JSBS.HHE to acc freqlimits 0.001 0.002 40
50
write change jsbs jsbs-noinst-acc
q

```

SAC macros for converting data files from velocity to displacement:

e.g.

```

r jsbs.hhe
rmean
taper
transfer from polezero subtype SACPZs_JSBS.HHE to none freqlimits 0.001 0.002
40 50
write change jsbs jsbs-noinst-disp

```

q

Appendix C: Basin Profiles

I. Proshake

Modulus reduction and damping ratio curves

Table C-: Modulus Reduction and Damping Ratio curve data for Leda clay as obtained from Law et al. (1985) and H. Crow (pers. Comm., 2015) for 0.000001% strain

	Strain %	G/Gmax	D%
1	0.000001	1	0.3
2	0.001	1	1.65
3	0.002	1	1.72
4	0.003	1	1.73
5	0.004	1	1.77
6	0.005	1	1.79
7	0.006	1	1.81
8	0.007	0.998	1.84
9	0.008	0.996	1.86
10	0.009	0.992	1.89
11	0.01	0.99	1.92
12	0.015	0.973	
13	0.02	0.954	2.06
14	0.03	0.915	2.2
15	0.04	0.883	2.35
16	0.05	0.853	2.5
17	0.06	0.825	2.75
18	0.07	0.801	3.03
19	0.08	0.781	3.28
20	0.09	0.759	3.6
21	0.1	0.739	3.9
22	0.15	0.645	
23	0.2	0.57	7.8

II. Data for Basin Profiles

Original data and calculations in spreadsheets below are all included digitally with Supplementary Material, as are the *.dat files produced in Proshake for each profile. Note that the only columns included are those actual fields required to build the profiles in Proshake.

Kinburn basin

Layer #	Thickness (m)	γ_b (kN/m ³)	Vs (m/s)	Description
1	0.48	19.31	370	Leda Clay
2	0.06	18.83	350	Leda Clay
3	1.07	17.82	273	Leda Clay
4	0.73	17.49	210	Leda Clay
5	0.49	17.84	240	Leda Clay
6	1.60	16.13	192	Leda Clay
7	1.47	14.97	115	Leda Clay
8	1.60	14.70	110	Leda Clay
9	1.55	15.73	88	Leda Clay
10	0.94	14.90	89	Leda Clay
11	1.93	14.79	97	Leda Clay
12	2.21	14.88	111	Leda Clay
13	0.41	15.32	115	Leda Clay
14	1.96	15.28	126	Leda Clay
15	1.27	15.06	157	Leda Clay
16	0.89	15.51	173	Leda Clay
17	1.83	16.40	185	Leda Clay
18	1.60	16.37	190	Leda Clay
19	0.74	16.54	188	Leda Clay
20	2.39	17.02	188	Leda Clay
21	1.78	16.99	191	Leda Clay
22	1.40	17.14	193	Leda Clay
23	1.68	17.08	199	Leda Clay
24	1.37	17.22	202	Leda Clay
25	1.42	17.07	202	Leda Clay
26	1.47	17.46	204	Leda Clay
27	0.08	17.22	204	Leda Clay
28	1.57	17.46	209	Leda Clay
29	3.02	17.16	222	Leda Clay
30	0.51	17.14	226	Leda Clay

31	1.57	17.22	228	Leda Clay
32	1.37	17.41	231	Leda Clay
33	1.52	17.46	234	Leda Clay
34	1.52	17.53	237	Leda Clay
35	1.47	18.11	242	Leda Clay
36	1.55	17.82	249	Leda Clay
37	1.52	17.86	254	Leda Clay
38	1.47	17.97	260	Leda Clay
39	1.50	18.00	266	Leda Clay
40	1.52	17.71	273	Leda Clay
41	1.52	17.49	274	Leda Clay
42	1.35	17.22	271	Leda Clay
43	1.78	17.01	273	Leda Clay
44	4.62	17.26	279	Leda Clay
45	1.52	16.91	283	Leda Clay
46	1.32	17.20	279	Leda Clay
47	1.50	17.90	275	Leda Clay
48	1.65	17.13	280	Leda Clay
49	1.35	17.63	290	Leda Clay
50	1.55	17.52	299	Leda Clay
51	1.57	17.69	302	Leda Clay
52	1.65	17.58	313	Leda Clay
53	1.37	17.79	316	Leda Clay
54	1.57	17.45	315	Leda Clay
55	1.37	17.88	318	Leda Clay
56	1.60	17.48	315	Leda Clay
57	1.73	17.15	312	Leda Clay
58	1.32	17.89	319	Leda Clay
59	1.83	17.11	326	Leda Clay
60	1.14	19.23	323	Leda Clay
61	1.60	19.04	321	Leda Clay
62	1.65	17.80	320	Leda Clay
63	5.84	18.99	350	Leda Clay
64	26.05	21.70	580	Glacial till
65	inf.	26.00	2890	Paleozoic

Orleans basin

Layer #	Thickness (m)	γ_b (kN/m ³)	Vs (m/s)	Description
1	3	17.73	220.0	Leda Clay
2	0.5	17.57	207.0	Leda Clay
3	0.5	16.76	154.0	Leda Clay
4	0.5	16.14	123.0	Leda Clay

5	0.5	15.58	100.0	Leda Clay
6	0.5	15.13	85.0	Leda Clay
7	1	14.97	80.0	Leda Clay
8	0.5	15.35	92.0	Leda Clay
9	4.5	15.78	107.7	Leda Clay
10	1.5	16.12	122.0	Leda Clay
11	0.5	16.46	138.0	Leda Clay
12	0.5	16.56	143.0	Leda Clay
13	1.5	16.71	151.3	Leda Clay
14	1	16.80	156.5	Leda Clay
15	2	16.56	143.5	Leda Clay
16	2	16.99	167.5	Leda Clay
17	0.5	16.79	156.0	Leda Clay
18	1	16.65	148.0	Leda Clay
19	0.5	16.86	160.0	Leda Clay
20	1	16.97	166.5	Leda Clay
21	0.5	16.70	151.0	Leda Clay
22	0.5	16.52	141.0	Leda Clay
23	3	16.39	134.7	Leda Clay
24	0.5	16.61	146.0	Leda Clay
25	2.5	16.77	154.8	Leda Clay
26	2	17.11	175.3	Leda Clay
27	0.5	17.18	180.0	Leda Clay
28	0.5	17.26	185.0	Leda Clay
29	1	17.35	191.5	Leda Clay
30	1.5	17.45	198.1	Leda Clay
31	1.5	17.51	202.4	Leda Clay
32	1.5	17.56	206.6	Leda Clay
33	1.5	17.62	210.9	Leda Clay
34	1.5	17.67	215.3	Leda Clay
35	1.5	17.73	219.6	Leda Clay
36	1.5	17.78	224.0	Leda Clay
37	1.5	17.84	228.4	Leda Clay
38	1.5	17.89	232.8	Leda Clay
39	1.5	17.94	237.2	Leda Clay
40	1.5	17.99	241.7	Leda Clay
41	1.5	18.04	246.2	Leda Clay
42	1.5	18.09	250.8	Leda Clay
43	1.5	18.14	255.3	Leda Clay
44	1.5	18.19	259.9	Leda Clay
45	1.5	18.24	264.5	Leda Clay
46	1.5	18.28	269.1	Leda Clay
47	1.5	18.33	273.8	Leda Clay
48	1.5	18.38	278.5	Leda Clay
49	1.5	18.42	283.2	Leda Clay
50	1.5	18.47	287.9	Leda Clay

51	1.5	18.51	292.6	Leda Clay
52	1.5	18.56	297.4	Leda Clay
53	1.5	18.60	302.2	Leda Clay
54	1.5	18.65	307.0	Leda Clay
55	1.5	18.69	311.9	Leda Clay
56	1.5	18.73	316.8	Leda Clay
57	1.5	18.77	321.7	Leda Clay
58	1.5	18.81	326.6	Leda Clay
59	1.5	18.86	331.5	Leda Clay
60	1.5	18.90	336.5	Leda Clay
61	1.5	18.94	341.5	Leda Clay
62	10	21.70	580.0	Glacial Till
63	inf	26.00	2166.0	Shale Bedrock

Lefaivre basin

Layer #	Thickness (m)	γ_b (kN/m ³)	Vs (m/s)	Description
1	1.83	16.99	196.00	consolidated clay
2	1.74	16.26	205.00	leda clay
3	0.97	15.48	209.00	leda clay
4	1.09	15.86	204.00	leda clay
5	1.98	15.69	203.00	leda clay
6	1.40	15.91	164.00	leda clay
7	0.97	15.89	170.00	leda clay
8	1.14	16.20	156.00	leda clay
9	1.60	16.58	150.00	leda clay
10	0.81	16.07	153.00	leda clay
11	1.65	16.46	151.00	leda clay
12	0.53	16.13	154.00	leda clay
13	2.90	16.47	159.00	sand
14	3.15	18.00	170.00	leda clay
15	4.00	18.00	180.00	sand
16	4.00	18.00	195.00	sand
17	4.90	18.23	206.00	sand
18	1.83	17.89	208.00	sand
19	1.17	17.23	208.00	sand
20	1.22	17.18	211.00	leda clay
21	0.99	16.83	207.00	leda clay
22	0.84	17.93	208.00	leda clay

23	1.22	16.69	211.00	leda clay
24	0.81	16.93	218.00	leda clay
25	1.24	16.62	219.00	leda clay
26	0.97	16.84	222.00	leda clay
27	1.40	17.40	220.00	leda clay
28	11.61	16.79	223.87	sand
29	2.33	16.84	231.00	clay-deep water
30	2.92	16.83	235.00	clay-deep water
31	3.02	18.39	237.35	clay-deep water
32	1.60	16.62	239.00	clay-deep water
33	2.11	16.52	240.00	clay-deep water
34	1.19	16.59	242.00	clay-deep water
35	1.07	16.75	241.00	clay-deep water
36	3.38	16.76	242.09	clay-deep water
37	1.83	16.76	247.00	clay-deep water
38	1.04	16.55	248.00	clay-deep water
39	2.01	17.05	248.00	clay-deep water
40	2.97	16.77	250.00	clay-deep water
41	3.20	16.95	251.00	clay-deep water
42	1.91	17.09	252.00	clay-deep water
43	1.14	17.67	253.00	clay-deep water
44	2.90	17.02	255.00	clay-deep water
45	3.22	17.20	257.00	clay-deep water
46	3.79	17.45	260.00	clay-deep water
47	1.73	17.02	260.00	clay-deep water
48	1.85	17.62	261.00	clay-deep water
49	2.97	17.63	263.51	clay-deep water
50	2.46	17.45	266.00	clay-deep water
51	1.30	17.28	267.00	clay-deep water
52	11.69	20.31	273.36	glacial seds
53	2.82	20.62	278.61	glacial seds
54	5.43	22.59	287.80	glacial seds
55	2.03	21.68	292.87	glacial seds
56	5.71	22.65	295.02	glacial seds
57	1.98	22.27	299.00	glacial seds
58	6.20	26.00	304.03	glacial seds
59	inf	26.00	2566.50	bedrock-sandstone

Appendix D: Azigram

```
#!/usr/bin/python

'''
Determining azimuthal distributions of particle motion with time
Name: Sylvia HAYEK
'''

# Import modules and functions
import os
import matplotlib.pyplot as plt
import numpy as np
import obspy.signal
from scipy import signal
from obspy.core import read
from obspy.taup.taup import getTravelTimes as gtt
from obspy.core import UTCDateTime
from obspy.signal.rotate import rotate_NE_RT, rotate_RT_NE
from obspy.core.util.geodetics import gps2DistAzimuth as epi
from obspy.core.util.geodetics import kilometer2degrees as k2d
from obspy.signal.trigger import recSTALTA, plotTrigger
from math import sqrt, atan2, pi, log10, floor

# Change directory to where you downloaded the waveform data
#os.chdir("/home/shayek/Downloads/GEOL4301/TermPaper")

''' PART 1 '''

# Define the main() function
def main():
    # define timeslice and width of data bins in degrees
    binwidth = 10
    ts= 200

    # amount of time we want to look at and when to start
    window_start = input('Give start of window (in s): ')
    window = input('Give window length: ')
    overlap_percent = input('Give percent overlap: ')

    #find sac files and read them
```

```

station = ['ORHO', 'ORIO']
for sta in station:
    if sta == 'ORHO':
        stream = read("orho*")
    else:
        stream = read("orio*")

# Call data_prep function with arguments sta, channel, and t0

trace_n,trace_e,trace_z,t0 = data_prep(sta, stream, window_start, window)

    # make a copy of these traces to refer to in the future:
trace_n_orig = trace_n.copy()
trace_e_orig = trace_e.copy()
trace_z_orig = trace_z.copy()

# Define station and earthquake coordinates
sta_lat = trace_z.stats.sac.stla
sta_lon = trace_z.stats.sac.stlo
eq_lat = trace_z.stats.sac.evla
eq_lon = trace_z.stats.sac.evlo
eq_dep = trace_z.stats.sac.evdp
eq_mag = trace_z.stats.sac.user7

# Get epicentral distance, azimuth and back-azimuth
dist, az, baz = epi(eq_lat, eq_lon, sta_lat, sta_lon)
    # Change from m to km:
epi_dist = dist/1000
# Convert epicentral distance from m to degrees
dist_in_deg = k2d(epi_dist)

    # Get arrivals from travel time table (model iasp91)
# (get arrival time and phase name from gtt)
tt = gtt (delta=dist_in_deg, depth=eq_dep, model='iasp91')
tp = tt[0]['time']
phase_name = tt[0]['phase_name']

# extracting sample rate
sr = trace_z.stats.sampling_rate

```

```

# Set time scale for plotting
samples = np.arange(len(trace_n.data))
delta = trace_z.stats.delta
time = np.linspace(0.0,window,num=(window-0)/delta+1)
numbins = 360 / binwidth

print '*****'
print 'Date.Time: ', t0, ' Magnitude: ', eq_mag
print 'Lat, Long: ', eq_lat, eq_lon
print 'Distance: ', int(dist/1000), 'km; Azimuth: ', int(az), 'deg'
print 'bin width: ', binwidth, ' degrees'
print 'number of bins: ', numbins
print 'number of samples per bin: ', ts, ' samples'
timeslice = ts/100.0
overlap = timeslice*overlap_percent
print 'time slice: ', timeslice, 's'
print 'window start: ', window_start, 's Window length: ', window, 's'
print 'Percent overlap: ', overlap_percent, '% Samples overlap: ', overlap, 'samples'

# Call azi_prep:
amplitude,pm_angle,azigram,azigram_amp = azi_prep(trace_n, trace_e, samples,
binwidth, numbins, ts)

# BB filter data. For Orleans from 0.3 Hz to 5.0 Hz

# Filter traces between 0.3 and 5.0 Hz, corners = 2
# Make a copy of the original first.
trace_n.taper(max_percentage=0.05, type='hann')
trace_e.taper(max_percentage=0.05, type='hann')
trace_z.taper(max_percentage=0.05, type='hann')
trace_n.filter('bandpass', freqmin=0.3, freqmax=5.0, corners = 2, zerophase=True)
trace_e.filter('bandpass', freqmin=0.3, freqmax=5.0, corners = 2, zerophase=True)
trace_z.filter('bandpass', freqmin=0.3, freqmax=5.0, corners = 2, zerophase=True)

# Plot angles and 3 component time series

plt.figure('azi1')

```

```

plt.subplot(411)
plt.title('Direction of Particle Motion: %s \n Distance: %s km  Azimuth: %s deg' %
(sta, int(dist/1000), int(az)))
plt.plot(time, pm_angle, color='red', marker='o', ms=2, linestyle="None")
plt.subplot(412)
plt.plot(time, trace_z.data, color='blue')
plt.title('Time series')
plt.ylabel('Vertical')
plt.subplot(413)
plt.plot(time, trace_n.data, color='blue')
plt.ylabel('N-S')
plt.subplot(414)
plt.plot(time, trace_e.data, color='blue')
plt.ylabel('E-W')
plt.xlabel('Time (sec)')
plt.show()

# Recall aziprep to recalc amplitude and angle of particle motion with bb filter
amplitude,pm_angle,azigram,azigram_amp = azi_prep(trace_n, trace_e, samples,
binwidth, numbins, ts)

plt.figure('azi2-bb-filtered')
plt.subplot(211)

plt.title('Azimuths Filtered 0.3-5.0 Hz: %s\n time width = %s s; degree bin = %s
deg' % (sta, timeslice, binwidth))
plt.xticks(range(0, int(window/timeslice)+1, 2), range(0, int(window+timeslice),
int(timeslice*2)))
plt.yticks(range(0, numbins+1, 3), range(0, 360+30, 30))
plt.imshow(azigram, aspect='auto', origin='lower')
plt.axhline(y=az/binwidth, c='black', ls='--', lw=1)
plt.axhline(y=baz/binwidth, c='white', ls='--', lw=1)
plt.colorbar(orientation='horizontal', fraction=0.1)

plt.subplot(212)
plt.title('N = black; E = blue')
plt.plot(time, trace_n.data, color='blue')
plt.plot(time, trace_e.data, color='black')
plt.xlabel('Time (s)')

```

```

plt.ylabel('Horizontal Components')
plt.show()

plt.figure('azi3-bb-weighted')
plt.subplot(211)

plt.title('Azimuths weighted by amplitude: Filtered 0.3-5.0 Hz\n For station: %s:
time width = %s s; degree bin = %s deg' % (sta, timeslice, binwidth))
plt.xticks(range(0, int(window/timeslice)+1, 2), range(0, int(window+timeslice),
int(timeslice*2)))
plt.yticks(range(0, numbins+1, 3), range(0, 360+30, 30))
plt.imshow(azigram_amp, aspect='auto', origin='lower')
plt.axhline(y=az/binwidth, c='black', ls='--', lw=1)
plt.axhline(y=baz/binwidth, c='white', ls='--', lw=1)
#plt.colorbar(orientation='horizontal', fraction=0.1)

plt.subplot(212)
plt.title('N = black; E = blue')
plt.plot(time, trace_n.data, color='blue')
plt.plot(time, trace_e.data, color='black')
plt.xlabel('Time (s)')
plt.ylabel('Horizontal Components')
plt.show()

##### fundamental ~0.8 Hz #####
# Filter traces between 0.5 and 1.1 Hz, corners = 2
# Make a copy of the original first.
trace_n = trace_n_orig.copy()
trace_e = trace_e_orig.copy()
trace_z = trace_z_orig.copy()
trace_n.taper(max_percentage=0.05, type='hann')
trace_e.taper(max_percentage=0.05, type='hann')
trace_z.taper(max_percentage=0.05, type='hann')
trace_n.filter('bandpass', freqmin=0.5, freqmax=1.1, corners = 2, zerophase=True)
trace_e.filter('bandpass', freqmin=0.5, freqmax=1.1, corners = 2, zerophase=True)
trace_z.filter('bandpass', freqmin=0.5, freqmax=1.1, corners = 2, zerophase=True)

# Call azi_prep to recalc amplitude and angle with filter around fund:

```

```

amplitude,pm_angle,azigram,azigram_amp = azi_prep(trace_n, trace_e, samples,
binwidth, numbins, ts)

```

```

plt.figure('azi4-fundamental')
plt.subplot(211)

```

```

plt.title('Azimuths Filtered 0.5-1.1 Hz: %s\n time width = %s s; degree bin = %s
deg' % (sta, timeslice, binwidth))
plt.xticks(range(0, int(window/timeslice)+1, 2), range(0, int(window+timeslice),
int(timeslice*2)))
plt.yticks(range(0, numbins+1, 3), range(0, 360+30, 30))
plt.imshow(azigram, aspect='auto', origin='lower')
plt.axhline(y=az/binwidth, c='black', ls='--', lw=1)
plt.axhline(y=baz/binwidth, c='white', ls='--', lw=1)
plt.colorbar(orientation='horizontal', fraction=0.1)

```

```

plt.subplot(212)
plt.title('N = black; E = blue')
plt.plot(time, trace_n.data, color='blue')
plt.plot(time, trace_e.data, color='black')
plt.xlabel('Time (s)')
plt.ylabel('Horizontal Components')
plt.show()

```

```

plt.figure('azi4-fund-weighted')
plt.subplot(211)

```

```

plt.title('Azimuths weighted by amplitude: Filtered 0.5-1.1 Hz\n For station: %s:
time width = %s s; degree bin = %s deg' % (sta, timeslice, binwidth))
plt.xticks(range(0, int(window/timeslice)+1, 2), range(0, int(window+timeslice),
int(timeslice*2)))
plt.yticks(range(0, numbins+1, 3), range(0, 360+30, 30))
plt.imshow(azigram_amp, aspect='auto', origin='lower')
plt.axhline(y=az/binwidth, c='black', ls='--', lw=1)
plt.axhline(y=baz/binwidth, c='white', ls='--', lw=1)
#plt.colorbar(orientation='horizontal', fraction=0.1)

```

```

plt.subplot(212)
plt.title('N = black; E = blue')

```

```

plt.plot(time, trace_n.data, color='blue')
plt.plot(time, trace_e.data, color='black')
plt.xlabel('Time (s)')
plt.ylabel('Horizontal Components')
plt.show()

##### 1st harmonic ~1.8 Hz #####
# Filter traces between 1.5 and 2.1 Hz, corners = 2
# Make a copy of the original first.
trace_n = trace_n_orig.copy()
trace_e = trace_e_orig.copy()
trace_z = trace_z_orig.copy()
trace_n.taper(max_percentage=0.05, type='hann')
trace_e.taper(max_percentage=0.05, type='hann')
trace_z.taper(max_percentage=0.05, type='hann')
trace_n.filter('bandpass', freqmin=1.5, freqmax=2.1, corners = 2, zerophase=True)
trace_e.filter('bandpass', freqmin=1.5, freqmax=2.1, corners = 2, zerophase=True)
trace_z.filter('bandpass', freqmin=1.5, freqmax=2.1, corners = 2, zerophase=True)

# Call azi_prep to recalc amplitude and angle with filter around fund:
amplitude,pm_angle,azigram,azigram_amp = azi_prep(trace_n, trace_e, samples,
binwidth, numbins, ts)

plt.figure('azi4-1st')
plt.subplot(211)

plt.title('Azimuths Filtered 1.5-2.1 Hz: %s\n time width = %s s; degree bin = %s
deg' % (sta, timeslice, binwidth))
plt.xticks(range(0, int(window/timeslice)+1, 2), range(0, int(window+timeslice),
int(timeslice*2)))
plt.yticks(range(0, numbins+1, 3), range(0, 360+30, 30))
plt.imshow(azigram, aspect='auto', origin='lower')
plt.axhline(y=az/binwidth, c='black', ls='--', lw=1)
plt.axhline(y=baz/binwidth, c='white', ls='--', lw=1)
plt.colorbar(orientation='horizontal', fraction=0.1)

plt.subplot(212)
plt.title('N = black; E = blue')
plt.plot(time, trace_n.data, color='blue')

```

```

plt.plot(time, trace_e.data, color='black')
plt.xlabel('Time (s)')
plt.ylabel('Horizontal Components')
plt.show()

plt.figure('azi4-1st-weighted')
plt.subplot(211)

plt.title('Azimuths weighted by amplitude: Filtered 1.5-2.1 Hz\n For station: %s:
time width = %s s; degree bin = %s deg' % (sta, timeslice, binwidth))
plt.xticks(range(0, int(window/timeslice)+1, 2), range(0, int(window+timeslice),
int(timeslice*2)))
plt.yticks(range(0, numbins+1, 3), range(0, 360+30, 30))
plt.imshow(azigram_amp, aspect='auto', origin='lower')
plt.axhline(y=az/binwidth, c='black', ls='--', lw=1)
plt.axhline(y=baz/binwidth, c='white', ls='--', lw=1)
#plt.colorbar(orientation='horizontal', fraction=0.1)

plt.subplot(212)
plt.title('N = black; E = blue')
plt.plot(time, trace_n.data, color='blue')
plt.plot(time, trace_e.data, color='black')
plt.xlabel('Time (s)')
plt.ylabel('Horizontal Components')
plt.show()

##### 2nd harmonic ~2.9 Hz #####
# Filter traces between 2.6 and 3.2 Hz, corners = 2
# Make a copy of the original first.
trace_n = trace_n_orig.copy()
trace_e = trace_e_orig.copy()
trace_z = trace_z_orig.copy()
trace_n.taper(max_percentage=0.05, type='hann')
trace_e.taper(max_percentage=0.05, type='hann')
trace_z.taper(max_percentage=0.05, type='hann')
trace_n.filter('bandpass', freqmin=2.6, freqmax=3.2, corners = 2, zerophase=True)
trace_e.filter('bandpass', freqmin=2.6, freqmax=3.2, corners = 2, zerophase=True)
trace_z.filter('bandpass', freqmin=2.6, freqmax=3.2, corners = 2, zerophase=True)

```

```
# Call azi_prep to recalc amplitude and angle with filter around fund:
amplitude,pm_angle,azigram,azigram_amp = azi_prep(trace_n, trace_e, samples,
binwidth, numbins, ts)
```

```
plt.figure('azi4-2nd')
plt.subplot(211)
```

```
plt.title('Azimuths Filtered 2.6-3.2 Hz: %s\n time width = %s s; degree bin = %s
deg' % (sta, timeslice, binwidth))
```

```
plt.xticks(range(0, int(window/timeslice)+1, 2), range(0, int(window+timeslice),
int(timeslice*2)))
```

```
plt.yticks(range(0, numbins+1, 3), range(0, 360+30, 30))
```

```
plt.imshow(azigram, aspect='auto', origin='lower')
```

```
plt.axhline(y=az/binwidth, c='black', ls='--', lw=1)
```

```
plt.axhline(y=baz/binwidth, c='white', ls='--', lw=1)
```

```
plt.colorbar(orientation='horizontal', fraction=0.1)
```

```
plt.subplot(212)
```

```
plt.title('N = black; E = blue')
```

```
plt.plot(time, trace_n.data, color='blue')
```

```
plt.plot(time, trace_e.data, color='black')
```

```
plt.xlabel('Time (s)')
```

```
plt.ylabel('Horizontal Components')
```

```
plt.show()
```

```
plt.figure('azi4-2nd-weighted')
```

```
plt.subplot(211)
```

```
plt.title('Azimuths weighted by amplitude: Filtered 2.6-3.2 Hz\n For station: %s:
time width = %s s; degree bin = %s deg' % (sta, timeslice, binwidth))
```

```
plt.xticks(range(0, int(window/timeslice)+1, 2), range(0, int(window+timeslice),
int(timeslice*2)))
```

```
plt.yticks(range(0, numbins+1, 3), range(0, 360+30, 30))
```

```
plt.imshow(azigram_amp, aspect='auto', origin='lower')
```

```
plt.axhline(y=az/binwidth, c='black', ls='--', lw=1)
```

```
plt.axhline(y=baz/binwidth, c='white', ls='--', lw=1)
```

```
#plt.colorbar(orientation='horizontal', fraction=0.1)
```

```
plt.subplot(212)
```

```

plt.title('N = black; E = blue')
plt.plot(time, trace_n.data, color='blue')
plt.plot(time, trace_e.data, color='black')
plt.xlabel('Time (s)')
plt.ylabel('Horizontal Components')
plt.show()

##### 3rd harmonic ~4.1 Hz #####
    ## This harmonic is less well defined, so giving broader filter +/- 0.5Hz
    # Filter traces between 3.6 and 4.6 Hz, corners = 2
# Make a copy of the original first.
trace_n = trace_n_orig.copy()
trace_e = trace_e_orig.copy()
trace_z = trace_z_orig.copy()
trace_n.taper(max_percentage=0.05, type='hann')
trace_e.taper(max_percentage=0.05, type='hann')
trace_z.taper(max_percentage=0.05, type='hann')
trace_n.filter('bandpass', freqmin=3.6, freqmax=4.6, corners = 2, zerophase=True)
trace_e.filter('bandpass', freqmin=3.6, freqmax=4.6, corners = 2, zerophase=True)
trace_z.filter('bandpass', freqmin=3.6, freqmax=4.6, corners = 2, zerophase=True)

# Call azi_prep to recalc amplitude and angle with filter around fund:
amplitude,pm_angle,azigram,azigram_amp = azi_prep(trace_n, trace_e, samples,
binwidth, numbins, ts)

plt.figure('azi4-3rd')
plt.subplot(211)

plt.title('Azimuths Filtered 3.6-4.6 Hz: %s\n time width = %s s; degree bin = %s
deg' % (sta, timeslice, binwidth))
plt.xticks(range(0, int(window/timeslice)+1, 2), range(0, int(window+timeslice),
int(timeslice*2)))
plt.yticks(range(0, numbins+1, 3), range(0, 360+30, 30))
plt.imshow(azigram, aspect='auto', origin='lower')
plt.axhline(y=az/binwidth, c='black', ls='--', lw=1)
plt.axhline(y=baz/binwidth, c='white', ls='--', lw=1)
plt.colorbar(orientation='horizontal', fraction=0.1)

plt.subplot(212)

```

```

plt.title('N = black; E = blue')
plt.plot(time, trace_n.data, color='blue')
plt.plot(time, trace_e.data, color='black')
plt.xlabel('Time (s)')
plt.ylabel('Horizontal Components')
plt.show()

```

```

plt.figure('azi4-3rd-weighted')
plt.subplot(211)

```

```

plt.title('Azimuths weighted by amplitude: Filtered 3.6-4.6 Hz\n For station: %s:
time width = %s s; degree bin = %s deg' % (sta, timeslice, binwidth))

```

```

plt.xticks(range(0, int(window/timeslice)+1, 2), range(0, int(window+timeslice),
int(timeslice*2)))

```

```

plt.yticks(range(0, numbins+1, 3), range(0, 360+30, 30))

```

```

plt.imshow(azigram_amp, aspect='auto', origin='lower')

```

```

plt.axhline(y=az/binwidth, c='black', ls='--', lw=1)

```

```

plt.axhline(y=baz/binwidth, c='white', ls='--', lw=1)

```

```

#plt.colorbar(orientation='horizontal', fraction=0.1)

```

```

plt.subplot(212)

```

```

plt.title('N = black; E = blue')

```

```

plt.plot(time, trace_n.data, color='blue')

```

```

plt.plot(time, trace_e.data, color='black')

```

```

plt.xlabel('Time (s)')

```

```

plt.ylabel('Horizontal Components')

```

```

plt.show()

```

```

def data_prep(sta, stream, window_start, window):

```

```

    #split streams into comps (per station); define data & resp files

```

```

    stream_z = stream.select(component="Z")

```

```

    respfile_z = 'RESP.CN.' + sta + '..HHZ'

```

```

    trace_z = stream_z[0]

```

```

    stream_n = stream.select(component="N")

```

```

    respfile_n = 'RESP.CN.' + sta + '..HHN'

```

```

    trace_n = stream_n[0]

```

```

    stream_e = stream.select(component="E")

```

```

respfile_e = 'RESP.CN.' + sta + '..HHE'
trace_e = stream_e[0]

# extract the start time of the trace
t0 = UTCDateTime(trace_z.stats.starttime)

# detrend data
trace_z.detrend
trace_n.detrend
trace_e.detrend

# select a time window, detrend, define a time axis (see Lab 2-2)
trace_z.trim(t0+window_start, t0 + window_start+window)
trace_n.trim(t0+window_start, t0 + window_start+window)
trace_e.trim(t0+window_start, t0 + window_start+window)

''' Omitting this as station pairs have same response. cancels out.
'''

# Return traces
return trace_n, trace_e, trace_z, t0

def azi_prep(trace_n, trace_e, samples, binwidth, numbins,ts):
    #defining azigram array with just counts and then weighted by amplitude
    #print 'size of azigram: ', repr(numbins), ' x ', len(trace_n.data)/ts+1
    azigram=np.zeros(shape=(numbins,len(trace_n.data)/ts+1))
    azigram_amp=np.zeros(shape=(numbins,len(trace_n.data)/ts+1))

    amplitude = [sqrt(n**2+e**2) for n,e in zip(trace_n.data, trace_e.data)]
    pm_angle = [atan2(e,n)*180/pi for e,n in zip(trace_e.data, trace_n.data)]
    for x in samples:
        if pm_angle[x] < 0.0:
            pm_angle[x] += 360.0
        if pm_angle[x] >= 360.0:
            pm_angle[x] -= 360.0

    # y is angle bin number (i.e. angle/width of bin > rounded off)
    y = int(pm_angle[x]/binwidth)
    #Use print statement below to verify angle output
    #print ('E: ',trace_e.data[x], ' N: ', trace_n.data[x], ' Angle: ', pm_angle[x], 'deg \n')

```

```
    azigram[y][int(x/ts)] += 1
    azigram_amp[y][int(x/ts)] += 1*amplitude[x]
    return (amplitude, pm_angle, azigram, azigram_amp)
```

```
# Call main() function to execute
main()
```